UNIVERSITY OF ROCHESTER
LABORATORY FOR LASER ENERGETICS

Volume 99
April–June 2004
DOE/SF/19460-555

LLE Review

Quarterly Report

About the Cover:

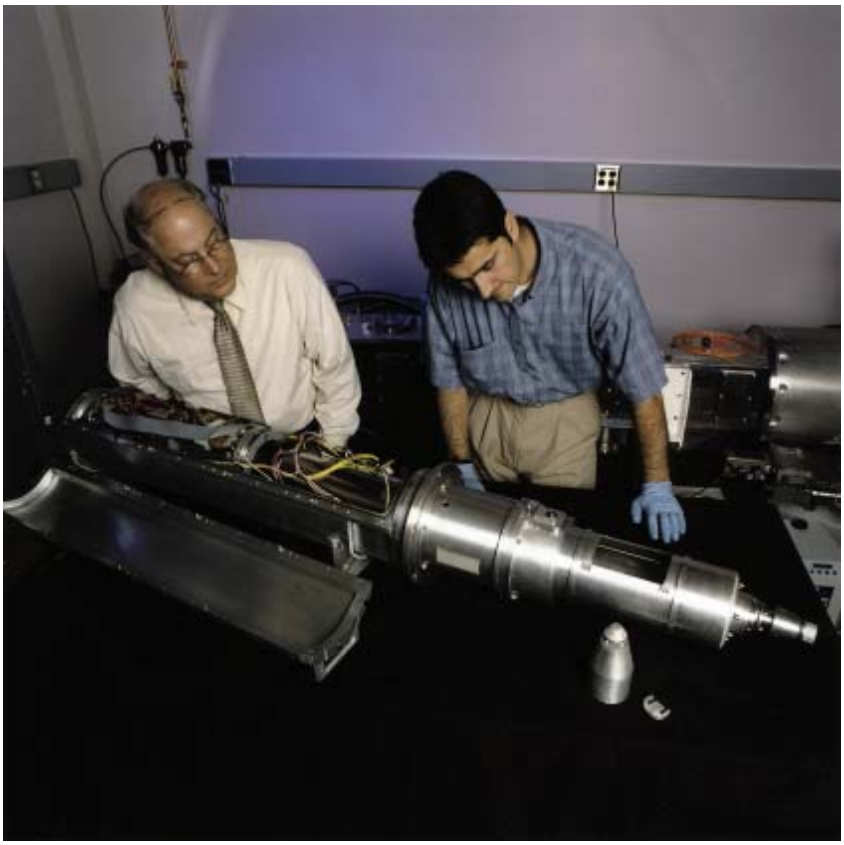

Senior Scientist James Knauer and Doctoral Candidate Orlin Gotchev prepare for the insertion of the x-ray-mirror assembly into the new, modular Kirkpatrick–Baez x-ray microscope. By mixing iridium-coated mirrors with multilayer ones, they will obtain simultaneous images in distinct x-ray energy bands, a major advantage whenever large changes in the plasma attenuation length occur within the instrument's field of view. Used in the imaging of small, high-spatial-frequency perturbations in high-temperature, laser-generated plasmas, this versatile, quick-adjust instrument is detailed in the article featured on p. 183.

The work described in this volume includes current research at the Laboratory for Laser Energetics, which is supported by New York State Energy Research and Development Authority, the University of Rochester, the U.S. Department of Energy Office of Inertial Confinement Fusion under Cooperative Agreement No. DE-FC03-92SF19460, and other agencies.

Printed in the United States of America
Available from
National Technical Information Services
U.S. Department of Commerce
5285 Port Royal Road
Springfield, VA 22161

Price codes: Printed Copy A05
Microfiche A01

For questions or comments, contact Ansgar W. Schmid, *Editor*, Laboratory for Laser Energetics, 250 East River Road, Rochester, NY 14623-1299, (585) 275-3541.

Worldwide-Web Home Page: http://www.lle.rochester.edu/

UNIVERSITY OF ROCHESTER
LABORATORY FOR LASER ENERGETICS

Volume 99
April–June 2004
DOE/SF/19460-555

LLE Review

Quarterly Report

UR LLE

Contents

In Brief

The key article in this volume of the LLE Review, covering April–June 2004, deals with "Multidimensional Simulations of Plastic-Shell Implosions on the OMEGA Laser" by P. B. Radha, V. N. Goncharov, T. J. B. Collins, J. A. Delettrez, D. E. Keller, P. W. McKenty, J. P. Knauer, J. A. Marozas, S. Skupsky, V. Yu. Glebov, F. J. Marshall, D. D. Meyerhofer, S. P. Regan, T. C. Sangster, and C. Stoeckl; and R. P. J. Town (LLNL) (p. 139). In it, the multidimensional hydrodynamic code *DRACO* is applied to studies of shell stability during the acceleration phase in the presence of nonuniform illumination and target roughness. Simulations show that for thick shells remaining integral during the acceleration, the target yield is reduced by a combination of long-wavelength modes due to surface roughness and beam-to-beam imbalance and intermediate modes due to single-beam nonuniformities. Compared to 1-D predicitions, the neutron-production rate for these shells truncates. Diminished yield for thin shells is mainly due to shell breakup at short-wavelength scales of the order of the in-flight shell thickness. *DRACO* simulation results are consistent with experimental observations.

Additional highlights of recent research presented in this issue include the following:

- D. R. Harding, L. M. Elasky, S. Verbridge, W. Seka, R. S. Craxton, L. D. Lund, D. Edgell, M. D. Wittman, and E. L. Alfonso provide a comprehensive overview of the methodology of, and issues involved in, the preparation of deuterium-ice layers in OMEGA targets (p.160). The process of first forming and then smoothing the ice layer is governed by multiple parameters that, when optimally controlled, yield ice layers approaching a 1-μm-rms roughness in low-spatial-frequency modes.

- O. V. Gotchev, P. A. Jaanimagi, J. P. Knauer, F. J. Marshall, and D. D. Meyerhofer describe the development and fielding of a new, modular x-ray streaked imager that combines a four-mirror Kirkpatrick–Baez microscope with a high-current PJX streak tube (p. 183). Performance optimized for use at 1.5 keV, the instrument provides better-than-5-μm spatial resolution over its central 200-μm field of view

- V. Bagnoud, I. A. Begishev, M. J. Guardalben, J. Puth, and J. D. Zuegel; and T. Mooney and P. Dumas (QED Technologies) report on improving laser power-amplifier performance through compensating laser-rod bulk inhomogeneities by magnetorheological single-surface wavefront correction (p. 194). Large-aperture rods corrected in this manner render nearly diffraction limited output-beam performance.

- V. N. Glebov, C. Stoeckl, T. C. Sangster, and S. Roberts; and G. J. Schmid, R. A. Lerche, and M. J. Moran (LLNL) discuss several prototypes of NIF neutron-time-of-flight detectors developed and tested on OMEGA (p. 202). Based on OMEGA results, these detectors will be able to measure ion temperatures of, and neutron yields from, NIF targets generating between 10^9 and 10^{19} neutrons.

- R. Rey-de-Castro, D. Wang, X. Zheng, A. Verevkin, M. Mikulics, P. Kordoš, A. Mycielski, and R. Sobolewski report on ultrafast current sensing that has reached a new level of sensitivity and speed by taking advantage of the magneto-optic Faraday effect in CdMnTe single crystals (p. 208). To date, response times of a few hundred femtoseconds can be realized at a current sensitivity of ~0.1 mA at 10 K.

- J. Li, W. R. Donaldson, and T. Y. Hsiang introduce a submicron-scale ultraviolet photodiode based on a metal-semiconductor-metal structure on GaN (p. 212). The authors built, tested, and then simulated the circuit by a distributed-circuit approach that yielded close agreement between theory and observation of the impulse-response, space-charge-screening broadening found in the device.

- Q. Guo, X. Teng, and H. Yang offer a new method for patterning nanoparticles and self-assembled monolayers through the use of elastomeric stamps and their controlled deformation by overpressure (p. 218). Their method enables pattern formation on a scale length up to an order of magnitude smaller than the original stamps as well as patterns that do not exist in the original masters. As one example, magnetic ring and anti-ring structures are being fabricated for memory-device applications.

Ansgar W. Schmid
Editor

Two-Dimensional Simulations of Plastic-Shell, Direct-Drive Implosions on OMEGA

Introduction

In direct-drive inertial confinement fusion (ICF),[1] nominally identical beams of a laser are incident on a nearly spherically symmetric target. The target's outer surface ablates, driving the shell inward like a rocket. The shell first accelerates and then, shortly after the laser drive is turned off, coasts before decelerating toward peak compression; disassembly then follows. The goal is to implode the target, resulting in sufficiently high temperatures and densities to propagate a self-sustaining burn wave through the target, giving rise to energetic neutrons with a total energy greater than the laser energy. Ignition target designs require layers of cryogenic deuterium–tritium (DT) ice[2] and relatively high laser energies such as those available on the National Ignition Facility (NIF).[3] To provide an understanding of target dynamics, a large number of implosions on the 60-beam OMEGA laser[4] have been devoted to warm capsules,[5–8] which include plastic (CH) shells filled with deuterium (D_2) gas. While a number of papers have been written on the experimental results from CH-shell implosions on OMEGA,[5–8] the range of nonuniformity wavelengths that influence fusion yields has been an outstanding question.

In this article, a detailed analysis of the CH-shell implosions using one- and two-dimensional simulations and analytical modeling is performed. The goal of this work is to identify, by using the hydrodynamic code *DRACO*,[9] the nonuniformity seeds that influence target performance. Mechanisms that influence yields are also identified. In addition, comparisons to experimental results are presented.

Imperfect illumination and target roughness seed the nonuniformity growth in direct-drive implosions. The incident laser irradiation on the target includes nonuniformities that result from energy and power imbalances between beams and from nonuniformities within each beam. While the former will be shown to result in long-wavelength ($\ell < 10$, where $\ell = 2\pi R/\lambda$ is the Legendre mode number, R is the target radius, and λ is the nonuniformity wavelength) perturbations that lead to an overall deformation of the shell, the latter manifest themselves in the intermediate-wavelength ($10 < \ell < 50$) and short-wavelength ($\ell > 50$) nonuniformities that may lead to shell breakup during the acceleration phase as well as a disruption in final fuel assembly.

Nonuniformities grow due to the Rayleigh–Taylor (RT) instability[10] during the acceleration phase of the implosion. The RT growth rates are smaller than classical values due to the ablative effects.[10–13] Nevertheless, the RT growth factors of the short-wavelength modes in the thin shells are large enough to compromise shell integrity during the acceleration phase. Shell breakup results in degradation in the shell's compressibility, which leads to a reduction in the final core temperature and density and consequently a reduction in the neutron-production rates.

Nonuniformity growth during the coasting and deceleration phases of the implosions is seeded by feedthrough to the inner surface of the shell. As will be shown later in the text, the fuel–pusher interface distortions grow significantly during the coasting phase because of convergent effects (Bell–Plesset growth).[14,15] Further, truncation of the neutron-production rate occurs due to the flow of fuel into the colder bubbles at the D_2–CH interface during shell deceleration. Truncation is also caused by the increased heat conduction out of the core due to the larger surface area caused by shell distortions.

This article is organized as follows: (1) one-dimensional and multidimensional hydrodynamic modeling are described; (2) overall shell dynamics is discussed; (3) the four phases of the implosion (shock transit, acceleration, coasting, and deceleration) are analyzed in the context of single-mode growth; (4) multidimensional simulations of beam-to-beam imbalances and single-beam nonuniformity are described, and the combined effects of all nonuniformity sources are discussed; and (5) conclusions are presented.

Radiation-Hydrodynamics Modeling

The one-dimensional (1-D) target dynamics discussed in this article is modeled using the code *LILAC*,[16] which has been described extensively in the literature and is not discussed any further.

Multidimensional behavior (2-D) of plastic targets is modeled using the code *DRACO*.[9] *DRACO* is a one-, two-, and three-dimensional arbitrary Lagrangian Eulerian (ALE) code based on a structured mesh. The implosions described here are simulated in one and two dimensions. The compressible hydrodynamic scheme is based on the work by Amsden *et al*.[17] Shocks are treated using the scheme of Wilkins.[18] Several artificial grid-smoothing algorithms are available to control numerical grid distortions (bowties and herringbone distortions). These are based on Refs. 17–19; only Ref. 19 is used in this work.

In a purely Lagrangian mode, interfaces between materials are maintained at cell edges; however, a significant growth of perturbations results in a severely distorted grid. As a result, the grid must be "rezoned" for the simulation to proceed. The new grid can be constructed using several prescriptions. While some grid movement options are heuristically derived, others are based on Winslow-regridding–type[20] schemes. *DRACO* allows for cells with mixed materials resulting from this grid rezoning. Rezoning is possible through a first-order (donor-cell) or a direction-split second-order scheme.[21] Material interfaces are reconstructed before every rezoning step using a scheme based on Young's method,[22] which has been extended to allow for the distorted Lagrangian cells. In this scheme, the interface between materials in a cell is represented by a straight line; the slope of this line is obtained through the gradient of the fractional volumes occupied by the material in the neighboring cells.

The pressure in each mixed-material cell is obtained by adding the partial pressures of the constituent cell materials. A single temperature for the materials in the cell is obtained using the prescription described in Ref. 23. While this interface tracking scheme cannot be used to model turbulent regimes,[22] it has been used to model the highly nonlinear growth of buried layers that burn through to the corona.[9]

Various physical processes, such as heat conduction, radiation transport, etc., are treated using an operator splitting procedure. *DRACO* includes the deposition of laser energy through ray tracing and inverse bremsstrahlung. Both normal-incidence laser energy deposition and the ray-trace approach are used in this work. Since normal incidence does not include refractive energy losses, it can significantly overestimate the energy coupled to the target. Consequently, the laser pulse shape is iteratively adjusted in 1-D simulations to provide the same overall dynamics of the implosion, including shock-breakout times, the final convergence of the shell, ablation velocities, density scale lengths, etc., as obtained with a full ray trace. This modified pulse shape is used in two-dimensional (2-D) simulations involving modes ≥20. Spherically symmetric 2-D simulations with this modified pulse shape compare very well with 1-D simulations using a full ray trace. For simulations that include only long-wavelength modes, we use a refractive ray trace. This ray trace uses a quasi-1-D scheme, where rays are not allowed to cross angular sector boundaries. This scheme accounts for refractive losses reasonably accurately when the distortions are of relatively long wavelengths. In this technique, an angular spectrum describing the distribution of energy with angle of incidence is launched from a chosen surface each time step. This distribution takes into account both the single-beam ray distribution and beam overlap. In the limit of a spherically symmetric problem, this approach yields the same results as a full ray trace.

Several equation-of-state options (ideal gas, *SESAME*,[24] Thomas–Fermi,[25] and QEOS[26]) are available; the analytic Thomas–Fermi formulation is used for the simulations described in this work. Heat conduction and multigroup diffusive radiation transport are included. Tabular opacities assuming local thermal equilibrium are used for the materials while in unmixed cells. An ion-number weighted opacity is used in mixed cells for radiation transport. Radiation transport is solved in parallel across several processors.

The simulations use the "group-parallel" approach where each energy group is solved on one processor and the resulting radiation energy density is broadcast to all other processors. Four radiation groups, reduced from very fine opacity tables,[27] are included in all the calculations in this work. The choice of the four energy groups is optimally made to closely match the 1-D dynamics corresponding to 48 energy groups. The parallel scientific library, PetSc,[28] is used to solve the diffusion equation via a preconditioned conjugate-gradient scheme. Message Passing Interface (MPI)[29] is used to communicate between processors.

Particle production from nuclear reactions is calculated using Ref. 30. Alpha-particle transport and depletion of fuel material for modeling ignition are included in *DRACO* but are not necessary in simulating OMEGA target implosions.

DRACO has been tested extensively against analytic problems (shock-tube problems, blast-wave problems, etc.), against other codes (*LILAC*,[17] *ORCHID*[31]), and against the ICF post-processor described in Ref. 32 for single-mode growth. Good agreement is obtained with the known solutions for all the problems considered.[9]

Shell Dynamics

This work focuses on targets with plastic (CH) shells filled with D_2 gas. Two cases are considered (Fig. 99.1): (1) a 20-μm-thick CH shell with 15 atm of D_2 with a convergence ratio CR ~ 13 (CR is defined as the ratio of the initial radius to the compressed radius of the fuel–shell interface at the peak of the neutron production); (2) a 27-μm-thick CH shell with 15 atm of D_2 (CR ~ 12). A 1-ns square pulse with ~23 kJ of energy is used to irradiate these targets with full beam smoothing [two-dimensional smoothing by spectral dispersion[33] (2-D SSD) with polarization smoothing (PS)[34]]. Case (1) has been chosen to illustrate implosion dynamics (Fig. 99.2). The laser pulse and shell acceleration history are shown in Fig. 99.2(a). The magnitude of the gradient of the natural logarithm of the pressure, $|\partial \ln P/\partial r|$, is shown in Fig. 99.2(b). The dark lines correspond to shock trajectories. The dashed line is the trajectory of the fuel–shell interface. Since the rise time of the laser is relatively fast (~200 ps), a strong shock is driven into the target, setting the shell material on a high adiabat, $\alpha \sim 5$, defined as the ratio of the pressure at a given density to the cold Fermi pressure at that density. The rarefaction wave launched at the breakout of the shock (at ~0.4 ns) from the shell reaches the ablation surface, where a compression wave is consequently launched into the target. At this time the shell starts to accelerate inward as indicated by the negative acceleration in Fig. 99.2(a). The compression wave travels down the decreasing density gradient and breaks out of the shell as a shock (at ~0.8 ns). Both shocks meet in the gas (at ~1 ns) before reaching the center. The four main phases of the implosion are shown in Fig. 99.2(a). The acceleration phase occurs after shock transit and continues until shortly after the laser pulse turns off (at ~1.4 ns), at which time the shell starts traveling with a constant velocity (coasting phase). Deceleration of the shell begins when the shock reflects from the center and returns to the shell (at ~1.75 ns). This impulsive deceleration is followed by a period of continuous deceleration due to pressure buildup in the gas [Fig. 99.2(a)].

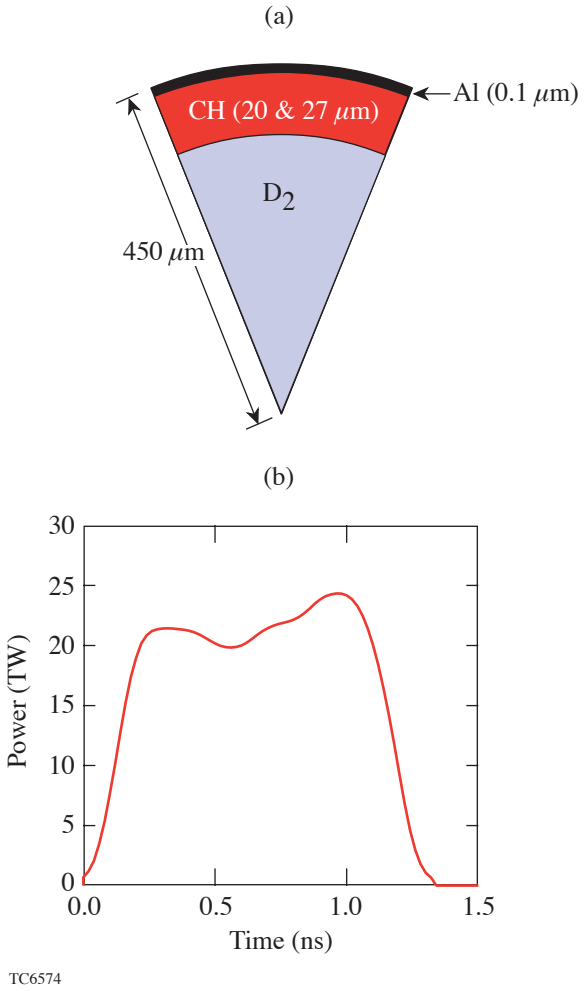

Figure 99.1
(a) Plastic-shell targets of two thicknesses—20 μm and 27 μm—with D_2 fills were considered in this work. (b) The pulse shape (1-ns square) used to irradiate these targets sets the shell on a relatively high adiabat (~5).

Shock breakout is later in the thicker, 27-μm implosion (at ~0.5 ns compared to ~0.4 ns). The more-massive, 27-μm-thick shell moves more slowly during the coasting phase than the 20-μm-thick CH shell. It therefore coasts for a longer time (~650 ps compared to ~350 ps). The shell's convergence ratio for the coasting phase, defined as the ratio of the shell radius at the beginning and end of the coasting phase, is 3.0 for the thicker shell compared to 2.2 for the thinner shell.

Single-Mode Simulations

In this section, the evolution of nonuniformities through single-mode simulations is described. The seeding of nonuniformities is described in "Shock Transit." The growth during the three phases—acceleration, coasting, and deceleration—is described in subsequent subsections.

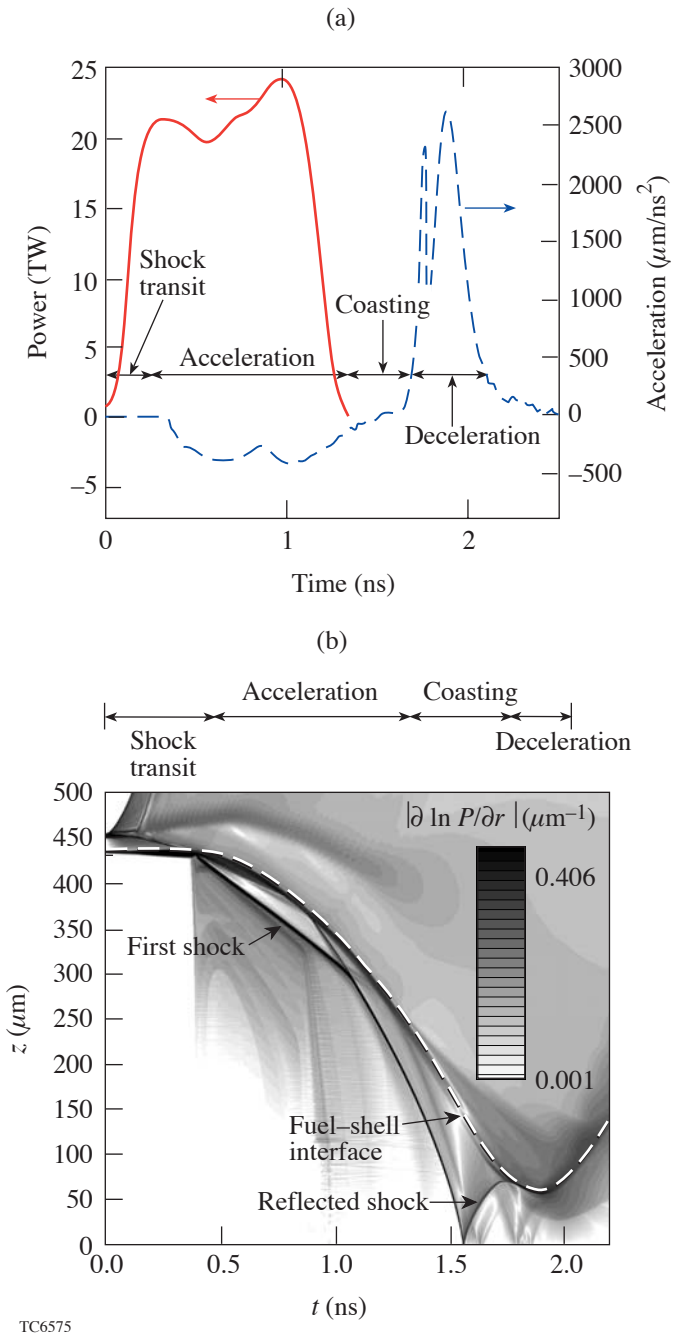

Figure 99.2
(a) Acceleration and laser pulse shape history (1-ns square) for the 20-μm CH shell irradiated with a 1-ns square pulse at 23 kJ of energy. (b) Contour plot of the magnitude of the gradient of the natural log of pressure for the target in (a). The darker contours correspond to shock trajectories. The dashed line is the trajectory of the fuel–shell interface. Also shown is the duration of the four phases of the implosion (shock-transit, acceleration, coasting, and deceleration).

1. Shock Transit

As mentioned in the last section, a strong shock is launched into the shell at the beginning of the pulse. Since there is no significant acceleration of the ablation front during the shock propagation through the shell, the shell nonuniformities are not susceptible to Rayleigh–Taylor instability. The perturbations, however, grow during this phase because of nonuniform laser illumination (power imbalance, beam mistiming, and single-beam nonuniformities or laser imprint). The initial outer-surface roughness, in general, can be amplified as well by Richtmyer–Meshkov[35] instability at the ablation front; such a growth, however, is totally stabilized by ablation.[36] As a result, the mode spectrum due to the initial outer-surface roughness does not significantly change during shock transit.

First, the evolution of long-wavelength modes seeded by power imbalance among the 60 OMEGA beams is described. This imbalance is due to beam mispointing, different beam shapes, beam mistiming, and energy imbalance between beams. The resultant laser illumination amplitudes due to all these sources are shown in Fig. 99.3 for the dominant modes. The tilt that might be introduced to each beam pulse shape is not included in these calculations. Azimuthal asymmetries in each phase plate are also not modeled. The perturbation amplitude for a given mode is obtained by overlapping and decomposing

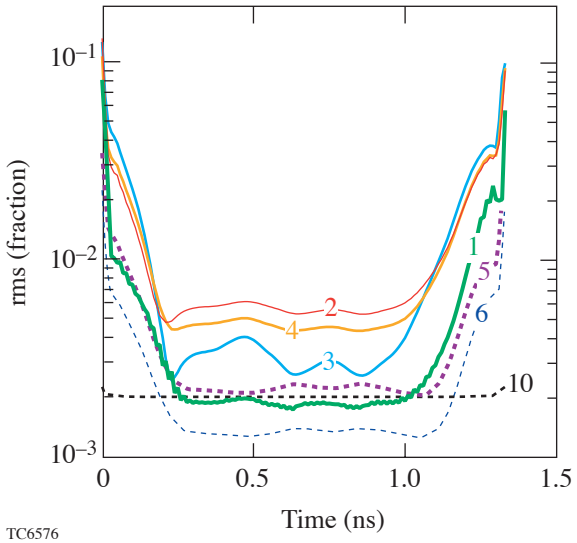

Figure 99.3
Modal amplitudes of the dominant modes due to beam imbalances as a function of time. The early-time large amplitudes correspond to beam mistiming. The values at the peak of the pulse (0.2 ns to 1.1 ns) are due to energy imbalance between beams, beam mispointing, and differences in spot shapes.

the 60-beam energies on a sphere into spherical harmonics. The amplitude of the corresponding Legendre mode is obtained by adding all the m-mode amplitudes in quadrature. The phase of the mode is chosen to be that of the $m = 0$ spherical harmonic. The large perturbation amplitudes of the Legendre modes correspond to the beginning of the laser pulse and are mainly due to beam mistiming (~12-ps rms). Once the peak intensity is reached, the nonuniformity reaches its asymptotic value corresponding to the energy imbalance in the beams (beam energies of the 60 OMEGA beams from a typical shot are used to apply energy imbalance), beam mispointing (~24-μm rms),[37] and differences in beam shapes (~11-μm rms in super-Gaussian radius and ~0.6% rms in super-Gaussian exponent). These values are typical of OMEGA. The target is assumed to be at the target chamber center. (Typically on OMEGA, plastic shells are within 5 μm of target chamber center at shot time.) Mode numbers 2 and 4 have the largest amplitudes as indicated by Fig. 99.3. Mode number 10 is due to the 60-beam OMEGA geometry.

A model that describes the seeding of the ablation surface due to the long-wavelength nonuniformities is described in Appendix A. This sharp-boundary model relates the modal amplitudes at the fuel–shell interface to the modulation in drive pressure, which in turn is related to the modulations in laser intensity using the "cloudy-day" model.[38] Here, the results of this model are compared with the full 2-D simulation involving modes up to 10. The modal amplitudes of the D_2–CH interface at the onset of the acceleration phase are shown in Fig. 99.4 for the 20-μm-thick implosion. These are obtained by decomposing the interface perturbations from the 2-D simulation into Legendre modes (solid circles). The amplitudes obtained from the model (x's) are also shown in Fig. 99.4. The results of the simulation are reproduced well by the simple model.

Next, the evolution of target nonuniformities caused by single-beam modulations (laser imprint) is described. Since laser imprint stays in the linear regime during shock transit, the mode spectrum is calculated by carrying out a series of single-mode, 2-D simulations up to the beginning of the acceleration phase. Imprint simulations are performed by imposing a 1% single-mode modulation in the laser illumination. 1-THz, 2-D SSD[32] is applied to the perturbation amplitudes. SSD is modeled nondeterministically. Each mode is characterized by a coherence time given by $t_c = \left[\Delta\nu \sin\left(n_c \pi \ell / \ell_{\max}\right)\right]^{-1}$, where $\ell_{\max} = 2\pi R_0/\delta$ is the mode number corresponding to half the speckle size δ ($\delta = 2.35$ μm for the OMEGA system), R_0 is the initial outer shell radius, $\Delta\nu$ is the SSD bandwidth, and n_c is the number of color cycles on the laser system. The phase of the mode is chosen randomly every coherence time (the "flipping" approximation). This scheme mimics the average response of the target to the laser modulations. Averaged over time T, the single-beam rms nonuniformity, for a constant-intensity laser pulse, decreases as $\sqrt{t_c/T}$. For each mode in the simulation, the sequence of phases corresponds to a discrete two-state random walk. The number of the statistically independent phase sequences is limited by a finite maximum angular spread $\Delta\theta$ of the light propagating through the laser. The averaged mode amplitude cannot be reduced by SSD to levels below the asymptotic limit. This limit is inversely proportional to the square root of the number of statistically independent speckle patterns $N_{\text{stat}}(\lambda) = \left(4S^x_{\max}/\lambda\right)\left(4S^y_{\max}/\lambda\right)$, where $\lambda = 2\pi R_0/\ell$ is the nonuniformity wavelength, $S^{x(y)}_{\max} = F\Delta\theta^{x(y)}$ is the maximum spatial shift in the $x(y)$ direction, F = 180 cm is the focal length, and $\Delta\theta^x$ = 50 μrad and $\Delta\theta^y$ = 100 μrad for the OMEGA laser system. The asymptotic limits are modeled in the flipping approximation by selecting only N_{stat} independent choices for the sign of the nonuniformity amplitude. The average over a large number of runs will then correspond to the expected response of the target to the single mode. The calcu-

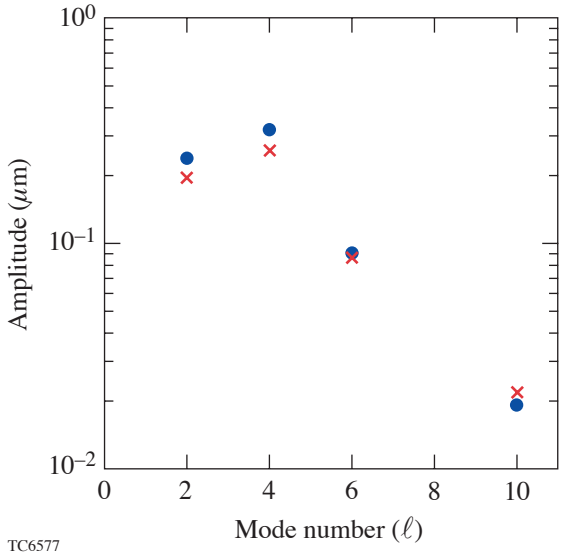

Figure 99.4
Single-mode amplitudes of the fuel–shell interface at the beginning of acceleration from a 2-D simulation for the 20-μm-thick CH implosion (solid circles). The values obtained from the model described in Appendix A are also shown (x's). The "cloudy-day" model relates the amplitudes at the fuel–shell interface to modulation in laser drive. Good agreement between the simulations and model indicates that the seeding of the interface is well understood.

lated ablation-front amplitude at the beginning of the acceleration phase $\eta_{\%}$ is a decaying function of the mode number ℓ.[39] This is due to both the shorter decoupling time and the stronger dynamic overpressure stabilization of the higher-ℓ modes. When the effect of SSD is included, the imprint efficiency scales linearly with the mode wavelength. For the plastic shells driven by a 1-ns square pulse with 1-THz, 2-D SSD, the numerical calculations give the following ablation-front amplitude per 1% laser nonuniformity:

$$\eta_{\%} \simeq 6\times 10^{-5}\left(6.7+2\pi R_0/\ell\right), \tag{1}$$

where the initial shell radius R_0 and $\eta_{\%}$ are in microns. To calculate the mode spectrum at the ablation front due to the laser imprint, amplitude $\eta_{\%}$ is multiplied by σ_{rms} of the laser nonuniformity of a particular mode.

Calculation of the laser $\sigma_{\text{rms}}(\ell)$ includes the effects of the distributed phase plates (DPP's).[40–42] Laser beams are phase converted by being passed through the DPP's on the OMEGA laser. The DPP's improve the focused single-beam uniformity by removing the large-scale beam structure with a higher imprint efficiency [see Eq. (1)], leaving intensity profiles with a well-controlled envelope modulated by fine-scale speckle with a lower imprint efficiency. An analytical model that describes this fine speckle[43] is used to model the static single-beam nonuniformity in 2-D simulations in which the ℓ-mode nonuniformity is given as

$$\sigma^2_{\text{rms}}(\ell) = \frac{16\ell}{\pi\ell^2_{\max}}\left[\cos^{-1}\left(\frac{\ell}{\ell_{\max}}\right) - \frac{\ell}{\ell_{\max}}\sqrt{1-\left(\frac{\ell}{\ell_{\max}}\right)^2}\right]. \tag{2}$$

This mode spectrum was confirmed experimentally in Ref. 44. The illumination nonuniformity given by Eq. (2) is shown in Fig. 99.5 as a function of mode number. Note that the laser nonuniformity amplitudes increase initially as a function of mode number (up to $\ell \sim 600$), opposite to the decay in the imprint efficiency with the wave number [Eq. (1)].

Polarization smoothing further reduces the amplitude by a factor of $\sqrt{2}$.[34] Further reduction in modal amplitudes is obtained with beam overlap. This reduction factor is obtained by comparing the result of overlapping 60 OMEGA beams on a sphere with the single-beam DPP amplitudes. A reduction factor of $\sqrt{12}$ reproduces the resultant overlapped amplitude pattern on a sphere. Overall amplitudes in the *DRACO* simulation are correspondingly reduced. The resulting imprint spectrum (dotted line) at the ablation front is plotted in Fig. 99.6. Figure 99.6 also shows the ablation-surface amplitude due to imprint from one multimode *DRACO* simulation up to mode number 200 (solid line). The multimode simulation

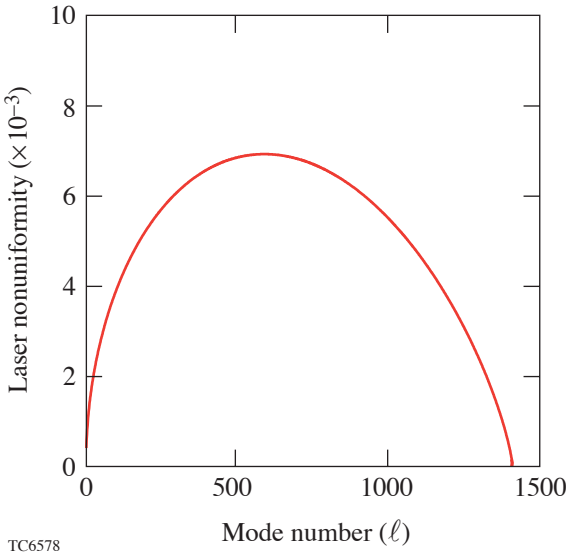

Figure 99.5
Nonuniformity spectrum due to phase-plate speckle. This nonuniformity peaks around $\ell \sim 600$.

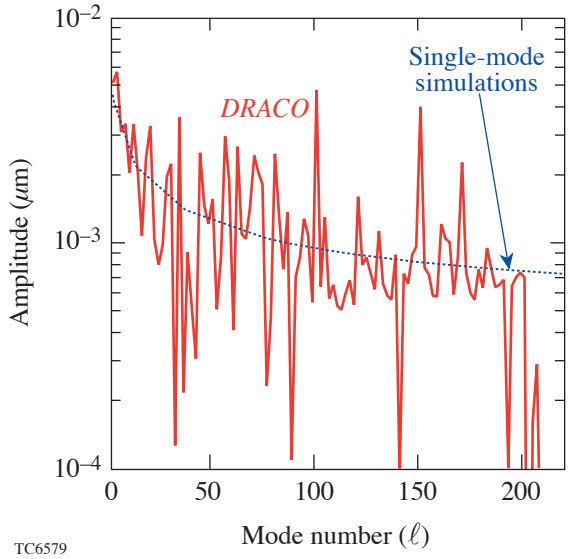

Figure 99.6
Imprint spectrum from single-mode simulations (dotted line) and multimode simulation (solid line). The good agreement confirms linear behavior of imprint. Note that imprint efficiency decreases with increasing mode number. This is opposite in behavior to the laser nonuniformity (Fig. 99.5).

shows variations in the imprint spectrum due to the nondeterministic scheme used to model SSD. Good agreement, on average, between the two calculations confirms the linear behavior of imprint prior to shell acceleration.

The seeding due to all three nonuniformity sources is compared in Figs. 99.6 and 99.7. The contribution of the ablation-surface nonuniformity from power imbalance and surface roughness[45] is shown in Fig. 99.7. The comparison of this spectrum with Fig. 99.6 shows that the main contribution to the low-ℓ modes comes from beam imbalances. Surface roughness has a smaller contribution at low ℓ. Laser imprint dominates the intermediate ($10 < \ell < 50$)- and high-ℓ-mode seeding (not shown).

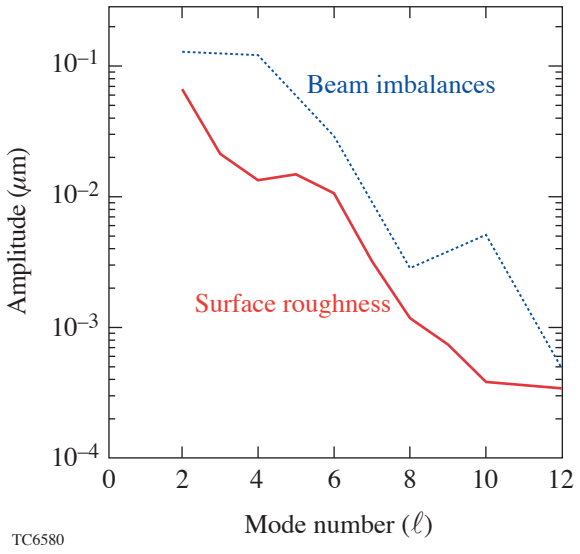

Figure 99.7
Long-wavelength perturbations at the ablation surface due to beam imbalances (dotted line) and surface roughness (solid line) at the start of acceleration. Beam imbalances provide the larger contribution to long-wavelength nonuniformity seeds.

2. Acceleration Phase

The two main sources of perturbation growth during the acceleration phase are (1) the RT instability caused by the opposite directions of the pressure and density gradients at the ablation front and (2) the secular growth due to the asymmetries in the laser drive. The latter growth is important only for low-ℓ modes where the wavelength is much longer than the distance between the laser deposition region and the ablation front (conduction zone). Shorter-wavelength drive nonuniformities are smoothed out by the thermal conduction in the conduction zone (the cloudy-day effect). In addition, the RT growth rate increases with mode number; therefore, secular growth becomes negligible at the shorter wavelengths.

The relative importance of the secular growth versus the RT growth for different long-wavelength modes is illustrated in Appendix B using a simple model. The model indicates that the final amplitudes at the end of the acceleration phase caused by secular growth alone are significantly smaller than when RT growth is also included. This suggests that power balance is extremely important during the period of shock transit when the seeds for RT growth are established. During acceleration, beam imbalances are less important because the resulting secular growth is dominated by RT growth. This is confirmed by the results of the simulations shown in Fig. 99.8. In simulation 1 (solid line), beam imbalance is turned off at the start of acceleration, whereas in simulation 2 (dotted line), it is retained throughout the laser pulse. The ablation-surface amplitudes vary by less than 20%, confirming that beam balance is important primarily during shock transit.

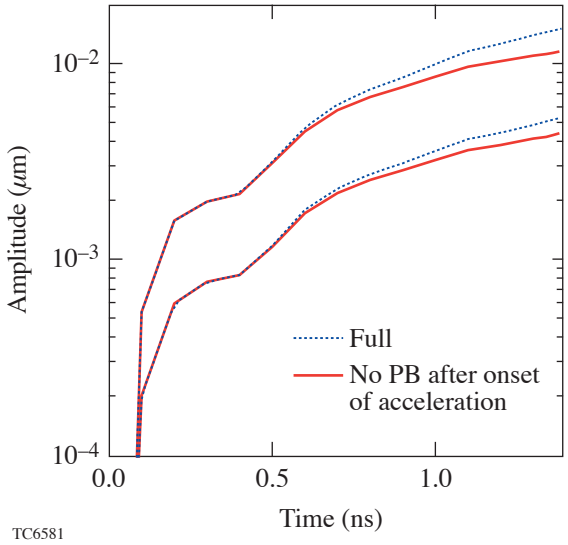

Figure 99.8
Amplitudes of the D_2–CH interface versus time for mode numbers 2 and 4 for beam imbalances throughout the pulse (dotted) and beam imbalances imposed on target only until the start of acceleration (solid). The small effect of beam imbalances during the acceleration phase indicates that long-wavelength modes are seeded primarily during shock transit.

Next, evolution of the intermediate ($10 < \ell < 50$)- and short-wavelength modes ($\ell > 50$) is considered. The main seed of these modes comes from the single-beam nonuniformity (laser imprint). The initial spectrum of imprint perturbations at the ablation surface is peaked at the low-ℓ modes (Fig. 99.6). The RT growth rate, however, increases with the mode number,

shifting the spectrum maximum during acceleration toward shorter wavelengths. It is well known that mass ablation significantly reduces RT growth rate compared to the classical limit.[11–13] As shown in Ref. 44, a rather complicated expression for the growth rate can be fitted with much simpler formulas:

$$\gamma = \alpha_1 \sqrt{kg} - \beta_1 k V_a, \quad Fr >> 1, \tag{3}$$

$$\gamma = \alpha_2 \sqrt{\frac{kg}{1+kL_m}} - \beta_2 k V_a, \quad Fr << 1, \tag{4}$$

where $Fr = V_a^2 / (gL_0)$ is the Froude number, L_0 is the characteristic thickness of the ablation front, L_m is the minimum density-gradient scale length, and V_a is the ablation velocity defined as the mass ablation rate divided by the shell density. The coefficients $\alpha_{1,2}$ and $\beta_{1,2}$ are functions of the Froude number and the effective power index for thermal conduction ν. The dispersion formulas described in Eqs. (3) and (4) have been verified experimentally in Ref. 45 for CH. For the 20-μm-thick plastic shell considered in this article, the time-averaged acceleration, ablation velocity, ablation-front thickness, and power index, respectively, are $g = 320$ μm/ns^2, $V_a = 3.2$ μm/ns, $L_0 = 0.18$ μm, $L_m = 0.72$ μm, and $\nu = 1$; therefore, the Froude number is small, $Fr = 0.18$, and Eq. (4) can be used to calculate the RT growth rate. The fitting procedure described in Ref. 44 gives the following coefficients: $\alpha_2 = 0.94$ and $\beta_2 = 1.50$. Growth rates from single-mode simulations (solid circles in Fig. 99.9) compare very well with this analytic formula (dotted line in Fig. 99.9). Each simulation point in Fig. 99.9 is a single-mode simulation with a small amplitude perturbation to the laser nonuniformity, such that the mode growth remains in the linear regime during the acceleration. Equation (4) also indicates that the cutoff occurs at very high ℓ modes, $\ell_c = 1220$, and the growth rate does not decrease significantly even for mode numbers as high as $\ell \sim 600$ for these plastic ablators. Modes above $\ell \sim 600$, however, have a much smaller initial amplitude and experience nonlinear saturation. Their contribution to the total nonuniformity budget, therefore, is insignificant.

It is instructive to point out the stabilizing role of the radiation. Reabsorption of the emission from the corona by the shell raises the shell adiabat near the ablation front, leading to adiabat shaping by radiation in the shell. This increases the ablation velocity (from ~2.2 μm/ns to ~3.2 μm/ns) and the density-gradient scale length (from $L_m = 0.1$ μm to 0.7 μm). Since the density is much sharper when the radiation transport is turned off, the Froude number increases, $Fr = 0.7$ (compare to $Fr = 0.18$ with radiation). Fitting the growth rate gives the following result: $\gamma_{\mathrm{NoRad}} = 0.92\sqrt{kg/(1+kL_m)} - 1.59\ kV_a$. The cutoff mode number in this case increases from $\ell_c = 1200$ to $\ell_c = 4000$, and the growth rate of mode $\ell = 200$ increases from $\gamma = 7.8$ ns^{-1} to 10.1 ns^{-1}. The growth rates for the cases with and without radiation transport are summarized in Fig. 99.9.

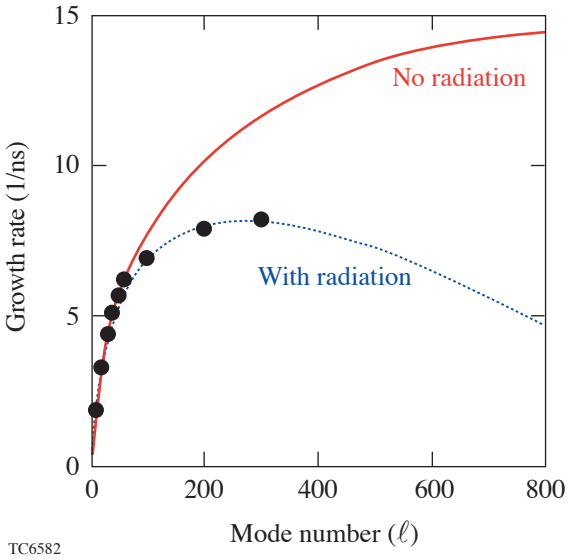

Figure 99.9
Good agreement is obtained with simulated single-mode growth rates (solid circles) and the Betti formula for plastic (dotted line). Also shown is the Betti formula for growth rates when radiation transport is not included in the simulation (solid line). Reabsorption of radiation from the corona plays an important role in stabilizing the growth of perturbations at the ablation surface.

The results from single-mode simulations using the realistic imprint amplitudes caused by the use of phase plates are shown in Fig. 99.10. SSD and polarization smoothing are applied to smooth the nonuniformity over time. Since beam smoothing is modeled nondeterministically, the average of several simulations is used for the ablation-surface amplitude. Each simulation point in Fig. 99.10 is the ablation-surface amplitude obtained from the average of five simulations with the error bar representing the standard deviation of these five simulations. It can be seen that modes up to at least 400 contribute to the ablation-surface nonuniformity. A full 2-D simulation would require, therefore, at least 400 modes to realistically model shell stability during the acceleration phase.

The more-massive, 27-μm-thick plastic shell accelerates less (g = 240 μm/ns^2) and consequently has lower growth

rates. The nonuniformity seeds at the end of the acceleration phase from feedthrough are, therefore, also smaller at the D_2–CH interface.

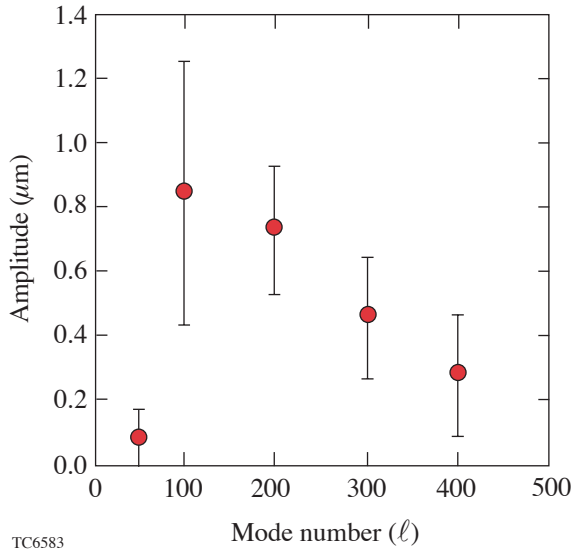

Figure 99.10
Single-mode amplitudes at the end of the acceleration phase. The solid circles are averages of five simulations, each with a different choice of random number seed for the nondeterministic SSD model. The error bars represent the standard deviation of the amplitude across the five simulations. The relatively large values of $\ell = 400$ indicate that such short wavelengths will contribute significantly to the ablation-surface nonuniformity.

3. Coasting Phase

Shortly after the laser drive is turned off, the shell stops accelerating and starts to coast with a spatially averaged velocity that is constant in time. The coasting phase lasts until the main shock reflects from the center and begins to interact with the incoming shell. Even though the shell perturbations are not subject to the RT instability while the shell coasts inward, the perturbations are still amplified by Bell–Plesset growth. This growth is due to convergence and scales approximately as $\eta \sim (\rho r^2)^{-1}$. Since the shell coasts inward, the shell radius decreases and the perturbation amplitude grows. Furthermore, both the front and back surfaces of the shell and the D_2–CH interface expand (in the frame of reference moving with the shell) with the local sound speed, leading to a decrease in the density that further amplifies the perturbations. In general, the equation governing the perturbation evolution in the absence of acceleration has a weak mode-number dependence.[32] Simulations, however, show a strong ℓ-dependence of the Bell–Plesset growth, especially for long- and intermediate-wavelength modes (see Fig. 99.11). Such dependence is due to the differences in long- and short-wavelength growth prior to the coasting phase. Since the low-ℓ RT growth rate scales as a square root of the mode number ℓ, the longer-wavelength perturbations have lower RT growth rates during shell acceleration. Therefore, at the end of the pulse, the velocity perturbation at the D_2–CH interface is proportional to the square root of the mode number. To illustrate how mode dependence appears in the convergence growth, we adopt the simplest model for the perturbation evolution during the coasting phase:[15]

$$\frac{d}{dt}\left[\frac{d\left(\rho r^2 \eta\right)}{dt}\frac{1}{\rho r}\right] = 0. \tag{5}$$

Integrating Eq. (5) twice with the initial conditions $\eta(t=0) = \eta_0$ and $d\eta/dt\,(t=0) = \eta_0' \simeq \sqrt{\ell/R_0 g}\,\eta_0$ gives the perturbation growth factor

$$\frac{\eta}{\eta_0} = C_c^2\left[\frac{\rho_0}{\rho} + \left(-\frac{2V_{\text{imp}}}{\rho R_0^2} + \sqrt{\frac{\ell g}{R_0}}\frac{1}{\rho R_0}\right)\int_0^t \rho(t')r(t')\,dt'\right], \tag{6}$$

where C_c is the shell convergence ratio during the coasting phase, R_0 is the shell radius at the end of the acceleration phase, ρ_0 is the density at the end of the acceleration phase, and V_{imp} is the implosion velocity. Equation (6) shows that the longer-

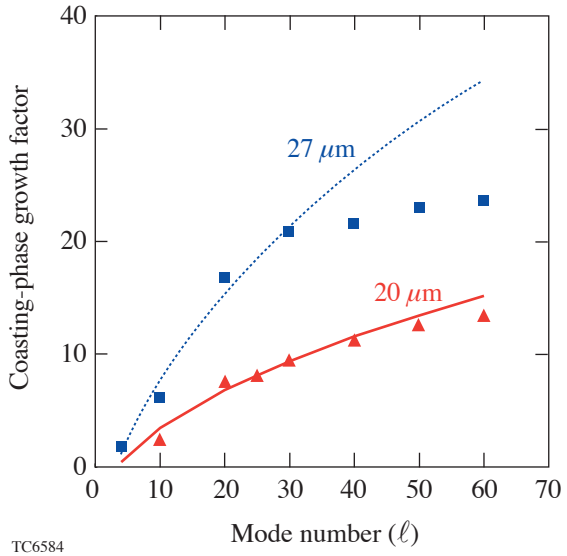

Figure 99.11
Single-mode growth factors for the coasting phase for the 20-μm-thick (triangles) and 27-μm-thick (squares) CH implosions. The lines are $\sim\sqrt{\ell}$ - fit to the growth factors for $\ell < 30$. Growth factors clearly saturate for $\ell > 30$ for the 27-μm-thick CH shell.

wavelength modes experience smaller growth factors, in agreement with the results of simulations (see Fig. 99.11). The behavior of shorter wavelengths ($\ell > 50$), however, is different from Eq. (6). The perturbations at the D_2–CH interface for such modes decouple from the unstable ablation front during shell acceleration when $\Delta_{int}\ell/r$ becomes greater than unity, where Δ_{int} is the distance between the ablation front and the interface. After decoupling, the interface ripple starts to oscillate with increasing amplitude due to the convergence effects. The growth factor for such modes is defined as the ratio of the interface amplitude at the end of shell coasting to the amplitude maximum during the acceleration phase; then, $\eta_0' \neq \sqrt{\ell/rg}\,\eta_0$ and ℓ-dependence of the solution of Eq. (5) becomes much weaker than $\sqrt{\ell}$. This is confirmed in Fig. 99.11, which shows a clear saturation of the growth factors after $\ell \sim 30$ for the 27-μm-thick implosion. The lines in Fig. 99.11 are a $\sqrt{\ell}$ fit to the growth factor for $\ell < 30$. For the 20-μm-thick implosion, this saturation is less apparent. The 27-μm shell moves slower during the acceleration phase; hence, it coasts for a longer time ($C_c = 2.2$ for 20-μm shell and $C_c = 3.0$ for 27-μm shell). This leads to larger coasting-phase growth factors in thicker shells. It is important to note that the larger D_2–CH growth factors during coasting partially compensate for the smaller nonuniformity seeds at the start of the coasting phase for the thicker, 27-μm implosion. At shell stagnation, therefore, the interface distortions exhibit very little sensitivity to shell thickness.

4. Deceleration Phase

The coasting phase is followed by shell deceleration when the main shock reflected from the center begins to propagate outward inside the shell. The shell at the deceleration phase is defined as the high-density portion of the CH material (according to a standard definition, the shell is bounded by the ρ_{max}/e points on both sides from the position of the maximum density ρ_{max}; also Fig. 99.12). The fuel, together with the inner lower-density, high-temperature CH, forms the hot spot. As the shell converges and temperature inside the hot spot increases, the heat front advances outward and ablates the colder portion of the shell. Therefore, the mass of the higher-temperature hot spot increases during the deceleration phase. This is similar to the hot-spot formation in cryogenic ignition designs.[46] The main difference between cryogenic implosions and the gas-filled plastic implosions is that the hot spot in a cryogenic target consists only of the fuel, while the plastic implosions have two materials—fuel and CH. Since there is a mismatch in the average ion charge Z of the two materials, the density and thermal conductivity are discontinuous across the material interface. The density jump is easily obtained from the pressure continuity condition across the interface in the absence of radiative effects. The total pressure of the ionized gas is $p = \rho T/A$, where T is the temperature, $A = m_i/(1+Z)$, and m_i is the average ion mass. Since the heat flux is continuous across the interface, the temperature must be continuous as well; therefore, the jump in density becomes

$$\frac{\rho_{CH}}{\rho_{DD}} = \frac{m_{CH}}{m_{DD}}\frac{1+Z_{DD}}{1+Z_{CH}}. \tag{7}$$

Substituting $m_{CH} = 6.5\ m_p$, $m_{DD} = 2m_p$, $Z_{CH} = 3.5$, and $Z_{DD} = 1$ into Eq. (7) gives $\rho_{CH}/\rho_{DD} = 1.44$, which leads to the Atwood number $A_T = 0.18$. Here, m_p is the proton mass. Such a density jump across the material interface creates conditions for the RT growth. There are two RT unstable regions during the deceleration phase: (1) the classically unstable CH–D_2 interface with $A_T = 0.18$ and (2) the rear surface of the shell. Density profiles at peak neutron production are shown in Fig. 99.12 to illustrate this point. The simulation without radiative effects (solid) shows two distinct regions of instability: the fuel–shell interface with an Atwood number of 0.18 and a less-steep density gradient leading up to the peak density. While the first region is unstable for all mode numbers, the growth rate at the second region is significantly reduced by the density-gradient scale length and mass ablation. With radiative effects included in the calculation (dotted), however, the effective Atwood number at the interface significantly increases to

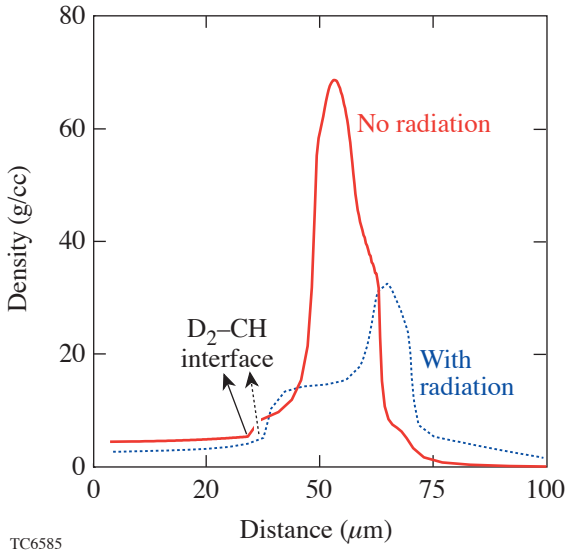

Figure 99.12
Density profiles at peak neutron production from a 1-D simulation with (dotted) and without (solid) radiation transport. Radiation plays an important role during deceleration by raising the effective Atwood number for long and intermediate wavelengths.

~0.5 from the relatively small value of 0.18. This effect is due to the ablation of the colder shell material. As the shell material ablates and is heated by the thermal conduction from the core, the bremsstrahlung radiation increases. The radiation losses lead to additional cooling and compression of the blowoff CH. The simulation with radiation transport in Fig. 99.12 (dotted line), at peak neutron production, has a larger A_T compared to the simulation without radiation (solid line). As a consequence of this increased Atwood number, there is an increase in the RT instability growth rate for long and intermediate wavelengths. The RT instability creates a lateral flow of the fuel along the interface that moves the fuel from the hotter spike region into the colder bubbles. This leads to an effective cooling of the fuel and degradation in the neutron production rate. Such a mechanism of the neutron-yield truncation is dominant for the thicker shell, which is stable enough during the acceleration phase to maintain its integrity.

As mentioned earlier, the main shock reflected from the target center starts to propagate across the shell at the beginning of the deceleration phase. The material behind the shock stagnates, transferring the shell's kinetic energy into the internal energy of the hot spot. It is easy to understand intuitively that the larger momentum flux of the shell material across the shock results in higher hot-spot stagnation pressure. To estimate the dependence of the final hot-spot pressure P_f on the shell's parameters, we use the continuity conditions across the shock propagating inside the shell, which moves with implosion velocity $V_{\rm imp}$ and has density $\rho_{\rm sh}$. In the shock-front frame of reference, the mass-flow continuity reads as

$$\rho_c U_2 = \rho_{\rm sh} U_1, \tag{8}$$

where U_1 and U_2 are the fluid velocities ahead and behind the shock and ρ_c is the compressed density behind the shock. Since the material behind the shock stagnates in the laboratory frame of reference, $U_2 = U_s$ and $U_1 = V_{\rm imp} + U_s$, where

$$U_s \simeq \sqrt{\frac{\gamma+1}{2}\frac{P_f}{\rho_{\rm sh}}} \tag{9}$$

is the shock velocity in the strong-shock limit and $\gamma = 5/3$ is the ratio of specific heats. Combining Eqs. (8) and (9) and using $\rho_c \simeq 4\rho_{\rm sh}$ gives

$$P_f \sim \rho_{\rm sh} V_{\rm imp}^2 \sim \frac{E_{\rm kin}}{R_{\rm hs}^2 \Delta_{\rm sh}}. \tag{10}$$

At shell stagnation, the kinetic energy of the shell $E_{\rm kin} = M_{\rm sh} V_{\rm imp}^2 / 2$ is transferred into the internal energy of the hot spot $2/3\, P_f R_{\rm hs}^3$. Equation (10) shows that the stagnation radius is proportional to the shell thickness $R_{\rm hs} \sim \Delta_{\rm sh}$; therefore, the final pressure of the compressed fuel is larger for a "compact" shell with higher density and smaller shell thickness for a given shell kinetic energy. In other words, the kinetic energy of the converging shell heats the hot spot more efficiently in shells with larger compressibility (smaller entropy). Comparing 20- and 27-μm shells, we conclude that the stagnation radius of the thicker shell is larger; thus the final pressure and the neutron-production rate are smaller. On the other hand, if one compares the shell that remains integral during the acceleration phase with a shell whose stability is severely compromised by RT growth, the integral shell has a lower entropy and smaller shell thickness. It, therefore, stagnates at a smaller radius reaching a higher hot-spot pressure and temperature. This leads to a larger neutron-production rate in the integral shell in comparison with the significantly distorted shell.

The larger shell thickness in the implosion with compromised shell integrity also implies that the rate at which neutron production decreases should be less steep during shell disassembly. Between the time of peak neutron production and peak compression, the neutron rate decreases due to the falling temperature in the gas. The subsequent decrease in the neutron-production rate occurs due to shell disassembly. If the shell is thicker, disassembly occurs later in the implosion as follows: The time between the interaction of the reflected shock (which is very similar for both integral and severely distorted shells) and when the shock breaks out of the shell is given by $t_s = \Delta_{\rm sh}/U_s$. From Eqs. (9) and (10), $U_s \simeq \sqrt{E_{\rm kin}/R_{\rm hs}^2 \Delta_{\rm sh} \rho_{\rm sh}}$. Since $E_{\rm kin}$ is very similar between the integral shell and severely distorted shell implosion (only a small portion of the total energy goes into lateral flow in the distorted shell implosion) and mass $\left(\propto R_{\rm hs}^2 \Delta_{\rm sh} \rho_{\rm sh}\right)$ is conserved, the shock velocity is very similar in both cases; therefore, $t_s \propto \Delta_{\rm sh}$ and is longer for the thicker shell, and disassembly is delayed. Consequently, neutron production falls less steeply in the implosion where shell stability is compromised than in the implosion with an integral shell.

Multimode Simulations

1. Effects of Beam-to-Beam Imbalances

We now turn to multimode simulations using *DRACO*. As mentioned in the **Shock Transit** section (p. 142), imbalances between beams result in long-wavelength modes on target. Even modes between 2 and 10 are used to simulate the effect of low-order modes using the amplitudes in Fig. 99.3. The

power in odd modes is added in quadrature to the even-mode amplitudes. Figure 99.13 shows the fuel–shell interface amplitudes versus time for the dominant modes in the simulation for the 20-μm-thick shell implosion. The initially unperturbed interface acquires a perturbation shortly after shock breakout around 0.4 ns. When the compression wave returns to the interface, it causes another jump in the perturbation around 0.8 ns. Significant growth is simulated after this time due to the feedthrough of the perturbation from the ablation surface and the convergent Richtmyer–Meshkov instability. Modes 6 and up start oscillating shortly after the end of the acceleration phase as they decouple from the ablation surface. The reflected shock from the center returns to the interface around 1.75 ns, when $\ell = 4$ changes phase. Rayleigh–Taylor growth occurs shortly after that as the shell continuously decelerates toward stagnation.

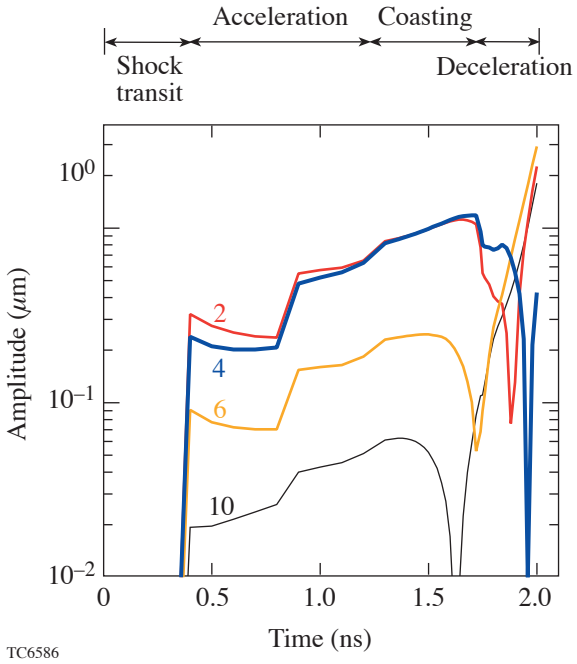

Figure 99.13
Modal amplitudes versus time at the fuel–shell interface for the low-order multimode simulation (due to beam imbalances) of a 20-μm-thick CH shell. The interface becomes perturbed shortly after shock breakout around 0.4 ns. A second jump in the amplitude is modeled at ~0.8 ns when the second shock breaks out of the shell. Shorter wavelengths such as modes 6 and 10 decouple during the coasting phase when they change phase. Longer wavelengths (modes 2 and 4) change phase when the shock returns to the interface at ~1.75 ns.

The yield is only marginally affected by low-order modes with 2-D simulation, resulting in ~95% of the 1-D yield for the 20-μm-thick shell and ~94% of 1-D for the 27-μm-thick shell.

Figure 99.14 shows the density contours at peak neutron production for the 20-μm-thick implosion. The D_2–CH interface is marginally distorted. Areal-density variations of ~23% at peak neutron production (for both shell thicknesses) are simulated.

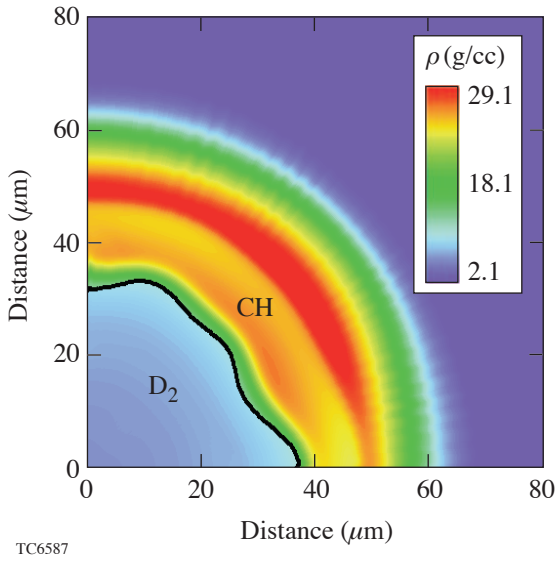

Figure 99.14
Density contours at peak neutron production from a multimode simulation including only low-ℓ modes ($\ell < 10$) for the 20-μm-thick CH implosion. An areal-density variation of 23% is calculated at this time in the implosion. The solid line corresponds to the D_2–CH interface.

The marginal effect of low-order modes is consistent with the experimental beam-balancing work described in Ref. 37. In that work, on-target beam balance was changed in a controlled manner; the estimated decrease in the amplitude of these modes was between 30%–50%. While a decrease in areal-density variations was observed, only a marginal difference was observed in absolute neutron yields.

2. Effects of Single-Beam Nonuniformity

Single-beam nonuniformity influences intermediate- and short-wavelength seeds on target. As mentioned earlier, modes up to at least 400 are required to realistically model shell stability. A full 2-D simulation including the effects of power imbalance would then require modes between 2 and 400. Resolving mode 400 in such a simulation requires a large number of computational zones—far beyond the scope of this work. We illustrate the effect of laser imprint on shell stability by performing simulations with a smaller set of modes. The simulations include beam-smoothing techniques modeled as

described in the **Acceleration Phase** section (p. 145). Figure 99.15(a) shows a plot of density contours at the end of the acceleration phase from a simulation that includes even modes up to $\ell = 200$ for the 20-μm-thick CH shell. The shortest wavelength in this simulation is resolved using 14 cells, resulting in a 200×700 zone simulation. Since odd modes are not included in the simulation, their power is added in quadrature to the amplitudes of the even modes. The shell indicated by the high-density regions is considerably distorted with portions of the shell at less than solid densities. The peak-to-valley variation in the center-of-mass radius is calculated to be 6.6 μm at the end of the acceleration phase, significantly greater than the 1-D shell thickness of ~5 μm. It is expected that shell distortion will increase only when even-shorter wavelengths are included in the calculation. Therefore, short wavelengths play an important role in increasing the adiabat of the shell by introducing additional degrees of freedom for the fluid flow. This will influence the compressibility of the shell and, therefore, neutron yields. In comparison, the 27-μm-thick implosion [Fig. 99.15(b)] has an integral shell at the end of the acceleration phase with a peak-to-valley amplitude of 3.4 μm in the center-of-mass radius compared to a shell thickness of ~6.8 μm. The effect of the still-shorter wavelengths not included in the calculation ($\ell > 200$) can be estimated using a RT postprocessor[31] to the 1-D simulation. This postprocessor indicates that the thicker, 27-μm-thick shell remains integral during the acceleration phase while the stability of the 20-μm-thick shell is severely compromised.

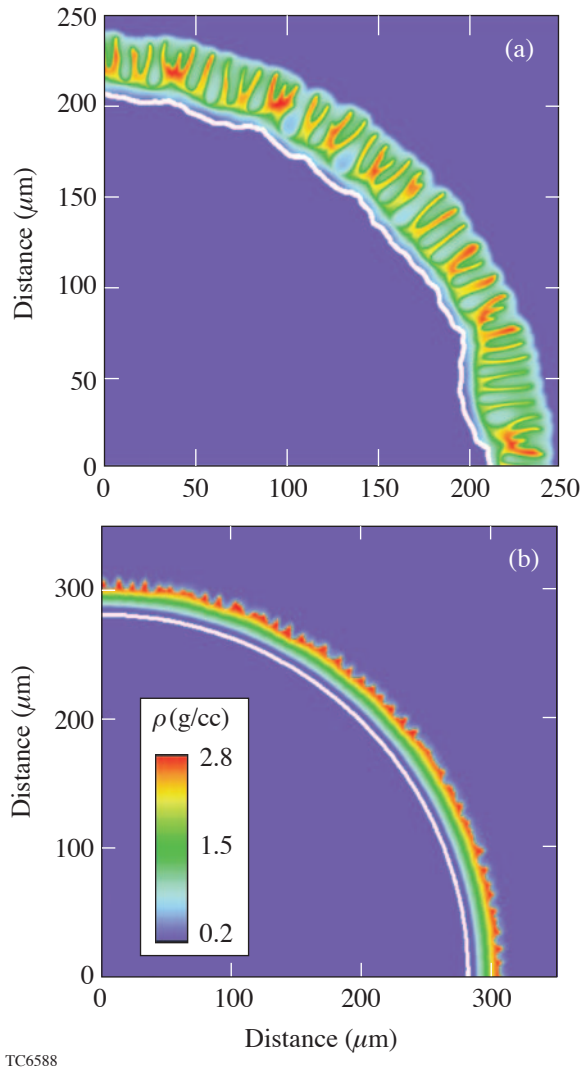

Figure 99.15
Density contours at the end of the acceleration phase for (a) a 20-μm-thick CH shell and (b) a 27-μm-thick CH shell from a multimode simulation of laser imprint. The solid lines correspond to the D_2–CH interface. Note that the shell (indicated by the higher-density contours) is significantly more distorted for the 20-μm implosion than the 27-μm implosion.

Due to the large number of computational cells in these simulations, it is extremely challenging to reliably simulate these implosions until peak compression. Instead, we assess the effect of the various nonuniformity sources by simulations that include only a few modes but represent reasonably well the shell's stability. The goal of these simulations is to identify the mechanisms that influence neutron yields. More-detailed comparisons with experimental observables will be performed in the future.

Combined Effects of All Sources of Nonuniformity

Simulations that include a few modes are useful to shed light on which modes influence target performance. The mode ranges are divided into three regions: long wavelengths ($\ell \leq 10$), intermediate wavelengths ($10 \leq \ell \leq 50$), and shorter wavelengths that include all the higher mode numbers. In the **Effects of Beam-to-Beam Imbalances** section (p. 149), it has been pointed out that low-order modes ($\ell \leq 10$) alone have a marginal influence on target performance. We consider simulations involving two modes corresponding to mode numbers 4 and 20 that combine the effect of long and intermediate wavelengths. These simulations and those described later are performed on a 45° wedge. The initial amplitude for each mode is chosen from the amplitudes added in quadrature of a range of mode numbers (from the DPP spectrum for $\ell = 20$ using modes between 15 and 40 as the mode range and from the initial power balance and surface-roughness data for modes $2 < \ell < 10$ for mode $\ell = 4$). The neutron-production rate is shown in Fig. 99.16(a) for the 20-μm-thick implosion and Fig. 99.16(b) for the 27-μm-thick implosions. The rate from

the two-mode simulations (dotted line) deviates from the 1-D simulation, and the burn truncates relative to 1-D. This is the case for both thicknesses. The two-mode simulation illustrates the mechanisms for yield reduction through burn truncation. The RT and RM growth at the fuel–shell interface results in the flow of fuel into the colder bubbles, decreasing the yield. This is illustrated in Fig. 99.17, where the fluid velocity vectors (arrows) in the frame moving radially with the fluid are overlaid on the contour plot of ion temperature at peak neutron production. This result is shown from a single-mode simulation of mode number 20, where this mode has the same initial amplitude as the previous two-mode simulation. Due to heat conduction, the temperature contours are more spherically symmetric than the material interface (solid line). As the vectors indicate, fuel flows into the colder bubbles. This truncates the neutron-production rate. The second mechanism for the truncation of the neutron rate occurs because of the distortion of the high-density shell. The increased surface area enhances heat conduction out of the core, cooling the fuel and decreasing the yield. These mechanisms for the truncation of neutron yield cannot be included in 1-D mix models that have been used previously to model these implosions.[6,8,49] It is also to be noted that the single intermediate-mode simulation has a yield relative to 1-D of 78% (for both thicknesses). The addition of long wavelengths ($\ell = 4$) reduces this value to 55% for the 20-μm-thick shell and 61% for the 27-μm-thick shell. Thus, the combination of the low and intermediate modes has a greater effect on yield than each range of modes alone.

To investigate the role of the shorter wavelengths on yield, we perform a three-mode simulation including mode numbers 4, 20, and 200. In this simulation, modes 4 and 20 have the

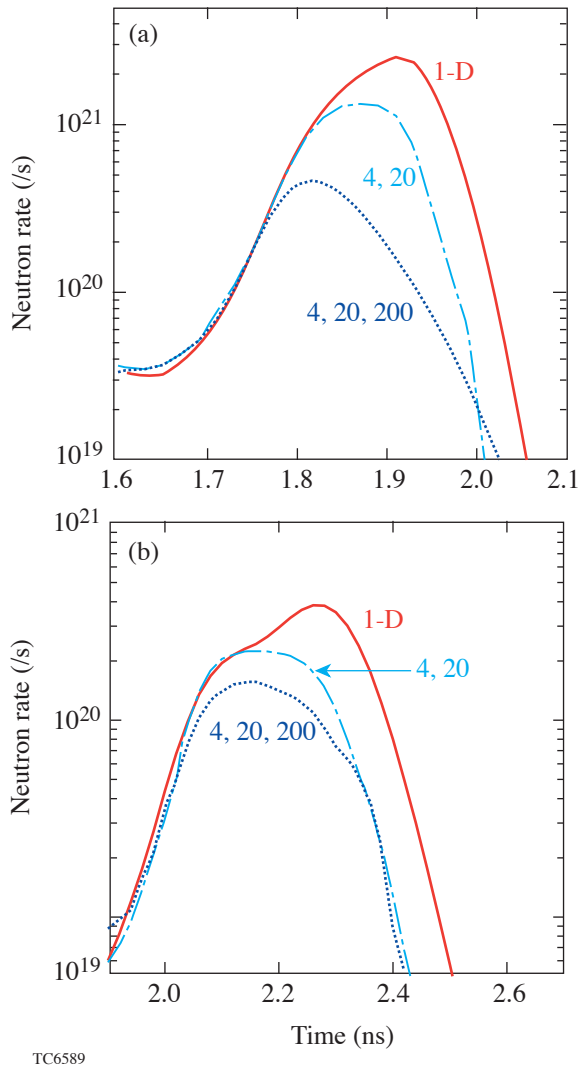

Figure 99.16
Neutron-production rates from the simulation including only low- and intermediate-mode numbers (dashed–dotted line) and the simulation including short wavelengths (dotted line) compared to 1-D (solid line) for (a) the 20-μm-thick CH shell and (b) the 27-μm-thick CH shell. Note that the addition of mode 200 in the simulation including short wavelengths results in a less-steep fall of the neutron production rate for the 20-μm implosion and retains burn truncation for the 27-μm case.

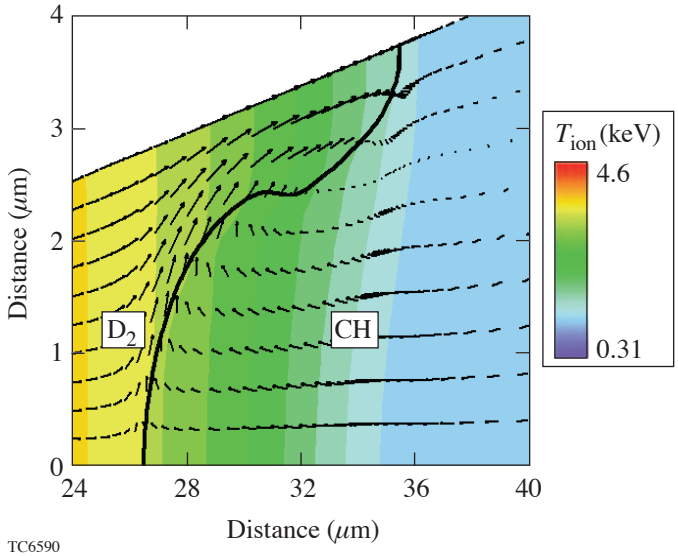

Figure 99.17
Fluid velocity vectors in a frame moving radially with the fluid overlaid on a contour plot of ion temperature at peak neutron production for the 20-μm-thick CH shell. The simulation, from a single-mode perturbation, illustrates one mechanism for burn truncation. As the velocity vectors indicate, fuel flows into the colder bubbles due to RT growth resulting in burn truncation.

same amplitude as the simulation discussed earlier. The amplitude for mode $\ell = 200$ is chosen by adding in quadrature the power between modes 100 and 300. Contours of mass density for the two shell thicknesses are shown at peak neutron production in Fig. 99.18. The significant shell distortion corresponds to the intermediate mode $\ell = 20$. Even though the growth rate at the D_2–CH interface is highly nonlinear for the short wavelength ($\ell = 200$), the bubble amplitude is, at most, 1 μm. Larger mixing widths (~20 μm) have been inferred based on spherically symmetric 1-D mix models.[6,8] Since 1-D mix models need to account for the increased volume due to long-wavelength distortions, it is very likely that they overestimate the mixing length. An order of magnitude estimate for the mixing length can be obtained as follows: since a hydrodynamic code such as *DRACO* cannot follow materials into the turbulent regime, we consider the amplitude of the short wavelength as a "mix thickness." The simulated thickness is consistent with expectations from turbulent mixing. The turbulent-mixing layer grows self-similarly with a mixing thickness h, given by Ref. 50:

$$h = \alpha A_T g t^2, \tag{11}$$

where α is a dimensionless constant.

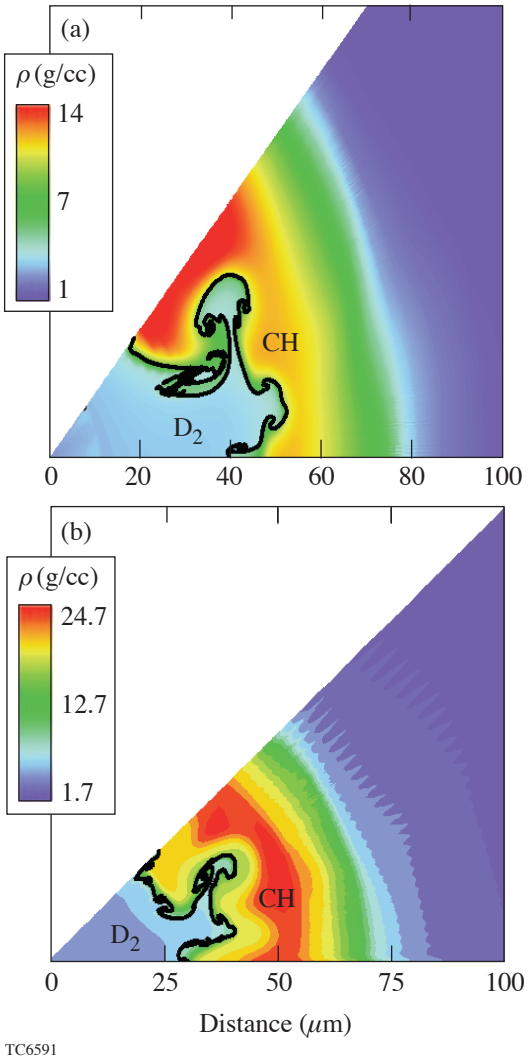

Figure 99.18
Density contours for simulations including short wavelengths at peak neutron production for (a) the 20-μm-thick CH shell and (b) the 27-μm-thick CH shell. The solid line is the fuel–shell interface. The short wavelengths ($\ell \sim 200$) have an amplitude of ~1 μm, consistent with estimates of mixing thicknesses from turbulence observations.[48]

As described in the **Deceleration Phase** section (p. 148), bremsstrahlung cooling increases CH density in the hot spot. Consequently, the Atwood number varies continuously during the deceleration phase, reaching a maximum value of 0.5. The increased density, however, does not significantly alter the perturbation growth rate of short wavelengths due to the stabilizing effects of the density-gradient scale length and thermal conduction. Taking $A_T = 0.18$ for the D_2–CH interface gives $\alpha = 0.05$ (Ref. 48), which leads to $h = 0.9$ μm. This compares favorably with the amplitude of $\ell = 200$ inferred from simulation. In previous work, homogenous mixing of D_2 and CH[6–8,49] has been inferred from experimental observables such as secondary neutron ratios,[6,8] argon spectral lines,[7] D^3He yields in ^{3}He-filled CD shells,[6,8] etc. Primary neutron yields have not been used directly to determine the presence of turbulence. The relatively small turbulent mixing layer (compared to the overall deformation of the interface due to intermediate mode numbers) suggests that the experimentally inferred turbulence plays a small role in determining primary neutron yields.

The simulations including $\ell = 200$ also indicate an interesting trend in neutron production when compared to the simulations including only low and intermediate modes (Fig. 99.16). For both shell thicknesses, the peak in the neutron-production rate deviates earlier. For the 20-μm-thick shell, however, neutron production does not decrease as steeply as the previous two-mode simulation. For the 27-μm-thick shell, the neutron-production history is very similar in width to the two-mode simulation. This difference in trends can be explained as follows: The shell is integral for the 27-μm-thick shell and the density and temperature distribution compare favorably with 1-D [this is shown in Fig. 99.19(b)]. The solid black line is the

1-D result, whereas the other two lines correspond to radial lineouts from the simulations (dashed–dotted at 36° and dotted at 0°). For the 20-μm-thick shell, the profiles from the 2-D simulation are significantly different from 1-D [Fig. 99.19(a)]. The peak densities are much lower, and the shell has a wider extent due to the increased adiabat from shell breakup during acceleration. This profile results in delayed stagnation as the shock takes much longer in this case to reach the back of the shell [see the **Deceleration Phase** section (p. 148)]. This delayed shell disassembly results in a persistence of neutron production compared to the simulation including only low and intermediate modes. Figures 99.19(c) and 99.19(d) show the corresponding radial temperature lineouts from the simulation. The lower temperature in the 27-μm implosion [Fig. 99.19(d)] is caused by shell distortion and increased heat flow from the core. The 20-μm implosion [Fig. 99.19(c)], in addition, shows lower temperature caused by the decreased compression. The yields relative to 1-D are 21% for the 20-μm-thick CH shell compared to 47% for the 27-μm-thick CH shell. Experimentally, the yields relative to 1-D are

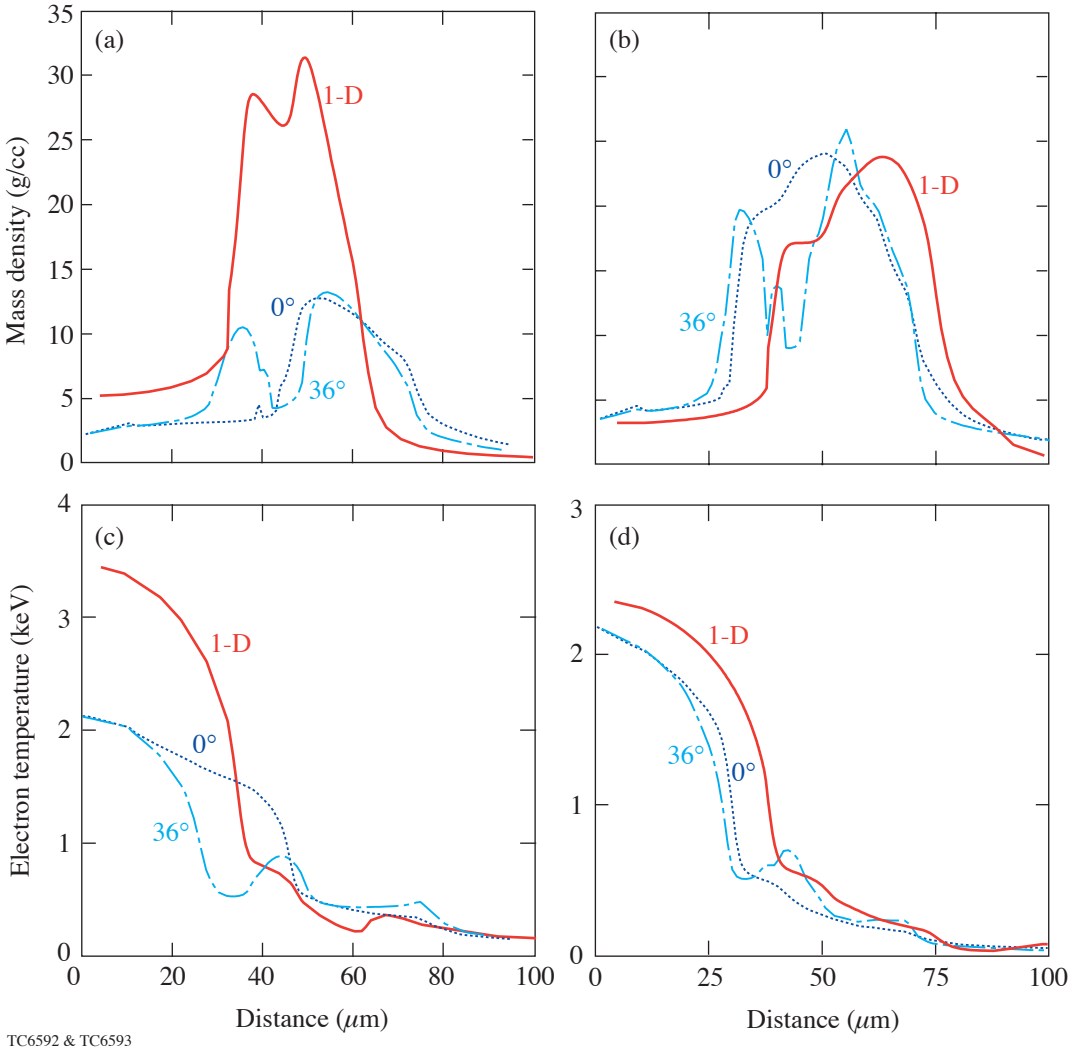

Figure 99.19
Radial lineouts of density from the simulation including short wavelengths for (a) the 20-μm-thick CH shell and (b) the 27-μm-thick CH shell at two different polar angles [0° (dotted) and 36° (dashed–dotted)], compared to the 1-D simulation (solid line). Note that the thinner shell has significantly lower densities compared to 1-D. The shell is considerably thicker for the 20-μm implosion. Radial lineouts of temperature are shown for (c) the 20-μm implosion and (d) the 27-μm implosion. All lineouts are at peak neutron production in 1-D. The temperatures in the core are lower than 1-D due to enhanced heat conduction out of the distorted core (both thicknesses) and the overall lower compression in the 20-μm-thick implosion.

~40% and ~45% for the 20-μm and 27-μm thicknesses, respectively. Since mode ℓ = 200 has a larger effect on the 20-μm implosion, the smaller yield relative to 1-D in the simulation for the 20-μm implosion points to an overestimate of the initial amplitude of ℓ = 200 in the simulation.

Similar trends in neutron-production rates are observed in experiments. Figure 99.20 shows the neutron-production rates from experiment (dotted line), and the 1-D simulation (solid line), for the 20-μm-thick implosion [Fig. 99.18(a)] and the 27-μm-thick implosion [Fig. 99.18(b)]. Since absolute timing in these experiments was unknown, the 1-D rates are overlaid on the experimental rates by aligning the rise times of the two neutron-rate curves. For the thinner shell, the experimental burnwidth is closer to 1-D, whereas for the thicker, more-stable shell, the burnwidth is truncated compared to 1-D. This trend persists: a still thicker shell (33 μm) shows increased burn truncation, and even thinner shells (15 μm) indicate a widening of the neutron-production history. The 2-D simulation of the 20-μm implosion shows a slower fall of the neutron-production rate compared to the experimentally observed rate. This is likely due to the larger value for the initial amplitude of the ℓ = 200 mode in the simulation compared to that in the experiment.

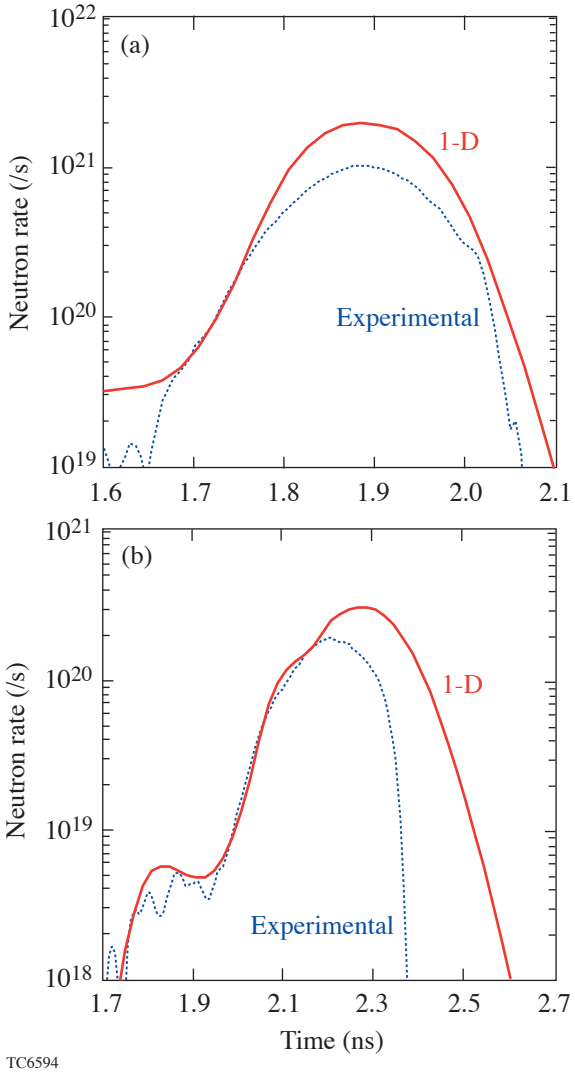

Figure 99.20
Comparison of calculated (1-D) neutron rates (solid line) with experiment (dotted) for (a) the 20-μm-thick implosion (shot number 30628) and (b) the 27-μm-thick implosion (shot number 22088). Burn truncation is evident for the 27-μm-thick implosion. Neutron production rate persists and is almost as wide as 1-D for the 20-μm-thick implosion.

In summary, the combination of intermediate and low modes significantly influences yields, which manifests itself as burn truncation in the neutron-production rates. The short wavelengths significantly affect shell stability for the thinner shells and can consequently influence stagnation. This in turn widens the burnwidth and also influences yields. For the thicker shells, the burnwidth does not change significantly with the addition of short-wavelength modes. In both cases, the neutron rates deviate earlier from 1-D with the addition of short wavelengths in simulation.

Conclusions

One-dimensional dynamics of plastic-shell implosions of two different thicknesses irradiated by a smooth laser is discussed. Seeding and evolution of nonuniformities are discussed for the different phases of the implosion. We show that during the acceleration phase, modes up to at least ~400 should contribute to shell stability. Multimode simulations using the code *DRACO* indicate that the shell stability in the implosion of a 20-μm-thick plastic shell is significantly compromised due to Rayleigh–Taylor instability during the acceleration phase, whereas the 27-μm-thick shell is only marginally distorted. Long-wavelength multimode simulations indicate that imbalances between the laser beams have a small effect on target yields. Intermediate modes appear to influence yields significantly. Short wavelengths result in qualitatively different behavior between the two shell thicknesses: widening the burnwidth for the thinner shell and marginally influencing burnwidth for the thicker shell. This trend in neutron-production rates is also observed in experiment. Future work will include detailed comparisons of charged-particle spectra with experimental observations, an additional analysis to relate

small-scale mix thicknesses to observations of homogenous mixing in experiments, and the comparison of x-ray images of the compressed core with experiments.

ACKNOWLEDGMENT

This work was supported by the U.S. Department of Energy Office of Inertial Confinement Fusion under Cooperative Agreement No. DE-FC52-92SF19460, the University of Rochester, and the New York State Energy Research and Development Authority. The support of DOE does not constitute an endorsement by DOE of the views expressed in this article. This work has been supported in part by LLE (subcontract PO412163G) with the University of Wisconsin for the implementation of the PetSc Libraries in *DRACO*.

Appendix A: Seeding of the Long-Wavelength Modes due to Drive Asymmetry

The nonuniformities in laser intensity result in asymmetries in drive pressure ΔP. To relate the ablation pressure and laser-intensity nonuniformities ΔI, we adopt the "cloudy-day" model.[38] Using the scaling $P \sim I^{2/3}$ yields the following relation:

$$\frac{\Delta P}{P} \simeq \frac{2}{3}\frac{\Delta I}{I}e^{-kD_c} \equiv \frac{2}{3}\tilde{I}, \tag{A1}$$

where D_c is the size of the conduction zone (the distance between the ablation front and critical surface) and k is the wave number. For the set of experiments described in this article, the conduction zone grows linearly in time, $D_c = V_c t$ with $V_c \simeq 68$ μm/ns. Since the laser intensity is spatially modulated, the shocks driven by the peaks in the laser illumination travel faster than the shocks launched at the intensity minimums; therefore, the shock and ablation fronts get distorted. This distortion growth can be estimated for long-wavelength modes using the following simple model: The shock velocity, in the strong-shock limit, is proportional to the square root of the drive pressure P:

$$U_s \simeq \sqrt{\frac{\gamma+1}{2}\frac{P}{\rho_0}}, \tag{A2}$$

where ρ_0 is the initial (undriven) shell density and γ is the ratio of specific heats ($\gamma = 5/3$ for the monoatomic ideal gas). Modulations in the drive pressure distort the shock front according to

$$\frac{d\eta_s}{dt} = \Delta U_s = \frac{dU_s}{dP}\Delta P_s \simeq \frac{2}{\sqrt{5}}c_s\frac{\Delta P}{P}, \tag{A3}$$

where c_s is the sound speed of the shock-compressed shell, ΔP_s is the pressure modulation at the shock, and η_s is the shock-front modulation. We approximate ΔP in the latter equation with the modulation at the ablation front [Eq. (A1)]. Such an approximation is justified only for the long-wavelength modes when the lateral fluid motion can be neglected. The distortion in the ablation front is caused by the perturbations in the post-shock velocity $U_{\rm ps} = -\rho_0/\rho U_s$, where $U_{\rm ps}$ is calculated in the shock frame of reference. Such perturbations are due to (1) modulations in the shock velocity, $-(\rho_0/\rho)\Delta U_s$; (2) modulations $\Delta\rho$ in the shock-compressed density, $(\rho_0/\rho)(\Delta\rho/\rho)U_s$; and (3) modulations in the position of the shock front. It can be shown that the density modulation right behind the shock is small for strong shocks ($\Delta\rho/\rho \sim M_s^{-2}\,\Delta P/P$, where M_s is the shock Mach number) and can be neglected. The resulting modulation in the post-shock velocity takes the form

$$\Delta U_{\rm ps} \simeq (\rho_0/\rho - 1)\Delta U_s = \frac{3}{4}\Delta U_s. \tag{A4}$$

Since ablative stabilization and lateral flow can be neglected for the long-wavelength modes, $d\eta_a/dt = \Delta U_{\rm ps}$. Integrating the latter equation gives the ablation-front modulation η_a:

$$\eta_a(t) \simeq \frac{1}{\sqrt{5}}\int_0^t dt'\tilde{I}(t')c_s(t'),\ \eta_s = \frac{4}{3}\eta_a. \tag{A5}$$

It is also important to determine the modulation in the CH–gas interface $\eta_{\rm int}$ at the beginning of the acceleration phase. The modulation at the interface is seeded by the perturbed shock. As soon as the shock breaks out of the shell, the rear surface starts to expand with the velocity $3\,c_s$ (Ref. 51) with respect to the shock-compressed material. Therefore, the amplitude of the CH–gas interface takes the value $\eta_{\rm int} = 3\,c_s\delta t$, where $\delta t = \eta_s/U_s$ is the shock transit time across the modulation amplitude. Using the strong shock limit, one obtains $\eta_{\rm int} 3\sqrt{5}\,\eta_s/4$. Taking into account the relation between η_s and η_a yields $\eta_{\rm int} = \sqrt{5}\eta_a$. As shown in Ref. 52, the gas–CH interface is unstable during the rarefaction-wave (RW) propagation through the shell. Since such a growth is linear in time and proportional to the modulation wave number, there is very little change in the amplitude of the fuel–pusher interface between the shock breakout and the beginning of the acceleration phase. To determine the mode amplitudes at the beginning of the acceleration phase, we integrate Eq. (A5) using the laser nonuniformity profiles shown in Fig. 99.3. The spectrum thus obtained is plotted in Fig. 99.4 and compared against the results of the full 2-D power-balance simulation. Observe that the simple model reproduces the results of simulations very well. To calculate the initial conditions for the RT growth, in addition to the initial

amplitude, we must calculate the perturbed front velocity η_a'. This velocity has two components: the first is given by Eqs. (A3) and (A4), and the second is due to the rippled RW breakout at the ablation front. Indeed, when the first shock reaches the rear surface, the RW is launched toward the ablation front. The RW travels with the local sound speed c_s; therefore, if the shock amplitude is η_s, the rarefaction amplitude then becomes $\eta_{\mathrm{RW}} = c_s\left(\eta_s/U_s\right) = \sqrt{5}\eta_s/4$. The phase of the modulation in the rarefaction head is opposite to the phases of the rear-surface and ablation-front perturbations. Upon reaching the ablation front, the leading edge of the RW establishes the pressure gradient, accelerating the front. Since the peaks of the RW break out at the ablation front prior to the valleys, the ablation-front ripple gains an additional velocity perturbation $\delta v = g\delta t$, where g is the acceleration and $\delta t = \eta_{\mathrm{RW}}/c_s = \sqrt{5}/3\left(\eta_a/c_s\right)$. Combining the two contributions, the initial ripple velocity takes the form

$$\frac{d\eta_a}{dt}\left(t_0\right) = \tilde{I}\left(t_0\right)\frac{c_s}{\sqrt{5}} + \frac{\sqrt{5}g}{3c_s}\eta_a\left(t_0\right), \tag{A6}$$

where t_0 is the time at the beginning of acceleration phase. Equations (A5) and (A6) show that the ablation-front amplitude changes slope at $t = t_0$. Substituting $g = c_s^2/\left(\gamma\Delta_{\mathrm{sh}}\right)$ into Eq. (A6) and also approximating $\eta_a\left(t_0\right) \sim \langle\tilde{I}\rangle_{\mathrm{sh}}\left(c_s/U_{\mathrm{sh}}\right)4\Delta_{\mathrm{sh}}$, we can rewrite Eq. (A6) as

$$\eta_a'\left(t_0\right) \sim \tilde{I}\left(t_0\right)\frac{c_s}{\sqrt{5}} + \left\langle\tilde{I}\right\rangle_{\mathrm{sh}}\frac{c_s}{\sqrt{5}}. \tag{A7}$$

The second term on the right-hand side of Eq. (A7) is proportional to the laser nonuniformity averaged over the shock transit time, $\langle\tilde{I}\rangle_{\mathrm{sh}}$. Taking into account that beam mistiming significantly increases $\tilde{I}$ at the beginning of the pulse (during the pulse rise), $\langle\tilde{I}\rangle_{\mathrm{sh}}$ becomes much larger than $\tilde{I}\left(t_0\right)$ (in most cases by a factor of 5). This conclusion is valid for a large variety of target designs, including the ignition design, since the laser reaches its peak intensity prior to the acceleration phase. One must keep in mind, however, that Eq. (A6) assumes sharp interfaces of the CH–gas boundary and the ablation front. In reality the radiation preheat relaxes the density at the CH–gas interface prior to the first shock breakout. In addition, the ablation front has a finite thickness. These effects cause deviations of the initial condition from simple estimates [Eqs. (A5) and (A7)]. Comparison with the results of 2-D simulations, however, shows that finite interface thickness effects do not significantly modify the perturbation amplitudes (Fig. 99.4).

Appendix B: Growth of Long-Wavelength Modes During the Acceleration Phase

The equation describing the perturbation growth for the long-wavelength modes (ablation effects are neglected) during the acceleration phase can be written as[32]

$$\frac{d}{dt}\left(\frac{1}{\rho r}\frac{d}{dt}\rho r^2\eta\right) - \ell g\eta = \ell\frac{\Delta P}{\rho} = \ell\frac{2}{3}\frac{\delta I}{I}\left(\frac{r}{r_c}\right)^{\ell} g\Delta_{\mathrm{sh}}, \tag{B1}$$

where ΔP is the drive-pressure nonuniformity, r is the shell radius, g is the shell acceleration, ρ is the shell density, Δ_{sh} is the shell thickness, r_c is the position of the average laser-deposition surface, and η is the ablation-front modulation amplitude. The factor $\left(r/r_c\right)^{\ell}$ is due to the cloudy-day effect. Equation (B1) is subject to the initial conditions (A5) and (A6). The shell thickness is Δ_{sh} = 5 μm for the 20-μm shell and Δ_{sh} = 6.8 μm for the 27-μm shell. During this phase of the implosion, the shell density remains approximately constant, so we can cancel ρ in Eq. (B1). For simplicity we assume constant shell acceleration $r = r_0 - gt^2/2$. To compare a relative importance of the RT growth versus the secular growth during the shell acceleration, we compare $\ell g\eta$ with the right-hand side of Eq. (B1). The lower limit of this term is

$$\min\left(\ell g\eta\right) = \ell g\eta\left(t_0\right) \simeq \ell g\left\langle\tilde{I}\right\rangle_{\mathrm{sh}}\frac{\Delta_0}{\sqrt{5}}\frac{c_s}{U_{\mathrm{sh}}} = \ell g\Delta_{\mathrm{sh}}\left\langle\tilde{I}\right\rangle_{\mathrm{sh}}, \tag{B2}$$

where Δ_{sh} is the in-flight shell thickness (which is approximately four times smaller than the initial thickness Δ_0) and $\langle\tilde{I}\rangle_{\mathrm{sh}}$ is the intensity modulation averaged over the shock-propagation time. Comparing the latter expression with the right-hand side of Eq. (B1), we observe that $\Delta P/\rho << g\eta$ during the acceleration phase. The latter inequality is satisfied for very long wavelengths (ℓ < 10) because $\langle\tilde{I}\rangle I_{\mathrm{sh}} >> \tilde{I}\left(t_0\right)$ due to beam mistiming early in the pulse. Shorter wavelengths (ℓ > 10), on the other hand, experience a large attenuation due to thermal smoothing in the conduction zone; therefore, the right-hand side of Eq. (B1) is also small for such mode. Thus, we can conclude that the secular growth during the acceleration phase is much smaller than the RT amplification of the initial amplitude and velocity of the ablation-front modulation. This growth can be estimated using the WKB solution of the homogeneous part of Eq. (B1) with the following initial conditions:

$$\eta_0 = \left\langle\tilde{I}\right\rangle_{\mathrm{sh}}\Delta_{\mathrm{sh}}, \quad \eta_0' = \frac{c_s}{\sqrt{5}}\left[\tilde{I}\left(t_0\right) + \left\langle\tilde{I}\right\rangle_{\mathrm{sh}}\right]. \tag{B3}$$

Using results of Ref. 31, the solution takes the form

$$\eta_a = C_r^{5/4}\left[\eta_0 \cosh\Psi + \eta_0' \sqrt{\frac{r_0}{(\ell+2)g}} \sinh\Psi\right], \qquad \text{(B4)}$$

where $\Psi = \sqrt{2(\ell+2)}\arcsin\sqrt{1-C_r^{-1}}$ and C_r is the convergence ratio during the acceleration phase. During the acceleration phase, the convergence ratio of the 20-μm shell and the 27-μm shell is $C_r = r_0/r \simeq 1.7$ and $C_r \simeq 1.4$, respectively, where $r_0 = 430\ \mu$m is the ablation-front radius at the beginning of the shell acceleration. The dominant role of the RT growth over the secular growth is confirmed by the results of *DRACO* simulation. Figure 99.8 shows a plot of the perturbation amplitude with full power imbalance (dashed–dotted line) and with the power imbalance turned off (solid line) during the acceleration phase.

REFERENCES

1. J. Nuckolls *et al*., Nature **239**, 139 (1972).
2. C. P. Verdon, Bull. Am. Phys. Soc. **38**, 2010 (1993).
3. M. D. Campbell and W. J. Hogan, Plasma Phys. Control. Fusion **41**, B39 (1999).
4. T. R. Boehly, D. L. Brown, R. S. Craxton, R. L. Keck, J. P. Knauer, J. H. Kelly, T. J. Kessler, S. A. Kumpan, S. J. Loucks, S. A. Letzring, F. J. Marshall, R. L. McCrory, S. F. B. Morse, W. Seka, J. M. Soures, and C. P. Verdon, Opt. Commun. **133**, 495 (1997).
5. D. D. Meyerhofer, J. A. Delettrez, R. Epstein, V. Yu. Glebov, V. N. Goncharov, R. L. Keck, R. L. McCrory, P. W. McKenty, F. J. Marshall, P. B. Radha, S. P. Regan, S. Roberts, W. Seka, S. Skupsky, V. A. Smalyuk, C. Sorce, C. Stoeckl, J. M. Soures, R. P. J. Town, B. Yaakobi, J. D. Zuegel, J. Frenje, C. K. Li, R. D. Petrasso, D. G. Hicks, F. H. Séguin, K. Fletcher, S. Padalino, M. R. Freeman, N. Izumi, R. Lerche, T. W. Phillips, and T. C. Sangster, Phys. Plasmas **8**, 2251 (2001).
6. P. B. Radha, J. Delettrez, R. Epstein, V. Yu. Glebov, R. Keck, R. L. McCrory, P. McKenty, D. D. Meyerhofer, F. Marshall, S. P. Regan, S. Roberts, T. C. Sangster, W. Seka, S. Skupsky, V. Smalyuk, C. Sorce, C. Stoeckl, J. Soures, R. P. J. Town, B. Yaakobi, J. Frenje, C. K. Li, R. Petrasso, F. Séguin, K. Fletcher, S. Padalino, C. Freeman, N. Izumi, R. Lerche, and T. W. Phillips, Phys. Plasmas **9**, 2208 (2002).
7. S. P. Regan, J. A. Delettrez, F. J. Marshall, J. M. Soures, V. A. Smalyuk, B. Yaakobi, V. Yu. Glebov, P. A. Jaanimagi, D. D. Meyerhofer, P. B. Radha, W. Seka, S. Skupsky, C. Stoeckl, R. P. J. Town, D. A. Haynes, Jr., I. E. Golovkin, C. F. Hooper, Jr., J. A. Frenje, C. K. Li, R. D. Petrasso, and F. H. Séguin, Phys. Rev. Lett. **89**, 085003 (2002).
8. C. K. Li, D. G. Hicks, F. H. Séguin, J. Frenje, R. D. Petrasso, J. M. Soures, P. B. Radha, V. Yu. Glebov, C. Stoeckl, J. P. Knauer, F. J. Marshall, D. D. Meyerhofer, S. Skupsky, S. Roberts, C. Sorce, T. C. Sangster, T. W. Phillips, and M. D. Cable, Rev. Sci. Instrum. **72**, 864 (2001).
9. D. Keller, T. J. B. Collins, J. A. Delettrez, P. W. McKenty, P. B. Radha, B. Whitney, and G. A. Moses, Bull. Am. Phys. Soc. **44**, 37 (1999).
10. Lord Rayleigh, Proc. London Math Soc. **XIV**, 170 (1883); G. Taylor, Proc. R. Soc. London Ser. A **201**, 192 (1950).
11. S. E. Bodner, Phys. Rev. Lett. **33**, 761 (1974).
12. H. Takabe *et al*., Phys. Fluids **28**, 3676 (1985).
13. R. Betti, V. N. Goncharov, R. L. McCrory, P. Sorotokin, and C. P. Verdon, Phys. Plasmas **3**, 2122 (1996).
14. G. I. Bell, Los Alamos National Laboratory, Los Alamos, NM, Report LA-1321 (1951).
15. M. S. Plesset, J. Appl. Phys. **25**, 96 (1954); D. L. Book and S. E. Bodner, Phys. Fluids **30**, 367 (1987); Laboratory for Laser Energetics LLE Review **94**, 81, NTIS document No. DOE/SF/19460-485 (2003). Copies of the last item may be obtained from the National Technical Information Service, Springfield, VA 22161.
16. M. C. Richardson, G. G. Gregory, R. L. Keck, S. A. Letzring, R. S. Marjoribanks, F. J. Marshall, G. Pien, J. S. Wark, B. Yaakobi, P. D. Goldstone, A. Hauer, G. S. Stradling, F. Ameduri, B. L. Henke, and P. Jaanimagi, in *Laser Interaction and Related Plasma Phenomena*, edited by H. Hora and G. H. Miley (Plenum Press, New York, 1986), Vol. 7, pp. 179–211.
17. A. A. Amsden, H. M. Ruppel, and C. W. Hirt, Los Alamos National Laboratory, Los Alamos, NM, Report LA-8095 (1980).
18. M. L. Wilkins, J. Comput. Phys. **36**, 281 (1980).
19. G. Maenchen and S. Sack, in *Methods in Computational Physics*, edited by B. Alder, S. Fernbach, and M. Rotenberg, Fundamental Methods in Hydrodynamics (Academic Press, New York, 1964), Vol. 3, pp. 181–210.
20. A. M. Winslow, J. Comput. Phys. **2**, 149 (1967); S. Atzeni and A. Guerrieri, Laser Part. Beams **9**, 443 (1991); J. U. Brackbill and J. S. Saltzman, J. Comput. Phys. **46**, 342 (1982).
21. B. van Leer, J. Comput. Phys. **23**, 276 (1977).
22. D. L. Youngs, in *Numerical Methods for Fluid Dynamics*, edited by K. W. Morton and M. J. Baines (Academic Press, London, 1982), pp. 273–285.
23. D. J. Benson, Comput. Methods Appl. Mech. Eng. (Netherlands) **99**, 235 (1992).
24. S. P. Lyon and J. D. Johnson, Los Alamos National Laboratory, Los Alamos, NM, Report LA-UR-92-3407 (1992).
25. A. R. Bell, Rutherford Appleton Laboratory, Chilton, Didcot, Oxon, England, Report RL-80-091 (1980).
26. R. M. More, K. H. Warren, D. A. Young, and G. B. Zimmerman, Phys. Fluids **31**, 3059 (1988).
27. W. F. Huebner *et al*., Los Alamos National Laboratory, Los Alamos, NM, Report LA-6760-M (1977).

28. S. Balay *et al.*, in *Modern Software Tools for Scientific Computing*, edited by E. Arge, A. M. Bruaset, and H. P. Langtangen (Birkhäuser, Boston, 1997), Chap. 8, pp. 163–202.

29. MPI Version 1.2 Standard for IRIX—A Communication Language for Parallel Processing (2001).

30. L. M. Hively, Nucl. Fusion **17**, 873 (1977).

31. R. L. McCrory and C. P. Verdon, in *Inertial Confinement Fusion*, edited by A. Caruso and E. Sindoni (Editrice Compositori, Bologna, Italy, 1989), pp. 83–124.

32. V. N. Goncharov, P. McKenty, S. Skupsky, R. Betti, R. L. McCrory, and C. Cherfils-Clérouin, Phys. Plasmas **7**, 5118 (2000).

33. S. Skupsky, R. W. Short, T. Kessler, R. S. Craxton, S. Letzring, and J. M. Soures, J. Appl. Phys. **66**, 3456 (1989).

34. T. R. Boehly, V. A. Smalyuk, D. D. Meyerhofer, J. P. Knauer, D. K. Bradley, R. S. Craxton, M. J. Guardalben, S. Skupsky, and T. J. Kessler, J. Appl. Phys. **85**, 3444 (1999).

35. R. D. Richtmyer, Commun. Pure. Appl. Math. **XIII**, 297 (1960); V. A. Andronov *et al.*, Sov. Phys.-JETP **44**, 424 (1976).

36. V. N. Goncharov, Phys. Rev. Lett. **82**, 2091 (1999).

37. F. J. Marshall, J. A. Delettrez, R. Epstein, R. Forties, R. L. Keck, J. H. Kelly, P. W. McKenty, S. P. Regan, and L. J. Waxer, Phys. Plasmas **11**, 251 (2004).

38. S. E. Bodner, J. Fusion Energy **1**, 221 (1981).

39. V. N. Goncharov, S. Skupsky, T. R. Boehly, J. P. Knauer, P. McKenty, V. A. Smalyuk, R. P. J. Town, O. V. Gotchev, R. Betti, and D. D. Meyerhofer, Phys. Plasmas **7**, 2062 (2000).

40. C. B. Burckhardt, Appl. Opt. **9**, 695 (1970).

41. Y. Kato *et al.*, Phys. Rev. Lett. **53**, 1057 (1984).

42. Laboratory for Laser Energetics LLE Review **65**, 1, NTIS document No. DOE/SF/19460-117 (1995). Copies may be obtained from the National Technical Information Service, Springfield, VA 22161.

43. R. Epstein, J. Appl. Phys. **82**, 2123 (1997).

44. S. P. Regan, J. A. Marozas, J. H. Kelly, T. R. Boehly, W. R. Donaldson, P. A. Jaanimagi, R. L. Keck, T. J. Kessler, D. D. Meyerhofer, W. Seka, S. Skupsky, and V. A. Smalyuk, J. Opt. Soc. Am. B **17**, 1483 (2000).

45. R. C. Cook, R. L. McEachern, and R. B. Stephens, Fusion Technol. **35**, 224 (1999).

46. R. Betti, V. N. Goncharov, R. L. McCrory, and C. P. Verdon, Phys. Plasmas **5**, 1446 (1998).

47. J. P. Knauer, R. Betti, D. K. Bradley, T. R. Boehly, T. J. B. Collins, V. N. Goncharov, P. W. McKenty, D. D. Meyerhofer, V. A. Smalyuk, C. P. Verdon, S. G. Glendinning, D. H. Kalantar, and R. G. Watt, Phys. Plasmas **7**, 338 (2000).

48. R. Betti, K. Anderson, V. N. Goncharov, R. L. McCrory, D. D. Meyerhofer, S. Skupsky, and R. P. J. Town, Phys. Plasmas **9**, 2277 (2002).

49. D. C. Wilson, C. W. Cranfill, C. Christensen, R. A. Forster, R. R. Peterson, H. M. Hoffman, G. D. Pollak, C. K. Li, F. H. Séguin, J. A. Frenje, R. D. Petrasso, P. W. McKenty, F. J. Marshall, V. Yu. Glebov, C. Stoeckl, G. J. Schmid, N. Izumi, and P. Amendt, Phys. Plasmas **11**, 2723 (2004).

50. G. Dimonte, Phys. Plasmas **6**, 2009 (1999).

51. L. D. Landau and E. M. Lifshitz, *Fluid Mechanics*, 2nd ed., Course of Theoretical Physics, Vol. 6 (Butterworth-Heinemann, Newton, MA, 1987), p. 36.

52. J. G. Wouchuk and R. Carretero, Phys. Plasmas **10**, 4237 (2003).

Formation of Deuterium-Ice Layers in OMEGA Targets

When the OMEGA Cryogenic Target Handling System (CTHS) became operational in July 2000, it was the culmination of a seven-year engineering effort to build the infrastructure needed to produce cryogenic inertial confinement fusion (ICF) targets. These targets are used for implosion experiments that are a one-third scale of the experiments to be performed on the National Ignition Facility (NIF). These experiments allow issues that affect the quality of the implosion, such as the hydrodynamic stability and laser imprint, to be correlated to the laser performance and target specifications.

This article discusses the process of forming a cryogenic target—specifically, how to make a 0.9-mm-diam shell of deuterium ice constrained in a thin-walled plastic shell. The process differs from that developed for earlier cryogenic systems in many aspects: (1) there is sufficient deuterium mass to form thick-walled (100-μm) shells; (2) the deuterium is permeated into the plastic shell, eliminating the need for a filling tube, which can perturb the thermal environment and influences the process; (3) the system possesses all of the engineering features needed to deliver a target for implosion, so the effect of those features are included in the process demonstrated to make cryogenic targets; and (4) the CTHS system can also produce cryogenic NIF-sized targets, which will allow the cryogenic processes to be demonstrated on full-sized ignition targets, even if the targets are too massive to be imploded on OMEGA in meaningful experiments. Schematics of OMEGA- and NIF-scale, direct-drive cryogenic targets are shown in Fig. 99.21. The OMEGA cryogenic target is a 0.9-mm-diam plastic shell with a 3-μm wall that is diffusion filled to a maximum pressure of 1500 atm. This gas density equates to a solid-deuterium wall thickness of up to 130 μm—one-third scale of a NIF direct-drive-ignition target.

Overview of the Process Used to Make Cryogenic Targets

The process of transforming a plastic shell containing liquid deuterium into a cryogenic ICF target where a uniformly thick wall of deuterium ice adjoins the inner plastic wall is referred to as "layering."

Initially, an empty plastic shell is at vacuum and room temperature inside a pressure vessel. A hydrogen-isotope gas (deuterium presently and a deuterium–tritium mixture in the future) is added to the vessel until the pressure is approximately 1000 atm (depending on the desired ice thickness and shell dimensions). For any pressure ramp lower than the ratio of the shell's buckle pressure to the permeation rate (typically 1 atm per minute), the hydrogen gas will diffuse through the plastic without buckling the shell. Once the plastic shell

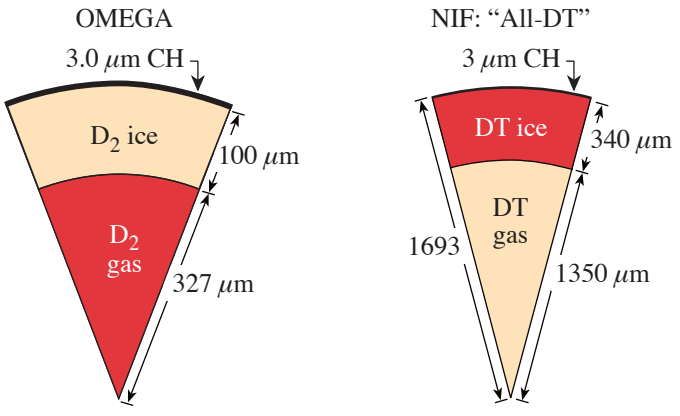

Figure 99.21
Schematic showing the dimensions of direct-drive targets for use on OMEGA and the NIF.

contains sufficiently dense hydrogen gas (~0.1 g/cm^3), it is gradually cooled: the liquid phase first appears at the critical point (38 K) and the solid forms at the triple point (18.72 K). At 18.72 K the hydrogen fuel is a solid "lump" with a vapor pressure of less than 200 Torr. The plastic shell is removed from the pressure vessel and transferred, inside a cryostat, to the mobile cryostat that transports the target to the OMEGA target chamber. The latter cryostat has two critical components: (a) a 2.5-cm-inner-diam isothermal copper shell that is placed around the target and (b) the "life-support" equipment required to sustain the target at all times.

When the target is centered inside the isothermal copper shell (called the *layering sphere*), it is bathed in infrared light at a wavelength that is absorbed by the deuterium. The combination of volumetric heating from the IR light and the isothermal boundary at the layering sphere creates a temperature gradient within the deuterium: the deuterium is warmest where it is thickest and closest to the center of the sphere. In minimizing this temperature gradient, the ice/liquid redistributes itself on the inside surface of the plastic shell. Eventually the ice forms a contiguous shell wall with an isothermal inner surface. The goal is a uniform-thickness deuterium-ice wall with a root-mean-square (rms) thickness variation of less than 1 μm.

The metric for the ice-layer quality is the roughness of the inner surface, which is equated to the ice-wall-thickness uniformity; however, the suitability of this value as a proxy for ice-thickness uniformity depends on the sphericity of the outer deuterium wall and, hence, the plastic shell, which defines the geometry. Typically, a plastic shell possesses an eccentricity of 0.1 μm to 0.5 μm and the wall thickness varies by <0.2 μm—values that can affect the ice-thickness uniformity and cause the ice roughness and thickness uniformity to differ. For a uniformly thick plastic shell with an isothermal outer surface, the ice shell will be uniformly thick if the radial thermal conductance is constant around the target. Under these optimal circumstances, any roughness on the inner surface of the ice will be due to the crystalline structure of the ice. In practice, such higher-spatial-frequency roughness is overwhelmed by low-mode roughness caused by imperfections in the target and asymmetries in the layering sphere.

Four years' experience in producing cryogenic targets identifies the elimination of the low-mode ice roughness as the major challenge to producing high-quality implosion targets. The highest-quality ice layers have an rms roughness of 1.2 μm, averaged over the entire surface (see Fig. 99.22). More typically, the roughness averages 3 μm to 6 μm, although values as great as 8 μm to 10 μm also occur. This article analyzes potential causes for the low-mode roughness and provides experimental data quantifying the effect of the perturbations on the roughness magnitude. Thermal and ray-tracing models make explicit how sensitive the ice roughness is to its environment. This allows a better understanding of the required level of control from the cryogenic equipment and provides better direction for improving the equipment.

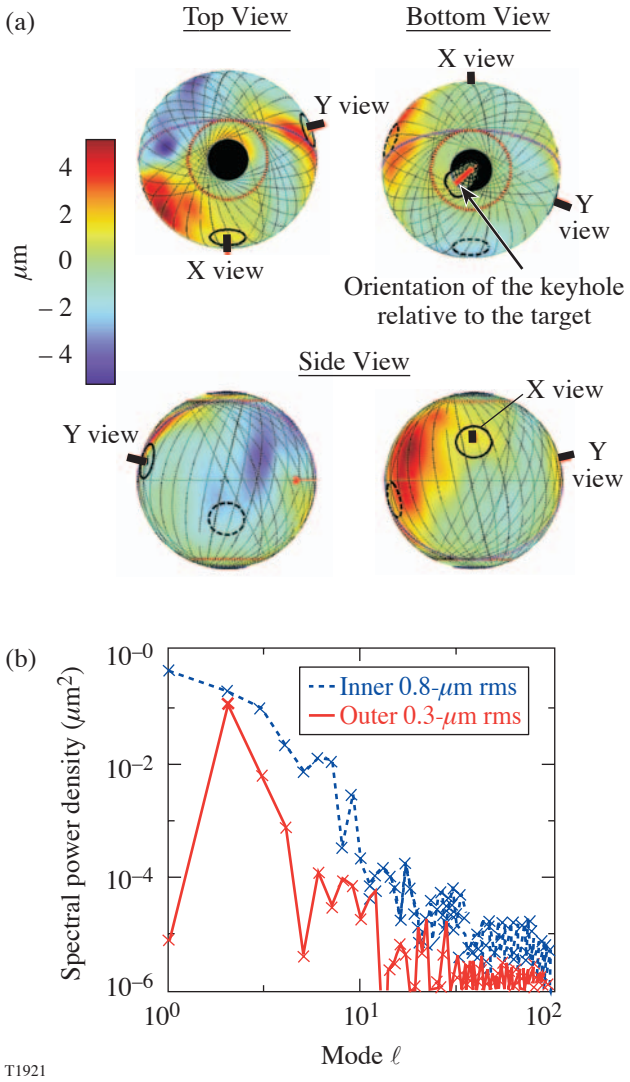

Figure 99.22
(a) Four views of the surface of an 80-μm-thick, 880-μm-diam spherical ice layer. The shading shows the variation in thickness of the ice. The 3-D profile is compiled from 50 2-D views. (b) Two-dimensional power spectra of the inner ice surface and the outer plastic surface.

Introduction

The concept of layering was first demonstrated by radioactively inducing sublimation in solid tritium.[1] Subsequent work at Los Alamos National Laboratory (LANL) and Lawrence Livermore National Laboratory (LLNL) expanded the science and better quantified the process. This work relied on heat generated by the decay of a triton atom yielding a ^{3}He nucleus, a beta electron, and an antineutrino with 18.6 keV of energy collectively. The average β energy is 6 keV and equates to a volumetric heating rate of 51 kW/m^3 (0.977 W/mol, hereafter referenced as 1 Q_{DT}). Subsequent work at LLNL demonstrated that volumetric heating could also be achieved by radiatively heating the hydrogen-isotope ice using infrared illumination.[2] This method made it possible to "layer" nontritium hydrogen isotopes and is used to make the deuterium-ice layers studied and reported here.

An important difference between work reported here and earlier layering work is the geometry of the layering environment and the absence of a fill tube; earlier studies used geometries such as hemispheres, cylinders, and other surrogate geometries. These compromises simplified both filling the targets (a diffusion-filling capability is both complex and expensive) and diagnosing the layering process. However, the fill tube affected the thermal environment around the target, which affects the layering process itself. A protocol for a fill-tube-free layering method, and the resulting layer quality, is presented in the remaining sections, which (1) deal with the principles of the layering process, (2) examine the methodology of experimentally measuring the success of layering, (3) discuss how various parameters affect the layering process, and (4) present a summary and discussion.

Layering Process

Experimentally, the process used to form a layer is straightforward: The target is centered in a 2.5-cm-diam, temperature-controlled, hollow sphere—the layering sphere (Fig. 99.23). The sphere contains helium gas to conduct the heat away from the target. The internal surface of the sphere is purposely roughened to form an "integrating sphere," which allows the target to be uniformly irradiated with infrared light at 3.16 μm, a frequency that corresponds to the strongest absorption band in the deuterium-ice [the $Q_1(1) + S_0(0)$ and $Q_1(0) + S_0(0)$ bands] molecular crystal,[3] in which each crystal-lattice site is occupied by one D_2 molecule.

There are two procedures for layering targets: One process starts with the target below the triple point (18.72 K) and a frozen lump of deuterium in the bottom of the target. Deuterium absorbs the IR light and becomes warmer than the plastic shell's outer surface. Solid deuterium sublimes from where it is thickest (and therefore hottest because of volumetric heating) and condenses where it is thinnest. In theory, the ice wall will become uniformly thick. In practice, there is an ~10- to 20-μm peak-to-valley variation in ice thickness formed by this method.

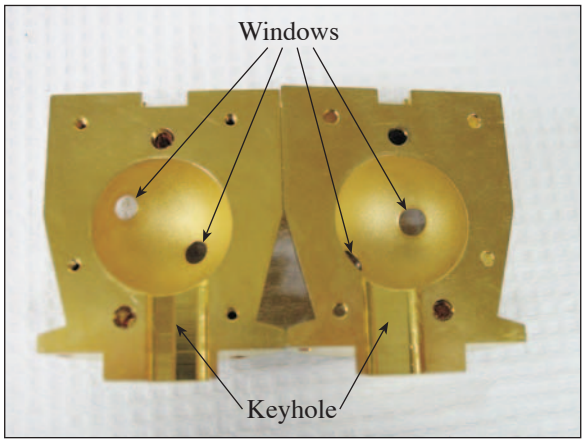

T1933

Figure 99.23
The two hemispheres that comprise the layering sphere are shown side by side. The "keyhole" opening at the base of the layering sphere is where the target is inserted and removed.

A second, more-successful method for forming a smooth ice layer starts with the deuterium in the liquid phase and then gradually cools the target through the triple point. The initial thermal environment *inside* the target is shown in Fig. 99.24. The temperature gradient along the interface between the gas and the liquid is determined by the helium gas pressure outside the target and the heat coupled into the deuterium. Properly executed, this process forms a single crystal within the melt that is first observed near the target's equator and then propagates azimuthally and vertically within the shell.

Figure 99.25 shows the same target produced using both methods. It demonstrates the importance of controlling the solidification rate: all parameters other than the temperature difference between the layering sphere and target, which controls the heat flux from the target (and hence the solidification rate), were kept constant; the same target was maintained in the identical position and orientation in the layering sphere, and the same volumetric heating rate was used. The smoother ice layer (2.5-μm rms) was produced at a temperature ~0.1 K

below the triple point; the second, rougher ice layer (4.3-μm rms) was produced at a temperature ~0.2 K below the triple point, in a faster solidification process. This difference in roughness can be attributed only to the intrinsic properties of the ice (the crystallographic structure and how well it attaches to the inner plastic wall). Both images show features that can be eliminated by carrying out the process still closer to the triple point (within 5 to 10 mK).

Ultimately, if the outer surface of the plastic capsule is isothermal, the ice will possess equivalent thickness everywhere if all of the following conditions are identical throughout the capsule: (1) heat conductance through the ice; (2) heat resistance at the ice/plastic interface; (3) heat conductance through the plastic; and (4) volumetric heating into the ice (and plastic). In the above comparison, the importance of the solidification rate on the resulting ice smoothness was demonstrated because only conditions (1) and (2) could vary. The effect of items (3) and (4) remained invariant because the plastic shell and its position in the layering sphere were the same.

One final consideration is to determine how precisely the solidification process must be controlled to achieve a "perfectly" uniform thick layer. The stochastic nature of the freezing process will always cause some variability to the layer quality, and this contribution to the overall roughness will become more important as extraneous, equipment-related perturbations to the ice are eliminated (examples include nonuniform heating or the position of the target in the layering sphere).

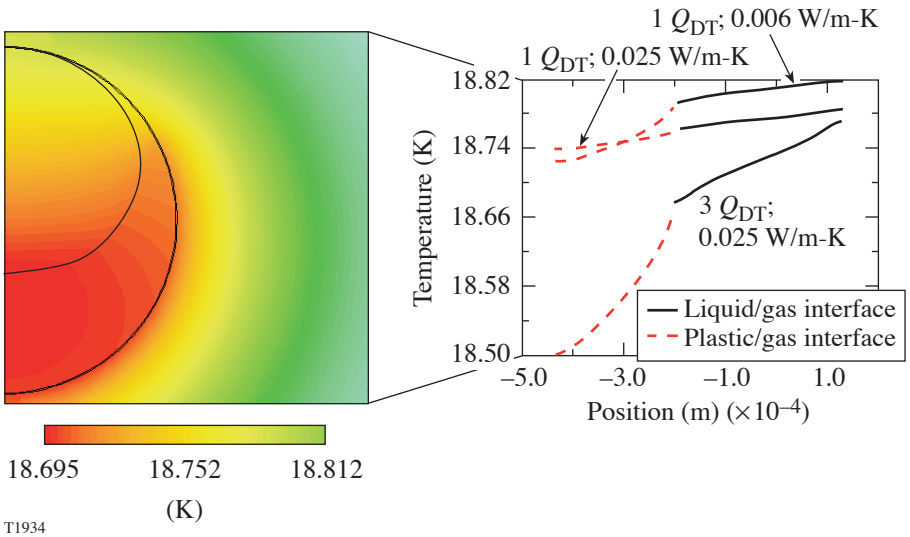

Figure 99.24
Temperature distribution inside a liquid-D_2–containing OMEGA target. Three different volumetric heat loads (1 and 3 Q_{DT}) and two different helium exchange gas pressures, which yield different thermal conductivities, are plotted.

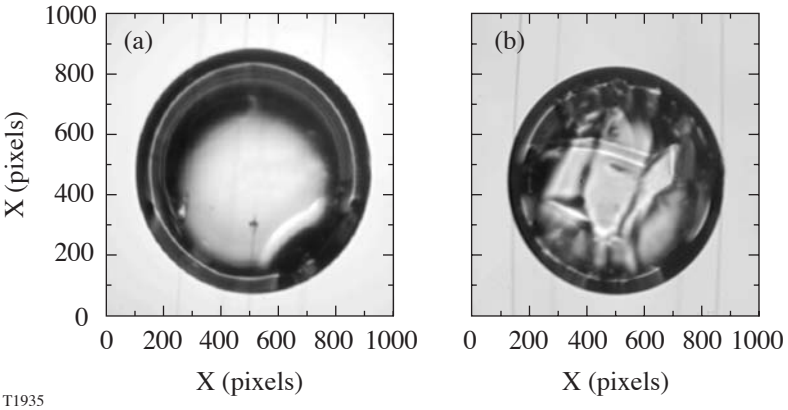

Figure 99.25
Image of the same target with two different ice layers. The first layer (a) is formed gradually at a temperature that is close to the triple-point temperature (within 0.1 K). The second layer (b) occurs when liquid is frozen instantaneously at a temperature and then allowed to layer.

Characterizing the Ice Layer

1. Experimental Configuration

The optical system used to measure the ice-layer roughness is shown in Fig. 99.26. The layering sphere has two pairs of opposing windows oriented along axes corresponding to the viewing axes in the OMEGA target chamber. The windows corresponding to the X- and Y-axis cameras are positioned 26.6° and 12° above and below the equator, respectively, and 110° apart.

The light-emitting diodes that back-illuminate the target are opposite the cameras. The diodes operate at 1 Hz and 0.15 A with a 30-ms to 300-ms exposure. The emission wavelength is 612 nm, i.e., in a spectral region where the deuterium (or tritium) ice does not absorb but where the plastic shell has broadband absorption of 5% to 10%. These exposure conditions permit a target image to be acquired in a sufficiently short period that vibration-induced blurring is minimized. Also, the brief exposure duration minimizes the heat load to the target. Based on measurements, and supported by calculations, the heat load to the target is <10 nW. Operating the diodes at a higher duty cycle and current can produce heat loads (in the plastic shell) that approach 0.1 μW, a value that is a significant fraction of the 10 μW to 30 μW deposited in an OMEGA target by IR radiation during layering. The effect of higher diode-radiation loads on a target is shown in Fig. 99.27. Here, in an extreme example, the diode is seen to deplete the 100-μm ice layer along the illumination axis. That such a drastic effect is induced at high illumination intensities underscores the need for minimizing any nonuniform heat load to the target, including loads from all optical systems associated with positioning the target in the target chamber as well as from the target existence detector.

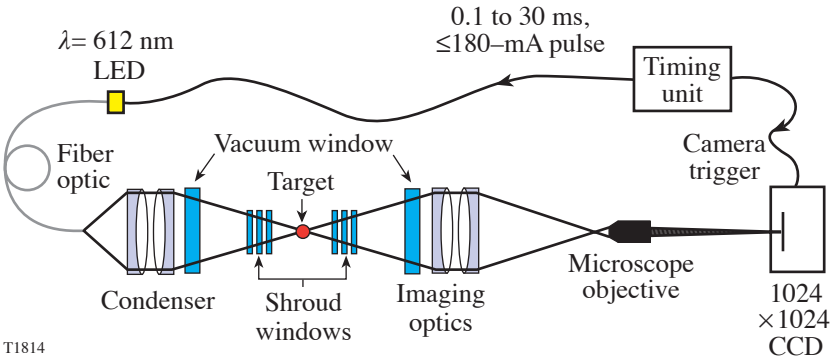

Figure 99.26
Schematic of the optical system used to acquire images of cryogenic targets.

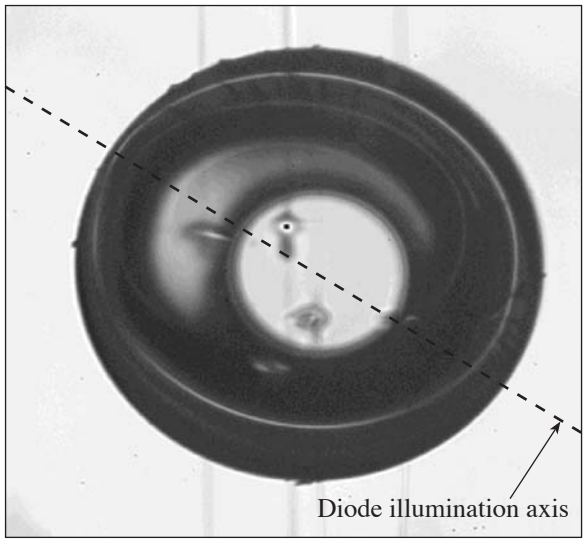

Figure 99.27
The ice layer is distorted (thinner) along the axis of the diode illumination used to backlight the target. The diode light (612 nm) was absorbed in the plastic to create localized hot spots.

2. Numerical Analysis

Backlighting the target provides an image as shown in Fig. 99.28. Notable are the outer limb of the plastic shell and narrow, concentric, circular, bright bands due to light reflecting off the inner ice surface. The brightest band is light reflected from the inner ice surface perpendicular to the illumination axis. Less-intense bands are reflections from different regions of the inner ice surface and may include multiple internal reflections. Only the brightest band is analyzed. The band may vary in intensity, or become discontinuous, due to either scattering centers in the ice (i.e., crystallographic features) or defects on the surface of the plastic shell that deflect light rays that would otherwise be captured by the viewing optics.

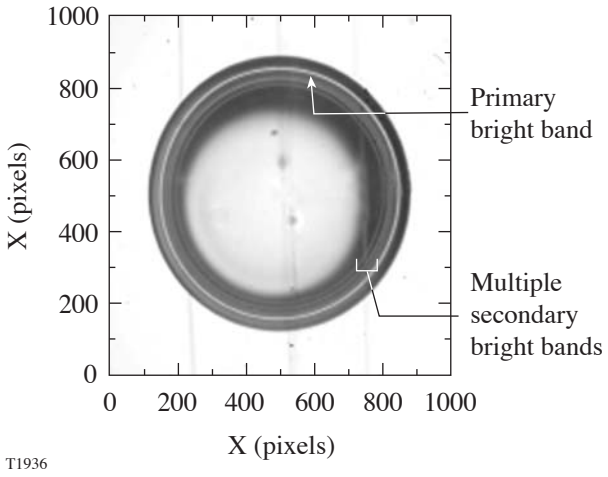

Figure 99.28
An example of a high-quality ice layer where both the primary bright band and multiple secondary bright bands are visible.

This technique, referred to more generally as *shadowgraphy,* yields a 2-D slice through the ice layer. Rotating the target and acquiring an image at each rotational position allows a 3-D tomographic image of the ice layer to be assembled.

The analysis algorithm calculates the center of the target from the outer limb of the plastic capsule and then determines the radial distance from the center to the inner ice surface. The variation in the distance is approximated using a Fourier cosine expansion. The coefficients of the expansion report the spectral power density in each mode. The layer roughness is calculated separately as an rms least-squares fit to the entire data set. The Fourier spectral decomposition better defines how the roughness is distributed. Phase information from the 2-D analysis is not used; that information is more easily visualized from the 3-D analysis.

The camera and optics provide a resolution of ~1.1 μm per pixel, and a total of ~350 pixels comprise the circumference of the bright band. Although the diffraction limit on the resolution is 3 μm to 4 μm, the statistics afforded by the large number of pixels allows the roughness to be determined with a precision better than 0.5 μm. This analysis assumes that the outer ice surface (the one contacting the plastic capsule) is perfectly circular, whereas the actual roughness ranges from 0.2 μm to 0.7 μm (as defined by the roughness and thickness uniformity of the plastic wall); clearly, as the ice roughness approaches the 1-μm goal, the existence of a 0.5- to 0.7-μm roughness due to the plastic will make the ice seem rougher than it really is. An example of this is shown in Fig. 99.29 where the ice roughness was 1.1 μm and the plastic roughness was 0.5 μm.

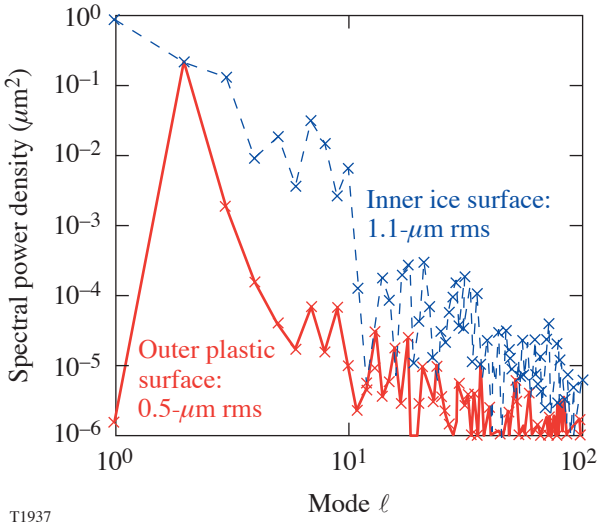

Figure 99.29
The power spectrum of a 100-μm ice layer shows that the smoothness is approaching the goal of 1-μm-rms roughness. The roughness is primarily in spectral modes 1 through 10, with comparatively little power in higher modes.

It is important to know the accuracy and repeatability of the analysis algorithm. Two methods were used to acquire this information: In the first method, a 1-mm sapphire ball with a measured ~0.05-μm-rms roughness (characterized using atomic force microscopy) was inserted into the layering sphere and the outer limb was analyzed with the optical system and software tools. The measured optical roughness was ~0.2 μm (rms), four times the roughness obtained using the more-accurate AFM technique. This suggests that the technique has an amplitude threshold below which the precision is increasingly dominated

by pixelated noise. In the second method, seven successive images of a target were acquired. Multiple ice layers were studied, and the difference between the average value of each data set of seven images and the actual value is shown in Fig. 99.30. A total of 382 data sets were analyzed and showed a repeatability of ±0.1 to 0.2 μm for most ice layers. Targets that vibrated significantly exhibited a greater variability in the roughness (up to 0.7-μm difference), despite the strobing effect of the pulsed illuminator. It is likely that different target views were imaged because a vibrating target also rotates slightly. These data suggest that a minimum of three and maximum of five images of each 2-D great circle be acquired in order to attain statistical confidence in the data.

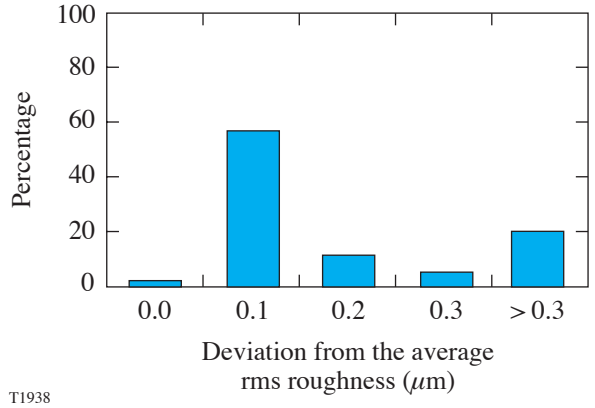

Figure 99.30
Histogram showing the variation of the inner ice surfaces' rms roughness from an average, as determined by the shadowgram analysis routine. The average rms roughness was calculated from seven repeat images of the same ice layer.

Ice-Layer Quality

1. Solidification Process

At the start, deuterium is a liquid with its meniscus extending 3/4 of the way up the side of the capsule. Although it cannot be imaged, a thin, contiguous fluid layer should exist around the entire capsule since liquid hydrogen effectively wets plastics; the contact angle is zero.[4] The temperature is initially 0.05 K to 0.1 K above the triple point and is lowered by 0.2 K to begin solidification. A seed crystal appears first near the equator and expands vertically up the sides of the capsule. This behavior differs from that observed in targets containing fill tubes where a seed crystal is always present at the fill tube (at the top of the target) and the crystal grows from gas condensation.[5] Throughout the process, the target is thermally loaded by 3.16-μm radiation at a constant rate.

To fully solidify the target, the latent heat of fusion must be removed. In an OMEGA-scale target, this amounts to a total of ~2 mJ. The solidification time depends on the temperature difference between the target and the layering sphere and the helium gas that may be in one of two possible pressure regimes. Equation (1) applies to sufficiently high helium-gas pressure (*continuum* or *kinetic* regime), where heat flow is independent of pressure:[6]

$$Q = 2k\left(T_{\text{target}} - T_{\text{layering sphere}}\right) d_i d_o / \left(d_o - d_i\right), \qquad (1)$$

where Q is the heat flow from the target to the layering sphere, d_i is the diameter of the inner sphere, d_o is the diameter of the layering sphere, and k is the thermal conductivity of helium gas. In this application, the only variable parameter in Eq. (1) is the temperature of the layering sphere: the target will completely freeze in <1 s for a temperature gradient of 1 K between the target and the layering-sphere boundary. Since the goal is to slowly freeze the target to achieve a *single* seed crystal from which a single ice crystal can grow, the solidification rate depends strongly on (1) knowing precisely the layering-sphere temperature that *corresponds to the triple point in the target* and (2) maintaining the layering-sphere temperature marginally (10 mK) below this "triple-point-equivalent" value. Rapidly freezing the target forms a polycrystalline ice structure that makes it difficult to observe the bright band and to achieve a smooth ice layer [Fig. 99.25(b)].

This temperature differential can be ascertained by performing the inverse of freezing, i.e., *melting* the ice. Typical volumetric heat loads to the target range from 8 μW to 30 μW. (This value is determined by forming an ice layer using IR light, isolating the IR source, raising the temperature of the layering sphere and target to 18.72 K, and switching on the IR heat source again. The time required for the solid to melt provides an estimate of the heat load since the heat of fusion for deuterium and the mass in the target are accurately known.) These heat loads predict a steady-state temperature difference between the target and the layering sphere of the order of 0.05 K to 0.2 K; the actual temperature difference is 0.7 K to 2 K. Such a discrepancy points toward a helium-gas pressure in the layering sphere well below the continuum limit where thermal conduction depends on gas pressure. This situation is plausible since the gas path to the layering sphere is not leak-tight (an unavoidable "real-world" consequence of the equipment having to provide targets for implosion experiments, as opposed to a single-purpose, scientific test bed).

Equation (1) applies when the mean free path of the gas is significantly shorter (1/100th or less) than the distance between the target and the layering sphere. When the mean free path is of the same order, or larger, than the scale length (the Knudsen number >1), the gas is in the *transition or molecular regime*, and heat transport between the target and the layering sphere is described as[7,8]

$$Q = (a_o/4)\left[(\gamma+1)/(\gamma-1)\right]\sqrt{2R/\pi M} \times P\left(T_{\text{target}} - T_{\text{layering sphere}}\right)\Big/\sqrt{T_{\text{target}}}, \quad (2)$$

where R is the universal gas constant, P is the pressure, M is the molecular weight, γ is the ratio of the specific heat capacity at constant pressure and volume $\left(\gamma = C_p/C_v\right)$, and

$$a_o = \frac{a_1 a_2}{a_2 + \left(\frac{A_2}{A_1}\right)(1-a_2)a_1}, \quad (3)$$

where a_1 (or a_2) is the accommodation coefficient of helium at a surface, A is the surface area, and 1 and 2 refer to the layering sphere and target, respectively.

Operating the layering process at a helium pressure below the continuum limit requires a lower temperature on the layering sphere to freeze the deuterium. This is to compensate for the diminished thermal transport through the gas. Figure 99.31(b) shows this effect.

A second effect of the low helium-gas pressure pertains to the temperature gradient that it establishes around the outside (θ,ϕ) of the plastic shell, which increases the temperature gradient across the void space within the target (Fig. 99.24): the temperature gradient increases from 0.05 K to 0.11 K, for a heat load of 1 Q_{DT}, when the helium pressure is decreased from the continuum to the molecular regime. This temperature gradient is important since it affects the heat flux from the target and the dynamics of crystal growth. Typically, the OMEGA CTHS operates in the transitional region between the kinetic and molecular regimes.

While the target freezes, the ice temperature remains at, or very close to, the triple point temperature of 18.72 K. Once the latent heat of fusion is removed, the target continues to cool until it reaches a temperature where the IR heat load into the target is balanced by the heat flow out of the target. This temperature depends only on the temperature of the layering sphere, the helium-gas pressure, and the heat in the target. There are consequences for lowering this temperature in terms of strain experienced by the ice. The farther the final target temperature reaches below the triple point, the greater the ice strain (ice contracts by ~0.45%/K; contraction in the plastic is negligible over this range). The induced strain adds to any intrinsic strain due to the crystal contorting to the confines of the shell. Once the local strain exceeds the yield point (~0.2% strain),[9] the induced stress will cause the ice to fracture. The radial-thermal-conduction uniformity, and hence the ice-thickness uniformity, will be affected by where, and how extensively, the ice fractures.

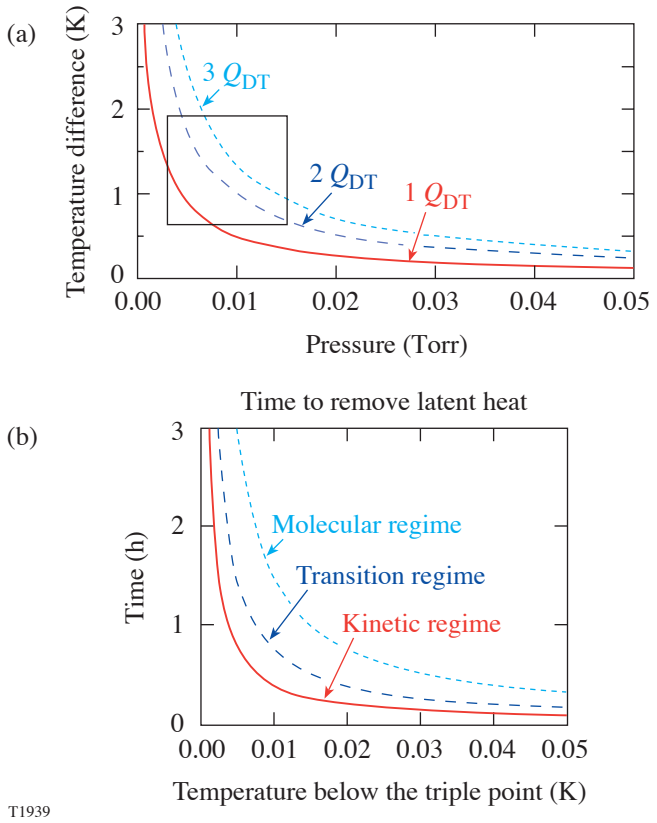

Figure 99.31
(a) The relationship between the helium-gas pressure and the temperature difference between the target and the layering sphere is shown for three heat loads (1, 2, and 3 Q_{DT}) (accommodation coefficient is 0.5). (b) The relationship between the time required to remove the latent heat from the target and the helium pressure and temperature gradient (between the target and the layering sphere). The inset box in (a) shows the typical region of operation.

2. Effect of the Solidification and Layering Process on the Resulting Ice Roughness

The solidification process is inherently stochastic. It depends on where a seed crystal forms, how many seeds form, and how quickly the resulting crystals grow and then interact. The resulting ice morphology, including facets or dislocations in the crystal structure, may influence the thermal-conduction path that in turn affects the final ice roughness.

To separate the effects of ice morphology and external perturbations on the ice roughness, and to quantify the inherent variability in the solidification process, a single target was repeatedly layered and melted using the identical protocol and configuration (the same IR heating power, helium-gas pressure, and target position). For each repetition, the liquid-containing target started at the same initial temperature, and layering was initiated using the same temperature decrement. The roughness of 11 separately formed ice layers is shown in a polar plot in Fig. 99.32. Each layer was rotated through 360°, and a 2-D image was acquired every 15°. The rms roughness of each great circle was plotted against the corresponding rotational angle. Three trends are noticeable: (1) The roughness of each great circle for a particular rotation shows good repeatability. The rms values are within ±1 μm of the average. (2) There is strong correlation between the roughness and the target's rotational orientation (±1-μm variability), and (3) there is significant variability in the roughness of each layer (±2 μm). This test was repeated using two different targets to determine if the rotational correlation was capsule dependent. The targets were layered, melted, and relayered three times with similar results (Fig. 99.33). Each layer's roughness repeated to within ±0.6 μm, and a similar azimuthal dependency of the roughness was observed. These data sug-

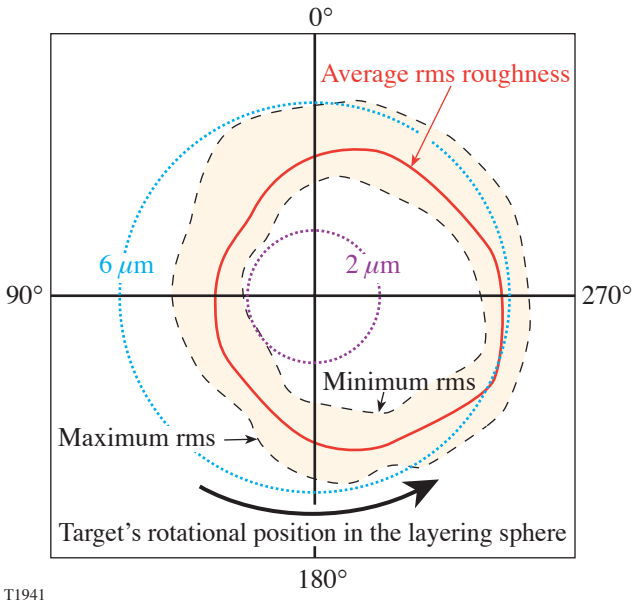

Figure 99.32
Polar plot showing the rms ice roughness of individual 2-D great circles through the target relative to the layering sphere. The average, minimum, and maximum roughness values of 11 different layers are shown for each 15° rotational angle.

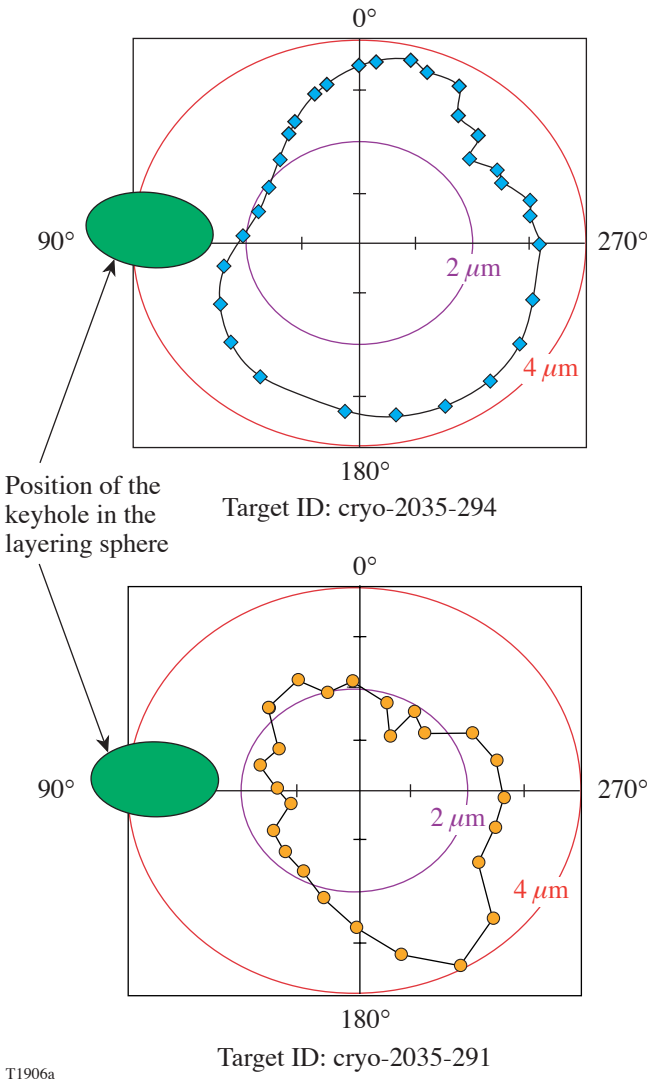

Figure 99.33
Polar plots showing the rms roughness of 2-D great circles relative to the layering sphere. Three separate ice layers were averaged for each plot. Each plot corresponds to a separate target.

gest the following: (1) the geometry of the layering sphere, not the plastic shell, is responsible for the azimuthal variation in roughness; and (2) the solidification and ice-layering process alone produced a variability of ±0.6- to 1-μm variability in the ice roughness.

Three-dimensional images of the ice-layer thickness of four of these layers (same target and layering conditions) are shown in Fig. 99.34. All layers have comparable roughness. The roughness distribution is similar: isolated regions of thicker ice are located at each target's equator and at varying azimuthal angles.

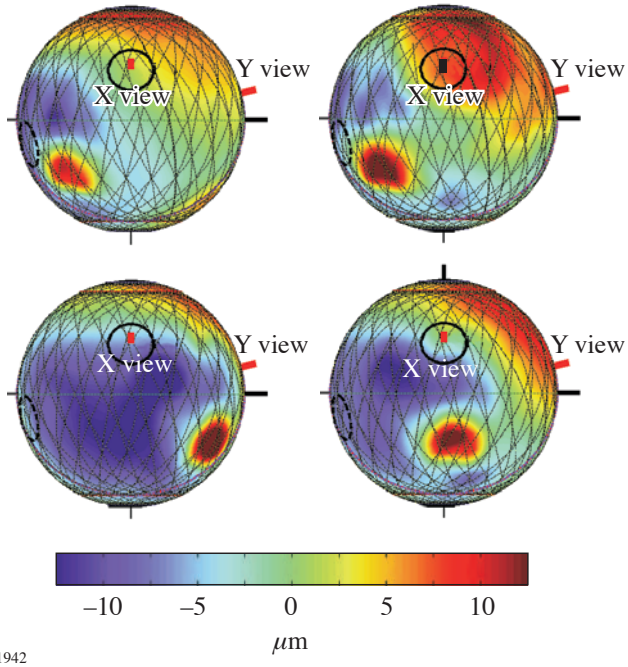

Figure 99.34
Three-dimensional plots of the ice thickness. Four separately formed ice layers in the same target are shown.

3. Effect of External Perturbations on the Ice-Layer Roughness

The environment surrounding the target will affect the ice-layer quality if there is insufficient control of the heat flows into and out of the target or if nonuniform illumination or thermal conditions exist. The stability of the heat flow *into* the target depends on the stability of the IR light source. The stability of the heat flow *out of* the target depends on a constant helium-gas pressure and constant temperature on the layering sphere. Uniform illumination of the target requires the layering sphere to perform as an integrating sphere to ensure uniform volumetric heating (no hot spots). Also, a uniform thermal boundary condition requires the layering sphere to be isothermal so that the outer surface of the plastic shell is isothermal *when* the ice is uniformly thick. The consequences of variations in any of these parameters are addressed next.

a. Stability of the IR source. The IR source is a pulsed optical parametric oscillator (OPO) supplied by Aculight, Inc. The pulse repetition rate is 30 kHz; the wavelength is tunable over the 2.9- to 3.3-μm range with a bandwidth of 10 nm. The IR light transits through a 60-ft optical fiber into the layering sphere. The layering sphere contains an indium antinomide (InSb) detector that measures the IR intensity and provides feedback for maintaining constant power. The maximum OPO output power is 200 mW, which is attenuated 60% to 80% by the fiber and coupling connectors. Of the 40 mW to 80 mW injected into the layering/integrating sphere, a maximum of 30 μW is coupled into the target. Reasons for this low efficiency are the low Q of the integrating sphere (ray tracing suggests that a ray traverses the sphere fewer than 20 times before exiting) and the low absorption in the 100-μm ice layer (~4%).

The long-term stability of the OPO power is important since the target's temperature needs to be below, but as close as possible to, the triple point. This limits the crystal to growing from a single seed, slows the growth rate, and minimizes the volume contraction that occurs when solidification is completed. Any drift in the OPO output power over the layering period may melt the ice crystal. For example, consider a layered target that is 0.01 K below the triple point: a +1% drift (increase) in OPO power (corresponding to an 0.08-μW variation) equates to a 0.001-K change in the target's temperature if the helium pressure is in the continuum regime; however, if the pressure is below the continuum limit, the temperature may increase by up to 0.060 K, which would melt the ice. A negative drift in OPO power does not lower the target's temperature, which is clamped at the triple point until solidification is complete, but will cause an imbalance in the overall heat flow and hence the solidification rate. The parametric relationship between the change in the target's temperature and the heat load and helium pressure for a 1% increase in the OPO power is shown in Fig. 99.35. As the layering-sphere temperature is controlled to ±0.001 K, it is the stability of the OPO source that controls the stability of the target's temperature.

Typical data for the long-term power stability of the OPO are shown in Fig. 99.36. The OPO drifts by ±4% over a 24-h period. When operated under closed-loop control, the drift in

power diminishes to less than ±1%. Short-term power fluctuations involving energy change substantially less than the latent heat of fusion may not melt or flash freeze the deuterium. They may, however, affect the crystal formation, i.e., a 1-μW increase in power (equal to 4% of 3 Q_{DT}), which places the target temperature above the triple point, will cause the target to slump within 10 min and to melt within a half hour.

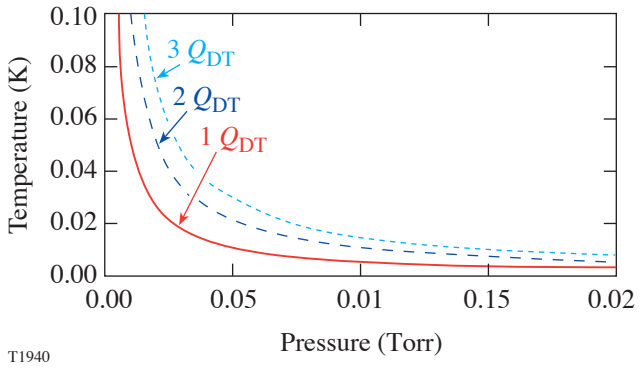

Figure 99.35
Graph showing the change in the target's temperature when the OPO power increases by 1%. The dependency of this response on different heat loads (1, 2, and 3 Q_{DT}) and helium-gas pressures is shown. The accommodation coefficient is 0.5.

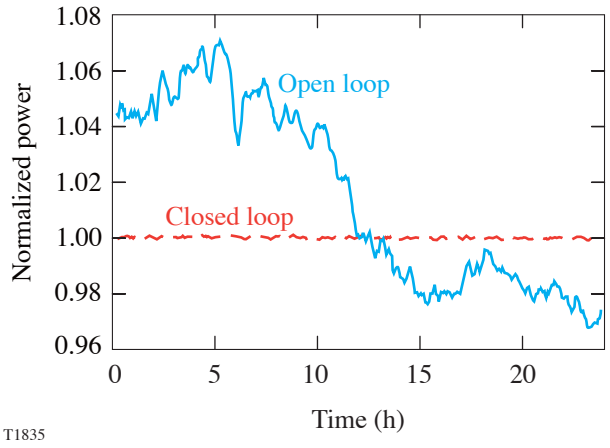

Figure 99.36
Plot showing the stability of the OPO when it is operated in closed-loop control and the magnitude of the drift when operated without feedback control.

b. Illumination uniformity of the layering sphere. As described earlier, the layering sphere containing the target is also the integrating sphere. The integrating feature is brought about by a purposely roughened, highly reflective Lambertian surface (gold coated) that is to provide a uniform IR intensity throughout the sphere. There are features, however, in the layering sphere that affect this illumination uniformity, including the four sapphire windows (~6-mm diam) and an entry hole at the base of the sphere used to insert and remove the target. The area of the entry hole is 2% to 3% of the total area and is the largest single feature affecting illumination uniformity. The effect of the shadow cast by this feature on the target was assessed by (1) tracing rays through the target to determine spatially where the heat was deposited in the ice, and (2) calculating how the resultant heat deposition affected the ice-layer thickness.

The ray-tracing calculation modeled only those rays that would originate from the "hole" region; rays originating elsewhere are uniformly distributed throughout the ice. The path of the rays through the ice was calculated from the refractive indices of the plastic, the ice, and the internal gas void, and the Fresnel coefficients when the angle of the ray relative to a surface was below a threshold.[10] The model was axisymmetric, and regions of the ice were zoned according to the ray density. Importantly, the ray density was not distributed isotropically (see Fig. 99.37). Because of the focusing effect of the ice, the density of rays at the target's rear surface is marginally greater than at the front surface. The largest variation in ray density was along a great circle perpendicular to the incident rays, but this was over a small area.

The assumed volumetric heat load into an axisymmetric thermal model of a cryogenic target was 8 μW (equivalent to the tritium decay energy in a DT target). Of this value, an average of 0.18 μW was subtracted from the target because of the absent rays that would have otherwise originated from the hole region. (This value is proportional to the ratio of the area of the hole to that of the entire surface.) The exact assignment of power into each zone was normalized to the ray density, where regions with the *highest* density of rays received the *largest reduction* in heat.

The resulting temperature profile on the internal ice surface was calculated using the computational fluid dynamic code FLUENT.[11] Simulating the ice-layering process manually, the ice-layer position was adjusted and the temperature distribution recalculated until the inner ice surface was isothermal.

The resulting ice-layer thickness is shown in Fig. 99.38. Spectral analysis of this great circle yields an ice roughness of ~4-μm rms.

Experimental evidence of this possible perturbation source is not straightforward since many competing sources can affect the ice-layer thickness. By examining only the smoothest targets, the contribution of other sources of roughness to the ice is reduced, which may allow the effect of the layering sphere to be more noticeable. Figures 99.39(a)–99.39(c) show a target with an average ice rms roughness of 1.2 μm (determined by averaging the roughness of 24 2-D great circles around a target) that possesses thinner ice facing the keyhole (bottom of the target) than at the rear surface (top of the target), which are the general locations predicted by the ray-tracing analysis. The light region in the image [Figs. 99.39(a)–99.39(c)] indicates a region of thicker ice and corresponds to the area where fewer rays coincide, possibly because of the shadow cast by the hole in the layering sphere.

The calculated ice thickness from the thermal model is shown in Fig. 99.39(d) for a 2-D great circle oriented along the same axis as the hole in the layering sphere. The volumetric heat load was obtained from the ray-trace calculation. The ice is thinnest where the target faces the hole (the darker hemisphere), and thicker opposite the hole. This pattern is similar to what is seen experimentally with the main difference being that the thick region of ice should be cylindrically symmetrical around the target's equator. While this is not conclusive evidence that the hole in the layering sphere is responsible for the observed ice-thickness variation, this possibility warrants a more-detailed study. Two limitations of the thermal model are that (1) it is only an axisymmetric model, not a 3-D model so that the modeled hole was circular, not of the more-complex

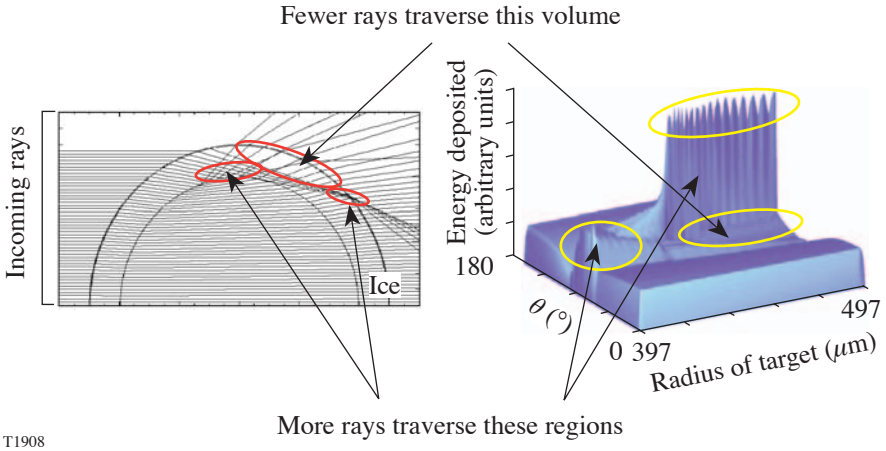

Figure 99.37
Ray trace through a symmetrical target showing where the IR energy is deposited in the ice. The focusing effect of the ice and internal reflection from the inner ice surface are responsible for the behavior. Q is the volumetric heat load.

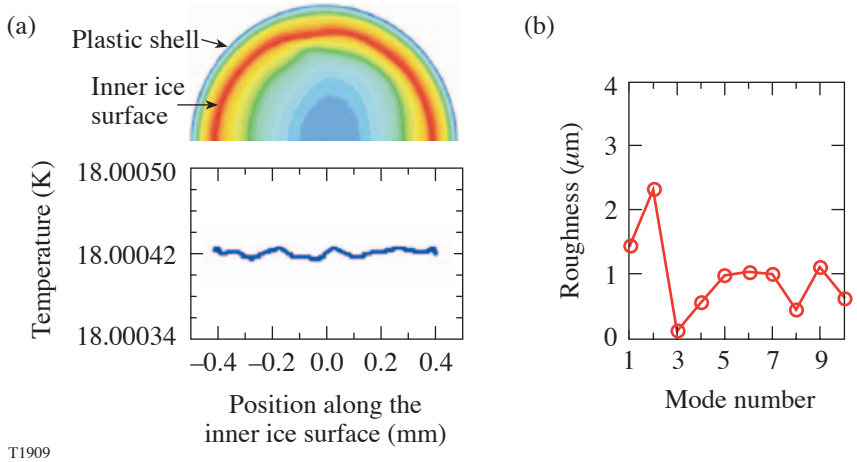

Figure 99.38
(a) Isotherms within an ice layer once the ice thickness is adjusted to account for the lack of illumination on the target (caused by the keyhole in the layering sphere). The associated power spectrum is shown in (b).

trapezoidal geometry of the actual hole, and (2) a constant-temperature thermal boundary condition was imposed on the outer surface of the target to provide sufficient grid (spatial) resolution for the calculation. This would exaggerate the ice thickness at the equator. The boundary condition should be on the layering sphere wall.

Lastly, the calculated 4-μm-rms roughness is greater than the roughness observed in any of the individual 2-D analyses of a target: this stems from the calculated 2-D great circle going through both the north and south poles—an orientation that cannot be viewed by either the X or Y viewing axes. Instead, the viewable 2-D great circles intersect only a portion of the great circle calculated above. The orientation of the ice-thickness distribution becomes apparent only after the 3-D surface is generated.

c. Stability of the target temperature and helium exchange gas. The temperature of the layering sphere is controlled to ±1 mK, using Cernox™ temperature sensors and heaters with a highly damped feedback-control algorithm. Fluctuations in target temperature are expected to be less than 1 mK, owing to the additional buffer provided by the low thermal diffusivity of the helium exchange gas. The effect of this temperature instability is insignificant compared to the effect of the power drift in the OPO, so much so that the temperature stability of the layering sphere does not affect the layering process.

It is important that the helium-gas pressure be stable for the duration of the layering. A variable heat flux would risk rapid freezing, the formation of multiple crystal growth sites, and the subsequent propagation of multiple crystals and facets. There is no experimental evidence that the gas pressure may vary.

An issue larger than the pressure stability is the lack of knowledge of the absolute pressure. This complicates, but does not compromise, the process by prolonging the time it takes to determine an optimal temperature setting on the layering sphere to commence layering. It may also be beneficial to be able to adjust the pressure in controlling temperature gradients around the target.

Furthermore, the accuracy of the target-temperature measurement depends also on the time available to make that determination. Experiments that freeze and melt the target at very slow rates (5 mK per two hours) ensure complete equilibration between the target's temperature and the temperature of the layering sphere, which compensates for the small heat-flow changes that occur relative to the latent heat of fusion. Under these conditions, it is possible to determine the target temperature to within 5 mK of its absolute value. Under such tight control, a geometrical effect comes into play: the liquid freezes at a slightly different temperature than the one at which the ice melts (because the slumped liquid layer covers only a portion of the plastic shell through which heat is removed).

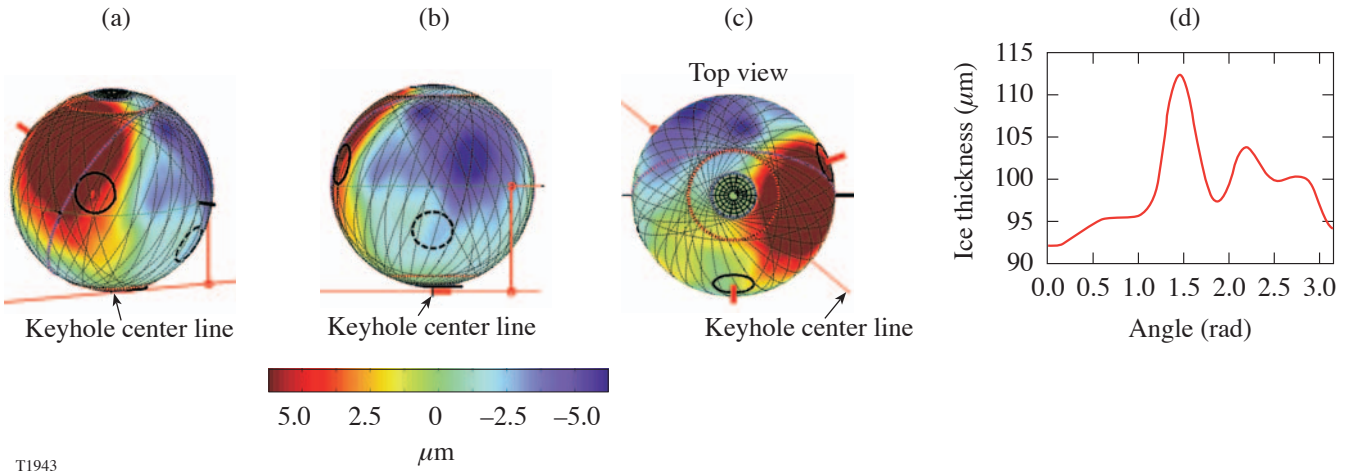

Figure 99.39
Images (a), (b), and (c) show the ice-thickness distribution in a target where the average ice rms roughness is 1.2 μm. The thickness variation along a great circle through the keyhole line is ~8 μm peak-to-valley. The calculated thickness variation, from the ray trace and thermal model, from the bottom of the target to the top and along the axis of the hole is shown in (d).

Thermal Analysis

The thermal environment within and around the target was modeled to quantify the thermal gradients that exist during the layering process. The results offered a better understanding of the layering process's sensitivity to extrinsically controllable and coupled parameters: IR power, gas pressure, and the temperature on the layering sphere. The primary motivation for this model was derived from an uncertainty about how accurately the solidification process can be controlled and what level of control was required for the desired ice-layer quality. Looking forward, such an analysis also helps to better determine the thermal requirements to refine cryogenic equipment.

4. Initial Phase of Forming the Ice Layer

The modeling results of the thermal environment at the initial stage of forming a layer are shown in Fig. 99.24: A melted target is centered in the layering sphere at a temperature slightly above the triple point. The temperature along the inner liquid surface varies between 0.05 K and 0.1 K, depending on the helium pressure. Based on actual experimental values, the model uses the following input parameters: The temperature on the layering sphere is 18.52 K, in accordance with the diminished helium-gas conductivity (0.006 W/m-K) due to the gas pressure being below the continuum limit. The heat load into the liquid and plastic is 1 Q_{DT} (the amount of heat from an equimolar DT solution). Raising the heat coupled into the target to 3 Q_{DT} raises the temperature gradient to 0.25 K.

With a 0.1-K temperature gradient around the target's external wall, and the average temperature of the target being within 0.005 K of the triple point, the liquid at the top of the target should form a crystal. If it does, the crystal should grow from this position. In practice, such a crystal growing from the top and propagating downward is not observed. Rather, the liquid around the equator of the target freezes first and a crystal grows upward (and in thickness) by vapor condensing on the crystal. Simultaneously, the crystal grows downward into the liquid melt, following classical solidification processes.

Multiple seed crystals form when the temperature decrement used to initiate freezing is large, and a low-quality, multifaceted, polycrystalline layer results. The parametric correlation between temperature difference, pressure, and heat flow from the target is shown in Fig. 99.31. The desirable operating pressure regime is in the flat portion of the curve, from 0.02 to 0.05 Torr, where the temperature gradient between the target and the wall of the layering sphere changes very little with temperature.

Even if slow solidification parameters, which favor single-crystal nucleation, and slow propagation are used, a layer will form within 1 h (Fig. 99.40). The rms roughness after that time is better than 10 μm.

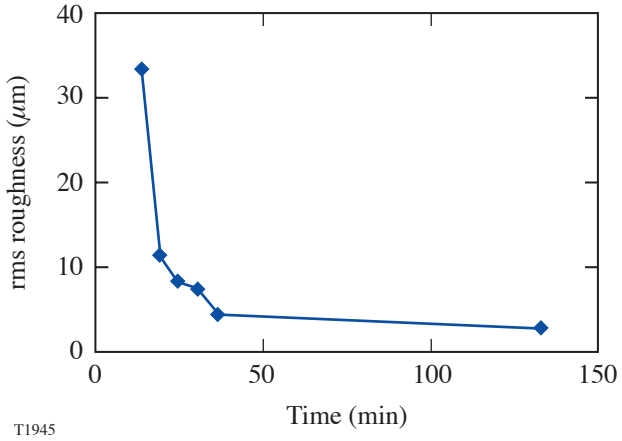

Figure 99.40
The time dependency of the ice-layer formation process indicates that an acceptably smooth ice layer can be achieved in under 3 h.

5. Final Phase of Forming the Ice Layer

Once the ice is mostly symmetrically distributed around the shell, only a small mass needs to be redistributed to create a uniform thickness. The time for this process depends on the sublimation rate, the temperature gradient along the ice/gas interface, and the diffusivity of the deuterium gas.

The sublimation rate depends on the difference between the gas pressure over the solid and the saturated vapor pressure. The pressure/temperature relationship for normal deuterium (near the triple point) is given by the equation[12]

$$P^{\text{vapor}} = \exp\left[19.192 - 177.48/T + 0.00663(T - 16.5\ \text{K})^2\right], \quad (4)$$

where T is the temperature and the rate of sublimation is[13]

$$dm/dt = \left(P^{\text{vapor}} - P^{\text{saturated}}\right) S/\sqrt{2\pi MRT}, \quad (5)$$

where m is mass, P is the pressure, M is the molecular mass, R is the universal gas constant, T is the temperature, and S is the sticking coefficient, which is ~1 for vapor in equilibrium with its solid.

As the ice layer converges to a constant thickness, the temperature gradient along its internal surface decreases. This decreases the vapor pressure and density gradients across the gas void, slowing the layering process. For an ice layer with a peak-to-valley thickness variation of less than 5 μm, the temperature variation along the inner ice surface is less than 0.001 K. This corresponds to a gas-density variation of less than 0.001%. The density/temperature relationship is shown in Fig. 99.41.

Figure 99.40 shows the measured change in the layer roughness of one shell as it converges over time to a 1.8-μm final roughness. The heat load into this target was ~2 Q_{DT}. The process took <3 h; during the last ~100 min, the layer smoothed from 5 μm to 2 μm, corresponding to ~10^{-6} of the total mass being redistributed. The associated temperature variation around the inner surface of the ice decreased from 1.4 mK to 0.15 mK (see Fig. 99.42; the range accounts for the uncertain helium-gas pressure, the converging thickness, and how well centered

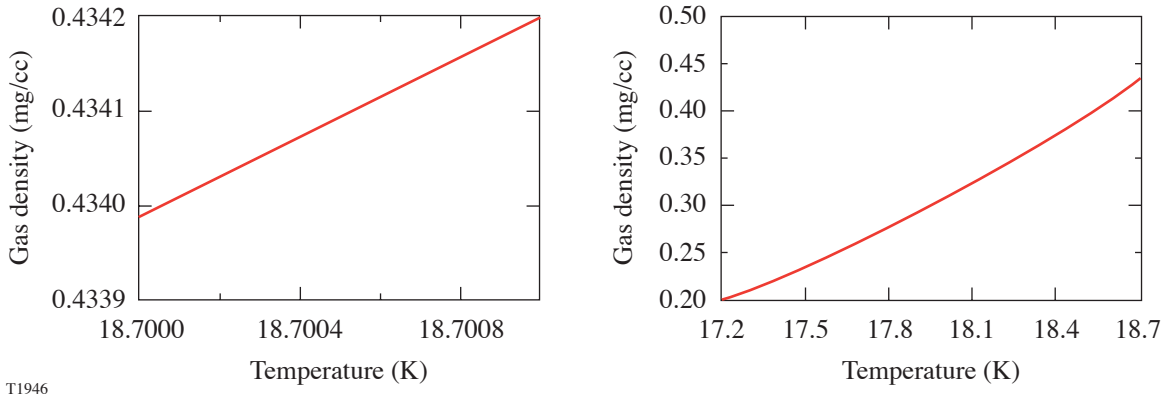

Figure 99.41
The relationship between the gas density and the temperature of the deuterium vapor.

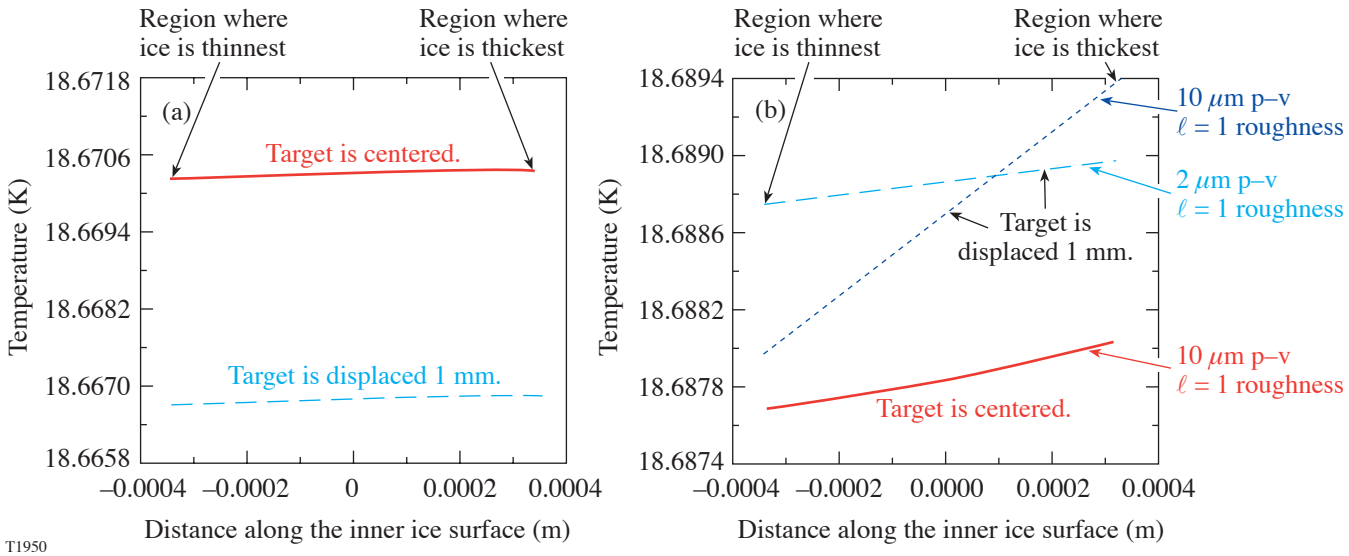

Figure 99.42
The temperature gradient on the inner ice surface is shown for varying conditions: (a) The ice layer has a 2-μm peak-to-valley (p–v) thickness variation, 1-Q_{DT} volumetric heat load, and sufficient helium exchange gas for the system to be in the kinetic gas region. The effect of decentering the target by 1 mm in the layering sphere on the temperature gradient is negligible. (b) This shows the effect of higher roughness, higher heat loads (2 Q_{DT}), and lower gas pressures (thermal conductivity is 1/5 the continuum regime value) on the temperature gradient on the inner ice surface.

the target was in the layering sphere), and the gas density gradient decreased from 0.09% to 0.003%. This density gradient should produce a substantially faster layering time than is observed if gas phase diffusion was the rate-limiting step (the diffusion coefficient is 1.4×10^{-6} m^2/s). Similarly, the D_2 pressure gradients should produce a faster layering rate than observed if the sublimation rate was the rate-limiting step. This infers that the density/pressure gradient is much lower than predicted for the measured ice thickness because the target is closer to an isothermal inner surface than the model predicts. This is achievable only if there is a variable thermal resistance around the target.

Historically, there has been an implicit assumption that the radial thermal resistance of the target is uniform for all (θ, ϕ) polar angles, and if it was nonuniform, the scale length would be sufficiently small for the consequences to be negligible. However, since the ice smoothness infrequently achieves the goal of 1-μm rms but more often is 2 to 3 μm, the validity of that assumption needs to be questioned. There are two parts to this evaluation: (1) the radial thermal resistance of the ice itself, and (2) the thermal resistance across the ice/plastic interface, which is not necessarily equal for all angles θ and ϕ. Two other possibilities are addressed later: (a) the plastic-wall thickness may not be constant and hence contribute a variable-distance thermal path, and (b) the outer plastic surface may not be isothermal.

Given the geometry and size of the target, it is not possible to *measure* the thermal-resistance uniformity between the ice and the plastic, or within the ice itself. Its presence can only be inferred by eliminating other perturbations to the ice. Thermal conduction (k) is proportional to

$$k \sim C_s \rho_s U \lambda, \tag{6}$$

where C_s is the crystal-lattice heat capacity, ρ_s is the density, U is the speed of sound, and λ is the phonon mean-free path. Of these, the phonon mean-free path is the most likely to vary and is affected by (a) the temperature, which influences the phonon density and causes phonon–phonon scattering, (b) the crystal size since grain boundaries scatter phonons, and (c) the local density of deuterium in the molecular $J = 1$ rotational state (J is the spin quantum number). At constant temperature, any variability would be caused by a disproportional distribution of either crystallite sizes or deuterium in the $J = 1$ rotational state (one-third of deuterium is in the $J = 1$ rotational state; the remainder is in the $J = 0$ state), which may occur if deuterium fractionates during the layering process (deuterium's triple point is 0.4 K lower if all the molecules are in the $J = 0$ state). While these are theoretically possible, they seem unlikely.

A second possibility for, and more likely the cause of, a variable thermal resistance is derived from the ice being partially detached from the plastic. If this occurred over a sufficiently wide cord length (of 100 μm or more), the thermal resistance between the inner ice surface and the plastic wall would rise appreciably, even if the gap thickness was very small (thermal conductivity of the gas is 2% that of the ice). The resulting higher ice temperature would cause the ice layer to thin in order to preserve an isothermal inner surface.

Figure 99.43 shows a cryogenic target with a pronounced gap between the ice and the plastic shell. This layer (~20-μm rms roughness) was obtained at a low heat load of ~0.2 Q_{DT}. Raising the heat load to 1 Q_{DT} eliminated the gap, due to the intrinsic layering process, and improved the roughness to 6 to 8 μm. While similar voids were not visible at more-typical 1- to 3-Q_{DT} heat loads, this is not proof that a thin delamination does not exist nor that any thermal resistance at the interface vanishes. It is possible that rapidly freezing a target causes precisely these delaminations, which makes it impossible to form high-quality layers. Figure 99.44 shows a thermal model and resulting ice-roughness power spectrum if a 1-μm-thick void with a length of 200 μm existed at the ice/plastic interface. The resulting rms roughness is 4 μm.

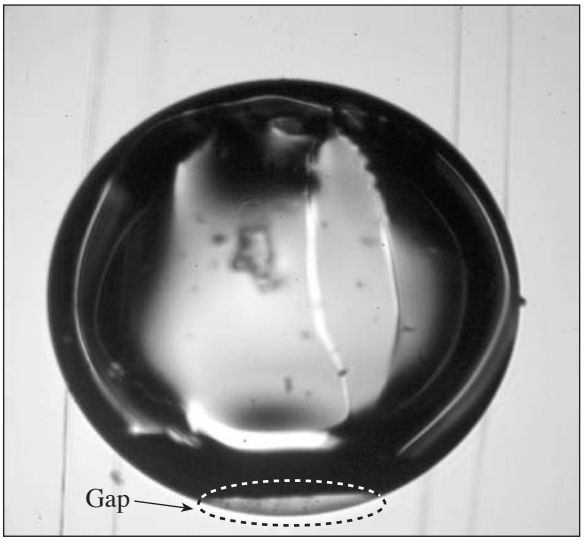

T1859

Figure 99.43
Image of a cryogenic target showing a gap between the plastic and the ice layer.

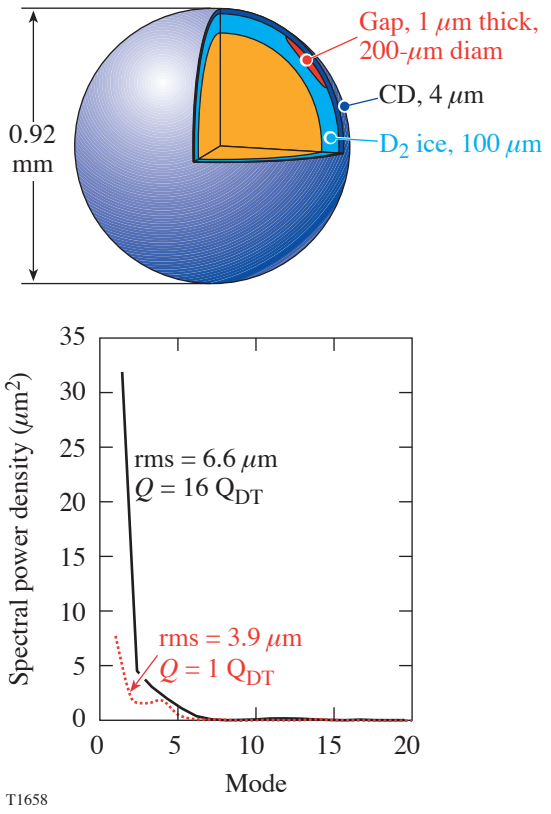

Figure 99.44
Thermal model showing the effect of a 1-μm-thick, 200-μm-diam gap between the ice and plastic on the uniformity of the ice layer.

Another method of affecting the inner ice temperature without changing the ice thickness is for the plastic wall to have variable thickness: if it is thicker on one side of the shell, it will provide a larger local thermal resistance that will make the inner ice surface warmer and will cause the ice layer to thin, relative to the opposing side, to maintain the isothermal property. For example, the thermal conductivity of plastic is one-tenth that of ice, so a 0.1-μm peak-to-valley nonconcentricity in the shell wall (the maximum allowable) would produce an ~1-μm peak-to-valley nonconcentricity in the ice wall. Table 99.I shows the effect of an extreme (0.75-μm) nonconcentricity in the wall of the plastic shell.

Lastly, the position of the target in the layering sphere during the solidification process may affect the eventual uniformity of the ice-layer thickness. It is possible that not centering a target in the layering sphere may result in the inner ice surface becoming isothermal before the ice is uniformly thick. This would occur if the side of the target with thicker ice was closer to the layering sphere. The following calculations investigate the sensitivity of the temperature gradient on the inner ice surface to the target's position in the layering sphere. A target with a 1-μm rough ice layer centered in the layering sphere will possess a temperature variation of 115 μK along the inner ice surface. Displacing the target by 1 mm within the layering sphere changes this variation by a maximum of 15 μK, depending on the alignment of the target's misplacement and ice-thickness variation. If the ice layer was perfectly smooth,

Table 99.I: The temperature gradient along the inner ice surface is calculated for different helium-gas thermal conductivities (due to low gas pressure), positional alignment in the layering sphere, and the effect of a nonconcentric plastic-shell wall.

Peak-to-valley nonconcentricity (ℓ = 1 roughness) in the ice layer	Thermal conductivity of the helium exchange gas (W/m-K)	Position of the target in the layering sphere	
		Centered	Displaced 1 mm from the center[a]
2 μm	0.025	0.115 mK	0.10 to 0.13 mK
		0.190 mK[b]	
	0.006	0.285 mK	0.27 to 0.30 mK
10 μm	0.025		0.55 to 0.60 mK
	0.006		1.42 to 1.44 mK

[a]These values cover the maximum/minimum range that depends on how the ice thickness variation is oriented relative to the target position in the layering sphere.
[b]The plastic-shell wall possessed a 0.75-μm nonconcentricity.

the induced temperature gradient would be only 5 μK for a target displacement of 1 mm. At lower helium pressures (where we currently operate), the temperature gradient around the inner ice surface would be greater (285 μK), but the sensitivity to target position would be the same. Repeating the same calculation for a 10-μm peak-to-valley ice-thickness variation yields a similar proportional trend (see Table 99.I). It is desirable for the temperature variation on the inner ice surface for any ice-thickness variation to be as large as possible to maximize the layering driving force, and for the inner ice surface to be isothermal where the ice is uniformly thick. This will decrease the time it takes for the ice surface to become isothermal. In summary, these data suggest that misplacing the target by 1 mm from the center of the layering sphere will not affect the ability to form an ice layer with 1-μm-rms roughness.

The smoothest target obtained possessed an average ice roughness of 1.2-μm rms; it took 3 h for the liquid to form an ice layer with 1.5-μm-rms average roughness and an additional two days for it to decrease to 1.2 μm. This added time may reflect the gradual mass redistribution that accompanies a very small temperature gradient on the inner ice surface.

Cooling Targets Below the Triple Point

The internal gas density of a cryogenic target is required to be $\sim 0.2 \times 10^{-3}$ g/cm^3, corresponding to a temperature that is ~1.5 K below the triple point (Fig. 99.41). Cooling the target by this much densifies the ice but has no effect on the plastic. Because the ice is attached to the plastic, a strain of ~1% is induced either in the ice or at the interface between the ice and the plastic. This strain is in addition to existing strains that may have developed during solidification. The resulting stress may cause the ice to delaminate from the plastic, or if the adhesion is sufficiently great, the ice may rupture along existing crystallographic planes or defects. Both of these events can affect the ice roughness.

It has been conclusively determined from numerous experiments that the only possible method for meeting both the ice-quality and the sub-triple-point-temperature specification is to form an initial high-quality ice layer and then cool it. For a sufficiently slowly cooled target, the ice quality can be preserved. Figure 99.45(a) shows the results for two different but comparably smooth targets that were cooled at slow rates: 0.02 K and 0.03 K every 20 and 60 min, respectively. The slow rate allowed the strain that was induced during cooling to be relieved before further strain was incurred upon additional cooling. The target that was cooled at the faster rate experienced a marginal increase in roughness [Fig. 99.45(b)], while the second target was unaffected. It is premature to attribute the difference in behavior to the cooling ramps; this is the subject of further experiments. In a separate experiment a target that had roughened during cooling recovered its original smoothness when it was annealed for 18 h [Fig. 99.45(c)]. This behavior, however, does not always occur: the ice shows the same variable behavior that is seen when targets are repeatedly frozen, melted, and refrozen using identical conditions, a behavior that depends on the specifics of the ice crystal.

One expected consequence of decreasing the ice temperature is an increased likelihood for the ice surface to form facets that would generate a sawtooth-like texture and increase the high-frequency roughness. Experimentally, when increased roughness was measured, that roughness was primarily in the lower spectral modes, although the roughness also increased in modes up to 100 (Fig. 99.46). This outcome may be explained by structural changes occurring in the ice as it cools, changes that affect the radial thermal resistance of the ice around the target, which perturbs the isothermal condition on the inner ice surface that causes the ice to relayer. The subsequent ability of the ice to, in some instances, "anneal" these defects and to recover its original smoothness may depend on the type of defect that caused the initial perturbation to the ice.

Effect of Ambient Radiation on the Cryogenic Target

Removing the thermal shrouds exposes the cryogenic target to blackbody radiation from the target chamber, which is calculated from Plank's radiation law to be 0.0047 W. The effect of this heat load on the smoothness of the ice surface and the internal gas density determines the maximum time the target can be exposed before it has to be imploded.

The linear motor used to retract the thermal shrouds can achieve a velocity of 5 ms^{-1} using a constant acceleration of 25 ms^{-2}. This corresponds to the target being exposed to ambient radiation for 0.05 s. The quality of the ice layer moments before implosion is determined using a high-resolution camera inside the target chamber to capture an image of the cryogenic target. The ice layer's smoothness does not appear to be degraded by this exposure time, which is encouraging; however, there is no way to measure the density (or temperature) of the gas in the center of the target. This information can be determined only by calculation. Should calculations also show that the rise in the density of the gas is sufficiently slow, it would be possible to slow the shroud's retraction. The extra time would allow any vibration in the target to be attenuated for longer, thereby allowing the target to be better centered in the target chamber.

Data from the camera inside the target chamber provided time-lapse images [Fig. 99.47(a)] that show how the cryogenic target behaves when the thermal shrouds are removed and the target is not imploded: first, the ice was observed to rotate inside the plastic shell (this occurred during the initial 2 s); then, as the liquid fraction increased, the ice/liquid slurry slumped (within 5 s) and melted after 10 s. The liquid continued to vaporize and the target exploded after 78 s. Immediately before the target exploded, it became transparent, indicating that the temperature had surpassed the critical point, which is the highest temperature where vapor and liquid coexist. Separate experiments determined that the temperature at which an OMEGA cryogenic target explodes is 43±1 K.

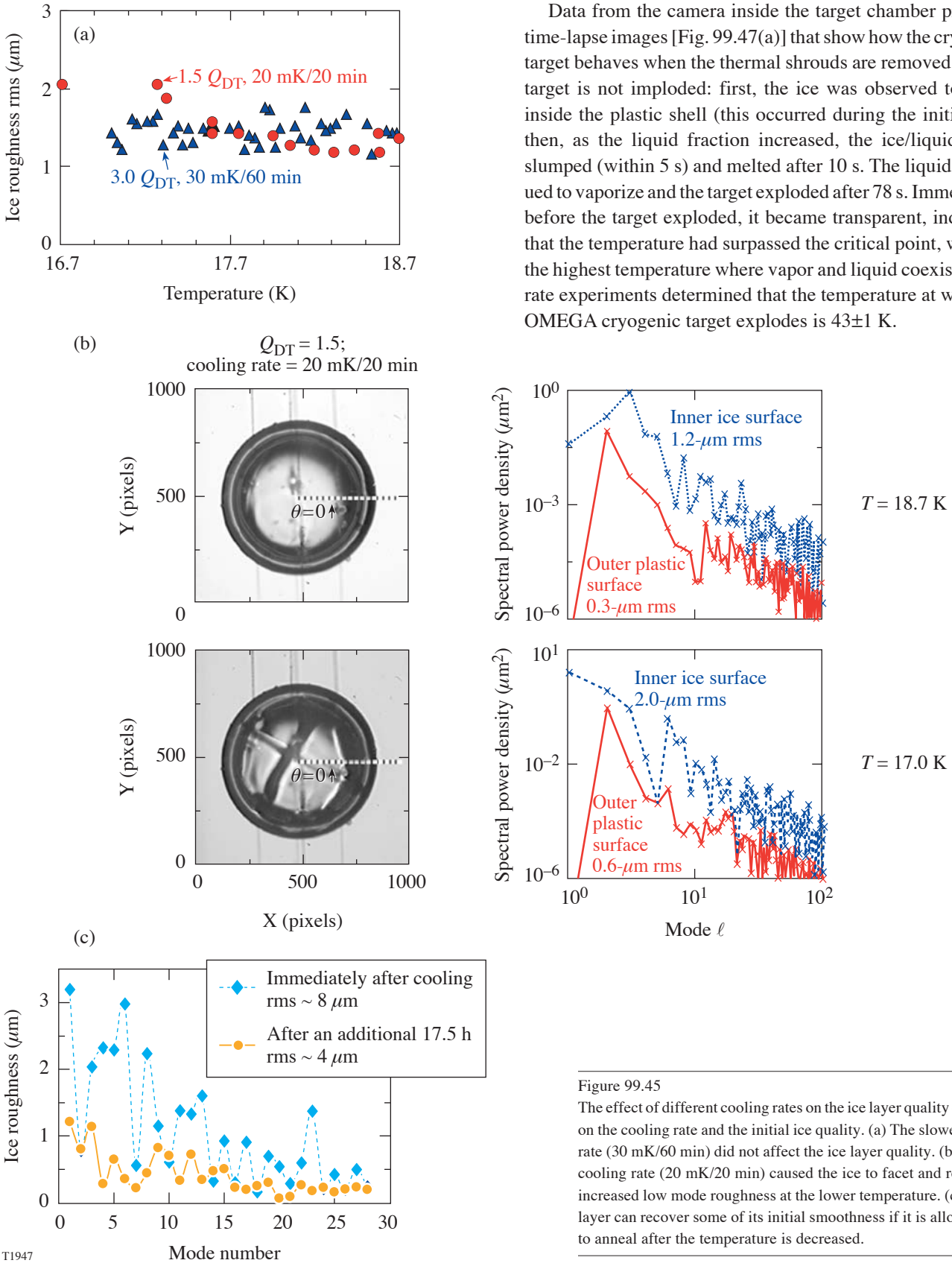

Figure 99.45
The effect of different cooling rates on the ice layer quality depended on the cooling rate and the initial ice quality. (a) The slower cooling rate (30 mK/60 min) did not affect the ice layer quality. (b) The fast cooling rate (20 mK/20 min) caused the ice to facet and resulted in increased low mode roughness at the lower temperature. (c) The ice layer can recover some of its initial smoothness if it is allowed time to anneal after the temperature is decreased.

The target contained 36×10^{-6} g of deuterium, and the combined specific heat of the solid, liquid, and gas required to raise the temperature from 17 K to 43 K was 290 J/g (Ref. 14). Combining this value with the latent heats of fusion and vaporization yielded the total energy required to explode the target, ~0.014 J. These values suggest that the power coupled into the target was 1.7×10^{-4} W, which was ~4% of the estimated 0.0047-W heat flux striking the target. Considering only the time required to melt the ice (10 s), and combining this with the latent heat of fusion for deuterium [50 J/g (Ref. 14)], the calculated heat deposited in the target was approximately 1.8×10^{-4} W.

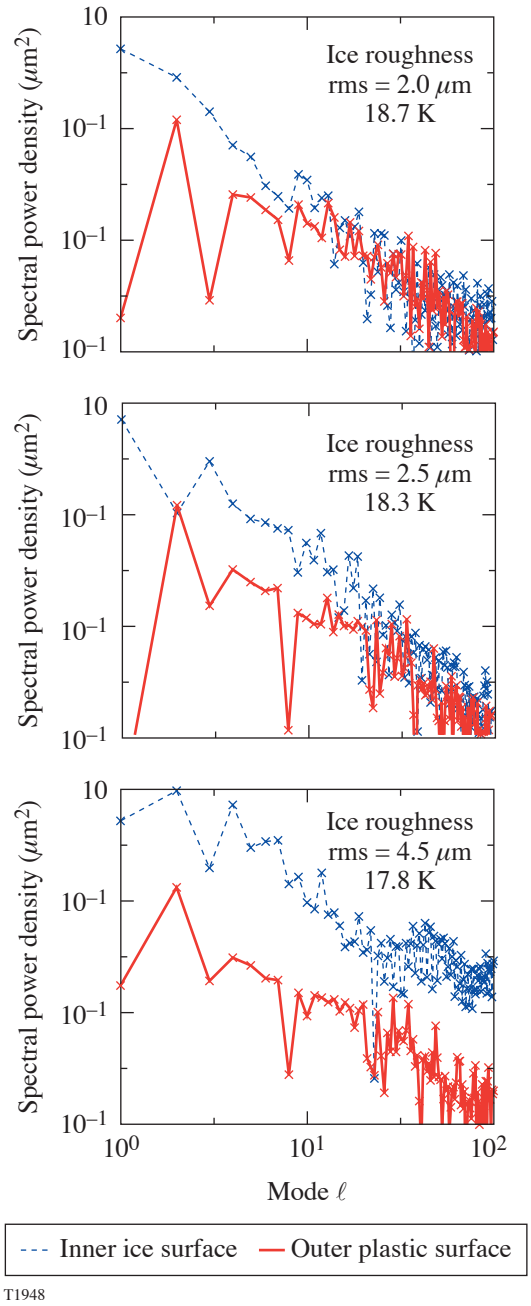

Figure 99.46
The change in the ice power spectrum is shown for a target that roughened when it was cooled.

A detailed thermal model of heat flow through the ice was used to determine how rapidly the temperature of the inner ice surface increased when the target was exposed to ambient radiation. This was done using the computational code FLUENT. For this model, the radiation heat load was coupled into the plastic shell wall alone, as deuterium ice and liquid absorb radiation over such a very limited spectral range (3.1± 0.3 μm) that the power coupled directly into the ice is negligible. The model included the temperature-dependent heat capacity of the solid and the latent heat of fusion for deuterium. The results reported are the time-dependent melt fraction of the ice, the temperature of the inner ice surface, and the heat flux to the inner ice surface. The time-dependent behavior of the ice layer is presented in Fig. 99.47(b) for comparison with the experimental data. In the simulation the ice layer was seen to melt closest to the plastic layer [Fig. 99.48(a)] and then slump on a time scale that was similar to that observed experimentally. This behavior gives confidence that the temperature calculations in the model are relevant.

The sequence of events that occurs once the target is exposed to ambient radiation can be described in more detail using the thermal model as a guide. Initially the ice is at 17 K with a very small radial temperature gradient (<0.1 K). When the shrouds are removed, the plastic absorbs radiation and heats rapidly since the heat capacity of the plastic at this temperature is extremely low (87 J/kg-K). The heat flux from the target to the surroundings is negligible since the target is in vacuum, so all of the heat conducts inward into the ice. The heat flux at the inner ice surface [Fig. 99.48(b)] reaches a peak at ~60 μW after 0.006 s and then decreases to <1 μW within 0.07 s. The behavior follows the radial temperature gradient: after 0.006 s has lapsed, the outer ice surface has reached the triple point (18.72 K) and cannot rise further until the ice is melted; meanwhile, the inner ice surface remained at 17 K. The delay time is due to the thermal diffusivity. Over the next 0.07 s, the outer ice surface remains at the triple point and the inner ice surface approaches the triple-point temperature. Once the inner surface is also at the triple-point temperature, the temperature gradient across the ice layer is negligible and

the heat flux is commensurately low. The time-dependent temperature profile of the inner ice surface is shown in Fig. 99.48(c). As the temperature of the inner ice surface increases, so does the saturated vapor pressure, and the heat flux determines how rapidly ice sublimes to maintain the equilibrium gas pressure. Fortunately, the low heat flux and sizeable latent heat of sublimation [367000 J/kg (Ref. 14)] limits how rapidly the gas density increases in the center of the target [Fig. 99.48(d)]. These data suggest that the gas density will not increase significantly over the sub-0.5 s exposure times when a target at a sub-triple-point temperature is exposed to 300-K radiation.

When a target 1.7 K below the triple point is heated back to the triple-point temperature, the deuterium ice experiences an ~1% volumetric expansion. Should this cause the ice to buckle instead of swelling uniformly, added roughness would be induced on the inner ice surface. Such roughness has not been observed in targets that were imaged in the target chamber, but that may only be because the spatial wavelength and amplitude of the roughness were beyond the resolution of the diagnostic. Ultimately, this effect may determine the allowable target exposure.

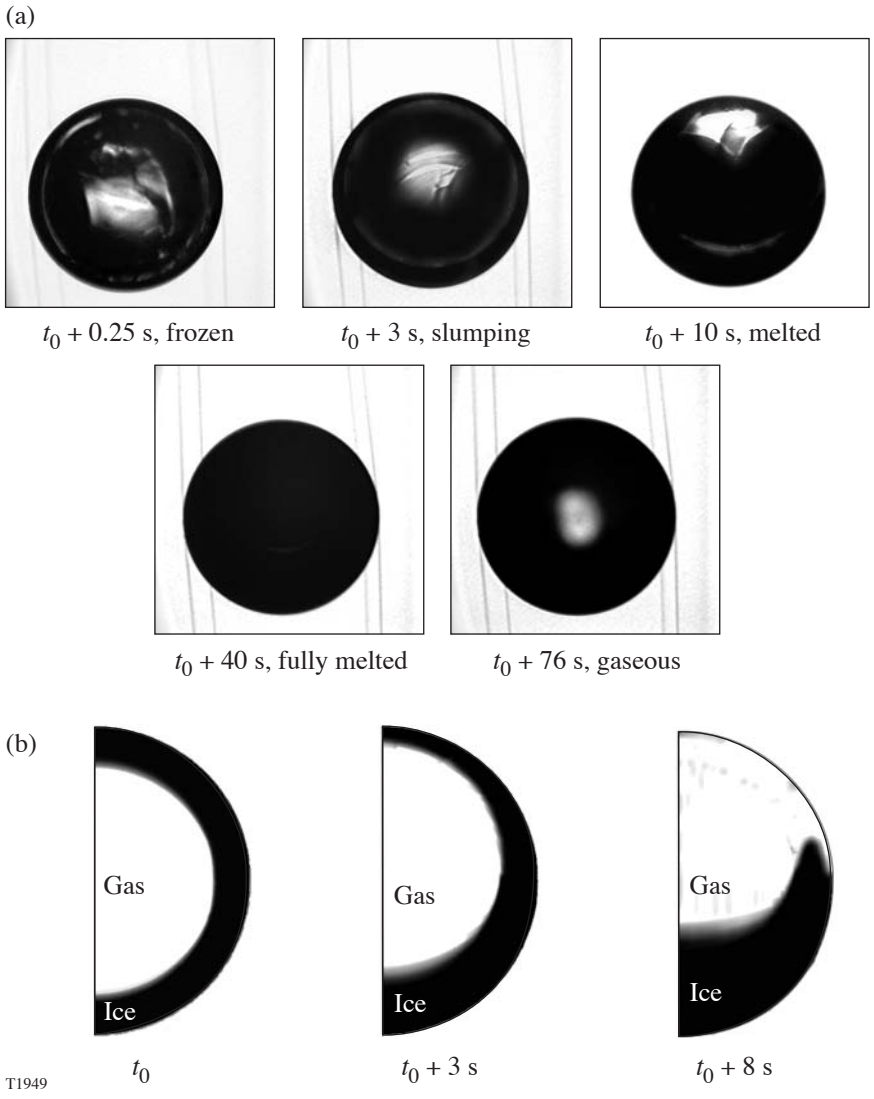

Figure 99.47
(a) Sequence of images showing the ice layer melting and slumping when the thermal shrouds were retracted; (b) calculated response of the ice when the shrouds are removed. The heat absorbed in the plastic caused the target to melt and slump in the same time period that was observed experimentally.

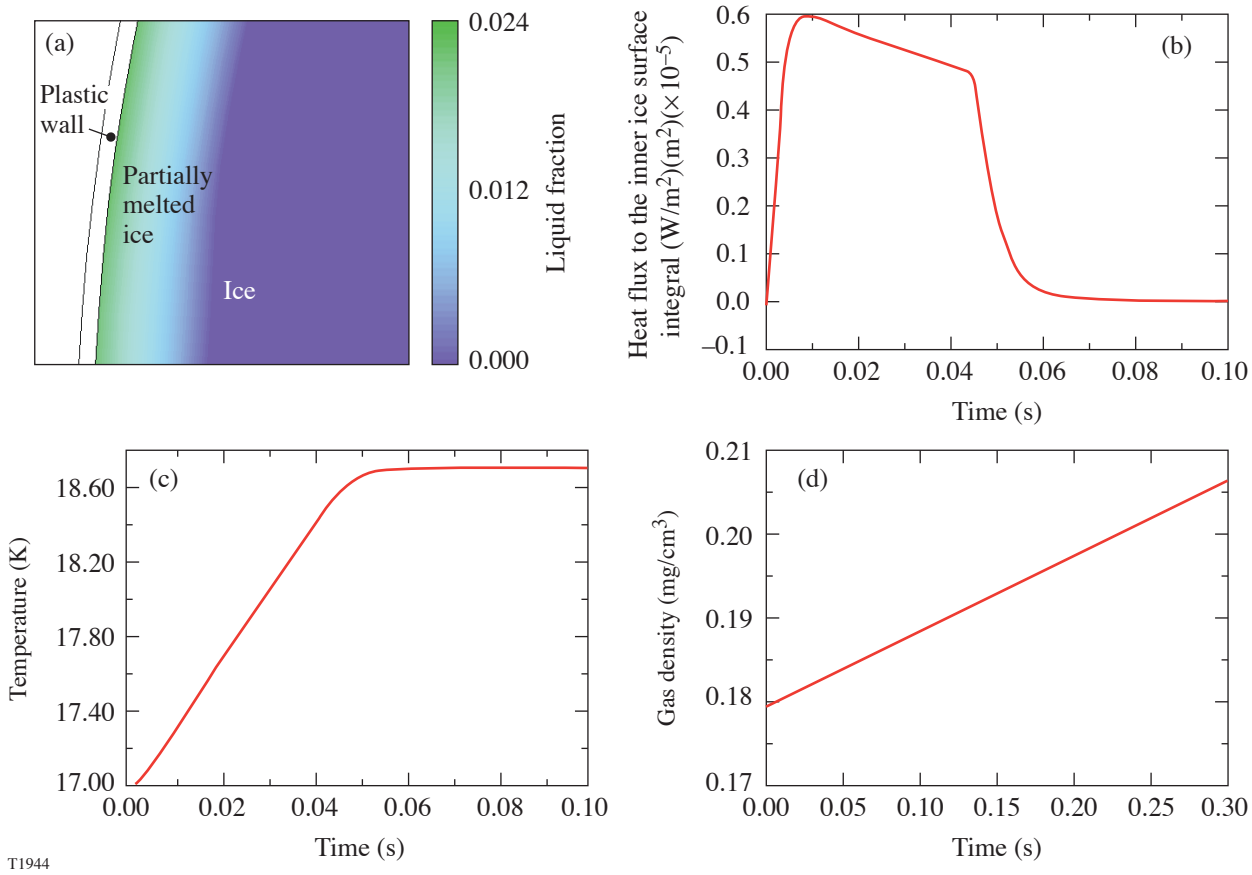

Figure 99.48
Calculated behavior of a cryogenic target when the thermal shroud is removed. (a) Liquid fraction of the outer region of a cryogenic target 0.1 s after being exposed to ambient radiation; (b) calculated heat flux to the inner ice surface; (c) rate of temperature increase of the inner ice surface; (d) density change of the gas in the center of the target.

Summary and Conclusion

High-quality cryogenic targets possessing an ice roughness averaging 1.2 μm for all modes, and for the entire surface, have been demonstrated. These values were achieved by controlling the thermal environment sufficiently to achieve a single initial ice crystal that subsequently grew slowly. A portion of this roughness may be attributable to the nonuniform irradiation of the target caused by the presence of the target-entry hole in the layering sphere. The correlation between this crystal growth phase and the extrinsically controllable parameters (heat flow into and out of the target) has been discussed in terms of the temperature environment within the target. These parameters provide guidelines for a more-complex protocol for controlling the solidification process.

The ice-layering process is controllable: the variability in ice roughness, when the same target is repeatedly layered and melted, is ±0.6 μm. The variability is attributed to intrinsic morphological features within the ice and at the ice/plastic-shell interface, which affects the uniformity of the thermal resistance. The layering process is shown to form a uniformly thick ice layer as evidenced by the ability to form very smooth ice (0.7- to 0.9-μm-rms roughness), albeit over a small cluster set of the 2-D great circles used to completely characterize a target.

It is possible to cool the target to 2 K below the triple point without changing the target's roughness; however, doing so requires a very slow cooling rate. The target's roughness is not

always unaffected even when using the slow cooling rate. When the roughness does change, it is primarily in the lower-order modes. Allowing the target to anneal for an extended period can reverse the roughening, but this does not guarantee that the smoothness will always recover. The variable behavior is attributed to structural changes that the ice undergoes during cooling and densification—changes that affect the radial thermal conductance sufficiently to influence the final ice thickness for which the inner ice surface must be isothermal.

ACKNOWLEDGMENT

This work was supported by the U.S. Department of Energy Office of Inertial Confinement Fusion under Cooperative Agreement No. DE-FC52-92SF19460, the University of Rochester, and the New York State Energy Research and Development Authority. The support of DOE does not constitute an endorsement by DOE of the views expressed in this article.

REFERENCES

1. J. K. Hoffer and L. R. Foreman, Phys. Rev. Lett. **60**, 1310 (1988).
2. G. W. Collins *et al.*, J. Vac. Sci. Technol. A **14**, 2897 (1996).
3. A. Crane and H. P. Gush, Can. J. Phys. **44**, 373 (1966).
4. R. J. Good and G. V. Ferry, in *Advances in Cryogenic Engineering*, edited by K. D. Timmerhaus (Plenum Press, New York, 1963), Vol. 8, pp. 306–310.
5. D. N. Bittner *et al.*, Fusion Technol. **35**, 244 (1999).
6. H. S. Carslaw and J. C. Jaeger, *Conduction of Heat in Solids*, 2nd ed. (Clarendon Press, Oxford, 1959).
7. E. H. Kennard, *Kinetic Theory of Gases, with an Introduction to Statistical Mechanics*, 1st ed. (McGraw-Hill, New York, 1938).
8. G. K. White, *Experimental Techniques in Low-Temperature Physics*, 2nd ed., Monographs on the Physics and Chemistry of Materials (Clarendon Press, Oxford, 1968).
9. D. N. Bol'shutkin, Yu. E. Stetsenko, and L. A. Alekseeva, Sov. Phys.-Solid State **12**, 119 (1970).
10. M. Wozniak, *2003 Summer Research Program for High School Juniors at the University of Rochester's Laboratory for Laser Energetics*, University of Rochester, Rochester, NY, Laboratory for Laser Energetics Report No. 332, NTIS document No. DOE/SF/19460-526 (2004). Copies may be obtained from the National Technical Information Service, Springfield, VA 22161.
11. Fluent USA Inc., Lebanon, NH 03766.
12. R. W. Powers, R. W. Mattox, and H. L. Johnston, J. Am. Chem. Soc. **76**, 5972 (1954).
13. D. S. Metzger and J. R. Gaines, Phys. Rev. **147**, 644 (1966).
14. P. C. Souers, *Hydrogen Properties for Fusion Energy* (University of California Press, Berkeley, 1986).

KB-PJX: A TIM-Mountable Streaked Imager Based on a Versatile X-Ray Microscope Coupled to a High-Current Streak Tube

Introduction

Experiments carried out on the OMEGA[1] laser place very stringent requirements on target-chamber diagnostics. For example, the development of early-time hydrodynamic instability measurements in inertial confinement fusion (ICF) targets involves x-ray radiographic techniques that require a diagnostic capable of detecting small perturbation amplitudes and high spatial frequencies. These are observed as variations in the areal density ρR:

$$\rho R(x,y;t) = \int_0^{d(x,y;t)} \rho(x,y,R;t)\,dR, \qquad (1)$$

where, in the simple case of planar geometry, $d(x,y;t)$ is the target thickness (changing with time due to compression and ablation), x and y are the lateral coordinates, R is the coordinate along the diagnostic line of sight, and ρ is the evolving target density. A new x-ray diagnostic system (KB-PJX) has been developed, characterized, and fielded to measure small, high-spatial-frequency perturbations. It is re-entrant and can be mounted in any of the six OMEGA ten-inch manipulators (TIM's) arrayed around the target chamber, greatly increasing the available experimental configurations and reducing the time required for system adjustments.

The KB-PJX is a streaked imager based on the advanced PJX streak tube and a modular optical front end built around a relatively simple Kirkpatrick–Baez[2] (KB) microscope design. It consists of two mechanically distinct modules (Fig. 99.49): the PJX air bubble that houses the streak tube, the CCD and the PJX electronics, and a retractor housing the optical front end. The retractor (Fig. 99.50) makes it easy to service the optics while mounted in a TIM (operations such as replacement of the blast shield protecting the mirrors are common). It also provides a reference base that allows for precise optical coupling of the front end to the PJX. A kinematic mount engages when the retractor is fully extended and provides repeatability in the optical alignment with a precision better than 25 μm. Another advantage of a retractor module versus a more-permanent fixture is the possibility of replacing the default optical front end with another x-ray optic for some experiments. This design also provides a choice between single and multiple image modes, with the ability to dynami-

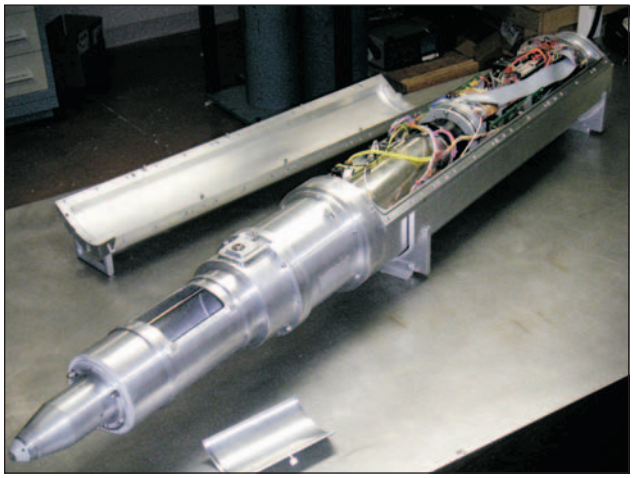

E13165

Figure 99.49
The KB-PJX diagnostic: the retractor in extended position and the PJX air bubble with the lid open.

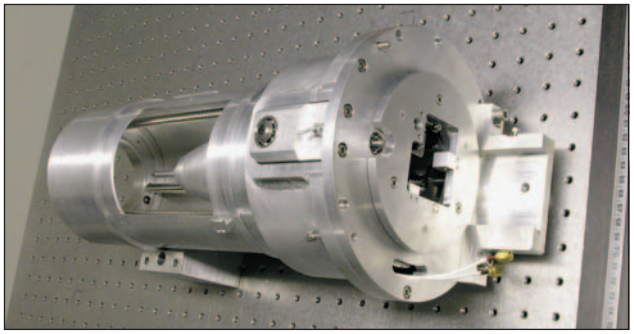

E12907

Figure 99.50
Front-end retractor housing the KB microscope. The side cover is removed to expose the microscope cone.

cally reconfigure for either option with minimal effort. This extends the utility of the streak camera, making its speed, resolution, and collection efficiency available for a broad range of experiments.

The following sections describe/discuss (1) the optical front end and its basic features, design advantages, and expandability; (2) the optical characterization of the microscope in its default configuration; (3) the PJX detector; (4) the resolving capabilities (both spatial and temporal) of the full system; and (5) the performance of the imager in OMEGA hydrodynamic-stability experiments that required high-throughput, high-resolution x-ray diagnostic. Finally, a new technique for measuring the mass ablation rate, a key parameter of the dynamics of ICF implosions, is presented. This method takes advantage of the KB-PJX's ability to provide a continuous high-resolution record of the evolving target areal density.

Kirkpatrick–Baez (KB) Microscope

The relative simplicity and optical characteristics[2,3] of a metal-coated KB x-ray microscope make it attractive for imaging high-temperature, laser-generated plasmas. Three implementations[3] of x-ray KB microscopes mounted in the target chamber of the OMEGA laser facility[1] were available prior to this work. All of them were fixed at their respective locations. The instrument described in this article is designed for deployment in an OMEGA TIM—an air-lock device, used to insert diagnostics into the vacuum chamber. Six nearly orthogonal TIM's are available on OMEGA, providing positioning flexibility and rapid reconfiguration of instrumentation for experiments. The microscope serving as the front end of the KB-PJX is a large-grazing-angle ($\theta_i = 2.1°$), four-mirror design (Fig. 99.51) that provides high throughput with a spatial resolution of less than 3 μm on axis.[4] The relatively large angle of incidence increases the optic's solid angle (~3×10^{-6} sr) and improves its resolution. The optimal resolution[5] of a single mirror in the assembly scales as

$$d_{\text{opt}} \sim \left(\frac{p\lambda^2}{\theta_i} \right)^{1/3}, \tag{2}$$

where p is the object–mirror distance, λ is the x-ray wavelength, and θ_i is the grazing angle. Details of the optical design, choice of coating process, angle of incidence, and mirror characterization are given in Ref. 4. The mirrors have spherical concave surfaces with radii of curvature R = 4250 mm. The surface roughness and the optical figure have been measured in Ref. 4 to be within the specified ranges. The surface roughness after coating was ~4.4-Å rms, and the surface figure (deviation from the best-fit sphere) was measured through interferometry to be $<\lambda/40$ (λ = 532 nm). The radius of curvature is sufficiently large (compared to mirror thickness along the optical axis) that each mirror obeys the thin-lens equation

$$\frac{1}{f} = \frac{1}{p} + \frac{1}{q} = \frac{2}{R\sin(\theta_i)}, \tag{3}$$

where f is the focal distance and p and q are the object and image distances. For the KB-PJX geometry, p = 90 mm, q = 560 mm (magnification of about 6), and f = 77.5 mm. These distances are measured from the center of assembly (the contact plane of the perpendicular mirrors), making f an average value. The slight difference in focal distance for the front and back mirrors in a pair (which have different p's and q's) is compensated by a slight change in the incidence angle [see Eq. (3)].

The traditional method of assembling fixed KB x-ray mirrors is optical contacting, a technique yielding strength and longevity. This technique is not amenable to adjustment. Another option for mirror assembly is using special epoxy mixtures to glue the elements together, but any errors can be expensive to fix, especially when dealing with high-cost

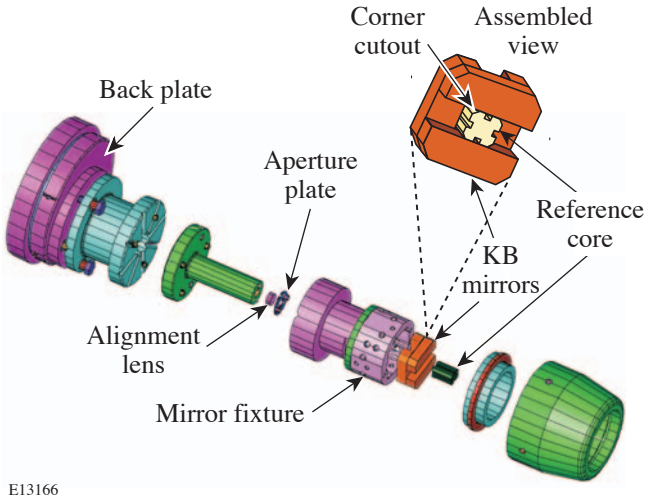

Figure 99.51
Assembled view of the microscope in the mounting mechanism. The mirrors are aligned against the reference core.

superpolished mirror elements. These methods provide robust assembly but limit the flexibility of the resulting optical systems, and fine-tuning their performance after assembly is difficult. The mechanical mirror mount used here allows for easy replacement or repositioning of the individual mirrors. Optimal mirror alignment is achieved by using a central reference core (the 10-mm-long, parylene-coated glass piece shown in Fig. 99.51) with the four Zerodur mirror elements pressed against it with ball plungers. The reference core is the most-unique feature of the optic's mechanical design. Its sides provide reference surfaces for the concave mirror faces, mitigating inaccuracies in the mirror element shape. The core was precisely machined to the specifications validated with numerical ray tracing. The assembly is built around a hollow Zerodur base. The front surface determines a reference plane along the optical axis and establishes the proper object distance for the microscope. An aluminum mirror fixture, mounted on this base as shown in Fig. 99.51, houses the mirror-core assembly and has screw holes for the ball plungers that provide fine mirror positioning and alignment by pressing each mirror against the reference core. Since Zerodur has one of the highest values for the Young's modulus (E = 91 GPa), available in a mirror material, the change of optical surface figure due to pressing stresses is not an issue. The estimated change in the surface figure, given the mirror element geometry and a maximum mounting force of 2.5 N is 0.7 nm, or about 20 times smaller than the acceptable surface figure. This assembly is resistant to vibrations and mechanical shocks associated with the operation of the TIM's. The rectangular profile of the central core provides for co-focusing of the mirrors in each imaging pair by introducing a small difference in the incidence angle (distance to optical axis) that compensates the difference in their position with respect to the object plane.[3] The glass core baffles the direct x rays not participating in image formation and is coated with parylene to reduce x-ray scattering. Both 1-D (reflections from a single mirror) and 2-D (two-mirror reflection) imaging modes are available from apertures in the mounting core. This is accomplished with the rectangular side grooves that define an aperture for single-reflection x rays and corner cutouts, defining apertures for double reflection (Fig. 99.51). For experiments where the photon signal levels are low, the microscope can be configured for use in the 1-D imaging mode with a streak camera as a detector and benefit from the $1/R$ (R being the Ir coating reflectivity) increase in photon flux. Due to its relatively large solid angle,[4] the optic can be used with streak cameras even in the 2-D mode, with the added benefit of precise spatial alignment in the target field of view. A special film pack that mounts to the back of the retractor mechanism and sits at the image plane (i.e., the PJX photocathode location) is available to optimize the fine alignment in 2-D object space. A thin (200-μm) Ta aperture plate at the back of the optic provides further baffling. The size and position of the apertures on the plate are determined by the mode of operation (1-D, 2-D, single or multiple images). By choosing the appropriate plate, one limits the x rays to those forming the desired image(s). The apertures are large enough not to act as pinholes (~0.5 mm on average) and are equivalent to field stops. This system of easily replaceable aperture plates and thick glass core, when combined with the mirror reflectivity cutoff, acts as an efficient filter for scattered, high-energy x rays that can lower image contrast. The mirror reflectivity is maximized by using superpolished mirror substrates, manufactured by Research Electro-Optics[6] and iridium-coated at LLE. The quality of the deposited Ir film was verified by measuring the mirror's x-ray reflectivity at grazing incidence. By matching the measured reflectivity curve with that predicted by a numerical model,[7] the film density was estimated to be about 98% of the bulk material density. Near-bulk (22.42-g/cm^3) density of the iridium film is needed to achieve the optimal reflectivity that strongly depends on the electron number density. The film surface finish was characterized with an atomic force microscope (AFM). The measured surface roughness was used in the numerical fit to the reflectivity curve to determine the film density. With the Ir-coated mirrors in its current configuration, the microscope has a spectral window centered at about 1.5 keV with 0.4-keV FWHM. The finite width of the working energy band is provided by a Be blast shield, acting as a high-pass filter in combination with the cutoff in mirror reflectivity at the high-energy end. This cutoff can be estimated from the classical dispersion theory

$$E_c \sim \frac{he}{\theta_i}\sqrt{\frac{n_e}{\pi m_e}}\,, \tag{4}$$

where n_e is the electron density in the coating, m_e is the electron mass, h is Plank's constant, e is the electron charge (all units in cgs), and θ_i is the grazing angle in radians. For iridium, the total-reflection cutoff is $E_c \sim 2.36$ keV.

Replacing some or all of the mirror elements can extend or change the working energy band. To address different experimental requirements (an example is given later), the versatility of the KB-PJX will be extended by converting it into a high-photon-energy diagnostic with the addition of two new multilayer designs. These mirrors are designed to be drop-in replacements of the current metal-coated elements. The substrates are made with the same surface roughness and optical

figure as their soft-x-ray counterparts. They have the same geometric shape and work at the same angle of incidence. This simplifies the replacement of elements (or the whole assembly) and allows for dual band imaging, when multilayer and iridium-coated elements are mixed in the same assembly. Obtaining two simultaneous images from x rays in distinct energy bands can be very valuable in situations where large changes in the attenuation length occur within the field of view. The specifications of the new multilayer mirror elements are listed in Table 99.II, and their spectral response is compared to that of the soft-x-ray design in Fig. 99.52. The response is the product of the squared mirror reflectivity R^2 and the transmission through a standard 25-μm Be blast shield. The reflectivity cutoff E_c discussed above, along with the absorption edge at 1.56 keV of the Al debris filter, determines the narrow spectral window of the Ir-coated mirror assembly. The reflectivity is calculated with a numerical algorithm[7] that uses the Fresnel equations and an analytic formula given by V. G. Kohn.[8] In

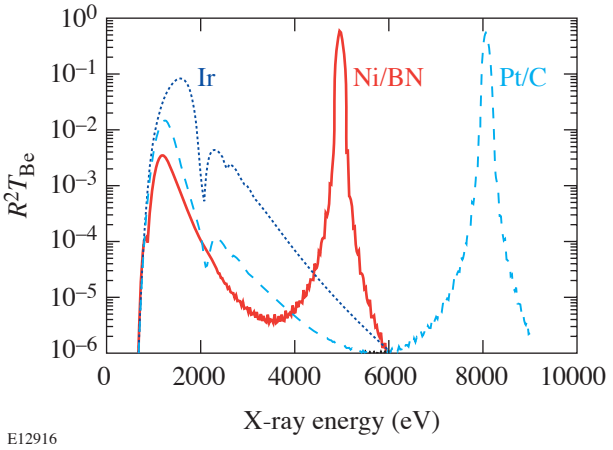

Figure 99.52
Comparison of the spectral windows of two new multilayer (Ni/BN and Pt/C) assemblies (tuned to work at 4.95 keV and 8.05 keV) with the response of the current Ir-coated mirrors.

Table 99.II, d is the period (layer thickness) and d_1/d is the thickness ratio of the metal layer to the period. The last column lists the x-ray energies for which these mirrors are tuned. As with previous designs,[9,10] the spectral windows of the multilayer elements are very narrow (<200-eV FWHM) since the Bragg condition $n\lambda = 2d \sin(\theta_i)$, determining the high reflectivity, is satisfied for a narrow band of wavelengths. This makes them good monochromators but limits the effective field of view of the optic by determining a preferential angle of incidence θ_i. A solution to this limitation is to use graded layer thickness across the mirror surface. Despite its complexity and higher cost, this method is now used routinely with good results.[11] This challenge can also be solved by using a sufficiently broadband backlighter and using the dispersive properties of the mirrors (a range of λ,θ_i pairs that satisfy the Bragg condition will exist). The field of view will then be expanded by angularly dispersing the signal in spatial direction. Since the efficiency of high-energy, broadband backlighters is low, a compound backlighter that emits in several spectral lines must be used. This results in discrete, spatially dispersed signal regions within the expanded field of view. For example, a brass backlighter [75% Cu (K_a = 8048 eV) and 25% Zn (K_a = 8639 eV)] is a good candidate for the 8-keV region. To register comparable intensity levels in the two spatial regions (which will map into the central 400 μm of the field of view), a two-strip Zn-Cu backlighter can also be used (Fig. 99.53).

Optic Characterization

After evaluating the reflectivity of each mirror,[4] the mirror assembly was placed in the retracting mechanism that houses the microscope during normal operation and provides proper coupling to the PJX streak tube. Fine alignment and resolution evaluation were performed under vacuum in an x-ray test chamber. A film pack loaded with Kodak direct exposure film (DEF) was placed at the image plane where the PJX photocathode would be located during normal operation. Several test exposures were taken using a tungsten target bombarded with

Table 99.II: Characteristics of the new, multiplayer, high-energy KB-PJX mirrors.

Type	Layer	D (nm)	Thickness Ratio d_1/d	X-Ray Energy (keV)
Ni/BN	60	3.5	0.4	4.95
Pt/C	100	2.13	0.37	8.05

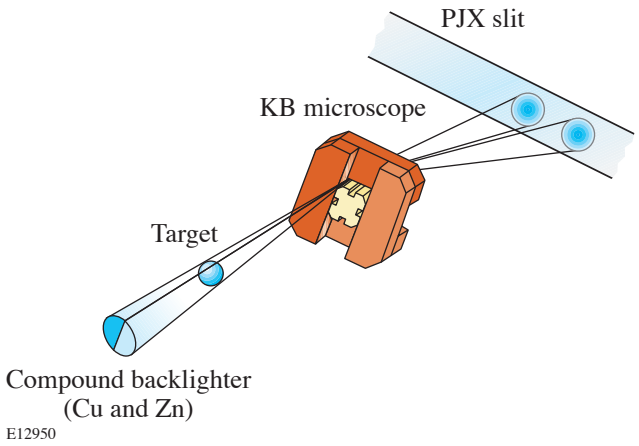

Figure 99.53
The field of view of a multilayer KB microscope is expanded by using a strip backlighter. The x rays are energy dispersed into two distinct regions at the image plane.

a 10-kV electron beam. Images of a 400-mesh grid as well as knife-edge images were acquired and analyzed to determine the system's modulation transfer function (MTF) and compare it with that predicted by numerical ray tracing[4] and the MTF of an 8-μm-pinhole array. Figure 99.54(a) shows a typical film image of a 400-mesh grid, digitized with a Perkin–Elmer photodensitometer with a 5-μm scanning aperture. A horizontal lineout through the image is shown in Fig. 99.54(b), where the profile was intensity converted using a semi-empirical formula[12] in the instrument spectral window centered around 1.5 keV. The MTF was calculated from both the grid images and an image of an opaque tantalum foil edge (knife edge). The edge response function (and the MTF, respectively) is treated independently for the two perpendicular directions determined by the grid lines. The MTF shown in Fig. 99.55 is averaged over the central 200 μm of the field of view and calculated by a method similar to that outlined in Ref. 3. After taking into account the system magnification $M = 6$, the diffraction MTF predicted by numerical ray tracing[4] was plotted on the same graph for comparison. It matches the shape of the edge MTF remarkably well. The slight deviations are most likely due to uncertainties in the determination of the line spread function from the edge data. It should be noted that the availability of a larger shadow region on the edge image provides for a more-accurate estimate of the transfer function for high spatial frequencies. Three MTF curves calculated from the edge image (for three different field positions) are shown on Fig. 99.56, along with the on-axis MTF of an 8-μm pinhole for comparison. In the central 600 μm of the field of view, the microscope has higher resolution than the pinhole. One can

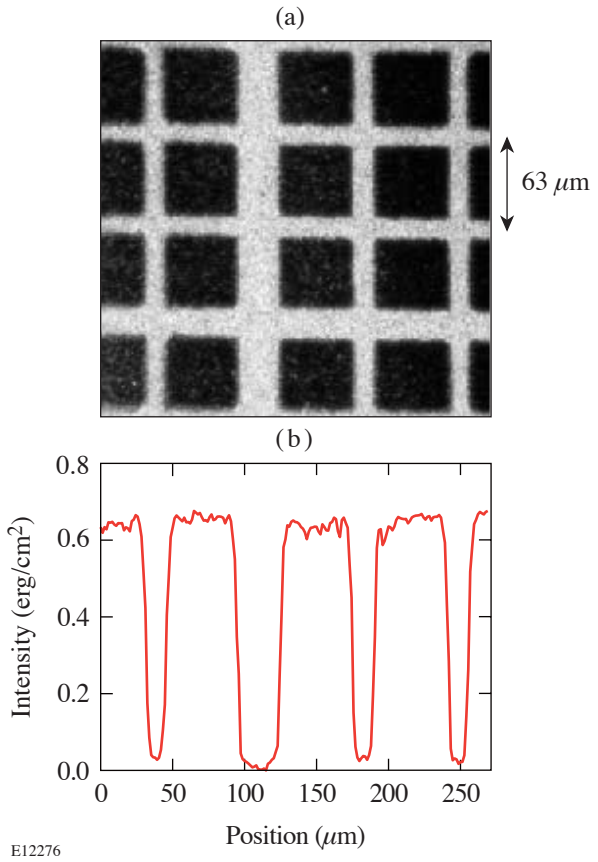

Figure 99.54
Film image (a) of a 400 LPI SEM grid and horizontal intensity profile (b) taken through the middle of it.

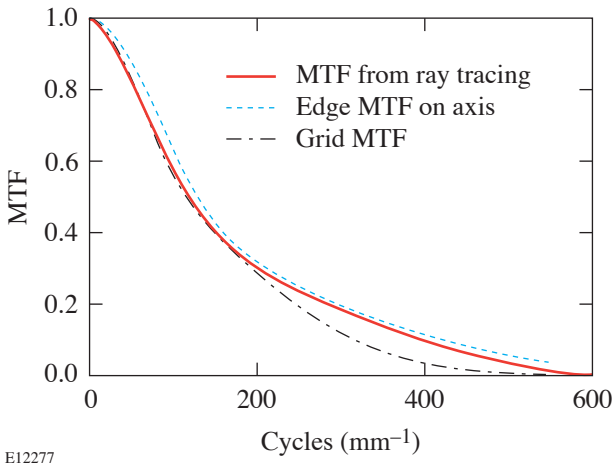

Figure 99.55
Modulation transfer function calculated from a grid image and vertical (perpendicular to the streak tube slit) knife edge.

also see the expected deterioration of resolution toward the edge of the field of view, where the resolution is comparable to the 8-μm pinhole.

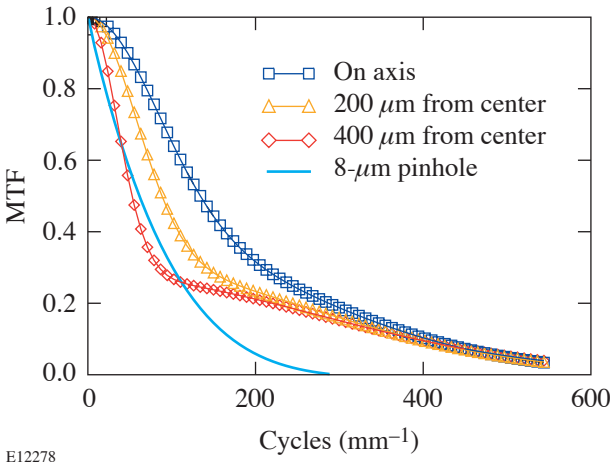

Figure 99.56
Modulation transfer functions calculated from an edge image at three different field positions are compared to the MTF of an 8-μm pinhole at a comparable magnification of 8×.

PJX Streak Tube

The instrument's detector combines several state-of-the-art features that were previously not combined into a single detector. The PJX streak tube is the result of collaboration between the Commissariat à l'Énergie Atomique (CEA), Photonis (formerly Philips Photonique, located in Brive, France), and LLE. The final electron-optics design was completed by LLE. The streak tube is physically large—13 cm in diameter and 50 cm long. The camera is routinely operated with a 15-kV cathode–anode potential that can be increased to 25 kV. A quadrupole doublet, combined with three octupole correctors that minimize the aperture aberrations, focuses the accelerated photoelectrons. The phosphor screen is fiber-optic–coupled directly to a back-illuminated CCD and has a 24-mm × 24-mm output format. The CCD has a 13.5-μm individual pixel size. The system gain[13] is 150 CCD electrons per streak-tube electron, enabling single-electron detection with a signal-to-noise ratio (SNR) >3. There is no image intensifier in the camera, eliminating an additional source of noise. The streak tube can operate in either of two modes, determined by the polarity of the quadrupole doublet: in standard mode, the input slit size is 60 mm by 0.4 mm, with a demonstrated current-handling capability of 12.5 mA, while in inverse mode, the effective slit size is reduced to 6 mm by 0.09 mm with 1.5-mA peak current. In standard mode, the electron-optic spatial magnification is 0.4× and the temporal is 4×. Switching to inverse mode reverses the spatial and temporal direction magnifications. The streak tube is designed to mount in the OMEGA TIM enclosed in its own air bubble that houses the tube and the water-cooled CCD camera. The power, control, and communication electronics are internal to the air bubble, making the PJX a highly integrated self-contained instrument (Fig. 99.57). Cooling the CCD camera and power electronics that must operate inside the vacuum chamber is simplified by this design. A fan drives air circulation inside the bubble, and the heat is extracted through a chilled-water line. Communication to and from the camera is via an optical fiber. The PJX is a heatsink, not a heat source, inside the vacuum chamber. Other advantages of the air-bubble concept are better electromagnetic interference (EMI) shielding, the freedom to use vacuum-incompatible materials for high-voltage insulation, and the protection of many serviceable components from DT contamination.

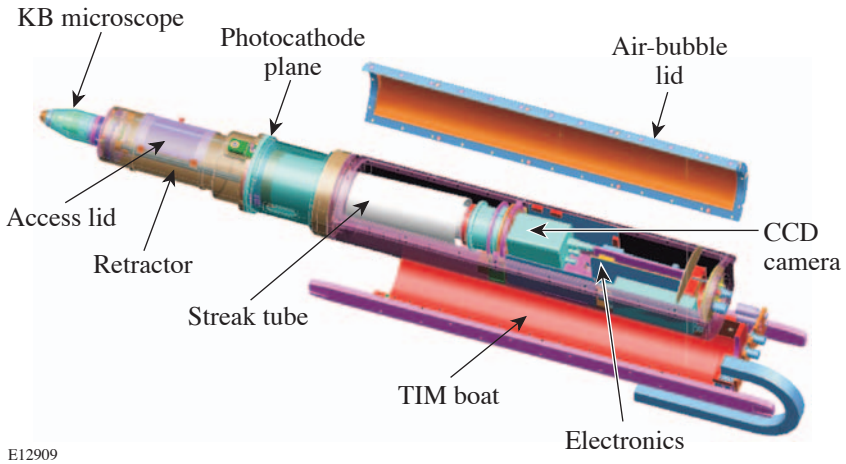

Figure 99.57
The PJX streak camera is kept at air in a "bubble" (shown with the lid open). This simplifies the cooling of both the CCD and power electronics.

The calculated time resolution of the PJX tube is less than 5 ps. The finite width D of the line spread function divided by the sweep speed v_{swp}

$$\Delta t_{st} = \frac{D}{v_{swp}} \tag{5}$$

is one of the primary factors that determine this.

For the inverse mode and an 8-ns sweep, Δt_{st} is 16-ps FWHM; it is proportionally less for faster sweep speeds. The energy dispersion of the secondary photoelectrons creates a spread in the transit time of the accelerated electrons,

$$\Delta t_{\varepsilon} = f\left[V(z), \vec{v}_0, x_0, y_0\right], \tag{6}$$

where $V(z)$ is the axial potential, $\vec{v}_0$ is the initial velocity vector of the secondary electrons, and (x_0,y_0) is the initial point of emission. Δt_{ε} has been calculated to be 1.26 ps on axis for the KBr photocathode, increasing to 3.0 ps for the extreme off-axis locations. Assuming Gaussian response curves, the FWHM of the combined temporal line-response function will then be given as the Gaussian convolution of the two effects:

$$\Delta t \cong \sqrt{\Delta t_{st}^2 + \Delta t_{\varepsilon}^2} \cong 16 \text{ ps}. \tag{7}$$

This value ($\Delta t \sim$ 16-ps FWHM) well represents the measured temporal resolution of the PJX in inverse mode. The number of time-resolution elements in the time window is ~300, based on a 50% contrast-ratio criterion.

It is currently difficult to measure the time-resolution limit of the PJX because of the lack of sufficiently short x-ray pulses at LLE. The resolution calculated in Eq. (7) was verified using 100-ps laser pulses available on OMEGA. A train of six 100-ps Gaussian, UV pulses separated by 1 ns illuminate a U backlighter to produce the x-ray pulses shown in Fig. 99.58(a) (recorded in inverse mode). Except for the first x-ray pulse, two overlapped OMEGA beams were used to generate each of the pulses. There are small aberrations away from the optical axis (center of the image), due to the spherically curved phosphor screen. This effect is characterized and corrected with an image-processing algorithm. A spatial average of the third x-ray pulse is shown in Fig. 99.58(b), along with the UV pulse that generated it. The time axis is calibrated, using a train of eight UV fiducial pulses fed into the camera with a fiber and recorded at the edge of the photocathode. The solid curve is the actual x-ray pulse, convolved with the time response (line-spread function) of the PJX. It provides a measure of the streak camera's time resolution. The only other information currently available is the shape (dashed curve) of the UV laser pulse that generated the x rays; however, the time resolution of the P510 streak camera (that recorded those) is of the order of the calculated PJX resolution. Using the UV pulse information is further complicated by the time history of the conversion of UV light to x rays. A phenomenological x-ray–conversion formula, such as that from Ref. 14, can be used to relate the intensity I_{UV} of UV light with the converted x-ray intensity I_x, using a power law $I_x \propto I_{UV}^{\gamma}$. With a value of $\gamma \sim 3.4$ as determined in Ref. 14 and using the FWHM D_{UV} = 109 ps of the recorded UV backlighter pulse, the σ parameter of the x-ray–converted UV Gaussian $I_x(t) \sim \exp\left[-(t-t_0)^2 / \left(2\sigma_{UVx}^2\right)\right]$ is given by

$$\sigma_{UVx} = \frac{\sigma_{UV}}{\sqrt{\gamma}} = \frac{D_{UV}}{2\sqrt{2\gamma \ln(2)}} \cong 25.1 \text{ ps}. \tag{8}$$

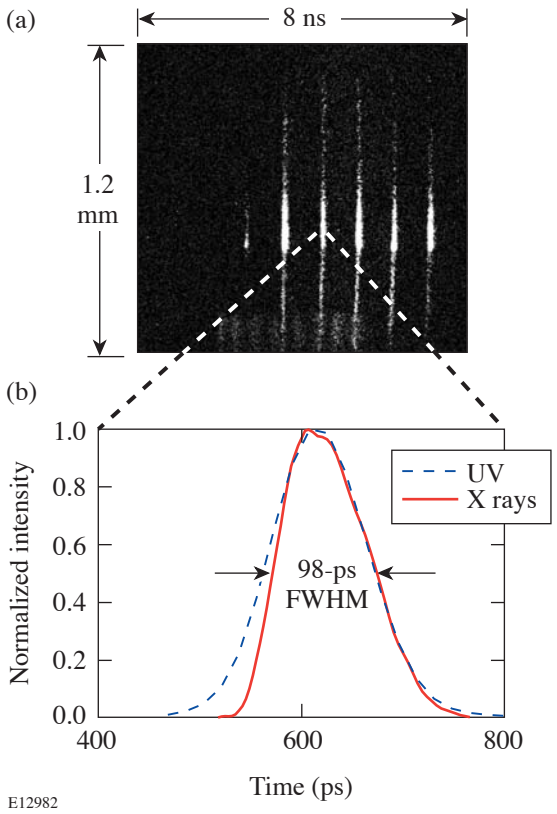

Figure 99.58
(a) A train of short backlighter pulses (100 ps) recorded with the KB-PJX in inverse mode and (b) spatial average of one such pulse and the generating UV pulse (dashed line).

The measured x-ray-intensity profile is fit by a combination of a Gaussian and an exponential decay function to account for the emission of x rays during the finite cooling time of the plasma. In Fig. 99.58(b), one can clearly see the asymmetry of the pulse due to this effect. The σ value of the Gaussian is found from the fit to be $\sigma_x = 32$ ps. Because this pulse is a convolution of the PJX time-response function with the incident x-ray pulse, the width of the time-response function is

$$\sigma_{\mathrm{PJX}} = \sqrt{\sigma_x^2 - \sigma_{\mathrm{UV}x}^2} \cong 19.8 \pm 4.0 \text{ ps}, \tag{9}$$

where the main contribution to the uncertainty comes from the determination of the power index γ. This result is consistent with Eq. (7).

The point-spread function (PSF) of the PJX streak camera in inverse mode has been measured to be ~18 μm (versus 125 μm in standard mode) at the photocathode plane. This suggests that the camera and microscope will have a comparable effect on the resolution limit at the system magnification of 6×. The total point-spread function is a convolution of the two similar PSF's; therefore the resolution limit of the full instrument is expected to increase by a factor of $\sqrt{2}$ from the microscope resolution of 3 μm to 4.5 μm. The magnification of the electron optics is 4×, resulting in a total magnification of 24× to the CCD plane. The sharp edge of a Pt foil was imaged to measure the MTF of the complete KB-PJX system. The resulting MTF curve, as calculated from the edge data, is shown in Fig. 99.59. The curve was averaged over several time slices to improve the signal-to-noise ratio. For comparison, the MTF's of the microscope, calculated on axis and 200 μm away from it, are plotted. It was verified from the target-positioning images that the edge was located 150 to 200 μm off axis, which explains the good match between the edge MTF and the microscope curve at 200 μm from the center. The expected $\sqrt{2}$ widening of the system PSF as compared to the optic's alone is detectable in this comparison. In this configuration the KB-PJX was used in a series of hydrodynamic stability experiments[15] requiring high throughput (thick CH targets were driven with ten OMEGA beams) and high resolution. The instrument provided a continuous record of the evolving single-mode (typical wavelengths of 20 μm) areal-density perturbations at the ablation front of these targets.

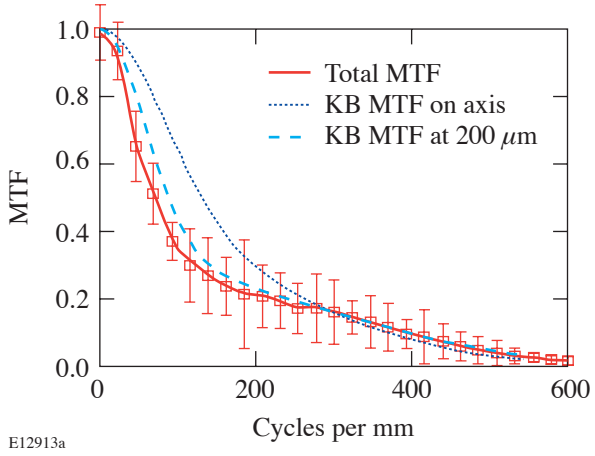

Figure 99.59
System MTF of the KB-PJX, calculated from its edge-response function and compared to the microscope MTF's at two field positions.

OMEGA Experiments

This KB optic coupled to the PJX streak camera has been used successfully to measure the time evolution of the areal density of a perturbed planar target during shock transit (prior to the arrival of the rarefaction wave at the laser-illuminated surface). A sinusoidal perturbation is imposed on the side of the target illuminated by the laser. The goal of the experiment is to measure the evolution of the perturbations and to compare it to various models. A continuous record of the evolution of target areal density (modulated by the ablation-front mass perturbations) was obtained (Fig. 99.60), showing phase inversion in the single-mode perturbations as part of a period of their oscillatory evolution. The temporal oscillations at the laser-illuminated surface are faster for mass perturbations with a shorter wavelength. The oscillation frequency is given by[15]

$$\omega = kV_a\sqrt{\rho_a/\rho_{\mathrm{bl}}}, \tag{10}$$

where k is the spatial modulation wave number, ρ_a and ρ_{bl} are, respectively, the densities in the shock-compressed and blowoff plasma regions, and V_a is the ablation velocity (defined as the mass ablation rate divided by the density ρ_a). This sets challenges for the diagnostics since one has to go to shorter wavelengths to observe a full oscillation before rarefaction breakout, when the onset of the Rayleigh–Taylor instability overpowers the oscillatory stabilization effect. Several limitations make a simple increase of the target thickness (i.e., shock transit time) impractical; these include (1) limits in backlighter photon flux, laser pulse duration (total energy) of the backlighter, and drive beams; and (2) limits in the target modulation depth driven by the requirement to have the single-mode perturbation amplitude much smaller than its wavelength in order to remain in the linear regime of evolution, etc. All of these factors are interdependent, restricting the parametric

space of the experiment. The KB-PJX, having both high spatial resolution and high throughput, is the appropriate diagnostic for these experiments. Compared to a previous experiment on the subject,[16] where part of an oscillation period for perturbation modes with wavelengths down to 30 μm was observed, the use of the KB-PJX allowed registering the evolution of perturbations with 20- and even 10-μm wavelengths, at the same target thickness and backlighter of equal or lower efficiency. In the experiments, CH targets were driven by ten of OMEGA's ultraviolet beams with a maximum intensity of 4×10^{14} W/cm^2 on target in a 1.5-ns, fast-rise, flattop pulse. They were backlit with x rays produced by a U target, illuminated by another 11 OMEGA beams for 2 ns. A 25-μm-thick Be blast shield filtered the x-ray self-emission from the CH foils. The backlighter and target were separated by a 5-μm-thick Al debris shield, whose transmittance along with that of the Be foil and energy-dependent mirror reflectivity forms the working energy band, as shown in Fig. 99.52. The backlighter and driver pulse widths were chosen so that the camera registered the target areal density for the duration of the shock transit, up to the arrival of the rarefaction wave at the front of the compressed target. The streaked images, such as the one in Fig. 99.60, allow us to verify the theoretical models and validate the capabilities of the imager. The streaked microscope met its resolution and throughput requirements, making it possible to measure the perturbation oscillations.[15] Resolution estimates from recorded data confirm that the imager can resolve modulations with a characteristic wavelength of 5 to 7 μm and an optical depth above 0.05 (about twice the typical noise level). Currently, the optic is also being used together with the PJX streak tube in the development of a side-on radiographic technique[17] for equation-of-state (EOS) experiments.

Mass-Ablation-Rate Measurements with the KB-PJX

The ability of the KB-PJX to provide a continuous temporal record (with high time resolution) of the target's optical depth can be used in a novel technique to measure the time evolution of the mass ablation in an ICF target. The level of self-emission of the ablated hot plasma in a CH target driven by ten of OMEGA's beams was measured without backlighting, using only the x rays emitted from its hot corona and attenuated through the remainder of the target. The measured intensity profile I_{SE} is shown in Fig. 99.61 along with the time history I_{BL} of an undriven, backlit target and one from a target that is both driven and backlit. Due to ablation, the backlighter x rays see less optical depth at later times since the ablated material loses its opacity rapidly by heating up as it moves along the temperature gradient, away from the ablation front. The hot, low-density corona is approximately transparent to the 1.5-keV x rays up to the ablation front, where the largest temperature jump occurs. In time, the growing ablated mass reduces the total areal density of the target. Figure 99.61 shows an increasing difference between the intensity I_D from the backlit and driven target (red curve) and the sum $I_{SE} + I_{BL}$ (blue curve) of intensities from the driven-only and backlit-only foils. Measuring the optical-depth evolution of the target material not yet ablated allows the mass-ablation rate to be inferred. Consider these three intensity terms as functions of time:

$$I_{BL}(t) = I^0_{BL}(t)e^{-\mu_0\rho_0 d_0} = I^0_{BL}(t)e^{-\mu_0 m_0}\ , \qquad (11)$$

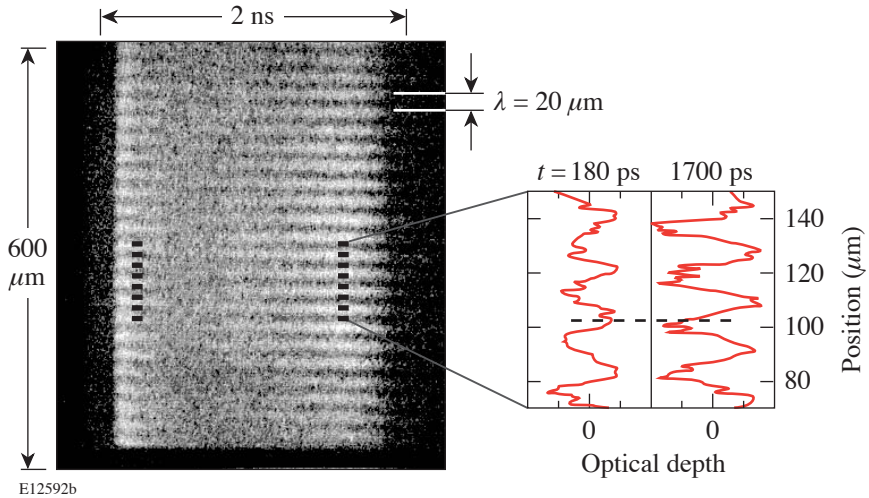

Figure 99.60
Streaked image of directly driven planar CH target with 60-μm thickness and single-mode ($\lambda = 20\ \mu$m) surface modulations on the front. Spatial profiles are shown at t = 180 and 1700 ps, respectively.

$$I_D(t) = I_{SE}(t) + I^0_{BL}(t)e^{-\mu_0(m_0-\rho_0 U_s t)-\mu_c\left(\rho_0 U_s t-\int_0^t \dot{m}dt'\right)}. \quad (12)$$

In Eq. (12) the spectrally weighted mass absorption coefficient μ_c in the compressed region (in the second exponential term) is assumed to change very little from its uncompressed-target value μ_0. The other approximation made in Eq. (12) is that the optical depth $\mu_{abl}m_{abl}$ of the ablated material is negligible (due to its low opacity). Both assumptions are supported by data from the 14000-group APL opacity tables,[18] for density and temperature profiles in the compressed and ablation regions, obtained from 1-D hydrodynamic simulations. Solving the last equation for the ablation rate yields

$$\dot{m}(t) = \frac{d(\Delta OD)}{\mu_0 dt} = \frac{d\left[\ln\dfrac{I_D(t)-I_{SE}(t)}{I_{BL(t)}}\right]}{\mu_0 dt}. \quad (13)$$

All of the intensities are measured and μ_0—the mass absorption coefficient of the cold target—is also readily available. Even though the various intensities are measured in different shots, the results can be combined to estimate the mass ablation rate. The growing optical depth ΔOD of the ablated mass is shown in Fig. 99.62. Due to the intensity-pulse-shape dissimilarities, it is reasonable to get an average value of the time-dependent mass-ablation rate by fitting ΔOD with a straight line and determining its slope. The slope as determined from the fit is 0.77 ns^{-1}. Using the spectrally averaged attenuation length $\lambda = 12$ μm and the density of cold CH $\rho_0 = 1.06$ g/cm^3 to obtain $\mu_0 = (\rho_0\lambda)^{-1}$, one finds the ablation rate to be ~0.98 mg/(cm^2 ns), in line with the average value obtained from simulations, using the measured pulse shapes. A more-precise experiment can be performed if a single shot is used to record both I_D and I_{BL}, while eliminating the target self-emission. This can be done if a high-energy backlighter is used in combination with the multilayer mirrors discussed in the **Kirkpatrick–Baez (KB) Microscope** section (p. 184). At 5 keV, for example, both the thicker target and the microscope's spectral window will filter out the soft-x-ray self-emission. A thicker target will be used since target thickness must be comparable to the spectrally weighted attenuation length (cold material) for maximum sensitivity to ablation. If the ablating target does not occupy the entire field of view, the intensity of the unattenuated backlighter can be recorded at the same time by recording part of the backlighter beam directly. This will allow the calculation of the mass-ablation-rate evolution curve from a single shot.

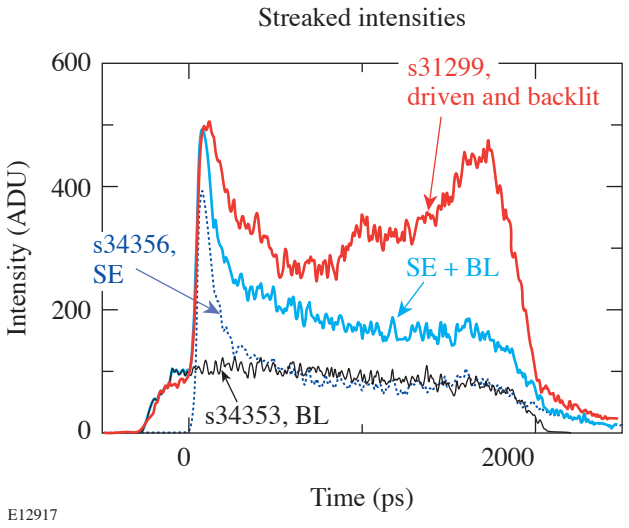

Figure 99.61
Intensity profiles of x rays transmitted through a 40-μm-thick CH target, which is driven and backlit (red curve), backlit only (black curve), and driven only (dotted curve). The sum of the thin solid and dotted lines (blue curve) does not match the solid, showing the effect of ablation.

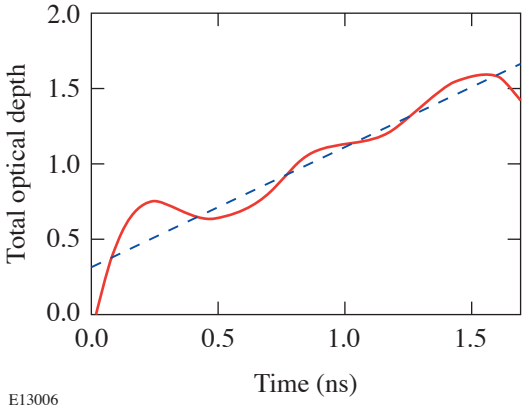

Figure 99.62
The difference in optical depth (ΔOD) (solid curve) grows due to mass ablation. An average value of the mass ablation rate is obtained by fitting the data with a straight line.

Conclusions

This article, in combination with Ref. 4, has shown that the KB-PJX is a versatile instrument, well suited for ICF experiments that (1) need a high-throughput diagnostic with high temporal and spatial resolution in x-ray radiography configurations and (2) can be set up for different x-ray-energy ranges. The imager has high temporal (less-than-20-ps) and spatial (better-than-5-μm) resolution in inverse mode, while demonstrating high-current-handling capabilities, matching the throughput of the optical front end. The PJX streak tube has met the experimental requirements, matching or surpassing the projected spatial (~18-μm) and temporal (<20-ps) resolution, while delivering high peak current in both modes of operation.

ACKNOWLEDGMENT

One of the authors (O. V. Gotchev) wishes to thank Dr. R. S. Craxton for his valuable comments on the opacity of CH plasma at various temperatures and densities. This work was supported by the U.S. Department of Energy Office of Inertial Confinement Fusion under Cooperative Agreement No. DE-FC52-92SF19460, the University of Rochester, and the New York State Energy Research and Development Authority. The support of DOE does not constitute an endorsement by DOE of the views expressed in this article.

REFERENCES

1. T. R. Boehly, D. L. Brown, R. S. Craxton, R. L. Keck, J. P. Knauer, J. H. Kelly, T. J. Kessler, S. A. Kumpan, S. J. Loucks, S. A. Letzring, F. J. Marshall, R. L. McCrory, S. F. B. Morse, W. Seka, J. M. Soures, and C. P. Verdon, Opt. Commun. **133**, 495 (1997).
2. P. Kirkpatrick and A. V. Baez, J. Opt. Soc. Am. **38**, 766 (1948).
3. F. J. Marshall and Q. Su, Rev. Sci. Instrum. **66**, 725 (1995); F. J. Marshall, M. M. Allen, J. P. Knauer, J. A. Oertel, and T. Archuleta, Phys. Plasmas **5**, 1118 (1998).
4. O. V. Gotchev, P. A. Jaanimagi, J. P. Knauer, F. J. Marshall, D. D. Meyerhofer, N. L. Bassett, and J. B. Oliver, Rev. Sci. Instrum. **74**, 2178 (2003).
5. G. R. Bennett, Rev. Sci. Instrum. **70**, 608 (1999).
6. Research Electro-Optics, Inc., Boulder, CO 80301.
7. E. M. Gullikson, Center for X-Ray Optics, Materials Sciences Division, E.O. Lawrence Berkeley National Laboratory, available at http://cindy.lbl.gov/optical_constants/; B. L. Henke, E. M. Gullikson, and J. C. Davis, At. Data Nucl. Data Tables **54**, 181 (1993).
8. V. G. Kohn, Phys. Status Solidi B **187**, 61 (1995).
9. J. H. Underwood and T. W. Barbee, Jr., Appl. Opt. **20**, 3027 (1981); J. H. Underwood, T. W. Barbee, Jr., and C. Frieber, Appl. Opt. **25**, 1730 (1986).
10. F. J. Marshall and G. R. Bennett, Rev. Sci. Instrum. **70**, 617 (1999).
11. Osmic, Inc., Auburn Hills, MI 48326.
12. B. L. Henke *et al*., J. Opt. Soc. Am. B **3**, 1540 (1986).
13. S. Ghosh, R. Boni, and P. A. Jaanimagi, "Optical and X-Ray Streak Camera Gain Measurements," submitted to Review of Scientific Instruments.
14. F. J. Marshall, J. A. Delettrez, R. Epstein, R. Forties, R. L. Keck, J. H. Kelly, P. W. McKenty, S. P. Regan, and L. J. Waxer, Phys. Plasmas **11**, 251 (2004).
15. O. V. Gotchev, T. J. B. Collins, V. N. Goncharov, P. A. Jaanimagi, J. P. Knauer, and D. D. Meyerhofer, "Experiments on the Ablative Richtmyer–Meshkov Instability in Planar Direct-Drive Targets on OMEGA," to be submitted to Physics of Plasmas.
16. Y. Aglitskiy *et al*., Phys. Rev. Lett. **87**, 265001 (2001).
17. L. B. Da Silva *et al*., Phys. Rev. Lett. **78**, 483 (1997).
18. W. F. Huebner *et al*., Los Alamos National Laboratory, Los Alamos, NM, Report LA-6760-M (1977).

A High-Energy, High-Average-Power Laser Using Nd:YLF Rods Corrected by Magnetorheological Finishing

Introduction

Optical parametric chirped-pulse amplification[1,2] (OPCPA) is well suited for the front end of modern petawatt glass laser chains.[3] The broadband gain available with OPCPA at a wavelength of 1053 nm offsets the gain narrowing that occurs in large Nd-doped glass amplifiers.[4] It can be scaled to large energies,[5] in contrast to the practical limits imposed by the mode volume of a laser cavity in regenerative amplification. Lastly, the OPCPA process is prepulse free[6] and can produce gains of up to 10^9 using a relatively simple optical system, which minimizes beam distortions.

Recently, we have shown that a high conversion efficiency of 30% and stable output energies[7] can be achieved in an OPCPA system using pump-laser pulses with uniform intensity profiles in both space and time. This significantly reduces the pump-laser energy requirements. Following this approach, an OPCPA system design[8] was proposed to amplify chirped pulses to more than 400 mJ while limiting the pump-laser requirement to approximately 1 J at a wavelength of 527 nm.

Several laser-amplifier architectures are capable of producing high pump-pulse energies. High-energy, *Q*-switched, unstable laser oscillators are commercially available and involve a relatively simple setup, but spatiotemporal coupling in the pump pulse limits the useful energy ultimately available for the OPCPA process, which in turn limits OPCPA conversion efficiency.[9] Master-oscillator, power-amplifier (MOPA) schemes utilizing amplifiers with progressively larger apertures cause large square-pulse distortions that pose a significant challenge when a temporally square output pulse is desired. More generally, amplification schemes that conjugate both high gain and large depletion of the gain medium limit the ability to control the pump-laser parameters. On the contrary, multipass geometries that utilize the full aperture of a gain medium avoid this difficulty since heavy gain saturation occurs only in the final passes. Multipass amplifiers also offer more-compact layouts and reduce pumping system complexity compared to linear MOPA systems.

Various active and passive multipass architectures offer unique advantages and disadvantages. Passive schemes with Faraday isolators or quarter-wave plates provide the simplest operational scheme but limit the number of passes in the gain medium. The number of passes in linear[10] and ring[11] laser-amplifier cavities can be selected by timing the *Q*-switching and cavity dumping with an intracavity Pockels cell, although this increases operational complexity. Angular multiplexing[12] eliminates the need for active switching but, as a result, is a less-flexible technique.

A limited number of gain media are suitable for high-energy laser applications. Among them, Nd:YAG was considered but not selected because of its high-stimulated emission cross section (low stored-energy density) and poor thermal behavior characteristics, such as a high thermal lensing effect and a high thermally induced stress birefringence. Nd:YLF operating at 1053 nm provides several advantages: First, a high saturation fluence (low-gain cross section) allows working at high laser fluence while minimizing pulse distortion. Second, strong static birefringence practically eliminates the impact of thermally induced stress birefringence, and Nd:YLF has a relatively weak thermal astigmatism. A final practical advantage is that it matches the gain peak of Nd-doped phosphate laser glasses, which permits employing a common front end for both pumping OPCPA systems and seeding large glass amplifiers used in large laser-fusion facilities. Unfortunately, the transmitted-wavefront quality of commercially available, large-aperture Nd:YLF laser rods was not previously sufficient for pumping an OPCPA system.

This article describes a multijoule laser amplifier based on a crystal large-aperture ring amplifier (CLARA) that is capable of producing high-energy pulses with the parameters required for a highly efficient OPCPA. The CLARA design uses 25.4-mm-diam Nd:YLF rods that can operate at a 5-Hz repetition rate because of their good thermal properties. Surface figure corrections were polished on one face of each CLARA rod using magnetorheological finishing (MRF)[13] to

compensate for the bulk inhomogeneities that cause the transmitted-wavefront errors. Correcting these errors increases the usable aperture of the Nd:YLF laser rods, which consequently increases the energy extraction from the laser rods. To our knowledge, this is the first reported application of MRF processing to correct the transmitted wavefront of a laser gain material.

The following sections (1) present the process and experimental realization of correcting the transmitted wavefront of a Nd:YLF laser; (2) describe the design of the CLARA laser amplifier, including an interferometric alignment technique that ensures that the MRF-corrected laser rods are properly aligned; (3) present experimental results demonstrating the benefits of the MRF correction on amplifier performance; and (4) discuss the potential applications of MRF to crystal laser material.

Magnetorheological Finishing of Nd:YLF Rods

Nd:YLF rods that are 25 mm in diameter represent the state of the art in crystal growth. Growing these laser rods with high optical-wavefront quality is extremely challenging, if not impossible. Even with the end-faces polished perfectly flat, up to several microns of wavefront distortion in the bulk crystal is typical. This makes these rods unsuitable for use in a high-energy laser system because these phase errors quickly turn into hot spots as the beam propagates. Additionally, large phase gradients introduced by the rod aberrations produce a beam divergence that phase-matches poorly in nonlinear optical processes, such as frequency doubling and OPCPA.

To overcome these limitations, surface figure corrections can be polished on one face of a laser rod using MRF to compensate for the bulk inhomogeneities that cause the transmitted wavefront errors, as shown schematically in Fig. 99.63. Correcting these errors increases the usable aperture of the Nd:YLF laser rods, which consequently increases the energy extraction.

The MRF process utilizes a small polishing spot formed on a rotating wheel carrying a ribbon of magnetorheological (MR) fluid that contains polishing abrasive, as shown in Fig. 99.64. As the ribbon of MR fluid passes between the poles of a powerful electromagnet, the MR fluid viscosity increases and distributes the polishing abrasive at the surface of the ribbon, where it produces a deterministic, two-dimensional removal-rate pattern. Once the removal-rate function for a material is characterized, a prescribed surface figure correction can be achieved by controlling the dwell time of the optic at each point on the surface as it moves under the wheel in

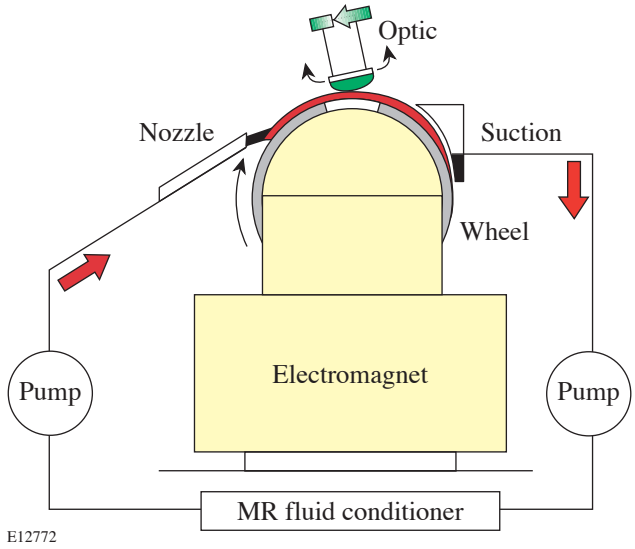

Figure 99.64
MRF principle. The MRF fluid is pumped to a rotating wheel that passes between the poles of a powerful electromagnet. In the magnetic field, the MRF fluid viscosity increases to a nearly solid consistency, which forms a sub-aperture polishing tool. After passing through the electromagnet, the MRF fluid is reconditioned and recycled.

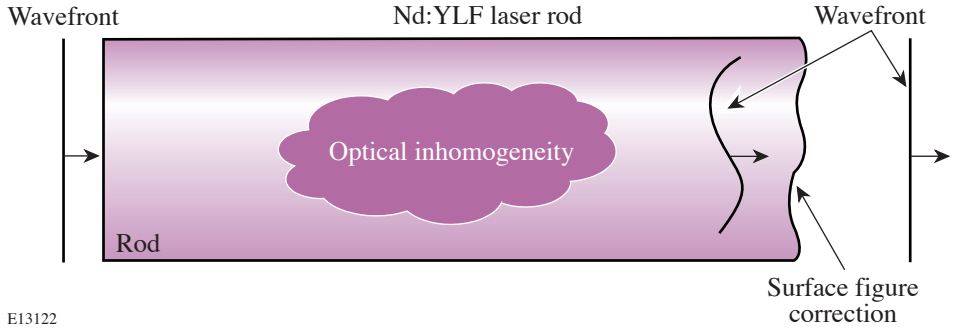

Figure 99.63
Transmitted-wavefront errors induced by bulk inhomogeneities in a Nd:YLF laser rod can be compensated by polishing a surface figure correction on one end-face of the rod.

either a raster or spiral pattern. Interferometry prior to an MRF polishing step measures the actual wavefront error of the sample, which is used to compute the MRF correction. Wavefront corrections converge quickly, usually requiring no more than two or three iterations.

Figure 99.65 shows the results of correcting a Nd:YLF laser rod. Initially, the transmitted-wavefront error for this laser rod was 0.60 λ (at 1053 nm) in the desired 20-mm clear aperture. After several MRF iterations, this error was reduced to 0.11 λ. Table 99.III summarizes the results of correcting five different laser rods. Final wavefronts of ~λ/10 were generally achieved, except when the spatial structure of the initial wavefront error approached or exceeded the resolution of the MRF correction process.

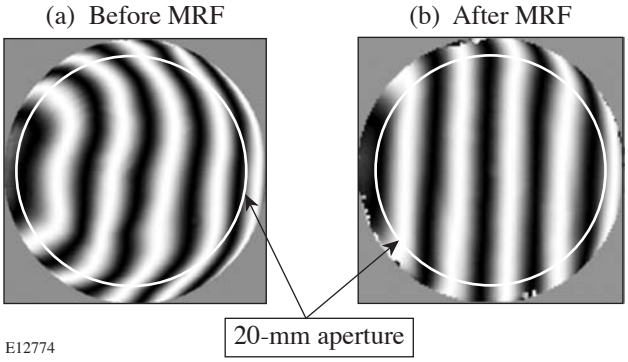

Figure 99.65
Interferograms for rod 2 show the transmitted-wavefront error (a) before and (b) after MRF correction. MRF corrections were applied to the central, 20-mm-diam circular region of the laser rod. The wavefront error was reduced from 0.60 λ to 0.11 λ (peak-to-valley at 1053 nm).

Table 99.III: Transmitted-wavefront distortion of 25-mm-diam Nd:YLF rods before and after MRF correction.

Rod number	Wavefront before MRF (peak-to-valley) in waves at 1053 nm	Wavefront after MRF (peak-to-valley) in waves at 1053 nm
Rod 0	3.9 λ	0.06 λ (15 × 15 mm^2)
Rod 1	1.5 λ	0.16 λ
Rod 2	0.60 λ	0.11 λ
Rod 3	0.92 λ	0.10 λ
Rod 4	3.2 λ	0.10 λ (18-mm diam)

Several issues associated with wavefront-correcting Nd:YLF laser rods were identified: First, the measured transmitted-wavefront distortion in Nd:YLF is different for linearly polarized light aligned with the *c* axis (1047 nm) or *a* axis (1053 nm). As a result, MRF corrections are required for the specific polarization used for laser operation.

Second, the transmitted-wavefront quality of MRF-corrected laser rods depends on its alignment. Transmitted-wavefront error of a laser rod results from the accumulation of different optical phase delays across the aperture in the propagation direction. Since MRF corrections are applied on a single end-face to correct for bulk inhomogeneities distributed throughout the laser rod, the operational alignment of a corrected rod must match that used for the interferometric measurement upon which the MRF correction is applied. The orientation of the laser rod during the interferometry measurements of successive MRF iterations must be repeatable for the corrections to converge. This alignment repeatability ultimately limits the residual wavefront error that can be achieved, which depends on the initial wavefront error.

Figure 99.66 shows the measured alignment sensitivity of three MRF-corrected laser rods. The transmitted-wavefront error was measured as a function of rod orientation using a Zygo GPIxps interferometer. The rods were first aligned with a tip-tilt stage to achieve the minimum transmitted-wavefront error, corresponding to the MRF-correction alignment orientation. The peak-to-valley transmitted-wavefront error was measured for a range of misalignment angles. Transmitted-wavefront errors better than λ/4 were obtained for angular misalignment of rods #2 and #3 not exceeding ±10 mrad, while a narrower range of ±4 mrad was observed for rod #4 since its initial wavefront quality was poorer. Given that alignment accuracy better than ±1 mrad can be achieved by standard alignment techniques, diffraction-limited performance is expected.

It is important to note that the MRF-correction process cannot address transmitted amplitude distortions that can arise from inclusions or scattering sites in the bulk material, or depolarization in a polarization-sensitive scheme such as a *Q*-switched laser cavity. To avoid these problems, a careful selection of the best Nd:YLF boules is required.

Experimental Setup

The laser system, including both the low-energy front end and the CLARA amplifier, is presented schematically in Fig. 99.67. Seed pulses are generated in a diode-pumped,

single-longitudinal-mode Nd:YLF laser[14] producing ~100-nJ, 100-ns pulses at 1053 nm at a 300-Hz repetition rate. The output of the oscillator is temporally shaped using an aperture-coupled-strip-line (ACSL) pulse-shaping system[15] that precompensates for the square-pulse distortion occurring in the amplifier. Timing jitter of this pulse shape with respect to an external timing reference signal is approximately 15-ps rms. The temporally shaped pulse is subsequently amplified from ~50 pJ to 3 mJ in a diode-pumped, Nd:YLF regenerative amplifier.[16] In addition to providing excellent spatial beam quality and energy stability, square-pulse distortion in this amplifier is relatively weak (0.8:1), which minimizes the dynamic range requirements of the pulse-shaping system. After the regenerative amplifier, the laser beam is up-collimated to 15 mm (FWHM) before spatially shaping the beam to a super-Gaussian profile with a serrated-tooth apodizer.[17]

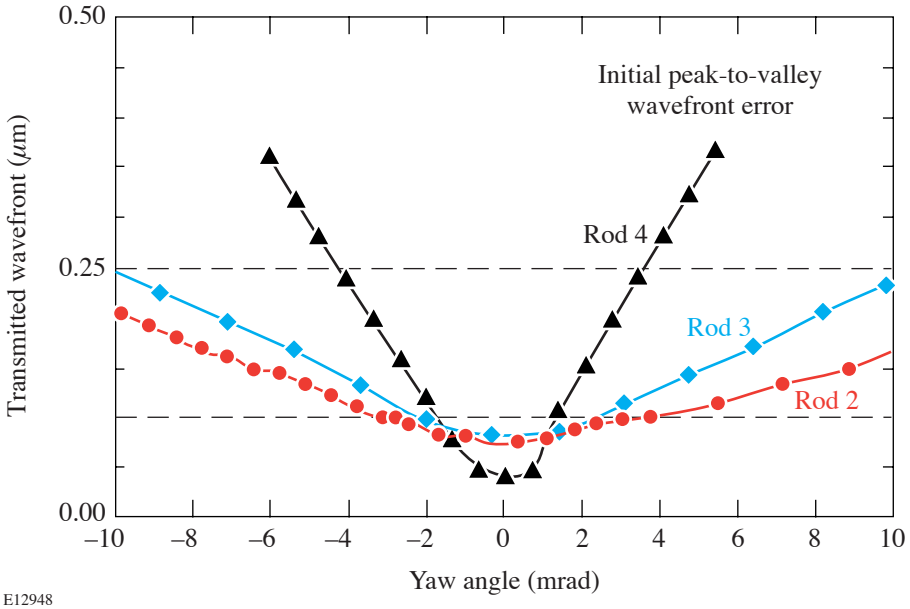

Figure 99.66
The transmitted-wavefront error of MRF-corrected rods is sensitive to its orientation. Optimum performance is achieved when the alignment matches the orientation used during measurements to perform the MRF correction. Increased alignment sensitivity is observed for rods with larger initial wavefront errors.

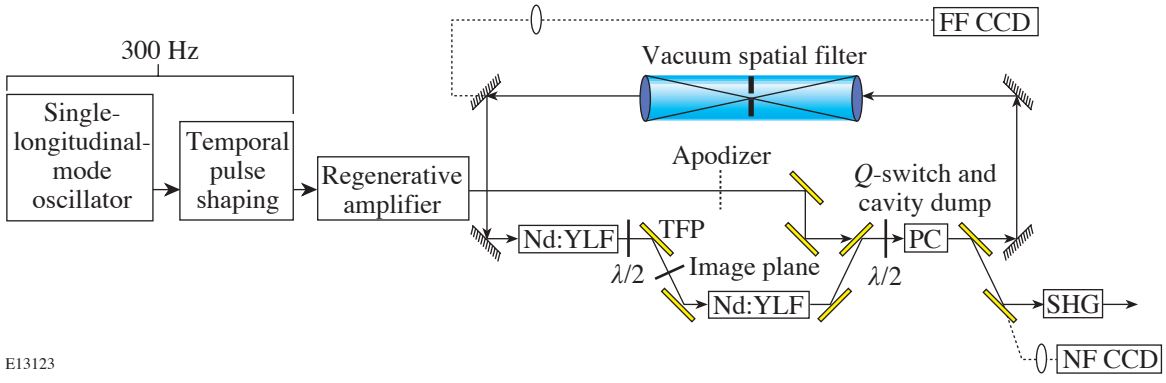

Figure 99.67
Experimental setup. The low-energy part includes a single-longitudinal-mode oscillator, the pulse-shaping system, and the regenerative amplifier. The CLARA setup includes the serrated-tooth apodizer, the CLARA ring, alignment cameras (NF CCD and FF CCD), and the frequency-conversion crystal. TFP: thin-film polarizer; SHG: frequency-doubling crystal; PC: Pockels cell; $\lambda/2$: half-wave plate.

Amplification to high pulse energies is accomplished using a CLARA amplifier, shown in Fig. 99.67. The CLARA architecture is based on a *Q*-switched, cavity-dumped, self-imaging laser cavity. After the pulse is injected through the intracavity Pockels-cell switch, the external apodizer location is imaged to a location between the two laser rods by a telephoto vacuum spatial filter. The spatial filter also image-relays the beam through successive round-trips in the cavity. Two 110-mm-long, 25.4-mm-diam, Nd:YLF, MRF-corrected laser rods are loaded into custom flash-lamp–pumped heads from Continuum with four flash lamps that achieve a single-pass small signal gain of approximately 3× per head. A pair of thin-film polarizers optically isolate the two laser heads to avoid parasitic lasing of the system on the higher-gain, 1047-nm gain transition. Orienting the 1053-nm gain axes of the two Nd:YLF laser rods at 90° cancels residual thermal astigmatism, leaving only a weak defocus that is easily accommodated by the beam-transport system. A 25.4-mm-aperture Pockels cell *Q*-switches the laser cavity and sets the number of round-trips in the 7-m (21-ns) round-trip cavity.

As described above, an MRF-corrected laser rod must be operated with an orientation identical to that used for the correction process. This is achieved by using an interferometric alignment technique for the CLARA laser system that will minimize the total accumulated wavefront error per round-trip through the CLARA. To measure the CLARA transmitted wavefront, an interference pattern is generated between the CLARA output beam and the reference beam. A CCD (charge-coupled-device) camera that images the CLARA image plane (labeled NF CCD in Fig. 99.67) records the interference pattern. Wavefront retrieval is achieved by applying a spatial interferometric technique[18] based on the analysis of tilt fringes and implemented for real-time operation. To produce the reference beam, a half-wave plate is placed in the CLARA, just before the Pockels cell, splitting the laser beam into two beams. This wave plate (shown in Fig. 99.67) is usually removed during operation of the CLARA. One beam propagates through the CLARA and is ejected at the next pass on the polarizer; the other beam, which does not go through the CLARA, is used as a reference beam. In addition to spatial overlap, temporal overlap of the laser pulses is required to have a visible interference pattern. Practically, two output pulses are produced from the regenerative amplifier by intentionally mistiming the cavity dumping. Since the round-trip times of the CLARA and regenerative amplifier are nearly identical, a pulse that travels one round-trip inside the CLARA temporally overlaps with the following pulse on the thin-film polarizer used for injecting the pulses. With temporal and spatial overlap, the interference pattern can be seen in the near field. By adjusting the half-wave plate, the interference fringes' contrast is maximized. A LabVIEW image acquisition and analysis utility records the interference pattern and retrieves the wavefront error in real time. Using this measurement technique, the lens separation in the spatial filter is adjusted with submillimeter accuracy, and the MRF-corrected laser rods can be aligned with great accuracy.

A simple three-dimensional amplification model, based on the Frantz–Nodvik equation,[19] was used to optimize the CLARA. The finite lifetime of the lower level of the Nd:YLF, 1053-nm lasing transition is treated by assuming that the system behaves as a three-level system at each pass, but with exponential decay of the lower-level population between round-trips. Given a lower-level decay time of 21.6 ns (Ref. 20), a pulse of 2 ns, and a round-trip time of 21 ns, we believe the approximation is valid. The model predicts that best energy extraction is achieved for five or six round-trips for a small signal gain of 4 and 3 per rod, respectively, and an injected energy of about 1 mJ. The more round-trips, however, the more wavefront distortion, so we decided to operate the system with four round-trips, where the energy extraction is lower but wavefront distortion is minimized. In addition, less saturation also means lesser distortion of the pump-laser parameters.

After amplification in the CLARA with four round-trips, a second spatial filter down-collimates the beam to a 15 × 15-mm^2-aperture, 10-mm-thick-lithium-triborate (LBO), second-harmonic-generation (SHG) crystal with a nominal incident intensity of 1 GW/cm^2.

Results

Results from operating the CLARA with a 10-mm round beam and uncorrected Nd:YLF laser rods are shown in Fig. 99.68. The figure shows the intensity distribution of the beam in the far field at the OPCPA crystal, where its diameter has been reduced to roughly 2 mm. The measured far field shows a large angular divergence that is unsuitable for pumping phase-matched processes like SHG and OPCPA. Inversion symmetry observed in this image results from the inverted imaging produced by the intracavity spatial filter. As a result, the spatial phase function of the beam is symmetrical, leading to a symmetrical energy distribution in the far field. Figure 99.68(b) shows the corresponding CLARA far-field measurement using MRF-corrected laser rods, which illustrates the greatly improved divergence of this beam. Unfortunately, MRF corrections for these Nd:YLF laser rods were not applied for the correct polarization corresponding to the 1053-nm gain

transition; nonetheless, a dramatic reduction in the angular divergence is realized.

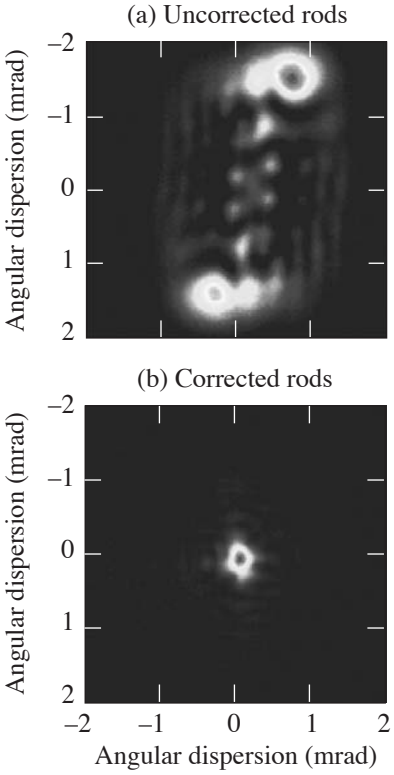

Figure 99.68
Pump-laser far-field distribution measured for a 2-mm beam used to pump an OPCPA preamplifier. (a) The divergence of the beam using uncorrected Nd:YLF rods is large and unsuitable for SHG and OPCPA. (b) Nearly diffraction limited divergence is achieved after MRF correcting the CLARA rods, although some residual divergence results from correcting the transmitted wavefront of the wrong polarization.

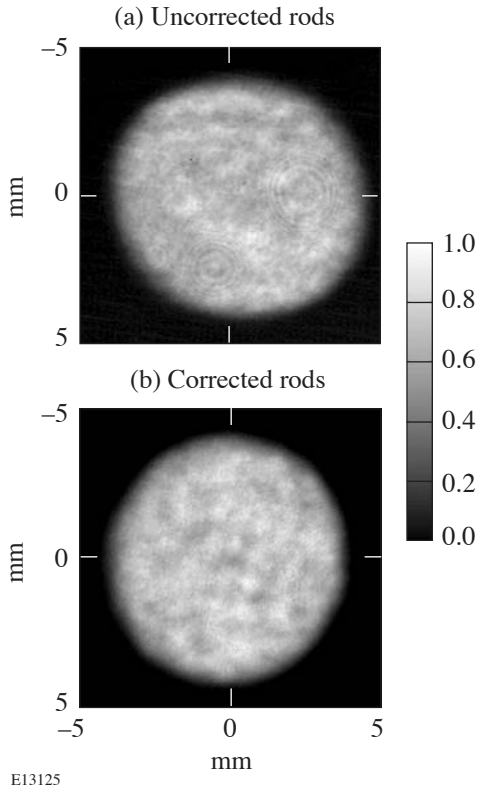

Figure 99.69
Near-field images of the laser beam, at 2ω, after frequency conversion. The dimensions reflect the beam size at this location, which is different from the beam size in the CLARA. (a) CLARA output beam with uncorrected rods and (b) CLARA output beam with MRF-corrected rods.

This improvement in the Nd:YLF laser rod quality increases the usable clear aperture and the stored energy available for extraction. Without MRF-corrected rods, it should be stressed that a 10-mm beam was the largest-diameter beam that could propagate through the amplifier without suffering huge spatial modulation or distortion. Figure 99.69 compares the CLARA output beam profile before and after the MRF correction for a similar input beam. The beam injected into the amplifier is limited by a circular tenth-order super-Gaussian apodizer that sets a 10-mm diameter (FWHM). The beam in Fig. 99.69(a) shows some important spatial distortion, which illustrates the maximum beam diameter that the system could support. The beam in Fig. 99.69(b) shows very little distortion, while the peak-to-mean value of the beam is improved from 49% to 41%. Except for beam distortion, which is important for an OPCPA system used as the front end of a larger system, the improvement in the near field is marginal, as may be expected for an imaged system.

The amplifier with MRF-corrected rods can amplify beams with a much larger area. Figure 99.70 shows spatial profiles of two larger beams amplified in the CLARA, when both (a) a round 17-mm-diam apodizer and (b) a square 14-mm-diam apodizer are used. The corresponding measured energies at 527 nm are 1.4 and 1.8 J, respectively, for a maximum average power of 9 W. In all cases, the SHG conversion efficiency using MRF-corrected rods exceeds 70%. The beam-intensity uniformity is 90% and 92% peak-to-mean for the round and square beams, respectively. The poorer beam-intensity uniformity could be explained by a beam extending slightly beyond the useful area of the rods and a poor matching of the input beam on the apodizer since the system was optimized for smaller-diameter beams. By carefully optimizing the input

beam diameter such that radial gain inversely matches the input beam's Gaussian shape at the apodizer, we believe near-top-hat conditions could be achieved.

The energy stability of the laser is remarkable. For instance, with large round beams, the energy stability is smaller than 0.5% rms over a 10,000-shot count at 5 Hz, as shown in Fig. 99.71 by the pulse energy versus shot number and the corresponding pulse-energy histogram. This excellent result for a flash-lamp–pumped system is attributed to the stable CLARA seed-pulse energy provided by the diode-pumped regenerative amplifier, strong simmering of the flash lamps, and heavy saturation of the SHG process.

Discussion and Conclusion

The transmitted wavefront of a laser gain material has been corrected for the first time by magnetorheological finishing. Polishing a surface figure correction with MRF directly on one surface of 25.4-mm-diam Nd:LF laser rods compensates for bulk inhomogeneities. The results show a dramatic increase in the energy and wavefront-quality performance of the CLARA laser amplifier. The CLARA amplifier demonstrates a high average power of 9 W, which could be increased by 20% to 30% by increasing the number of passes in the amplifier and using laser rods with wavefront corrections correctly applied for the 1053-nm polarization.

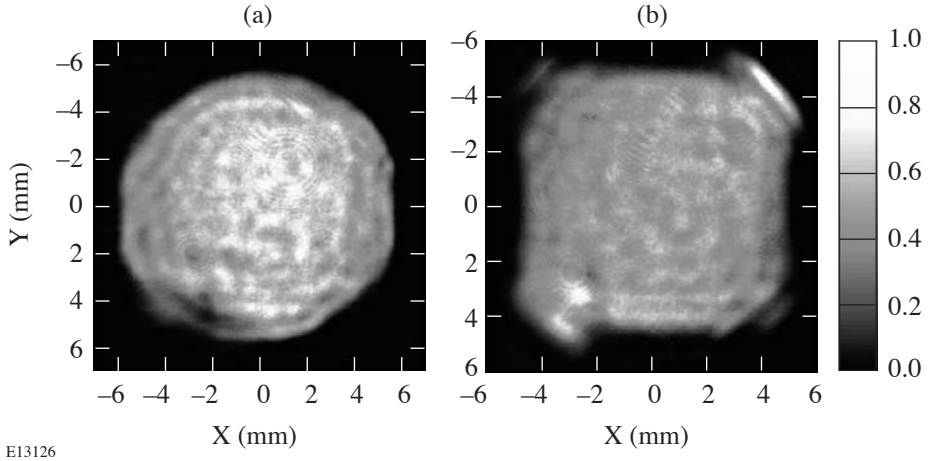

Figure 99.70
Larger beams can be amplified in the CLARA with MRF-corrected laser rods. Results with (a) a round, 17-mm-diam and (b) a square, 14-mm, 20th-order Gaussian spatial profile are demonstrated.

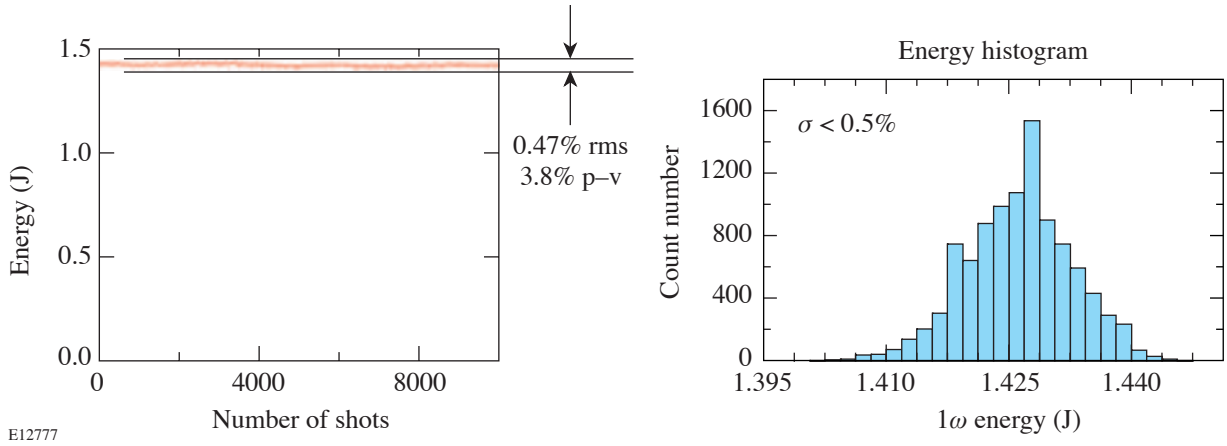

Figure 99.71
Energy stability at the output of the laser.

The MRF technique holds promise for additional applications, such as precompensating thermal aberrations and post-processing large-area laser crystals. Numerous techniques have been reported to mitigate thermal lensing in materials like Nd:YAG.[21,22] Since thermal lensing is a low-order error to the transmitted wavefront, MRF corrections to laser gain elements should easily statically precompensate for it without requiring any other elements in the laser cavity. It should be noted that MRF is probably not well-suited to small rods since edge effects and the finite MRF spot size become a problem with small areas. Efforts to produce large-area crystals of Yb:SFAP and Ti:sapphire are being pursued by diffusion bonding of smaller-aperture elements, but the transmitted-wavefront distortions are observed at the boundaries in such crystals. MRF wavefront corrections might solve this problem, as long as the wavefront gradients are not excessive.

In conclusion, use of a high-energy, high-average-power laser that is suitable for pumping an OPCPA-based front end for a petawatt laser system is demonstrated. Early results show a system that delivers 250-mJ pulses with 34% pump-to-signal energy conversion efficiency with a 10-mm round CLARA beam. This shows that the laser system is well suited to efficiently pumping a high-average-power OPCPA system. Further experiments are underway to use the full CLARA aperture and deliver >500-mJ OPCPA pulses.

ACKNOWLEDGMENT

The authors thank VLOC for providing the Nd:YLF samples used to characterize the MRF process. This work was supported by the U.S. Department of Energy Office of Inertial Confinement Fusion under Cooperative Agreement No. DE-FC52-92SF19460, the University of Rochester, and the New York State Energy Research and Development Authority. The support of DOE does not constitute an endorsement by DOE of the views expressed in this article.

REFERENCES

1. A. Dubietis, G. Jonusauskas, and A. Piskarskas, Opt. Commun. **88**, 437 (1992).
2. I. N. Ross *et al.*, Opt. Commun. **144**, 125 (1997).
3. H. Yoshida *et al.*, Opt. Lett. **28**, 257 (2003).
4. J. Collier *et al.*, Appl. Opt. **38**, 7486 (1999).
5. J. L. Collier *et al.*, "Progress Towards Petawatt Level OPCPA," to be published in *Inertial Fusion Sciences and Applications 2003*.
6. Y. Kitagawa *et al.*, IEEE J. Quantum Electron. **40**, 281 (2004).
7. L. J. Waxer, V. Bagnoud, I. A. Begishev, M. J. Guardalben, J. Puth, and J. D. Zuegel, Opt. Lett. **28**, 1245 (2003).
8. M. J. Guardalben, J. Keegan, L. J. Waxer, V. Bagnoud, I. A. Begishev, J. Puth, and J. D. Zuegel, Opt. Express **11**, 2511 (2003).
9. I. Jovanovic *et al.*, Appl. Opt. **41**, 2923 (2002).
10. V. Bagnoud, J. Luce, L. Videau, and A. Rouyer, Opt. Lett. **26**, 337 (2001).
11. A. Babushkin, J. H. Kelly, C. T. Cotton, M. A. Labuzeta, M. O. Miller, T. A. Safford, R. G. Roides, W. Seka, I. Will, M. D. Tracy, and D. L. Brown, in *Third International Conference on Solid State Lasers for Application to Inertial Confinement Fusion*, edited by W. H. Lowdermilk (SPIE, Bellingham, WA, 1999), Vol. 3492, pp. 939–943.
12. C. Le Blanc *et al.*, Opt. Lett. **18**, 140 (1993).
13. D. Golini, S. Jacobs, W. Kordonski, and P. Dumas, in *Advanced Materials for Optics and Precision Structures*, edited by M. A. Ealey, R. A. Paquin, and T. B. Parsonage, Critical Reviews of Optical Science and Technology (SPIE, Bellingham, WA, 1997), Vol. CR67, pp. 251–274.
14. A. V. Okishev and W. Seka, IEEE J. Sel. Top. Quantum Electron. **3**, 59 (1997).
15. M. D. Skeldon, Rev. Sci. Instrum. **71**, 3559 (2000).
16. A. V. Okishev, D. J. Battaglia, I. A. Begishev, and J. D. Zuegel, in *OSA TOPS Vol. 68, Advanced Solid-State Lasers*, edited by M. E. Fermann and L. R. Marshall, OSA Technical Digest (Optical Society of America, Washington, DC, 2002), pp. 418–422.
17. J. M. Auerbach and V. P. Karpenko, Appl. Opt. **33**, 3179 (1994).
18. M. Takeda, H. Ina, and S. Kobayashi, J. Opt. Soc. Am. **72**, 156 (1982).
19. L. M. Frantz and J. S. Nodvik, J. Appl. Phys. **34**, 2346 (1963).
20. J. D. Zuegel and W. Seka, IEEE J. Quantum Electron. **31**, 1742 (1995).
21. G. Vdovin and V. Kiyko, Opt. Lett. **26**, 798 (2001).
22. R. Weber, T. Graf, and H. P. Weber, IEEE J. Quantum Electron. **36**, 757 (2000).

Prototypes of NIF Neutron Time-of-Flight Detectors Tested on OMEGA

Introduction

The National Ignition Facility[1] (NIF) is a 2-MJ, 192-beam laser system currently under construction at Lawrence Livermore National Laboratory. One of the main missions of the NIF is to achieve thermonuclear ignition of fusion fuel in inertial confinement fusion (ICF).[2] In ICF experiments, primary neutrons are produced in two reactions:

$$\mathrm{D} + \mathrm{D} \rightarrow n(2.45\ \mathrm{MeV}) + {}^{3}\mathrm{He}, \tag{1}$$

$$\mathrm{D} + \mathrm{T} \rightarrow n(14.1\ \mathrm{MeV}) + \alpha. \tag{2}$$

Neutrons from reaction (1) are referred to as DD neutrons and neutrons from reaction (2) are referred to as DT neutrons.

Every large ICF laser facility, including Nova, OMEGA, and GEKKO, uses neutron time-of-flight (nTOF) systems to measure neutron yields and ion temperatures. Such nTOF systems are usually based on current-mode detectors consisting of a fast plastic scintillator optically coupled to a fast photomultiplier tube (PMT). A high-bandwidth transient digitizer records the signal. These systems, which are relatively inexpensive, have a large dynamic range and a fast time response. The nTOF detectors are reliable, and the information they record is fundamental to most ICF implosion experiments. It is for these reasons that the nTOF system was identified as a "core" diagnostic[3] for the NIF.

The 30-kJ, 60-beam OMEGA laser system[4] is currently the only facility that produces sufficient ICF neutrons for developing and testing prototype nTOF detectors for the NIF. Several nTOF detector prototypes have been built and tested on OMEGA. Based on the results of these tests, a set of nTOF detectors is proposed for use on the NIF to measure ion temperature and DD and DT neutron yields from 10^9 to 10^{19}.

NIF nTOF Detector Requirements

The nTOF system for the NIF must measure ion temperatures of implosion targets, ranging from 1 to 50 keV for yields between 10^9 and 10^{19} neutrons. The nTOF system must work in a harsh environment[5] of energetic neutrons, x rays, γ rays, and high electromagnetic pulse (EMP) noise. The main objective of an nTOF system is to measure ion temperature. Because nTOF-detector signals are proportional to the number of neutrons detected, they are easily adapted for simultaneous use as a yield monitor.

The neutrons produced in fusion reactions (1) and (2) are monoenergetic. Center-of-mass motion of the reacting ions causes spectral broadening of these energy lines. Because ICF targets are nearly ideal point sources in both time (<100 ps) and space (<100 μm) and neutrons travel to a detector without collisions, neutron spectra can be measured using the time-of-flight technique. The arrival time at a detector corresponds to the energy of the neutron. The time spread Δt of neutrons arriving at an nTOF detector is given by the following equations:[6]

$$\Delta t = 0.778 d\sqrt{T_i} \quad (\text{for DD}), \tag{3}$$

$$\Delta t = 0.122 d\sqrt{T_i} \quad (\text{for DT}), \tag{4}$$

where Δt is the full width at half maximum (FWHM) in nanoseconds, d is target-to-detector distance in meters, and T_i is the ion temperature in keV. The width of a measured signal is the width of the time-of-flight spread added in quadrature with the detector response.[7] To minimize measurement error, the nTOF detector response (FWHM) should be much less than the neutron temporal broadening being measured. For scintillator- and PMT-based detectors, this requirement leads to the use of fast microchannel-plate (MCP) PMT's with time resolutions of a few hundred picoseconds (FWHM).

The scintillator used in an nTOF detector must also be fast. Bicron's[8] ultrafast BC-422 scintillator has a rise time of less than 20 ps[9] and an exponential decay constant of 1.4 ns. The quenched version of the scintillator, BC-422Q, has a two-component decay with time constants of about 0.6 and 5 ns. In addition, the nTOF detector-response function includes the transit time of the neutrons across the thickness of the scintillator. A scintillator thickness of 20 mm corresponds to a 0.92-ns transit time for DD neutrons and provides a good match between scintillator decay and transit time through the scintillator. The cables and digitizer also contribute to detector response. A cable with a 3-GHz bandwidth and a 1-GHz or faster oscilloscope contributes relatively small dispersion to temperature measurements.

X rays and γ rays from an ICF implosion generate background[10] in nTOF detectors that can saturate a PMT and distort the neutron signal, causing errors in ion temperature and yield measurement. Shielding is therefore required to reduce the x-ray and γ-ray fluence entering PMT-based nTOF detectors. Lead-shielding thickness is limited to <30 mm to avoid neutron scattering that would appear as signal broadening in the detector. High-yield DT implosions create MeV γ rays from (n,γ) interactions in the target, target positioner, nearby diagnostics, and the target chamber walls. This γ-ray background is proportional to the DT neutron yield and will be very high at expected NIF yields. It is difficult to shield MeV γ rays without also shielding the energetic neutrons. New techniques[10] like single-stage MCP PMT's and chemical-vapor-deposition (CVD) diamonds,[11] which are less sensitive to MeV γ rays, are recommended for the NIF.

nTOF Detector Locations on the NIF

The optimum placement[12] of nTOF detectors is determined by a tradeoff between decreased time resolution at small distances from the target and a smaller statistical sample of detected neutrons at longer distances. It can be shown[13] that the number of neutrons needed to achieve a given statistical uncertainty should be a factor of 2 larger over that predicted by Poisson statistics. Therefore, in our design, we require at least 200 neutron interactions in the nTOF detectors to achieve 10% statistical uncertainty, which puts a restriction on detector location. Another requirement is that, at the lowest yields, the nTOF detector should provide a neutron signal with an amplitude five to ten times higher than the EMP noise of the system. The highest-measurable yield is determined by PMT saturation. The signal from a modern MCP PMT is linear to ~3 nC of integrated charge for low-repetition pulses. This was taken into account in estimating yield limits. A combination of the optimization[12] of the detector locations combined with background considerations provides several natural locations for nTOF detectors on the NIF.

Placing a detector outside the target chamber wall at 5 m from the target avoids vacuum interface and tritium contamination problems. A 5-m flight path is adequate for ion-temperature measurements. At this location the nTOF detector will not be affected by scattered neutrons and (n,γ) interactions with the target chamber. The EMP noise at the OMEGA target chamber is 2 to 20 mV, depending on shot and detector design. The EMP noise at the NIF target chamber will most likely be higher; therefore, at least a 500-mV signal is required at the target chamber wall. This location should be used only for D_2 implosions and low-yield DT shots as described in the next section and Table 99.IV.

Another natural location for nTOF detectors is outside the NIF target bay shield wall against existing, predrilled holes. The 2-m-thick concrete walls of the target bay can be used as shielding against scattered neutrons and γ rays. There are several such locations at the NIF where detectors can be placed 17 m to 20 m from the target. The digitizing oscilloscopes can be placed nearby, thereby shortening the signal and HV cables and decreasing EMP noise pickup. The EMP noise in this location should be much less of a problem than at the target chamber wall; therefore, the minimum signal requirement in this location is 100 mV.

The 20-m standoff distance is not adequate for pre-ignition and ignition targets producing 10^{17} to 10^{19} neutrons. Most of the nTOF detectors located 20 m from the target will saturate at such yields. The high neutron flux can also damage an oscilloscope and PC. Another location as far away from the target as possible with a clean flight path is needed for the ignition campaign. There is a line of sight at $\theta = 64°$ and $\phi = 275.62°$ with an opening in the target bay wall that exits outside the building just above the roof of the diagnostic building. The nTOF detectors can be installed on the roof of the diagnostic building at about 40 m from the target.

OMEGA Performance Scaled to the NIF

Three different types of fast detectors were used for the NIF nTOF prototype tests on OMEGA. The most-sensitive nTOF detector consists of a BC-422 scintillator coupled to a two-stage MCP PMT. The PMT has a response time of about 250 ps (FWHM), a gain up to 10^6, and a 40-mm-diam photocathode. Detectors based on a two-stage MCP PMT are relatively sensitive to hard-x-ray and γ-ray background and are good for

relatively low (10^9 to 10^{11}) neutron-yield NIF implosions, in which x-ray and γ-ray background is low as well. The first prototype has a 40-mm-diam, 20-mm-thick BC-422 scintillator coupled to a Photek[14] PMT240 PMT. To protect the prototype from the x-ray and γ-ray background inside the OMEGA Target Bay, it was heavily shielded on all sides by a thick lead housing (Fig. 99.72). The prototype was installed in the OMEGA Target Bay at 12.4 m from the target and connected by a 12-m-long LMR-400 cable to a 1-GHz Tektronix 684 oscilloscope. A Mini-Circuits model 15542 resistive splitter divides the detector signal between two oscilloscope channels with different sensitivity settings to increase the dynamic range of the recording system. The prototype was tested on D_2 implosions on OMEGA and calibrated against the standard suite of neutron diagnostics. Figure 99.73 shows a typical scope trace of the neutron signal taken for a shot yielding 1.2×10^{11} DD neutrons and having a $T_i = 4.1$ keV. The measured signal was fitted by a convolution of a Gaussian and an exponential decay, as described in detail in Ref. 7. Scaled to the 5-m distance on the NIF chamber wall, this detector will have ~200 neutron interactions and produce a signal amplitude of 500 mV for a DD yield of 1×10^9 neutrons. This detector installed on the NIF target chamber wall will be sensitive to DD and DT neutron yields from 5×10^8 to 5×10^{10}. Using relations derived by Lerche,[12] it is estimated that, at 5 m, this detector can measure ion temperature with 15% accuracy for 10^9 DD neutrons at 1 keV. Better than 10% accuracy is possible at higher yields or higher ion temperatures.

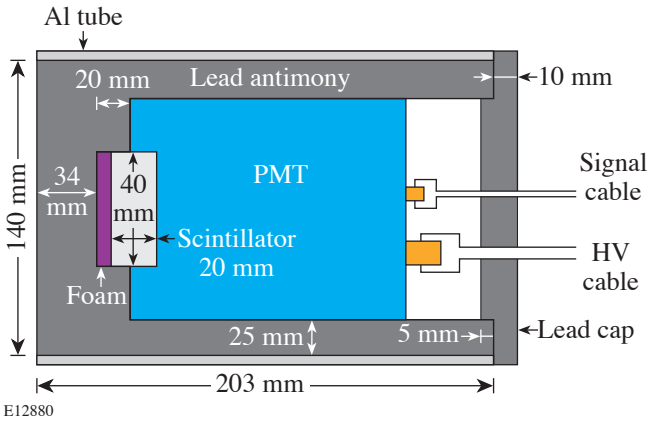

Figure 99.72
Schematic of the single-stage and two-stage MCP PMT nTOF prototypes tested on OMEGA at 12.4 m from the target.

Table 99.IV: Proposed set of nTOF detectors required for DD and DT temperature measurements for yields between 10^9 and 10^{19} neutrons.

N	Distance	Scintillator/ Wafer Size	Type	PMT	Yield Range
1	5 m	40 mm × 20 mm	BC-422	2 MCP	1×10^9 to 5×10^{10}
2	5 m	40 mm × 20 mm	BC-422	1 MCP	1×10^{10} to 5×10^{11}
3	5 m	10 mm × 1 mm	CVD diamond		5×10^{12} to 1×10^{15}
4	20 m	40 mm × 20 mm	BC-422	1 MCP	1×10^{11} to 5×10^{12}
5	20 m	40 mm × 20 mm	BC-422Q	1 MCP	1×10^{12} to 1×10^{14}
6	20 m	10 mm × 1 mm	CVD diamond		1×10^{14} to 5×10^{16}
7	40 m	10 mm × 5 mm	BC-422Q	1 MCP	1×10^{14} to 1×10^{16}
8	40 m	10 mm × 1 mm	CVD diamond		5×10^{14} to 1×10^{17}
9	40 m	2 mm × 0.5 mm	CVD diamond		2×10^{16} to 1×10^{19}

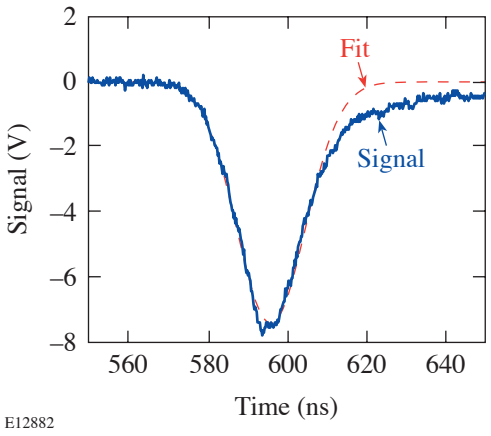

Figure 99.73
Neutron signal recorded for the two-stage MCP PMT prototype on D_2 shot 33949: yield = 1.2×10^{11} and T_i = 4.1 keV. The fit is a convolution of a Gaussian shape and a scintillator exponential decay.

The second nTOF detector designed for the NIF consists of a BC-422 or BC-422Q scintillator coupled to a single-stage MCP PMT. This PMT has a slightly faster response time of about 200 ps (FWHM), a gain up to 10^3, and a 40-mm-diam photocathode. The single-stage MCP PMT is less sensitive (by a factor of about 10^3) to x-ray and γ-ray background but has less gain by the same factor. Two versions of this detector were tested on OMEGA: The first version was designed to determine the maximum sensitivity achievable using a single-stage MCP Photek PMT140 PMT, coupled to a 20-mm-thick, 40-mm-diam BC-422 scintillator. It has 14-mm lead shielding in front and a 5-mm aluminum housing on all other sides. This prototype was tested on the OMEGA chamber wall, 1.65 m from the target, with DD implosions and calibrated against the standard neutron diagnostics. Figure 99.74 shows a typical oscilloscope trace of a neutron signal from this detector (DD yield of 6.7×10^{10} neutrons and T_i = 3.2 keV). This detector installed on the NIF target chamber wall will detect ~1900 neutron interactions and produce a 500-mV signal for a DD yield of 1×10^{10} neutrons. The same detector installed outside the NIF target bay at 20 m from the target will have ~1700 neutron interactions and produce a 450-mV signal for a DD yield of 1×10^{11}.

The second version of the single-stage MCP PMT system was designed to test upper-yield limits of such detectors. This prototype had a 40-mm-diam, 20-mm-thick BC-422Q (1% benzephenone) quenched scintillator, coupled with a Photek PMT140 PMT, and operated at a gain of 5×10^2. The detector was placed in a lead housing identical to that shown in Fig. 99.72 and installed in the OMEGA Target Bay at 12.4 m from the target, next to the two-stage MCP PMT prototype. This prototype was tested with DT implosions and calibrated against copper activation measurements. A scope trace of a neutron signal is shown in Fig. 99.75 (DT neutron yield of 5.0×10^{13} and T_i = 9.7 keV). If this detector is installed outside the NIF target bay at 20 m from the target, it will be sensitive to DT yields from 10^{12} to 10^{14} neutrons.

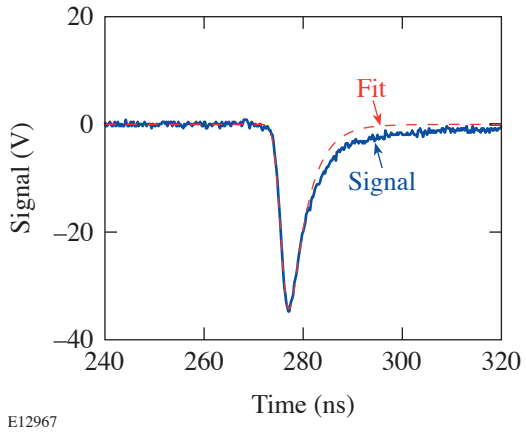

Figure 99.74
Neutron signal recorded for the singe-stage MCP PMT prototype on D_2 shot 33413: yield = 6.7×10^{10} and T_i = 3.2 keV. The fit is a convolution of a Gaussian shape and a scintillator exponential decay.

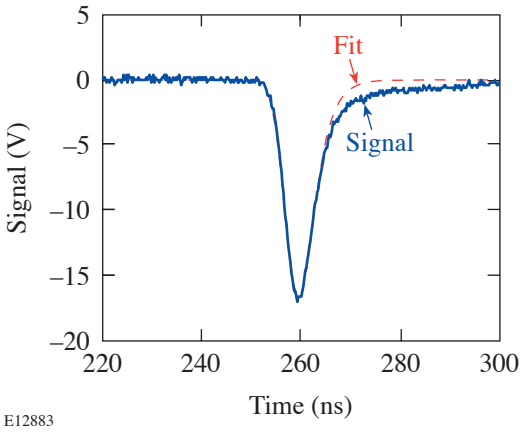

Figure 99.75
Neutron signal recorded for the single-stage MCP PMT prototype on DT shot 33797: yield = 5.0×10^{13} and T_i = 9.7 keV. The fit is a convolution of a Gaussian shape and a scintillator exponential decay.

The third prototype nTOF detector tested on OMEGA used a 10-mm-diam, 1-mm-thick CVD diamond wafer. Diamond detectors have low sensitivity[11] to hard-x-ray and γ-ray background and can be used at very-high DT yields. The CVD diamond detectors also have a larger dynamic range than PMT-based detectors. Such detectors[11] were previously tested inside the OMEGA target chamber. This time, the CVD diamond detector was installed outside the target chamber at 2.8 m from the target and biased at 1 kV. The CVD diamond prototype was tested with DT implosions and calibrated against copper activation. A typical scope trace is shown in Fig. 99.76 (DT yield of 5.0×10^{13} and $T_i = 9.7$ keV). This detector installed on the NIF target chamber wall will be sensitive to DT neutrons over a yield range from 5×10^{12} to 10^{15}. The same detector installed outside the NIF target bay at 20 m from the target will be sensitive to DT yields between 10^{14} and 5×10^{16} neutrons.

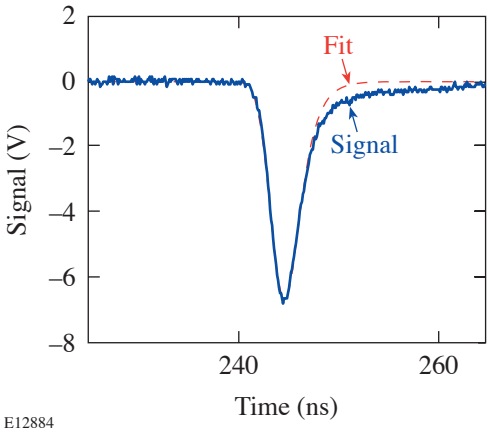

Figure 99.76
Neutron signal recorded for the CVD diamond prototype on DT shot 33797: 5.0×10^{13} and $T_i = 9.7$ keV. The fit is a convolution of a Gaussian shape and an exponential decay.

For pre-ignition and ignition targets on the NIF, less-sensitive detectors are needed about 40 m from the target. Scaled detectors based on a single-stage MCP PMT and a CVD diamond detector are chosen for this purpose. The proposed set of nTOF detectors to measure ion temperature and DD and DT neutron yields between 10^9 and 10^{19} is summarized in Table 99.IV.

The proposed set of detectors is a realistic, cost-effective approach to the NIF nTOF system and based on commercially available components. All of the nTOF detectors and components can be calibrated on OMEGA prior to installation and use on the NIF. The nTOF detector calibrations can be later cross checked against other yield-sensitive diagnostics, such as the PROTEX[15] and activation.[16]

Conclusions

Neutron time-of-flight (nTOF) detectors are part of the NIF core diagnostic suite providing a measurement of ion temperature and yield. Several NIF nTOF detector prototypes have been built and tested with D_2 and DT implosions on OMEGA. Prototypes for low and moderate NIF neutron yields are based on fast plastic scintillators and fast photomultiplier tubes. A third prototype is based on a CVD diamond detector. A set of nTOF detectors is proposed for the NIF to measure ion temperature and DD and DT neutron yields between 10^9 and 10^{19}.

ACKNOWLEDGMENT

This work was supported by the U.S. Department of Energy Office of Inertial Confinement Fusion under Cooperative Agreement No. DE-FC52-92SF19460, the University of Rochester, and the New York State Energy Research and Development Authority. The support of DOE does not constitute an endorsement by DOE of the views expressed in this article.

REFERENCES

1. E. I. Moses, Fusion Sci. Technol. **44**, 11 (2003).
2. J. D. Lindl, *Inertial Confinement Fusion: The Quest for Ignition and Energy Gain Using Indirect Drive* (Springer-Verlag, New York, 1998).
3. T. J. Murphy, C. W. Barnes, R. R. Berggren, P. Bradley, S. E. Caldwell, R. E. Chrien, J. R. Faulkner, P. L. Gobby, N. M. Hoffman, J. L. Jimerson, K. A. Klare, C. L. Lee, J. M. Mack, G. L. Morgan, J. A. Oertel, F. J. Swenson, P. J. Walsh, R. B. Walton, R. G. Watt, M. D. Wilke, D. C. Wilson, C. S. Young, S. W. Haan, R. A. Lerche, M. J. Moran, T. W. Phillips, T. C. Sangster, R. J. Leeper, C. L. Ruiz, G. W. Cooper, L. Disdier, A. Rouyer, A. Fedotoff, V. Yu. Glebov, D. D. Meyerhofer, J. M. Soures, C. Stockl, J. A. Frenje, D. G. Hicks, C. K. Li, R. D. Petrasso, F. H. Séguin, K. Fletcher, S. Padalino, and R. K. Fisher, Rev. Sci. Instrum. **72**, 773 (2001).
4. T. R. Boehly, D. L. Brown, R. S. Craxton, R. L. Keck, J. P. Knauer, J. H. Kelly, T. J. Kessler, S. A. Kumpan, S. J. Loucks, S. A. Letzring, F. J. Marshall, R. L. McCrory, S. F. B. Morse, W. Seka, J. M. Soures, and C. P. Verdon, Opt. Commun. **133**, 495 (1997).

5. J. L. Bourgade, V. Allouche, J. Baggio, C. Bayer, F. Bonneau, C. Chollet, S. Darbon, L. Disdier, D. Gontier, M. Houry, H. P. Jacquet, J.-P. Jadaud, J. L. Leray, I. Masclet-Gobin, J. P. Negre, J. Raimbourg, B. Villette, I. Bertron, J. M. Chevalier, J. M. Favier, J. Gazave, J. C. Gomme, F. Malaise, J. P. Seaux, V. Yu. Glebov, P. Jaanimagi, C. Stoeckl, T. C. Sangster, G. Pien, R. A. Lerche, and E. Hodgson, "New Constraints for Plasma Diagnostics Development due to the Harsh Environment of MJ-Class Lasers," to be published in Review of Scientific Instruments.

6. H. Brysk, Plasma Phys. **15**, 611 (1973).

7. T. J. Murphy, R. E. Chrien, and K. A. Klare, Rev. Sci. Instrum. **68**, 610 (1997).

8. Saint-Gobain Crystals, Newbury, OH 44065.

9. R. A. Lerche, D. W. Phillion, and G. L. Tietbohl, in *Ultrahigh- and High-Speed Photography, Videography, and Photonics '93*, edited by P. W. Roehrenbeck (SPIE, Bellingham, WA, 1993), Vol. 2002, pp. 153–161.

10. V. Yu. Glebov, C. Stoeckl, T. C. Sangster, and G. J. Schmid, "Hard-X-Ray and γ Background in Neutron Time-of-Flight Detectors on the NIF and LMJ," to be submitted to Review of Scientific Instruments.

11. G. J. Schmid, R. L. Griffith, N. Izumi, J. A. Koch, R. A. Lerche, M. J. Moran, T. W. Phillips, R. E. Turner, V. Yu. Glebov, T. C. Sangster, and C. Stoeckl, Rev. Sci. Instrum. **74**, 1828 (2003).

12. R. A. Lerche and B. A. Remington, Rev. Sci. Instrum. **61**, 3131 (1990).

13. T. J. Murphy *et al.*, Rev. Sci. Instrum. **72**, 850 (2001).

14. Photek Ltd., St. Leonards-on-Sea, United Kingdom.

15. M. J. Moran, V. Yu. Glebov, R. Rygg, and B.-E. Schwartz, "PROTEX: A Proton-Recoil Detector for ICF Fusion Neutrons," submitted to Review of Scientific Instruments.

16. G. W. Cooper and C. L. Ruiz, Rev. Sci. Instrum. **72**, 814 (2001).

Subpicosecond Faraday Effect in $Cd_{1-x}Mn_xTe$ and Its Application in Magneto-Optical Sampling

Introduction

Recent technological developments in electronics and optoelectronics have opened prospects for novel devices and digital circuits operating in the subpicosecond temporal regime.[1–5] As the operating speed of modern electrical devices increases, the problem of how to properly characterize them becomes progressively more difficult. Independent measurements of the voltage and the current transients are needed in order to get the full picture of the electromagnetic field distribution in the device or circuit under test and to be able to obtain the complex, frequency-dependent impedance characteristics of the tested element. Information on the voltage transient in the subpicosecond time range, corresponding to the device's THz operation rate, can be obtained using an electro-optical sampling (EOS) technique, based on a nonlinear optical crystal ($LiTaO_3$ in most cases) as the EO sensor.[6] Freeman[7,8] has recently developed a magneto-optical sampling (MOS) technique that is capable of directly measuring magnetic-field transients and, therefore, together with EOS, allows for the complete characterization of ultrafast devices and circuits. These previous realizations of MOS have been limited, however, to Tb-doped EuS[7] or garnet[8] crystals as the MO medium and could probe current pulses with experimentally demonstrated temporal resolution of the order of 10 ps at best. Part of the problem was that the implemented MO materials exhibited ferrimagnetic ordering,[9] leading to slow magnetization relaxation.

This article presents time-resolved studies of the Faraday effect in a diluted magnetic semiconductor $Cd_{1-x}Mn_xTe$ single crystal with $x > 0.5$, maintained at cryogenic (10 K) temperature. The $Cd_{0.38}Mn_{0.62}Te$ crystal has been implemented as the ultrafast MO transducer, allowing ultrafast current transients to be characterized with subpicosecond time resolution. Our MOS technique should also be applicable for accurate, time-resolved measurements of transient magnetic-field variations in modern spintronic devices.[10]

Faraday Effect and Magneto-Optical Sampling

The $Cd_{1-x}Mn_xTe$ crystals are very suitable materials for MO applications, in general, and for MOS, in particular, since, especially at low temperatures, they exhibit very high Faraday rotation under externally applied magnetic fields.[11,12] Alignment of Mn spins in $Cd_{1-x}Mn_xTe$ due to the applied magnetic field leads to a large Zeeman splitting of the excitonic energy levels[13] through the strong *sp–d* exchange interaction between the Mn spins and carriers. In turn, this mechanism induces a magnetic-field–dependent birefringence in both optical circular polarization directions, ultimately resulting in the polarization rotation angle θ_F given by[9]

$$\theta_F = \frac{\omega}{2c}\left(n_+ - n_-\right)L = VBL, \tag{1}$$

where ω is the light angular frequency, $n_+(n_-)$ are the right (left) components of the index of refraction of the circularly polarized light within the MO material, L is the optical beam magnetic-field B interaction length, and c is the speed of light. Equation (1) also shows that θ_F can be expressed as the product of the experimentally defined materials constant, so-called Verdet constant V, times B and L. In the time domain, it is predicted that the Mn ion spin–spin interaction time decreases exponentially with increasing x and reaches the subpicosecond range for $x > 0.5$.[14]

Figure 99.77 presents a schematic of our MOS experimental setup. The source of current pulses in our technique was a photoconductive LT-GaAs freestanding photoswitch capable of generating ~0.5-ps-wide electrical pulses.[15] The switch was integrated into a Ti/Au coplanar strip line (CSL) with 10-μm-wide metal strips with 10-μm separation, deposited on a transparent MgO substrate. The CSL was biased and could be shorted at one end in order to perform low-frequency V measurements. A 0.5-mm-thick, optically polished platelet cut from a $Cd_{0.38}Mn_{0.62}Te$ single crystal was placed on top of the CSL and acted as the MO transducer. Our $Cd_{1-x}Mn_xTe$ crystals were grown using a modified Bridgeman method. The synthesized material of proper stoichiometry in the form of a polycrystalline powder was used as the source material for the final crystal growth. The quality of our crystals was verified

through extensive x-ray diffraction measurements.[16] The entire arrangement presented in Fig. 99.77 was placed inside a temperature-controlled optical helium cryostat, and the measurements were taken at 10 K.

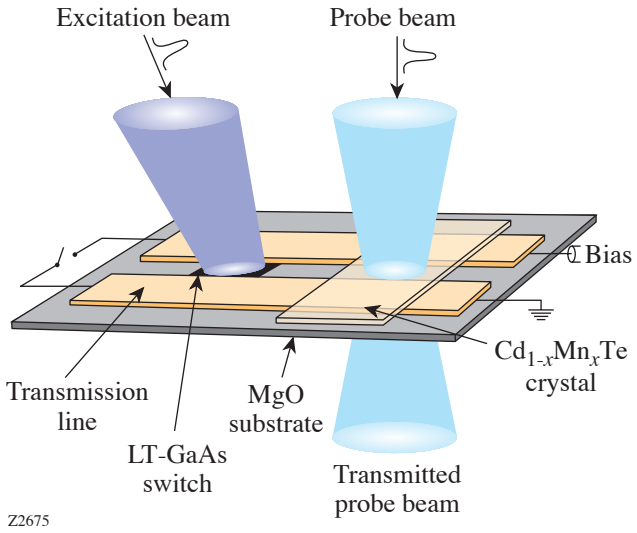

Figure 99.77
Schematic of the MOS setup, including the LT-GaAs freestanding photoswitch as an electrical pulse generator and the $Cd_{1-x}Mn_xTe$ crystal as an MO transducer. Both the switch and the transducer are integrated into a CSL fabricated on a transparent MgO substrate.

For our time-resolved Faraday rotation experiments, the LT-GaAs switch was excited by ~800-nm-wavelength, 100-fs-duration, 76-MHz-repetition-rate laser pulses generated by a commercial Ti:sapphire laser, while ~200-fs-wide probe pulses were generated by an optical parametric oscillator (OPO) with internal frequency doubling and their wavelengths covered the range from 570 nm to 615 nm. A 7:3 beam splitter was used to direct 70% of the optical energy to OPO; the remaining 30% was modulated by an acousto-optical modulator at 90 KHz and delivered to our LT-GaAs freestanding switch.[17] The linearly polarized femtosecond probe pulses from OPO traveled through the MO crystal between the metal CSL electrodes, about 300 μm away from the photoswitch. The CSL was connected to a bias source that charged the LT-GaAs switch. The polarizer and photodetector (not shown in Fig. 99.77) detected the polarization rotation of the transmitted probe light, which was displayed on a computer as a function of the excitation-probe delay time. The implemented two-color-beam approach allowed us to tune the probe-beam wavelength to reach the $Cd_{1-x}Mn_xTe$ maximum Faraday rotation, while, at the same time, exciting the LT-GaAs switch with the near-infrared (just above the bandgap) radiation. We could also maintain the excitation-probe synchronization needed for the sampling technique. Both the excitation and probe beams were focused to spots with an ~10-μm diameter.

Experimental Results and Conclusions

At the first phase of our measurements, we measured the spectral characteristics of our $Cd_{0.38}Mn_{0.62}Te$ crystal response and determined the static MO effect. A 3-KHz sinusoidal voltage was applied to one end of the CSL with no light excitation on the LT-GaAs switch, so its resistance remained of the order of 1 MΩ and its presence in the circuit could be neglected. When the other end of the line was shorted (see Fig. 99.77), a 3-KHz current signal was induced in the CSL and the polarization rotation of the probe beam, passing through the $Cd_{0.38}Mn_{0.62}Te$ crystal and between the CSL lines, was observed because of the Faraday effect. In the opposite situation, i.e., when the left end of the CSL was opened, no polarization rotation of the probe beam was observed, excluding any possibility of the EO effect in our MO crystal. Open circles in Fig. 99.78 show the results of the above measurements in a form of the V dependence on the probe-beam wavelength. We observe a broad local maximum centered at 593 nm, which corresponds to the earlier measured position of the exciton resonance in $Cd_{0.38}Mn_{0.62}Te$, although the significant (~6-nm) spectral width of our femtosecond probe

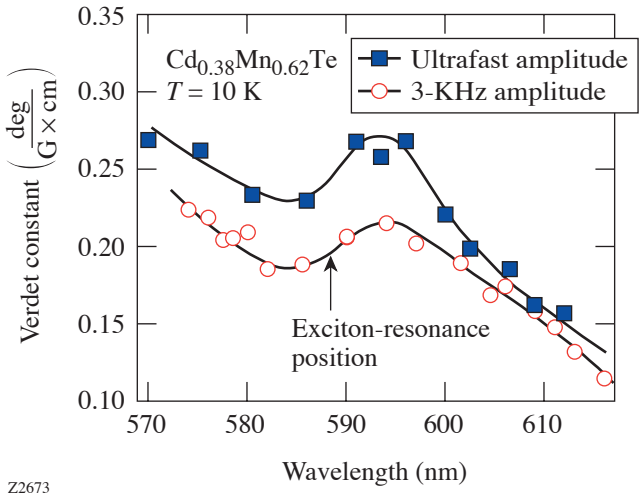

Figure 99.78
Spectral dependences of the transient (solid squares) and static (open circles) Verdet constant for a $Cd_{0.38}Mn_{0.62}Te$ single crystal measured using subpicosecond current pulses generated by the LT-GaAs switch and 3-KHz ac excitation. Both measurements were performed at 10 K in the tunability range of our OPO. The arrow shows the position of the exciton resonance. Solid lines are guides to the eye.

pulses did not allow us to resolve the resonance structure in detail. The V value obtained at the 593-nm wavelength compares favorably to other MO materials reported in literature.[9] Finally, one can also notice the increase of V at the bandgap edge below 580 nm. Faraday rotation experiments are not practical in this range due to the strong light absorption; however, one could try to implement the Kerr-effect–type measurements. We will discuss the MOS technique based on the Kerr effect in a separate publication.

When the excitation pulses were applied to the LT-GaAs switch, a train of subpicosecond electrical pulses was generated and propagated along the CSL. These electrical pulses induced the transient magnetic-field component in the CSL that coupled to our MO crystal and rotated the polarization of the transmitted probe beam. A 1.1-ps-wide magnetic pulse transient recorded using our MOS system for the probe-beam wavelength of 595 nm (corresponding to the maximum V value in Fig. 99.78) is shown in Fig. 99.79. The pulse rise time, defined as the 0.9-to-0.1-amplitude time difference, was measured to be about 0.6 ps, and the decay time, obtained using exponential fittings, was 1.1 ps. The MOS signal amplitude scan, performed for different probe-beam wavelengths (closed squares in Fig. 99.78), showed that the transient V value followed the low-frequency Verdet constant data. The latter confirms that the transient shown in Fig. 99.79 is due to the MO effect in $Cd_{1-x}Mn_xTe$, based on the ultrafast Mn ion spin–spin interaction.[14] We note, however, that within the exciton resonance range, the transient V values are consistently ~30% larger than the static ones obtained using low-frequency excitation (open circles in Fig. 99.78). From the MOS transient signal-to-noise ratio, we estimated the sensitivity of our system as ~ 0.1 mA at 10 K. This resolution could be obtained after averaging 100 data scans with 0.3-s lock-in amplifier time constant.

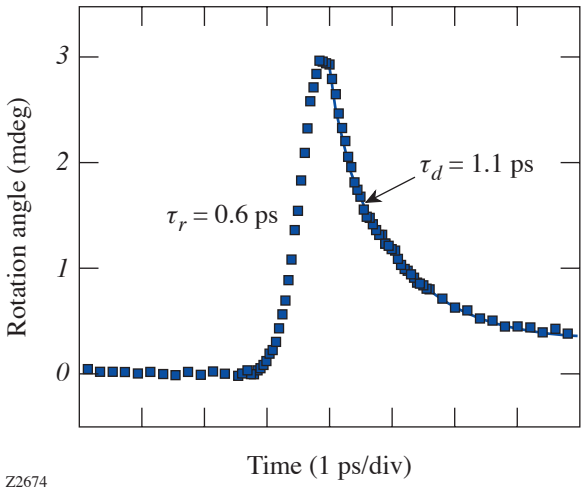

Figure 99.79
Time-resolved Faraday angle rotation as a function of time, measured using our MOS system. The probe-beam wavelength was 595 nm, and the experiment temperature was 10 K. Solid line is an exponential fit to the fall part of the signal.

To confirm the time dynamics of the MO effect in $Cd_{1-x}Mn_xTe$, we substituted the $LiTaO_3$ crystal for our MO crystal and performed the standard EOS testing at 10 K with the same LT-GaAs switch and CSL. The measured EOS response showed some additional oscillatory features due to apparent dielectric loading of the relatively large $LiTaO_3$ crystal, but the recorded MOS and EOS pulses exhibited essentially identical characteristic times. Since the response time of our $LiTaO_3$-based EOS system is 200 fs,[15] we can confirm that the response time of the cryogenic Faraday effect in $Cd_{1-x}Mn_xTe$ with $x > 0.5$ is of the order of a few hundred femtoseconds or less. The latter conclusion is in qualitative agreement with the data discussed in Ref. 14.

We have demonstrated subpicosecond dynamics of the Faraday effect in highly Mn-doped $Cd_{1-x}Mn_xTe$ at low temperatures and have implemented these crystals as MO transducers in the MOS system for time-resolved measurements of magnetic/current transients. The high sensitivity and subpicosecond temporal resolution of our MO sampler makes it practical for characterization of ultrafast current–driven (e.g., superconducting) devices and circuits. The presented sampler should also be very useful for testing the switching dynamics of spintronic logic elements. Finally, the $Cd_{1-x}Mn_xTe$ crystals should find applications as ultrafast MO modulators[18] for electrical-to-optical coupling of superconducting digital circuits.[19]

ACKNOWLEDGMENT

This work has been funded by the NSF grant DMR-0073366 and the ONR grant N00014-00-1-0237. Additional support was provided by the NYSTAR grant through the Center for Electronic Imaging System at the University of Rochester.

REFERENCES

1. M. M. Feiginov, Nanotechnology **11**, 359 (2000).

2. J. Mateos *et al.*, Nanotechnology **14**, 117 (2003).

3. K. Likharev, Phys. World **10**, 39 (1997).
4. P. Bunyk, K. Likharev, and D. Zinoviev, Int. J. High Speed Electron. Syst. **11**, 257 (2001).
5. R. Adam, M. Currie, C. Williams, R. Sobolewski, O. Harnack, and M. Darula, Appl. Phys. Lett. **76**, 469 (2000).
6. D. H. Auston and M. C. Nuss, IEEE J. Quantum Electron. **24**, 184 (1988).
7. M. R. Freeman, J. Appl. Phys. **75**, 6194 (1994).
8. A. Y. Elezzabi and M. R. Freeman, Appl. Phys. Lett. **68**, 3546 (1996).
9. A. K. Zvezdin and V. A. Kotov, *Modern Magnetooptics and Magneto-optical Materials* (Institute of Physics Publishing, Bristol, England, 1997).
10. S. A. Wolf *et al.*, Science **294**, 1488 (2001).
11. J. K. Furdyna, J. Appl. Phys. **64**, R29 (1988).
12. P. A. Wolff, in *Semiconductors and Semimetals*, edited by J. K. Furdyna and J. Kossut, Diluted Magnetic Semiconductors, Vol. 25 (Academic Press, Boston, 1988), Chap. 10, pp. 413–454.
13. D. D. Awschalom *et al.*, Phys. Rev. Lett. **55**, 1128 (1985).
14. T. Dietl *et al*. Phys. Rev. Lett. **74**, 474 (1995).
15. X. Zheng, Y. Xu, R. Sobolewski, R. Adam, M. Mikulics, M. Siegel, and P. Kordoš, Appl. Opt. **42**, 1726 (2003).
16. R. Rey-de-Castro, "Ultrafast Optical Properties and Applications of $Cd_{1-x}Mn_xTe$ Semimagnetic Semiconductors," Ph.D. thesis, University of Rochester, 2004.
17. R. Adam, M. Mikulics, A. Förster, J. Schelten, M. Siegel, P. Kordo□, X. Zheng, S. Wu, and R. Sobolewski, Appl. Phys. Lett. **81**, 3485 (2002).
18. R. Sobolewski and J.-R. Park, IEEE Trans. Appl. Supercond. **11**, 727 (2001).
19. R. Sobolewski, Supercond. Sci. Technol. **14**, 994 (2001).

Simulation of Submicronmeter Metal–Semiconductor–Metal Ultraviolet Photodiodes on Gallium Nitride

Introduction

Due to the high steady-state peak electron velocity[1–4] in gallium nitride (GaN) and the simplicity of fabrication, metal–semiconductor–metal photodiodes (MSM-PD's) fabricated on GaN have attracted intensive research effort. High-bandwidth, monolithic MSM devices have already been demonstrated.[5–8] Both Monte Carlo simulations[9] and experimental measurements[10] have shown that the intrinsic response time of the GaN MSM-PD's could be as fast as a few picoseconds. For practical applications, however, it is necessary to integrate the device into a fast package so that the photogenerated signal can be coupled out to standard timing instruments, such as a fast oscilloscope or a readout circuit. The packaging process will inevitably introduce a parasitic effect that limits the high-frequency performance of the devices. Our previous experimental results[5] showed the dominant role of the packaging fixture. To identify the performance-limiting factors and to design MSM-PD's with a required bandwidth and responsivity, it is essential to examine the dynamic behavior of the integrated unit including the photodiode and the packaging circuit.

In MSM-PD's, there are several design considerations in trying to improve their speed of response. Decreasing the interelectrode spacing has the beneficial effect of decreasing carrier-transit time (which decreases the response time), at the cost of an increase in the device capacitance (which increases the response time). To reduce the device capacitance, one can reduce the area of the interdigitated fingers. This requires a tighter focusing of the incident beam. Shrinking the total detector area would also increase the current density; thus the maximum total charge that can be delivered to the processing electronics must decrease. As a result, it is necessary to understand the behavior of UV MSM-PD's under a wide range of illumination levels. The transient behavior of infrared MSM-PD's subjected to optical pulse energies ranging from 0.01 to 316 pJ was reported recently.[11] The pulse broadening under high optical energy was attributed to the space-charge screening effect, which was studied in Refs. 12 and 13 for GaAs. However, theoretical simulations and experimental studies of the screening effect in GaN MSM-PD's under high illumination conditions have not appeared in the literature. This effect is part of our study and will be discussed in detail below.

Simulation

The MSM device with 0.3-μm feature size and the broadband circuit to be simulated are the same as reported previously[5] (see Fig. 99.80). The circuit has a strip-line structure with the switch attached on a G-10 board. At first, we tried to model the entire assembly by an equivalent circuit with the lumped electric elements and then solve the circuit by using *SPICE*. This approach is simple and straightforward. The photocurrent, however, must be input as a parameter rather than calculated directly. Therefore the model cannot explore the opto-electronic process that occurs under optical illumination. Furthermore, this method cannot monitor the circuit effect and space-charge screening effect as discussed below.

To better understand the transient behavior of the device, we developed a more-complicated numerical simulation using a distributed-circuit approach.[14–16] Similar simulations have been used to describe the electric field in high-voltage photoconductive switches, although this is the first time they have been applied to an MSM photodiode. Instead of tracking the detailed carrier dynamics,[12,13] we assume that the optically generated electron-hole pairs are swept out (with negligible recombination) at rates determined by the field-dependence velocities.[1] The transient current and voltages are computed simultaneously and dynamically to produce the device temporal response. A major advantage of this approach is that it allows us to conveniently include the effect of the packaging circuit.

The simulation assumes a transverse electromagnetic wave propagation. This is an approximation that ignores modal dispersion and the discontinuity in the dielectric constant between the strip line and the air. The entire circuit, including the charge source, the transmission line, the semiconductor, and the load, was sliced into 1024 small cells along the equipotential lines. Each cell is modeled by discrete elements: resistors, capacitors, and inductors (see Fig. 99.80; k is an even number) whose values are computed from the cell geometry.[17]

All of the cells have identical configurations and are linearly coupled to the two adjacent neighbors; therefore, we need to focus on solving only one such cell, and then the equations for the entire circuit can be mapped out. In each cell, only two unique nodes are considered: an "even" node and an "odd" node, as shown in Fig. 99.81, where R_t is the resistance of the small cell, the value of which depends on the material properties of the location and is photosensitive in the active area of the device; C_s is the capacitance across the resistance; C_g is the capacitance between the cell and the ground; L_s is the inductance of the cell; and V_k is the potential at each node. When the Kirchhoff's law of current continuity is applied to these nodes, the equations of voltage and current can be obtained.

Several assumptions were made in deriving the circuit equations: (1) The Schottky contact in MSM-PD's is noninjecting; that is, no electron can flow from metal cell to semiconductor cell on the boundary between materials. (2) The gap between fingers is fully depleted, resulting in high resistivity; this is justified by noting that the flatband[18] voltage across the gap is calculated to be 0.25 V, much lower than the applied bias voltage of 5 V. (3) The optical illumination is spatially uniform across the finger spacing since the size of the spacing (0.3 μm) is much smaller than that of the active area (50 μm) and the focal spot (~10 μm). (4) The 2-D dependence of the electric field is neglected, and the electric field is uniform across the finger gap of the devices. This 1-D simulation appears to be a good approximation in estimating the device response time.

It is worthwhile to note that a more fundamental approach detailing the carrier dynamics has been done previously[12,13] using a numerical Poisson solver. In the simplified, distributed-circuit approach presented here, the entire package was modeled by discrete circuits. While it is straightforward to describe the rest of the circuit, it took some effort to build the accurate model for the interdigitated MSM photodiode so that

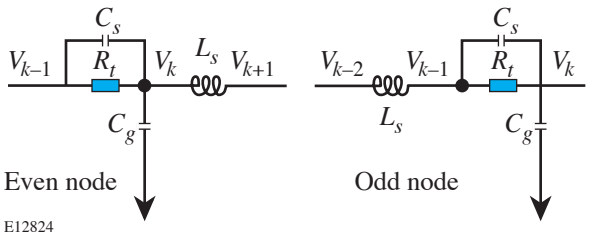

Figure 99.81
"Even" node and "odd" node of the lumped-element circuit. Here, R_t is the resistance of the small cell, C_s is the capacitance across the resistance, C_g is the capacitance between the cell and the ground, L_s is the inductance of the cell, and V_k is the potential at each node.

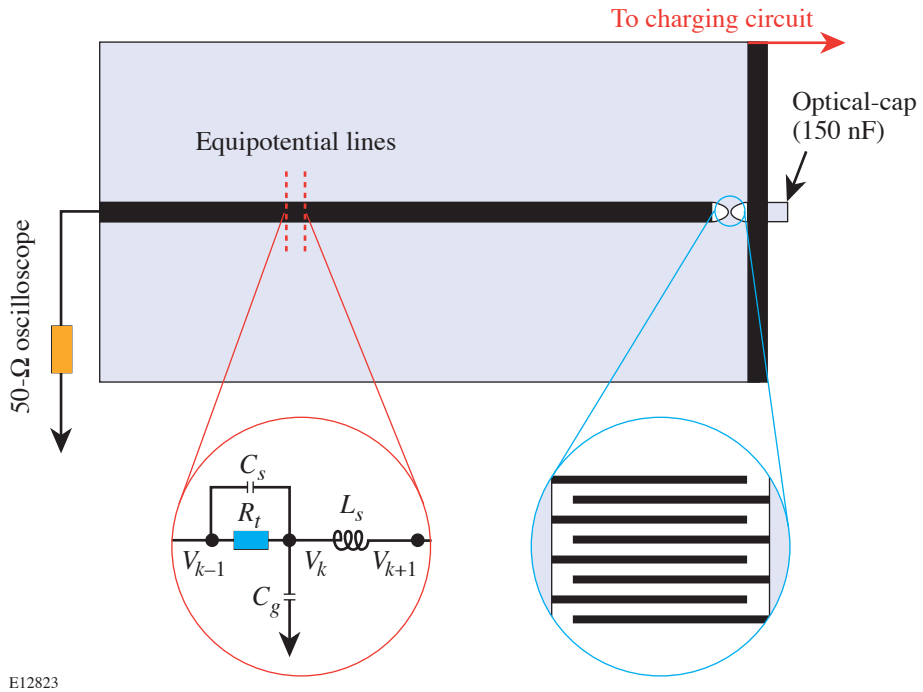

Figure 99.80
Top view of the broadband circuit designed for the MSM photodetectors. The one-dimensional transmission line was sliced into 1024 small cells along the equipotential lines and modeled as a lumped-element circuit as shown in the figure. To avoid an abrupt width change, a pad with a calculated curve tapers the transmission line down to the active area.

the 2-D structure can be degraded to a 1-D model. In the active region of the MSM photodiode, the gap between the finger electrodes was sliced into ten cells along the equipotential lines that follow the meandering shape of the fingers. When free carriers are generated optically in the gap, the carriers will move from one cell to the adjacent one under the external electric field. Transport perpendicular to the gap is ignored. Hence the time-dependent conductivity is 1-D between the finger electrodes. One concern about the 1-D model is that the electromagnetic waves may propagate along the fingers in real devices; however, the calculations show that the longest time for the electromagnetic wave to travel through the entire meander is less than 14 ps. This is small compared with the 40-ps rise time as shown below in the simulation results. Therefore, it is reasonable to ignore this propagation along the fingers and assume that the signal will travel from one finger electrode to the other finger electrode only so that the 1-D model is justified. The approach has an important advantage in that it allows the packaging circuit to be included in computing the response of the entire device assembly. A direct comparison with experimental results can then be made.

With the above assumptions, we can linearize the expressions for the currents and voltages in each cell. While the resistance in the metal transmission line is constant, the resistance in the semiconductor, which is a product of resistivity and length of the cell divided by the cross section of the cell, varies dynamically. The resistivity is calculated from the field-dependent expression

$$\rho(x,t)=\frac{1}{e\left[n(x,t)\mu_e(E)+p(x,t)\mu_h(E)\right]}(\Omega\,\mathrm{cm}), \qquad (1)$$

where the carrier densities n and p are calculated from the local optical intensity, absorption rate, and transport. The electron mobility μ_e, a function of electric field, is given by Ref. 1, while the hole mobility μ_h is fixed at 30 cm^2/Vs. After optical illumination, the electrons and holes separate under the influence of the applied electric field and are collected by electrodes. The changing electric field and carrier densities cause the resistance of the cell to evolve in time. This change of the resistance is coupled out to other cells by changing the values of the voltage and current in each node. The transient response of the detector is then computed according to the distributed-circuit model.[14]

With $V(t)$ as the voltage across the inductor at time t and $V(t')$ as the voltage at the previous time t', the currents at time t and t' in the inductor can be obtained by integrating $V(t)$ and $V(t')$ with the first-order Simpson's rule

$$\frac{1}{2}\left[V(t)+V(t')\right]=L_s\frac{dI}{dt}\approx\frac{L_s\left[I(t)-I(t')\right]}{\Delta t}, \qquad (2)$$

where L_s is the inductance and $\Delta t = t - t'$. Similarly, the current at time t in the capacitor can be written as

$$I(t)=C\frac{V(t)-V(t')}{\Delta t}, \qquad (3)$$

where C is the capacitance of a section of line of length Δx. In the simulation, the even nodes and odd nodes each generate a different set of equations. By applying Kirchhoff's law of current continuity, the circuit equation for the even nodes is

$$\begin{aligned}
&V_k\left(\frac{C_g}{\Delta t}+\frac{\Delta t}{2L_S}+\frac{C_s}{\Delta t}+\frac{1}{R_t}\right)+V_{k+1}\left(-\frac{\Delta t}{2L_S}\right)\\
&+V_{k-1}\left(-\frac{C_s}{\Delta t}-\frac{1}{R_t}\right)\\
&=I'_k+V'_k\left(\frac{C_g}{\Delta t}-\frac{\Delta t}{2L_S}+\frac{C_s}{\Delta t}\right)+V'_{k+1}\left(\frac{\Delta t}{2L_S}\right)\\
&+V'_{k-1}\left(-\frac{C_s}{\Delta t}\right), \qquad (4)
\end{aligned}$$

where $k = 2n$ (n changes from 1 to 1024), symbols with prime mean the variables at previous t', and symbols without prime mean the variables at present time t. Similarly, for the odd nodes we have

$$V_{k-1}\left(\frac{\Delta t}{2L_S}+\frac{C_s}{\Delta t}+\frac{1}{R_t}\right)+V_{k-2}\left(-\frac{\Delta t}{2L_S}\right)$$

$$+V_k\left(-\frac{C_s}{\Delta t}-\frac{1}{R_t}\right)$$

$$=-I'_{k-1}+V'_{k-1}\left(-\frac{\Delta t}{2L_S}+\frac{C_s}{\Delta t}\right)+V'_{k-2}\left(\frac{\Delta t}{2L_S}\right)$$

$$+V'_k\left(-\frac{C_s}{\Delta t}\right). \tag{5}$$

The above questions are complex; however, they can be written in matrix format as follows:

$$\begin{pmatrix} A_1 & B_1 & & & & & & \\ C_2 & A_1 & B_2 & & & 0 & & \\ & \bullet & \bullet & \bullet & & & & \\ & & \bullet & \bullet & \bullet & & & \\ & & & \bullet & \bullet & \bullet & & \\ 0 & & & & \bullet & \bullet & B_{N-1} & \\ & & & & & C_N & A_N & \end{pmatrix}\begin{pmatrix} V_1 \\ V_2 \\ \bullet \\ \bullet \\ \bullet \\ \bullet \\ V_N \end{pmatrix}=\begin{pmatrix} -I'_1 \\ I'_2 \\ \bullet \\ \bullet \\ \bullet \\ \bullet \\ I'_N \end{pmatrix}$$

$$+\begin{pmatrix} A'_1 & B'_1 & & & & & & \\ C'_2 & A'_2 & B'_2 & & & 0 & & \\ & \bullet & \bullet & \bullet & & & & \\ & & \bullet & \bullet & \bullet & & & \\ & & & \bullet & \bullet & \bullet & & \\ & 0 & & & \bullet & \bullet & B'_{N-1} & \\ & & & & & C'_N & A'_N & \end{pmatrix}\begin{pmatrix} V'_1 \\ V'_2 \\ \\ \\ \\ \\ V'_N \end{pmatrix}, \tag{6}$$

where N is equal to 2048 and the matrix elements are from the coefficients of the variables in Eqs. (4) and (5) and are defined as

$$A_i=\frac{C_g}{\Delta t}+\frac{\Delta t}{2L_S}+\frac{C_S}{\Delta t}+\frac{1}{R_t}$$

$$B_i=-\frac{\Delta t}{2L_S}$$

$$C_i=-\frac{C_S}{\Delta t}-\frac{1}{R_t}$$

$$\text{for } i=2n, \tag{7}$$

$$A'_i=\frac{C_g}{\Delta t}-\frac{\Delta t}{2L_S}+\frac{C_S}{\Delta t}$$

$$B'_i=\frac{\Delta t}{2L_S}$$

$$C'_i=-\frac{C_S}{\Delta t}$$

and

$$A_i=\frac{\Delta t}{2L_S}+\frac{C_S}{\Delta t}+\frac{1}{R_t}$$

$$B_i=-\frac{C_S}{\Delta t}-\frac{1}{R_t}$$

$$C_i=-\frac{\Delta t}{2L_S}$$

$$\text{for } i=2n-1. \tag{8}$$

$$A'_i=-\frac{\Delta t}{2L_S}+\frac{C_S}{\Delta t}$$

$$B'_i=-\frac{C_S}{\Delta t}$$

$$C'_i=\frac{\Delta t}{2L_S}$$

The initial values of current and voltage were determined from the dc-biased dark condition. These initial values were placed in matrix Eq. (6). The new values of voltage can then be solved. With the help of Eq. (2), the new values of current can be solved as well. Therefore, by iteration, the time response of the circuit can be numerically computed.

Results and Discussion

In simulations, the model parameters were chosen to match the actual MSM-PD's previously tested.[5] The active area was $50 \times 50\ \mu m^2$, and the finger width and spacing were both 0.3 μm. For calculating the illumination on the detectors, we selected a Gaussian pulse with a full width at half maximum (FWHM) of 500 fs at a wavelength of 270 nm. Different illumination conditions with optical energies ranging from 0.01 pJ to 1 nJ were simulated. The results for optical pulse energies of 1, 6, 10, and 20 pJ are plotted in Fig. 99.82 with normalized amplitude. When the illumination level was lower than 1 pJ, the electric impulses delivered to the 50-Ω load had similar pulse shapes. The rising edge was dispersed by the transmission line and was typically 40 ps, which is longer than the optical pulse. The oscillations after the main peak were caused by the impedance discontinuities in the package. The shortest pulse width was 48 ps, which is a little shorter than our measured result of 60 ps for the same device as reported in Ref. 5. We attribute this discrepancy between simulation and measurement to parasitic effects not included in the simulation, such as the connector discontinuities and the fact that in a microstrip transmission the field is not truly transverse electromagnetic.

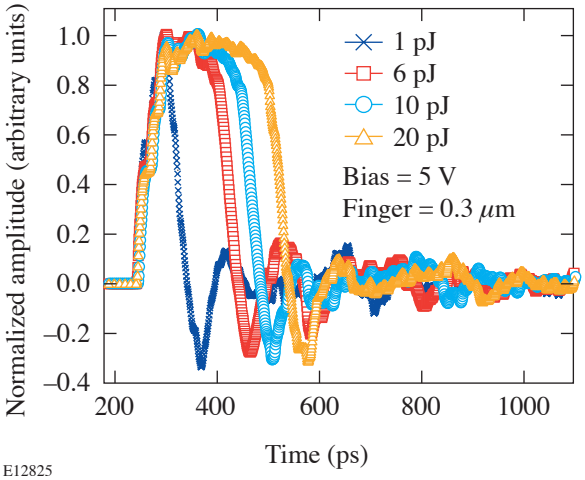

Figure 99.82
Simulated time responses of the detectors with different optical pulse energies of 1 pJ (×), 6 pJ (square), 10 pJ (circle), and 20 pJ (triangle) under 5-V bias. The amplitudes of the signal have been normalized to the peak values.

The most-distinguishing feature of the results is that the pulse width broadens markedly as the optical pulse energy increases. This trend is the same as observed in experiments.[5] This increase in pulse duration can be attributed to the screening of the dark electric field between the finger electrodes by the space-charge field induced by the separation of the photogenerated electrons and holes. Qualitatively, at high excitation intensity, carrier densities of both electrons and holes increase to the point when the normally depleted region of the detector now has a substantial conductivity that temporarily decreases the electric field. As a result, the carriers are now swept out at a lower speed, hence the slower detector response. This effect is essentially the same as was found in GaAs photodetectors reported in Refs. 12 and 13.

Comparison with Experiments

The pulse broadening, under high-level illumination, was observed in both experiments[5] and simulations. In this section the pulse width's dependence on the total optical energy will be compared for the two cases. In our simulations, the external quantum efficiency was assumed to be 100%; that is, each photon generates a free electron and hole pair. To compare the simulated and experimental results at the same illumination level, it is necessary to modify the optical pulse energy in experiments according to the measured external quantum efficiency, defined as the ratio of the number of the electron-hole pairs and the incident photons. The number of electrons generated by the optical pulse was obtained by integrating the photoelectric current; the number of photons in each optical pulse was determined by dividing the measured average laser power by the repetition rate (82 MHz for a Ti:sapphire laser) and the energy of each photon. In the case of the highest input of 391 pJ, η_{ex} was determined to be 1.77%. This factor was used to scale the experimental data. In Fig. 99.83, the simulated and measured FWHM's after the scaling are plotted together. With a single scaling factor, the experimental and simulated results are in close agreement.

Analysis of the data shows that the pulse width remains approximately constant until the optical energy exceeds a certain level (around 0.4 pJ) for both simulated results and scaled-experiment results. We can compute the photogenerated charge and compare its value to the stored charge in the device as follows: the capacitance of the MSM structure calculated to be 0.182 pF,[19] corresponding to a stored charge

of 9.1×10^{-13} C (or, about 5.7×10^{6} electrons) given 5-V bias. At an optical energy of 0.4 pJ, the depletion region would have a total carrier density equal to about 10% of the stored charge. This amount appears to be the threshold of the onset of the space-charge effect.

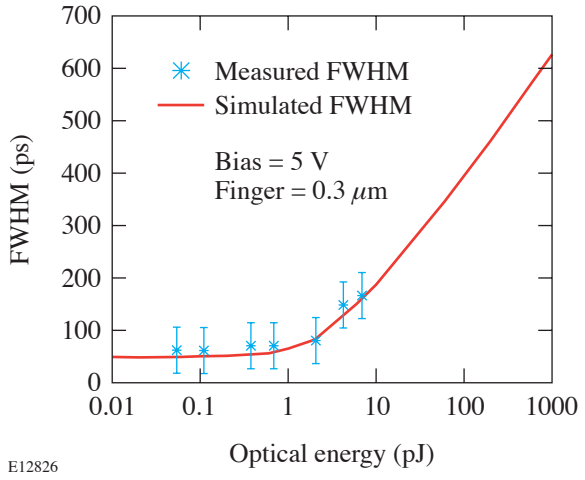

Figure 99.83
Comparison of FWHM's from stimulation and experiment. To compare them in the same illumination level, a single factor was used to scale down the optical energy in experiment.

Summary

In summary, a GaN interdigitized-finger MSMPD with 0.3-μm finger width and spacing was packaged with a specially designed fast circuit. The entire assembly was simulated by a simplified, distributed-circuit approach so that the circuit effect can be conveniently monitored. The space-charge screening effect causing the broadening of the impulse response was discussed and compared with experimental results. After a single scaling factor of external quantum efficiency, theory and experiment were brought to a close agreement.

ACKNOWLEDGMENT

This work was supported by the U.S. Department of Energy Office of Inertial Confinement Fusion under Cooperative Agreement No. DE-FC52-92SF19460, the University of Rochester, and the New York State Energy Research and Development Authority. The support of DOE does not constitute an endorsement by DOE of the views expressed in this article.

REFERENCES

1. U. V. Bhapkar and M. S. Shur, J. Appl. Phys. **82**, 1649 (1997).
2. J. D. Albrecht *et al.*, J. Appl. Phys. **83**, 4777 (1998).
3. J. Kolnik *et al.*, J. Appl. Phys. **78**, 1033 (1995).
4. B. Gelmont, K. H. Kim, and M. Shur, J. Appl. Phys. **74**, 1818 (1993).
5. J. Li, W. R. Donaldson, and T. Y. Hsiang, IEEE Photonics Technol. Lett. **15**, 1141 (2003).
6. J. C. Carrano *et al.*, J. Electron. Mater. **28**, 325 (1999).
7. J. C. Carrano *et al.*, Appl. Phys. Lett. **73**, 2405 (1998).
8. D. Walker *et al.*, Appl. Phys. Lett. **74**, 762 (1999).
9. R. P. Joshi, A. N. Dharamsi, and J. McAdoo, Appl. Phys. Lett. **64**, 3611 (1994).
10. J. Li *et al.*, Appl. Phys. Lett. **84**, 2091 (2004).
11. K. Aliberti *et al.*, Appl. Phys. Lett. **80**, 2848 (2002).
12. S. V. Averine and R. Sachot, IEE Proc., Optoelectron. **147**, 145 (2000).
13. S. V. Averine and R. Sachot, Solid-State Electron. **44**, 1627 (2000).
14. L. Mu and W. R. Donaldson, in *Proceedings of the Ninth IEEE International Pulsed Power Conference*, edited by K. Prestwich and W. Baker (IEEE, New York, 1993), pp. 629–632.
15. L. E. Kingsley and W. R. Donaldson, IEEE Trans. Electron Devices **40**, 2344 (1993).
16. W. R. Donaldson and L. Mu, IEEE J. Quantum Electron. **30**, 2866 (1994).
17. B. C. Wadell, *Transmission Line Design Handbook* (Artech House, Boston, 1991).
18. S. M. Sze, D. J. Coleman, Jr., and A. Loya, Solid-State Electron. **14**, 1209 (1971).
19. Y. C. Lim and R. A. Moore, IEEE Trans. Electron Devices **ED-15**, 173 (1968).

Overpressure Contact Printing and Its Applications in the Fabrication of Arrays of Magnetic Rings

The elastomeric property of poly(dimethylsiloxane) (PDMS) allows stamps made of this polymer to be widely used in replicating patterns with high fidelity through the conformal contact between the substrate and the stamp surfaces.[1–3] This unique property is also the origin of stamp deformations. Although the conformal contact is preferred in contact printing, the application of stamp deformations in nanofabrication is severely under investigated. Xia *et al*. were able to create patterns with size-reduced features by intentionally applying external forces to laterally deform the stamps during contact printing.[4] This article shows that not only can size reductions be achieved by applying pressure normal to the substrates during contact printing, but also new patterns different from those features on the stamps can be generated by this patterning approach. This method is referred to as overpressure contact printing (oCP). It is particularly worthwhile to mention that oCP is unique in the fabrication of new features while having the advantage of miniaturization.

As indicated, overpressure contact printing relies on the deformation of PDMS stamps. The mechanical properties of PDMS and the behaviors of PDMS stamps have been examined recently.[5,6] Delamarche *et al*. showed that the height-to-width ratios—the aspect ratios—of the relief structures on PDMS stamps need to be between about 0.2 and 2 in order to obtain defect-free printing. If the aspect ratio of the PDMS feature is too high, the roof of the feature may come into contact with a substrate under its own weight or under an external pressure. When the aspect ratios are too low, the relief structures are not able to withstand the stamp weight. The compressive forces of printing and the adhesion force between the stamp and the substrate can both cause the similar result.[5,7,8] This article will briefly describe the theoretical analysis of this deformation of PDMS.[8]

Figure 99.84(a) shows a basic geometry of a stamp that consists of periodic relief line features with height of h, feature width of $2w$, and trench width of $2a$. When pressure is applied to the stamp, several deformations occur, including in-plane lateral expansion, "sagging" of the trench, and relief feature from compression by the external stress. The in-plane expansion of the stamp could be minimized if a stiff backplane such as a glass plate on the elastomer is used since the Young's modulus of glass is much greater than that of PDMS. Because the strength of stress applied is typically of the order of the Young's modulus of PDMS, the Poisson expansion of the stamp bonded to the glass backplane can be several orders of magnitude lower than that of a stamp without a backplane and negligible.[8]

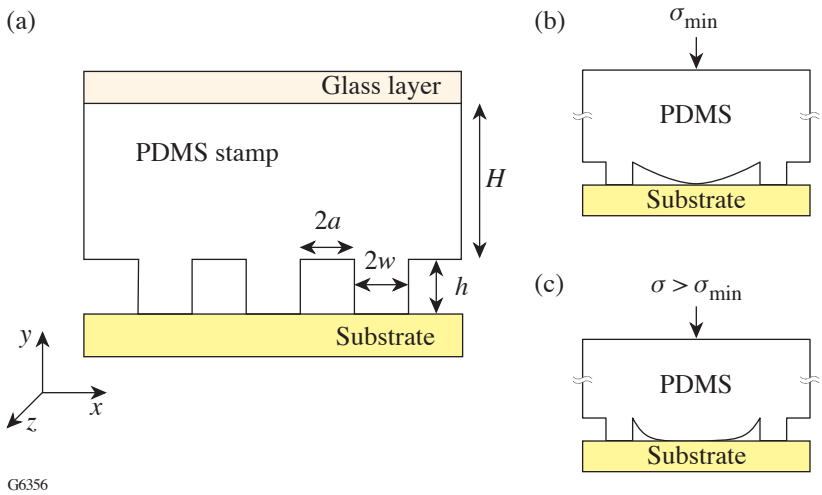

Figure 99.84
Illustrations of (a) the basic geometry of a PDMS stamp and stamps deformed into contact with substrates under (b) required minimum and (c) excess pressures.

Most elastomers are rubber elastic and incompressible with Poisson's ratio v of approximately 0.5. The Young's modulus of PDMS depends strongly on the mixing ratios between prepolymer precursor and curing agent and the preparation conditions, such as curing time and temperature. The Young's modulus (E) and density of the PDMS material with different mixing ratios have been studied by examining the deflection of a single-side clamped PDMS cantilever beam.[6] To keep the mechanical properties of the PDMS consistent, a mixing ratio of 10:1 between the polymer and curing agent was used along with a curing temperature of 70°C overnight for all the stamps tested in this work. The Young's modulus of PDMS stamps prepared at these conditions is ~0.75 MPa as indicated by Armani *et al*.[6] For a qualitative analysis, the height of the stamp backbone is neglected because it is normally much greater than the height of the relief features, and the amount of pressure from the weight of the stamp is negligible as compared to the amount of pressure applied. With these assumptions, the model for promoted contact between the roof and substrates under external stress [Fig. 99.84(b)] can be simplified as follows:[8]

$$V_{\max} = \frac{4\sigma_{\min}}{\pi E^*}(w+a)\cosh^{-1}\left\{\sec\left[\frac{w\pi}{2(w+a)}\right]\right\}, \qquad (1)$$

where $V_{\max}$ is the maximum displacement of the roof by an applied minimum external stress $\sigma_{\min}$ and $E^* = E\Big/\left(1-v^2\right)$. All variables in the equation are known except external stress σ, which can be varied to give different degrees of contacts between the roof and the substrate [Fig. 99.84(c)].

This article further demonstrates the application of the oCP technique in creating FePt magnetic ring and anti-ring structures from microwell patterns of $Pt@Fe_2O_3$ nanoparticles. We are particularly interested in making arrays of these magnetic structures because such patterns are candidates for magnetic random access memory (MRAM).[9] In MRAM, it requires a reproducible switching mechanism from one cycle to the next. In this context, flux closure magnetic elements are favorable as compared to linear magnetic elements because of less dependence on the edge domain effect. For linear elements, the randomly magnetized edge domains form at the flat edges, which can prevent repeatable magnetic switching. On the contrary, the circular disks and rings with flux closure magnetization are more sustainable to edge roughness and, therefore, are suitable for device fabrication. In magnetic disks, however, a center vortex can form, and vortex displacement may lead to an irreproducible switching. A ring-shaped magnetic element can form a stable flux closure magnetization without the central vortex because of the geometry confinement of the ring.[9] A vertical magnetoresistive random access memory based on ring elements has been proposed recently.[9]

Nano-rings have been fabricated by *e*-beam lithography or nanoimprinting.[10–12] Although *e*-beam lithography can create ordered arrays of nano-rings with controllable diameter and thickness, the process is usually cumbersome and inaccessible to the majority of researchers. More recently, Scott *et al*. have successfully fabricated ordered arrays of magnetic rings by using controlled dewetting of polymeric percursors.[13] This technique is versatile and able to create ordered ring arrays of iron- and cobalt-containing polymers. Upon thermal treatment, the polymers can decompose and form magnetic ceramics. The combined dewetting and pyrolysis processes tend to lead, however, to the formation of local organization of the magnetic nanoparticles within the bands, while the continuity is pivotal for the rings to exhibit the unique flux closure magnetization mode. Here, an alternative technique to fabricate nano-rings in a controlled fashion using oCP is presented. The capability of the oCP technique is illustrated using self-assembled monolayers (SAM) on gold. The application of this method in making arrays of FePt rings from pLB films[14] of 4-nm $Pt@Fe_2O_3$ core–shell nanoparticles[15] is then described.

Gold substrates used in this research were made by depositing a 45-nm-thick gold layer onto silicon wafers using an *e*-beam evaporator. The ink was hexadecanethiol in an ethanol solution (~1 mM).[2] The PDMS patterns were replicated from photoresist (Shipley 1813) patterns on silicon following the standard procedures.[16] The height of the photoresist features made from this photoresist is expected to be 1.3 μm and was examined using a tapping-mode atomic force microscope (AFM, Digital Instrument, Nanoscope IIIa). In a typical procedure, the gold substrates and stamps were first cleaned with ethanol and dried under a stream of N_2 gas. A small amount of ink solution was then applied on the stamp surface using a cotton tip. The excess thiol solution was washed away with ethanol and dried with N_2 gas for 2 min. The stamp was then placed in contact with the gold substrate. To ensure conformal contact between the stamp and the substrate, and contact between the roof of the features and the substrate surface, pressure (~0.3 MPa) was applied normal to the substrate surface by using an iron block (3.2 kg/cm^2) during printing. The size of the stamp was typically 1×1 cm^2. The unprotected gold regions were removed by an aqueous etching solution consisting of $K_3Fe(CN)_6$ (0.01 M), $K_4Fe(CN)_6$ (0.001 M), $K_2S_2O_3$ (0.1 M), and KOH (1 M). The optimized duration for etching away 45 nm of gold was about 8.5 min. The etched

substrates were washed thoroughly with ethanol and deionized water and dried with N_2.

The ability to pattern γ-Fe_2O_3 (Ref. 17) and $Pt@Fe_2O_3$ nanoparticles[15,18] using the patterned Langmuir–Blodgett (pLB) technique[14,15] has been demonstrated. Both monolayer and multilayer depositions of nanoparticles are possible using the pLB technique through a layer-by-layer approach. This pLB technique has been used to pattern $Pt@Fe_2O_3$ core–shell nanoparticle arrays of rings and anti-rings in conjunction with oCP. The experimental procedure is shown in Fig. 99.85. In a typical procedure of making nanoparticle patterns, designed multilayers of Langmuir films of ~4-nm $Pt@Fe_2O_3$ nanoparticles were transferred onto a PDMS stamp of microwell pattern (10 μm). The nanoparticle-coated stamp was then contact printed on a plasma-cleaned Si wafer at a pressure of ~0.3 MPa for 2–3 s. The initial printing (oCP) generated the anti-ring pattern of nanoparticles [Fig. 99.85(a)], while removing the particles from the centers of the roofs of the wells that made contact with the substrate. The stamp was then carefully released from the substrate and used for a second printing under a pressure of ~0.3 MPa and a stamping time of 10 s. Arrays of ring structures could be obtained from the second printing, which is referred to as extended oCP [Fig. 99.85(b)].

Field-emission SEM images were obtained using a LEO 982 microscope. Tapping-mode AFM and magnetic-force microscope (MFM) images were collected using a Digital Instrument Nanoscope IIIa microscope. The magnetic tips (MFMR) were purchased from Nanosensors. The cantilevers are coated with cobalt alloy (40 nm thick) on the tip side and aluminum (30 nm thick) on the detector side. The tip radii are typically less than 50 nm. The tips are magnetized using a permanent magnet (field strength: ~0.2 Tesla) prior to MFM imaging. MFM images were obtained using the interleave mode at a lift scan height of 50 nm.

To demonstrate the oCP technique, gold microstructures were created on silicon starting from SAM of thiolate on gold surfaces. In this case, the SAM acted as an etching resist layer. Several line patterns with various height/width aspect ratios have been tested. The physical dimensions and their corresponding aspect ratios of some of the relief line patterns on the PDMS stamps used in this project are listed in Table 99.V. These numbers have been obtained from SEM and AFM characterizations of the photoresist masters and the PDMS stamps (Fig. 99.86). In oCP, the roof of the stamp is intentionally deformed to promote the contact with the substrate [Fig. 99.84(b)]. The minimum amount of pressure σ_{min} required to make the initial contact between the roof of the stamp

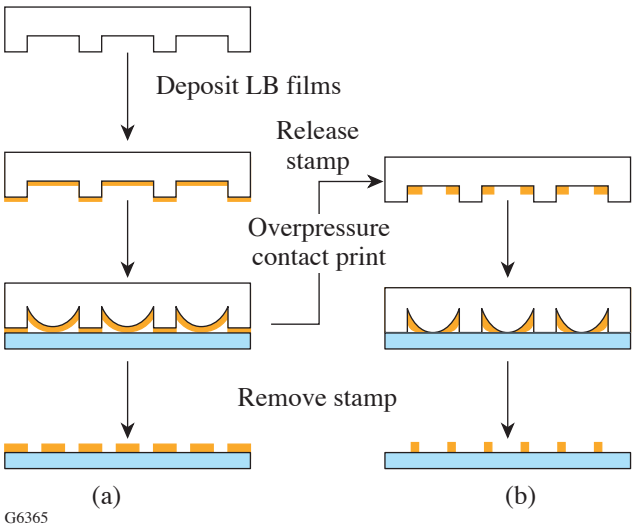

Figure 99.85
The experimental procedure for (a) overpressure and (b) extended overpressure contact printing.

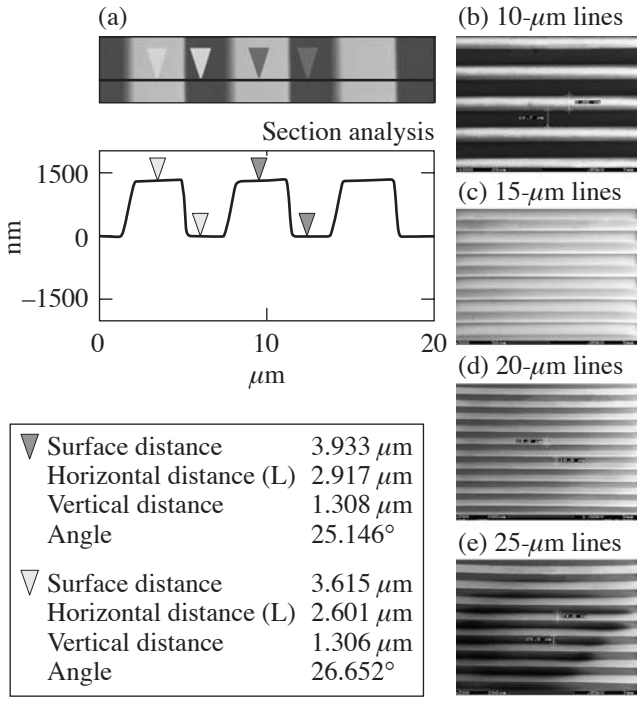

Figure 99.86
(a) AFM images and cross-section analyses showing the height (1.3 μm) of the PDMS stamps used in this work and [(b)–(e)] the SEM images of the photoresist masters of line patterns (10, 15, 20, and 25 μm) used in this study.

and the substrate was estimated for each of the stamps used based on the equation and data presented above; the results are listed in Table 99.V. The minimum pressures needed for the various stamps used were all below the Young's modulus of PDMS made at the current synthetic conditions (0.75 MPa)[6] and the amount of pressure applied (0.3 MPa). By applying pressure greater than the minimum, a higher degree of deformation can be obtained [Fig. 99.84(c)].

Figure 99.87 shows a series of SEM images of etched trenches on gold substrates fabricated by the oCP technique using the equally spaced line stamps presented in Table 99.V. The etched patterns consisted of arrays of gold lines separated by fine trenches (insets of Fig. 99.87). It is noticeable that the trenches between these lines were slightly uneven in width. This is most likely due to the unevenness of the weight when situated on top of the stamp. The contrast in SEM images of gold on silicon could also vary slightly. The light and dark line structures shown in Figs. 99.87(a) and 99.87(d) on both sides of the trenches were Au substrates resulting from the different etching resistance from the SAM's. During the initial oCP, the stamp was placed in intimate contact with the substrate where only the protruded structures on the stamp were able to contact the substrate [the lighter lines in Figs. 99.87(a) and 99.87(d)]. The roofs of the stamps were then brought into contact with the substrate by applying external pressure where coverage of thiolate on the Au substrate at the contact areas between the roof and the substrate (the darker lines) was different from feature regions. The difference between these two regions could be eliminated by controlling the etching conditions, as demonstrated in Figs. 99.87(b) and 99.87(c).

The sizes of the trenches made from each stamp of line patterns are summarized in Table 99.V. For a stamp with a roof height of 1.3 μm, the generated trenches have widths of about 1/10 or slightly less than 1/10 of those on the original patterns, when the applied pressure was ~0.3 MPa. For instance, a trench width of ~1 μm was fabricated by using a 10 × 10-μm–sized line stamp. The percentage of size reduction did not change

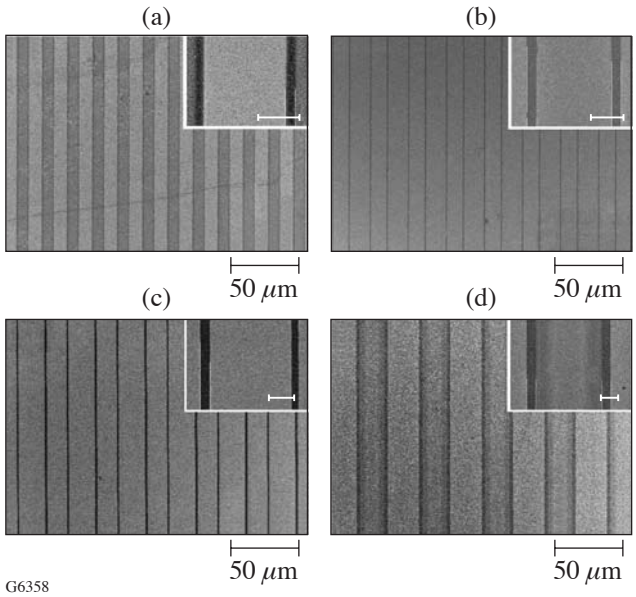

Figure 99.87
SEM images of trenches on surfaces of Au substrates fabricated using oCP from (a) 10 × 10-μm, (b) 15 × 15-μm, (c) 20 × 20-μm, and (d) 25 × 25-μm stamps. The scale bars in the insets are 5 μm.

Table 99.V: Dimensions and aspect ratios of the PDMS stamps of parallel lines used, the calculated minimum pressure for causing contacts between the roofs and substrates, the applied pressures, and the trench sizes fabricated in gold substrates using oCP.

Width (μm)		Height* h (μm)	Aspect ratio (h/w)	σ_{min}** (MPa)	$\sigma_{applied}$ (MPa)	Trench size fabricated (μm)		
Trench $2a$	Feature $2w$					Trench 1	Trench 2	Trench 3
10	10	1.30	0.13	0.13	0.3	0.99	1.09	1.0
15	15	1.30	0.087	0.87	0.3	1.01	1.30	1.2
20	20	1.30	0.065	0.065	0.3	1.48	1.80	1.6
25	25	1.30	0.052	0.052	0.3	2.31	2.32	2.3

*The height was estimated by AFM.
**Calculation was based on the equation given in the text.

substantially for patterns with line widths between 10 μm and 25 μm when the height of the roof was maintained the same and the features had height-to-width ratios varying between 0.052 and 0.13. All of these aspect ratios were smaller than the critical threshold value of 0.2 at which substantial external pressures is required to collapse the roof.[5] Our preliminary data indicate that the oCP technique can be extended to fabricate submicron and potentially nanometer-sized structures. Figure 99.88 shows an SEM image of submicron-sized trenches on the surface of the Au substrate fabricated from 1 × 1-μm line stamp with a height of ~0.5 μm using oCP technique. The average trench width was ~300 nm, although only a single trench per repeating unit has been produced. Careful design in stamp geometry is required for a systematic study in this size-reduced range.

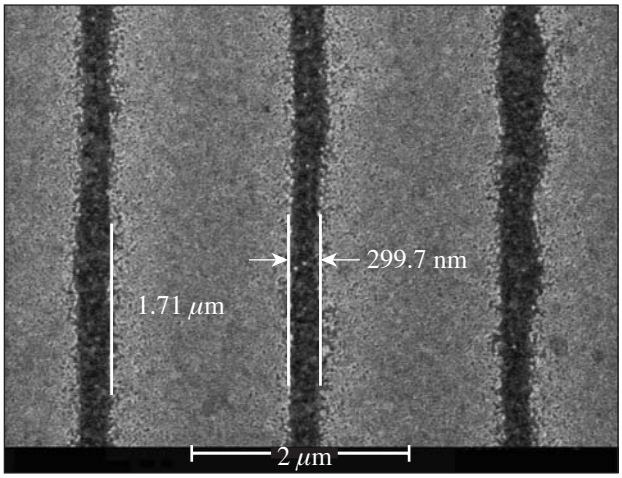

Figure 99.88
SEM image of submicron-sized trenches on the surface of Au substrate fabricated from 1 × 1-μm line stamps using oCP. Only a single trench per repeating unit has been produced.

The oCP technique was applied in patterning Pt@Fe_2O_3 core–shell nanoparticles to create anti-ring and ring structures. Langmuir films of ~4-nm Pt@Fe_2O_3 core–shell nanoparticles were transferred onto a PDMS stamp of well arrays (10 μm in well diameter with a well center-to-center distance of 15 μm). Overpressure and extended overpressure printing on plasma-cleaned Si substrates were used to obtain anti-ring and ring patterns, respectively. Figure 99.89 shows the SEM images of the single and arrays of fabricated anti-ring and ring patterns of Pt@Fe_2O_3 nanoparticles at different magnifications. The patterns were relatively uniform over a large area. The ring and anti-ring patterns obtained were not completely complimentary to each other. The average trench width of the anti-rings was ~1.3 μm, while the rings had an average line width of ~1.1 μm. Some of the rings were not completely closed loops or had variation in line width, which could be due to the rupture of the nanoparticulate films during contact printing. Similar defects at the inner and outer perimeters could be found for anti-ring patterns. This effect could be minimized by optimizing the thickness of the nanoparticulate films and using precise control in releasing the stamp.

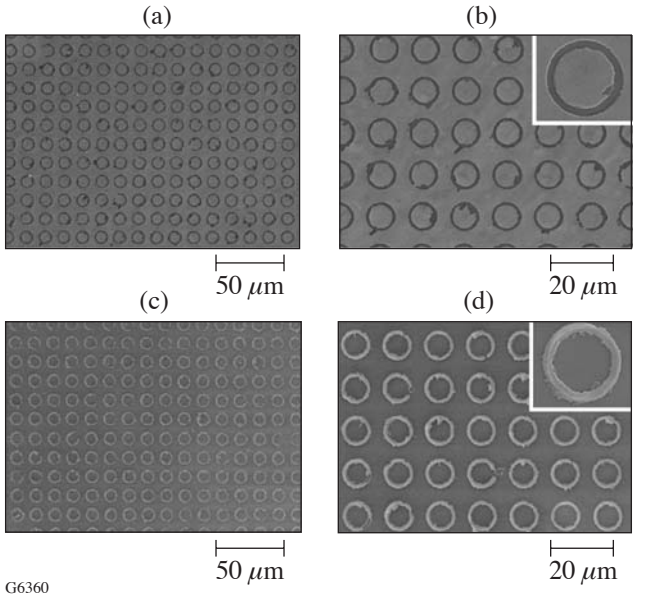

Figure 99.89
SEM images of [(a), (b)] anti-ring and [(c), (d)] ring patterns of Pt@Fe_2O_3 nanoparticles. Insets in (b) and (d) show the individual anti-ring and ring, respectively.

Tapping-mode AFM was used to examine the topology of the ring patterns made by extended oCP of Pt@Fe_2O_3 core–shell nanoparticles. Figures 99.90(a) and 99.90(b) show the three- (3-D) and two-dimensional (2-D) presentations of the ring structures of pLB films of Pt@Fe_2O_3 core–shell nanoparticles. The cross-section analysis shows that the rings had relatively uniform height [Fig. 99.90(c)]. The average height of the rings was ~285 nm, which corresponds to approximately 36 layers of nanoparticles. The number of layers in the rings was reasonable and further confirmed by measuring the height of six-layered unpatterned Pt@Fe_2O_3 nanoparticles to get an average thickness of a single particle layer. The AFM image and the cross-section analysis for an unpatterned six-layered film of Pt@Fe_2O_3 nanoparticles are shown in Fig. 99.91. The average thickness was 45 nm, which corresponds to a mono-

layer thickness of 7 to 8 nm. This value is reasonable since the 4-nm Pt@Fe_2O_3 core–shell nanoparticles are capped with oleic acid surfactants, which have a typical length of ~3 to 5 nm, depending on the configuration of hydrocarbon chains. The ruptured features observed in SEM were seen in the AFM image as well.

The patterned rings of Pt@Fe_2O_3 core–shell nanoparticles could be readily converted to face-centered tetragonal (fct) FePt alloy rings by thermal annealing in an atmosphere of 5% (*v*/*v*) hydrogen in argon at 450°C for 30 min.[15–19] Figures 99.92(a)–99.92(c) show the tapping-mode AFM images in 3-D and 2-D views and a cross-section analysis of the rings after the solid-state conversion. The average height of the patterns after annealing was approximately 140 nm. This value is reasonable considering the carbonization of surfactants and coalescence of nanoparticles upon annealing. The six-layered unpatterned film after the conversion had an average height of ~23 nm. Although the rings showed a large degree of shrinkage in height after the conversion, our cross-section analysis indicated that the line width of the ring did not show substantial broadening or shrinkage.

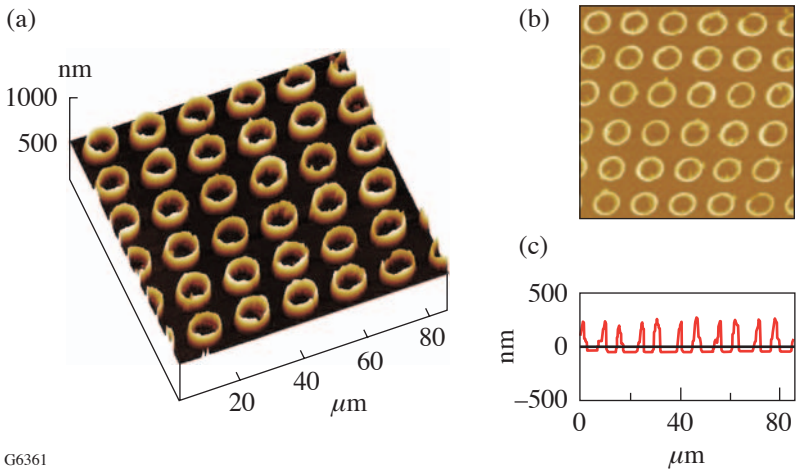

Figure 99.90
Tapping-mode AFM images of ring arrays of Pt@Fe_2O_3 nanoparticles: (a) 3-D representation, (b) 2-D representation, and (c) a cross-section analysis.

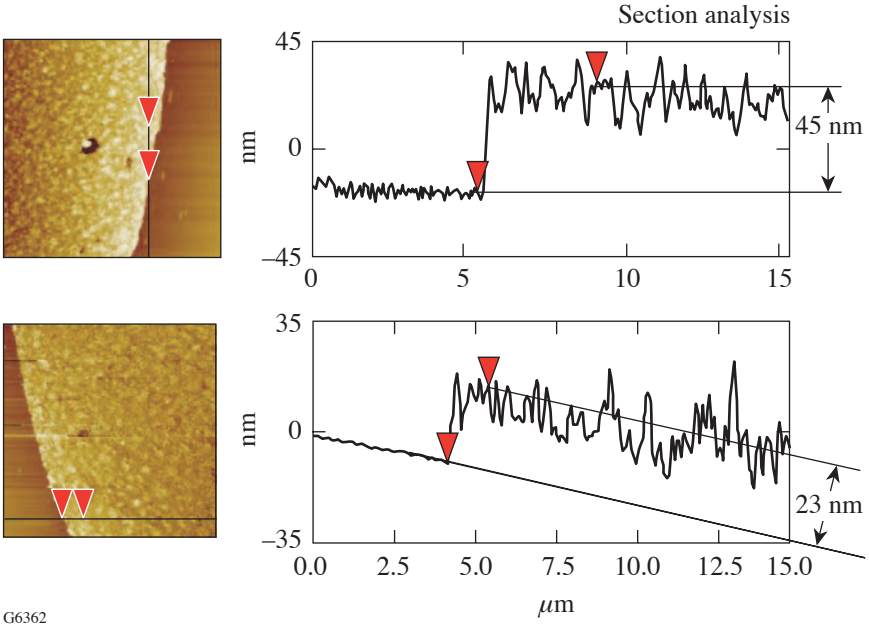

Figure 99.91
AFM images and their section analyses of six-layered unpatterned LB films of Pt@Fe_2O_3 core–shell nanoparticles (a) before and (b) after solid-state conversion.

MFM is a powerful tool to study magnetic properties of patterned structures.[20] In this technique, the topography contrast and magnetic interaction can be effectively separated by using tapping mode. As illustrated in Fig. 99.93(a), the phase contrast in an MFM image depends on the interaction of magnetic dipoles between the MFM tip coating layer and those of the substrate. Both low and high phase signals are possible for magnetic components on a substrate in comparison to nonmagnetic regions. The dark contrast indicates the magnetic repulsion between the tip and substrate, while the light-contrast region shows the attractive interaction. A relatively thick film was desired to have strong-enough magnetic signals for MFM characterization. Figure 99.93(b) shows the MFM study on the magnetization of the ring arrays characterized in Fig. 99.92. Both the tip and the substrate of FePt-magnetic ring on silicon have been premagnetized using a magnet (~0.2 to 0.25 Tesla). The magnetic response from the ring could be clearly visualized in the MFM image. The dark contrast indicated that the magnetic layer on the tip and the ring patterns repelled each other, which suggests that they were magnetized in the same direction.

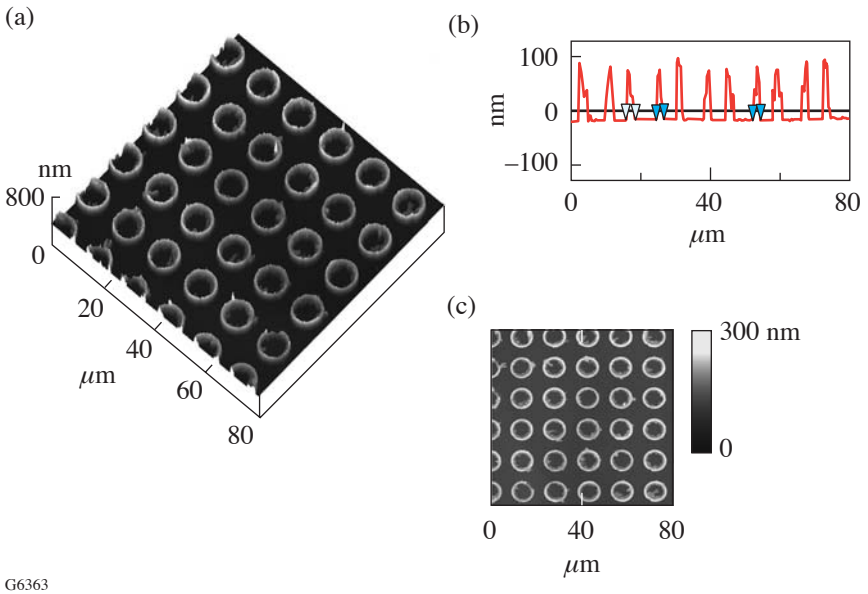

Figure 99.92
[(a)–(c)] Tapping-mode AFM images of FePt rings: (a) 3-D representation, (b) 2-D representation, and (c) cross-section analysis.

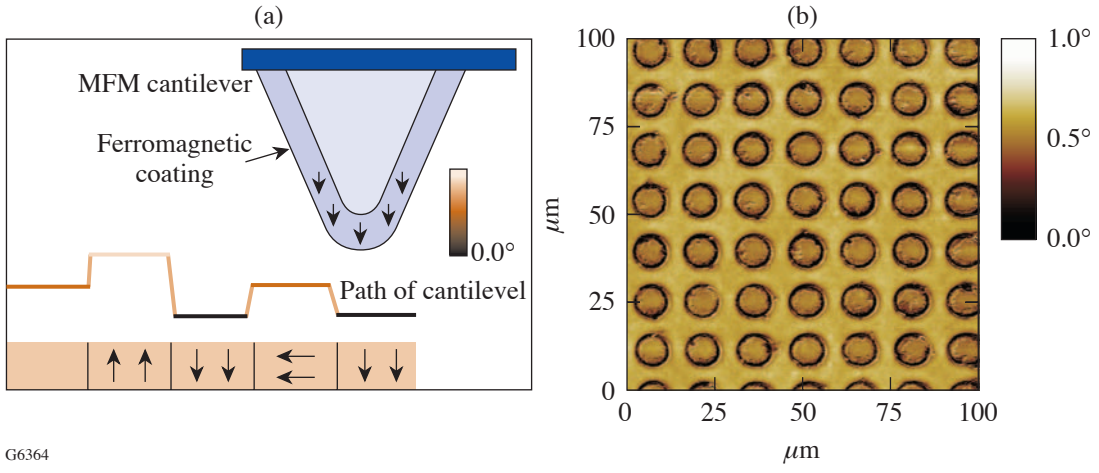

Figure 99.93
(a) An illustration of the magnetic interactions between MFM tip and patterned substrate and (b) MFM phase image of fct FePt magnetic rings made by extended oCP.

In conclusion, it has been demonstrated that a new patterning approach can be developed by controlling contact areas between the roof of an elastomeric stamp and the substrate surface to create size-reduced patterns. This technique is unique in that it offers a tool for making new patterns that may not exist on the original masters. The method is versatile and used to pattern self-assembled monolayers as well as thin films of nanoparticles. Fabrication of submicron-sized patterns is feasible with properly designed elastomeric stamps. The magnetic rings and anti-ring structures could have various novel applications, such as the study of magnetization reversal,[21] metastable states of magnetic rings,[12,22–24] and ring-based magnetic biological separations and manipulations.[25]

ACKNOWLEDGMENT

This work was supported by the National Science Foundation and the U.S Department of Energy (DOE, DE-FC52-92SF19460) through the Laboratory for Laser Energetics at University of Rochester. We thank Mr. Justin Jiang of Harvard University for the gold substrates and Dr. Semyon Papernov (AFM and MFM) and Mr. Brian McIntyre (SEM) for help. The support of DOE does not constitute an endorsement by the DOE of the views expressed in this article.

REFERENCES

1. Y. Xia *et al.*, Chem. Rev. **99**, 1823 (1999).
2. Y. Xia and G. M. Whitesides, Angew. Chem., Int. Ed. Engl. **37**, 550 (1998).
3. B. D. Gates *et al.*, Annu. Rev. Mater. Res. **34**, 339 (2004).
4. Y. Xia and G. M. Whitesides, Langmuir **13**, 2059 (1997).
5. E. Delamarche *et al.*, Adv. Mater. **9**, 741 (1997).
6. D. Armani, C. Liu, and N. Aluru, in *Twelfth IEEE International Conference on Micro Electro Mechanical Systems* (IEEE, Orlando, FL, 1999), pp. 222–227.
7. A. Bietsch and B. Michel, J. Appl. Phys. **88**, 4310 (2000).
8. C. Y. Hui *et al.*, Langmuir **18**, 1394 (2002).
9. J.-G. Zhu, Y. Zheng, and G. A. Prinz, J. Appl. Phys. **87**, 6668 (2000).
10. Y. Chen *et al.*, Microelectron. Eng. **57–58**, 405 (2001).
11. L. J. Heyderman *et al.*, J. Appl. Phys. **93**, 10,011 (2003).
12. F. J. Castaño *et al.*, Phys. Rev. B, Condens. Matter **67**, 184425 (2003).
13. S. B. Clendenning *et al.*, J. Mater. Chem. **14**, 1686 (2004).
14. Q. Guo *et al.*, J. Am. Chem. Soc. **125**, 630 (2003).
15. Q. Guo, X. Teng, and H. Yang, Adv. Mater. **16**, 1337 (2004).
16. H. Yang *et al.*, Adv. Mater. **13**, 54 (2001).
17. X. Teng and H. Yang, J. Mater. Chem. **14**, 774 (2004).
18. X. Teng *et al.*, Nano Lett. **3**, 261 (2003).
19. X. Teng and H. Yang, J. Am. Chem. Soc. **125**, 14,559 (2003).
20. X. Zhu and P. Grütter, MRS Bull. **29**, 457 (2004).
21. S. P. Li *et al.*, Phys. Rev. Lett. **86**, 1102 (2001).
22. M. Kläui *et al.*, Appl. Phys. Lett. **78**, 3268 (2001).
23. M. Kläui *et al.*, Appl. Phys. Lett. **84**, 951 (2004).
24. M. Steiner and J. Nitta, Appl. Phys. Lett. **84**, 939 (2004).
25. H. Lee *et al.*, Nano Lett. **4**, 995 (2004).

Publications and Conference Presentations

Publications

I. A. Begishev, V. Bagnoud, M. J. Guardalben, J. Puth, L. J. Waxer, and J. D. Zuegel, "Parasitic Second-Harmonic Generation in Optical Parametric Chirped-Pulse Amplification," in *OSA Trends in Optics and Photonics (TOPS) Vol. 94, Advanced Solid-State Photonics*, edited by G. J. Quarles (Optical Society of America, Washington, DC, 2004), pp. 32–34.

B. Buerke and D. D. Meyerhofer, "Measurement of Hydrogenic Tunneling Rates in a High-Intensity Laser Focus," Phys. Rev. A **69**, 051402 (2004).

A. C. A. Chen, S. W. Culligan, Y. Geng, S. H. Chen, K. P. Klubek, K. M. Vaeth, and C. W. Tang, "Organic Polarized Light-Emitting Diodes via Förster Energy Transfer Using Monodisperse Conjugated Oligomers," Adv. Mater. **16**, 783 (2004).

C. R. Christensen, D. C. Wilson, C. W. Barnes, G. P. Grim, G. L. Morgan, M. D. Wilke, F. J. Marshall, V. Yu. Glebov, and C. Stoeckl, "The Influence of Asymmetry on Mix in Direct-Drive Inertial Confinement Fusion Experiments," Phys. Plasmas **11**, 2771 (2004).

T. J. B. Collins, J. P. Knauer, R. Betti, T. R. Boehly, J. A. Delettrez, V. N. Goncharov, D. D. Meyerhofer, P. W. McKenty, S. Skupsky, and R. P. J. Town, "Reduction of the Ablative Rayleigh–Taylor Growth Rate with Gaussian Picket Pulses," Phys. Plasmas **11**, 1569 (2004).

J. E. DeGroote, H. J. Romanofsky, I. A. Kozhinova, J. M. Schoen, and S. D. Jacobs, "Polishing PMMA and Other Optical Polymers with Magnetorheological Finishing," in *Optical Manufacturing and Testing V*, edited by H. P. Stahl (SPIE, Bellingham, WA, 2003), Vol. 5180, pp. 123–134.

L. Disdier, R. A. Lerche, J. L. Bourgade, and V. Yu. Glebov, "Capillary Detector with Deuterated Scintillator for Inertial Confinement Fusion Neutron Images," Rev. Sci. Instrum. **75**, 2134 (2004).

J. A. Frenje, C. K. Li, F. H. Séguin, J. Deciantis, S. Kurebayashi, J. R. Rygg, R. D. Petrasso, J. A. Delettrez, V. Yu. Glebov, C. Stoeckl, F. J. Marshall, D. D. Meyerhofer, T. C. Sangster, V. A. Smalyuk, and J. M. Soures, "Measuring Shock-Bang Timing and ρR Evolution of D^3He Implosions at OMEGA," Phys. Plasmas **11**, 2798 (2004) (invited).

L. L. Gregg, A. E. Marino, J. C. Hayes, and S. D. Jacobs, "Grain Decoration in Aluminum Oxynitride (ALON) from Polishing on Bound Abrasive Laps," in *Optical Manufacturing and Testing V*, edited by H. P. Stahl (SPIE, Bellingham, WA, 2003), Vol. 5180, pp. 47–54.

D. F. Grosz, A. Agarwal, A. P. Küng, S. Banerjee, D. N. Maywar, and T. H. Wood, "Performance of a ULH Single Wide-Band All-Raman DWDM Transmission System Over Dispersion-Managed Spans," IEEE Photonics Technol. Lett. **16**, 1197 (2004).

D. F. Grosz, D. N. Maywar, A. P. Küng, A. Agarwal, and S. Banerjee, "Performance of Non-Fibre Based Dispersion Compensation for Long-Haul 10.7 Gbit/s DWDM Transmission," Electron. Lett. **40**, 825 (2004).

B. Hou, J. A. Nees, W. Theobald, G. A. Mourou, L. M. Chen, J.-C. Kieffer, A. Krol, and C. C. Chamberlain, "Dependence of Hard X-Ray Yield on Laser Pulse Parameters in the Wavelength-Cubed Regime," Appl. Phys. Lett. **84**, 2259 (2004).

S. D. Jacobs, "Innovations in Polishing of Precision Optics," in *International Progress on Advanced Optics and Sensors,* Frontiers Science Series, Vol. 40, edited by H. Ohmori and H. M. Shimizu (Universal Academy Press, Tokyo, Japan, 2003), pp. 3–14 (invited).

A. Korneev, P. Kouminov, V. Matvienko, G. Chulkova, K. Smirnov, B. Voronov, G. N. Gol'tsman, M. Currie, W. Lo, K. Wilsher, J. Zhang, W. Slysz, A. Pearlman, A. Verevkin, and R. Sobolewski, "Sensitivity and Gigahertz Counting Performance of NbN Superconducting Single-Photon Detectors," Appl. Phys. Lett. **84**, 5338 (2004).

T. Z. Kosc, K. L. Marshall, and S. D. Jacobs, "Polymer Cholesteric Liquid Crystal Flake Particle Displays Utilizing Maxwell-Wagner Polarization Effects for Switching," in the *Conference Record of the 23rd International Display Research Conference* (Society for Information Display, San Jose, CA, 2003), pp. 237–239.

C. K. Li, F. H. Séguin, J. A. Frenje, R. D. Petrasso, J. A. Delettrez, P. W. McKenty, T. C. Sangster, R. L. Keck, J. M. Soures, F. J. Marshall, D. D. Meyerhofer, V. N. Goncharov, J. P. Knauer, P. B. Radha, S. P. Regan, and W. Seka, "Effects of Nonuniform Illumination on Implosion Asymmetry in Direct-Drive Inertial Confinement Fusion," Phys. Rev. Lett. **92**, 205001 (2004).

A. V. Maximov, J. Myatt, W. Seka, R. W. Short, and R. S. Craxton, "Modeling of Stimulated Brillouin Scattering Near the Critical-Density Surface in the Plasmas of Direct-Drive Targets," Phys. Plasmas **11**, 2994 (2004).

P. W. McKenty, T. C. Sangster, M. Alexander, R. Betti, R. S. Craxton, J. A. Delettrez, L. Elasky, R. Epstein, A. Frank, V. Yu. Glebov, V. N. Goncharov, D. R. Harding, S. Jin, J. P. Knauer, R. L. Keck, S. J. Loucks, L. D. Lund, R. L. McCrory, F. J. Marshall, D. D. Meyerhofer, S. P. Regan, P. B. Radha, S. Roberts, W. Seka, S. Skupsky, V. A. Smalyuk, J. M. Soures, K. A. Thorp, M. Wozniak, J. A. Frenje, C. K. Li, R. D. Petrasso, F. H. Séguin, K. A. Fletcher, S. Padalino, C. Freeman, N. Izumi, J. A. Koch, R. A. Lerche, M. J. Moran, T. W. Phillips, G. J. Schmid, and C. Sorce, "Direct-Drive Cryogenic Target Implosion Performance on OMEGA," Phys. Plasmas **11**, 2790 (2004) (invited).

S. P. Regan, J. A. Delettrez, V. N. Goncharov, F. J. Marshall, J. M. Soures, V. A. Smalyuk, P. B. Radha, B. Yaakobi, R. Epstein, V. Yu. Glebov, P. A. Jaanimagi, D. D. Meyerhofer, T. C. Sangster, W. Seka, S. Skupsky, C. Stoeckl, D. A. Haynes, Jr., J. A. Frenje, C. K. Li, R. D. Petrasso, and F. H. Séguin, "Dependence of Shell Mix on Feedthrough in Direct-Drive Inertial Confinement Fusion," Phys. Rev. Lett. **92**, 185002 (2004).

S. Skupsky, J. A. Marozas, R. S. Craxton, R. Betti, T. J. B. Collins, J. A. Delettrez, V. N. Goncharov, P. W. McKenty, P. B. Radha, T. R. Boehly, J. P. Knauer, F. J. Marshall, D. R. Harding, J. D. Kilkenny, D. D. Meyerhofer, T. C. Sangster, and R. L. McCrory, "Polar Direct Drive on the National Ignition Facility," Phys. Plasmas **11**, 2763 (2004) (invited).

L. Veisz, W. Theobald, T. Feurer, H. Schwoerer, I. Uschmann, O. Renner, and R. Sauerbrey, "Three-Halves Harmonic Emission from Femtosecond Laser Produced Plasmas with Steep Density Gradients," Phys. Plasmas **11**, 3311 (2004).

A. Verevkin, A. Pearlman, W. Slysz, J. Zhang, M. Currie, A. Korneev, G. Chulkova, O. Okunev, P. Kouminov, K. Smirnov, B. Voronov, G. N. Gol'tsman, and R. Sobolewski, "Ultrafast Superconducting Single-Photon Detectors for Near-Infrared-Wavelength Quantum Communications," J. Mod. Opt. **51**, 1447 (2004).

D. C. Wilson, C. W. Cranfill, C. Christensen, R. A. Forster, R. R. Peterson, N. M. Hoffman, G. D. Pollak, C. K. Li, F. H. Séguin, J. A. Frenje, R. D. Petrasso, P. W. McKenty, F. J. Marshall, V. Yu. Glebov, C. Stoeckl, G. J. Schmid, N. Izumi, and P. Amendt, "Multifluid Interpenetration Mixing in Directly Driven Inertial Confinement Fusion Capsule Implosions," Phys. Plasmas **11**, 2723 (2004).

B. Yaakobi, D. D. Meyerhofer, T. R. Boehly, J. J. Rehr, B. A. Remington, P. G. Allen, S. M. Pollaine, and R. C. Albers, "Extended X-Ray Absorption Fine Structure Measurements of Laser Shocks in Ti and V and Phase Transformation in Ti," Phys. Plasmas **11**, 2688 (2004) (invited).

Forthcoming Publications

V. Bagnoud, I. A. Begishev, M. J. Guardalben, J. Keegan, J. Puth, L. J. Waxer, and J. D. Zuegel, "Optical Parametric Chirped-Pulse Amplifier as the Front End for the OMEGA Laser Chain," to be published in Inertial Fusion Sciences and Applications 2003.

T. R. Boehly, D. G. Hicks, P. M. Celliers, T. J. B. Collins, J. H. Eggert, S. J. Moon, E. Vianello, D. D. Meyerhofer, and G. W. Collins, "Properties of Fluid Deuterium Under Double-Shock Compression to Several Mbar," to be published in Physics of Plasmas.

T. J. B. Collins, S. Skupsky, V. N. Goncharov, R. Betti, P. W. McKenty, P. B. Radha, R. Epstein, A. Poludnenko, A. Frank, and S. Mitran, "High-Gain, Direct-Drive Foam Targets for the National Ignition Facility," to be published in Inertial Fusion Sciences and Applications 2003.

R. Epstein, "On the Bell–Plesset Effects: The Effects of Uniform Compression and Geometrical Convergence on the Classical Rayleigh–Taylor Instability," to be published in Physics of Plasmas.

Q. Guo, X. Teng, and H. Yang, "Overpressure Contact Printing," to be published in Nano Letters.

D. R. Harding, F.-Y. Tsai, E. L. Alfonso, S. H. Chen, A. K. Knight, and T. N. Blanton, "Properties of Vapor-Deposited Polyimide Films," to be published in the Journal of Adhesion Science and Technology (invited).

T. J. Kessler, J. Bunkenburg, H. Huang, A. Kozlov, C. Kelly, and D. D. Meyerhofer, "The Coherent Addition of Gratings for Pulse Compression in High-Energy Laser Systems," to be published in Inertial Fusion Sciences and Applications 2003.

J. P. Knauer and C. Gindele, "Temporal and Spectral Deconvolution of Data from Diamond, Photoconductive Devices," to be published in Review of Scientific Instruments.

J. A. Koch, T.W. Barbee, Jr., S. Dalhed, S. Haan, N. Izumi, R. W. Lee, L. A. Welser, R. C. Mancini, F. J. Marshall, T. C. Sangster, V. A. Smalyuk, J. M. Soures, and L. Klein, "Core Temperature and Density Profiles from Multispectral Imaging of ICF Plasmas," to be published in Inertial Fusion Sciences and Applications 2003.

J. A. Koch, T. W. Barbee, Jr., S. Dalhed, S. Haan, N. Izumi, R. W. Lee, L. A. Welser, R. C. Mancini, F. J. Marshall, D. D. Meyerhofer, T. C. Sangster, V. A. Smalyuk, J. M. Soures, L. Klein, and I. Golovkin, "Core Temperature and Density Gradients in ICF," to be published in the Proceedings of the 14th APS Topical Conference on Atomic Processes in Plasmas.

J. Li, W. R. Donaldson, and T. Y. Hsiang, "Simulation of Submicrometer Metal–Semiconductor–Metal Ultraviolet Photodiodes on Gallium Nitride," to be published in Solid-State Electronics.

S. G. Lukishova, A. W. Schmid, C. Supranowitz, A. McNamara, R. W. Boyd, and C. R. Stroud, Jr., "Dye-Doped Cholesteric-Liquid-Crystal Room-Temperature Single Photon Source," to be published in the Journal of Modern Optics.

R. L. McCrory, "Progress in Inertial Confinement Fusion in the United States," to be published in Inertial Fusion Sciences and Applications 2003.

R. L. McCrory, D. D. Meyerhofer, R. Betti, T. R. Boehly, R. S. Craxton, T. J. B. Collins, J. A. Delettrez, R. Epstein, V. Yu. Glebov, V. N. Goncharov, D. R. Harding, R. L. Keck, J. H. Kelly, J. P. Knauer, S. J. Loucks, L. Lund, J. A. Marozas, P. W. McKenty, F. J. Marshall, S. F. B. Morse, P. B. Radha, S. P. Regan, S. Roberts, W. Seka, S. Skupsky, V. A. Smalyuk, C. Sorce, C. Stoeckl, J. M. Soures, R. P. J. Town, B. Yaakobi, J. A. Frenje, C. K. Li, R. D. Petrasso, F. H. Séguin, K. A. Fletcher, S. Padalino, C. Freeman, and T. C. Sangster, "Direct-Drive Inertial Confinement Fusion Research at the Laboratory for Laser Energetics," to be published in the proceedings of Current Trends in International Fusion Research: A Review.

R. L. McCrory, D. D. Meyerhofer, S. J. Loucks, S. Skupsky, R. E. Bahr, R. Betti, T. R. Boehly, R. S. Craxton, T. J. B. Collins, J. A. Delettrez, W. R. Donaldson, R. Epstein, J. A. Frenje, V. Yu. Glebov, V. N. Goncharov, D. R. Harding, P. A. Jaanimagi, R. L. Keck, J. H. Kelly, T. J. Kessler, J. P. Knauer, C. K. Li, L. D. Lund, J. A. Marozas, P. W. McKenty, F. J. Marshall, S. F. B. Morse, R. D. Petrasso, P. B. Radha, S. P. Regan, S. Roberts, T. C. Sangster, F. H. Séguin, W. Seka, V. A. Smalyuk, C. Sorce, J. M. Soures, C. Stoeckl, R. P. J. Town, B. Yaakobi, and J. D. Zuegel, "Progress in Direct-Drive Inertial Confinement Fusion Research at the Laboratory for Laser Energetics," to be published in Nuclear Fusion.

J. Myatt, A. V. Maximov, W. Seka, R. S. Craxton, and R. W. Short, "Modeling Stimulated Brillouin Scattering in the Underdense Corona of a Direct Drive Inertial Confinement Fusion Target," to be published in Physics of Plasmas.

A. V. Okishev and J. D. Zuegel, "Highly-Stable, All-Solid-State Nd:YLF Regenerative Amplifier," to be published in Applied Optics.

J.-R. Park, W. R. Donaldson, and R. Sobolewski, "Characterization of Single- and Double-Fiber–Coupled Diffusing Spheres," to be published in Applied Optics.

B. A. Remington, G. Bazan, J. Belak, E. Bringa, M. Caturla, J. D. Colvin, M. J. Edwards, S. G. Glendinning, D. Ivanov, B. Kad, D. H. Kalantar, M. Kumar, B. F. Lasinski, K. T. Lorenz, J. M. McNaney, D. D. Meyerhofer, M. A. Meyers, S. M. Pollaine, D. Rowley, M. Schneider, J. S. Stölken, J. D. Wark, S. V. Weber, W. G. Wolfer, and B. Yaakobi, "Materials Science Under Extreme Conditions of Pressure and Strain Rate," to be published in Metallurgical and Materials Transactions A.

R. W. Short and A. Simon, "Theory of Three-Wave Parametric Instabilities in Inhomogeneous Plasmas Revisited," to be published in Physics of Plasmas.

S. Skupsky, R. Betti, T. J. B. Collins, V. N. Goncharov, J. A. Marozas, P. W. McKenty, P. B. Radha, T. R. Boehly, J. P. Knauer, F. J. Marshall, D. R. Harding, J. D. Kilkenny, D. D. Meyerhofer, T. C. Sangster, and R. L. McCrory, "Advanced Direct-Drive Target Designs for the NIF," to be published in Inertial Fusion Sciences and Applications 2003.

V. A. Smalyuk, V. N. Goncharov, T. R. Boehly, J. P. Knauer, D. D. Meyerhofer, and T. C. Sangster, "Self-Consistent Determination of Rayleigh–Taylor Growth Rates and Ablation-Front Density in Planar Targets Accelerated by Laser Light," to be published in Physics of Plasmas.

L. Zheng, A. W. Schmid, and J. C. Lambropoulos, "Surface Effects on Young's Modulus and Hardness of Fused Silica by Nanoindentation Study," to be published in the Journal of Materials Research.

Conference Presentations

A. Trajkovska-Petkoska, R. Varshneya, T. Z. Kosc, K. L. Marshall, and S. D. Jacobs, "Manufacture of Shaped Polymer Cholesteric Liquid Crystal Flakes Using Soft Lithography," 12th Annual University of Rochester Symposium on Materials Research (SOMR), Rochester, NY, 3 April 2004.

A. Marino, K. Spencer, J. DeGroote, and S. D. Jacobs, "Chemical Durability of Phosphate Glasses," Industrial Associates, Rochester, NY, 5 April 2004.

J. D. Zuegel, "Wavefront Correction of Laser Rods Using Magnetorheological Finishing (MRF)," QED Executive Symposium, Rochester, NY, 7 April 2004.

The following presentations were made at the 15th Topical Conference on High Temperature Plasma Diagnostics, San Diego, CA, 19–22 April 2004:

S. Ghosh, R. Boni, and P. A. Jaanimagi, "Optical and X-Ray Streak Camera Gain Measurements."

V. Yu. Glebov, C. Stoeckl, T. C. Sangster, S. Roberts, G. J. Schmid, R. A. Lerche, and M. Moran, "NIF Neutron Time-of-Flight Detector Prototypes Test on OMEGA."

O. V. Gotchev, P. A. Jaanimagi, J. P. Knauer, F. J. Marshall, and D. D. Meyerhofer, "KB-PJX—A Streaked Imager Based on a Versatile X-Ray Microscope Coupled to a High-Current Streak Tube" (invited).

J. P. Knauer and C. Gindele, "Temporal and Spectral Deconvolution of Data from Diamond, Photoconductive Devices."

F. J. Marshall, J. A. Oertel, and P. J. Walsh, "A Framed, 16-Image Kirkpatrick–Baez Microscope for Laser–Plasma X-Ray Emission."

V. A. Smalyuk, V. N. Goncharov, T. R. Boehly, J. P. Knauer, D. D. Meyerhofer, and T. C. Sangster, "Self-Consistent Determination of Rayleigh–Taylor Growth Rates and Ablation-Front Density in Planar Targets Accelerated by Laser Light."

C. Stoeckl, W. Theobald, T. C. Sangster, M. H. Key, P. Patel, B. B. Zhang, R. Clarke, S. Karsch, and P. Norreys, "Operation of a Single-Photon–Counting X-Ray CCD Camera Spectrometer in a Petawatt Environment."

The following presentations were made at the International Workshop on Fast Ignition and High Field Physics, Kyoto, Japan, 25–29 April 2004:

D. D. Meyerhofer, "Fast Ignition Research at LLE: Progress and Plans."

D. D. Meyerhofer, "Two High-Energy Beamlines at LLE: OMEGA EP."

W. Theobald, C. Stoeckl, J. A. Delettrez, V. Yu. Glebov, D. D. Meyerhofer, P. B. Radha, T. C. Sangster, V. A. Smalyuk, R. B. Stephens, S. P. Hatchett, J. A. Frenje, C. K. Li, R. D. Petrasso, F. H. Séguin, S. Fujioka, H. Shiraga, and K. A. Tanaka, "Fast-Ignitor Cone Target Fuel Assembly Experiments."

The following presentations were made at the 34th Anomalous Absorption Conference, Gleneden Beach, OR, 2–7 May 2004:

K. Anderson, R. Betti, J. P. Knauer, and V. N. Goncharov, "Simulations and Experiments on Adiabat Shaping by Relaxation."

R. S. Craxton, F. J. Marshall, S. Skupsky, J. A. Delettrez, R. Epstein, J. P. Knauer, P. W. McKenty, and W. Seka, "Polar-Direct-Drive Experiments on OMEGA."

J. DeCiantis, F. H. Séguin, J. R. Rygg, J. A. Frenje, S. Kurebayashi, C. K. Li, C. Chen, V. Berube, R. D. Petrasso, J. A. Delettrez, V. Yu. Glebov, D. D. Meyerhofer, S. Roberts, T. C. Sangster, and J. M. Soures, "Studying the Burn Region in ICF Implosions with Proton Emission Imaging."

J. A. Delettrez, J. Myatt, P. B. Radha, C. Stoeckl, and S. Skupsky, "Simulation of Enhanced Neutron Production in OMEGA EP Cryogenic Implosions."

R. Epstein and W. Fong, "Non-LTE Speed of Sound, Irreversibility, and Thermodynamic Consistency."

J. A. Frenje, C. K. Li, F. H. Séguin, J. DeCiantis, S. Kurebayashi, J. R. Rygg, R. D. Petrasso, J. A. Delettrez, V. Yu. Glebov, D. D. Meyerhofer, T. C. Sangster, J. M. Soures, S. P. Hatchett, S. W. Haan, M. Moran, G. J. Schmid, O. L. Landen, N. Izumi, and R. Stelter, "A High-Resolution Neutron Spectrometer for ρR_{fuel} and Ti Measurements at OMEGA and the NIF."

C. K. Li and R. D. Petrasso, "Stopping and Scattering of Directed Energetic Electrons in High-Temperature Hydrogenic Plasmas."

C. K. Li, F. H. Séguin, J. A. Frenje, R. D. Petrasso, J. A. Delettrez, P. W. McKenty, T. C. Sangster, R. L. Keck, J. M. Soures, F. J. Marshall, D. D. Meyerhofer, V. N. Goncharov, J. P. Knauer, P. B. Radha, S. P. Regan, and W. Seka, "Effects of Nonuniform Illumination on Implosion Asymmetry in Direct-Drive Inertial Confinement Fusion."

A. V. Maximov, J. Myatt, R. W. Short, W. Seka, and C. Stoeckl, "Modeling of Two-Plasmon-Decay Instability in Direct-Drive ICF Experiments."

J. Myatt, A. V. Maximov, R. W. Short, J. A. Delettrez, and C. Stoeckl, "Hybrid Particle-in-Cell Simulations of MeV Electron Transport in Fast-Ignition Targets."

J. R. Rygg, J. A. Frenje, C. K. Li, F. H. Séguin, R. D. Petrasso, J. A. Delettrez, V. Yu. Glebov, V. N. Goncharov, D. D. Meyerhofer, T. C. Sangster, J. M. Soures, and C. Stoeckl, "An Empirical, Dynamic Mix Model for ICF Implosions."

W. Seka, C. Stoeckl, R. Jiang, R. E. Bahr, T. C. Sangster, R. S. Craxton, J. A. Delettrez, A. V. Maximov, J. Myatt, and R. W. Short, "Scattered Light Measurements from Spherical Implosions on OMEGA."

R. W. Short, "On the Convective Two-Plasmon-Decay Instability in Inhomogeneous Plasmas."

The following presentations were made at CLEO 2004, San Francisco, CA, 16–21 May 2004:

V. Bagnoud, I. A. Begishev, M. J. Guardalben, J. Puth, and J. D. Zuegel, "Multiterawatt Laser as a Front End for the OMEGA EP (Extended Performance) Laser Chain."

J. Li, T. Y. Hsiang, and W. R. Donaldson, "Study of Metal–Semiconductor–Metal Ultraviolet Photodiodes in Picosecond Regime."

A. V. Okishev, J. R. Marciante, and J. D. Zuegel, "A Novel Discrete-Arbitrary-Picket-Pulse–Shaping System for the OMEGA Laser Fusion Facility."

J.-R. Park, W. R. Donaldson, K. Kearney, and R. Sobolewski, "Arbitrary Wave Profile Generation of a Laser Using a Digital Micromirror Device."

J. D. Zuegel, V. Bagnoud, T. Mooney, and P. Dumas, "Wavefront Correction of Laser Rods Using Magnetorheological Finishing (MRF)."

S. G. Lukishova, A. W. Schmid, C. M. Supranowitz, N. Lippa, A. J. McNamara, R. W. Boyd, and C. R. Stroud, Jr., "Deterministically Polarized, Room-Temperature Single-Photon Source: Single-Dye Molecule Fluorescence in Liquid Crystal Host," IQEC, San Francisco, CA, 16–21 May 2004.

A. Trajkovska-Petkoska, R. Varshneya, T. Z. Kosc, K. L. Marshall, and S. D. Jacobs, "Electro-Optical Response of Shaped Polymer Cholesteric Liquid Crystal Flakes in an AC Field," Great Lakes Photonics Symposium, Cleveland OH, 7–11 June 2004.

L. B. Glebov, L. N. Glebova, V. I. Smirnov, M. Dubinskii, L. D. Merkle, S. Papernov, and A. W. Schmid, "Laser Damage Resistance of Photo-Thermo-Refractive Glass Bragg Gratings," Solid State and Diode Laser Technology Review, Albuquerque, NM, 8–10 June 2004.

J. B. Oliver and D. Talbot, "Optimization of Electron-Beam Deposition for Large-Aperture NIF Substrates in a Planetary Rotation System," Optical Interference Coatings, Ninth Topical Meeting, Tucson, AZ, 27 June–2 July 2004.

V. Yu. Glebov, C. Stoeckl, T. C. Sangster, S. Roberts, and G. J. Schmid, "NIF Neutron Bang-Time Detector Prototype Test on OMEGA," ICOPS 2004 31st IEEE International Conference on Plasma Science, Baltimore, MD, 28 June–1 July 2004.

T. C. Sangster, "Progress Toward Validation of the Direct-Drive Ignition Concept at OMEGA," 31st European Physical Society Conference on Plasmas Physics, London, United Kingdom, 28 June–2 July 2004.

UNIVERSITY OF
ROCHESTER